CALLISTO:

INDUCTION SIGNALS, ATMOSPHERE AND PLASMA INTERACTION

INAUGURAL-DISSERTATION
ZUR
ERLANGUNG DES DOKTORGRADES
DER MATHEMATISCH-NATURWISSENSCHAFTLICHEN FAKULTÄT
DER UNIVERSITÄT ZU KÖLN

VORGELEGT VON
MARIO SEUFERT
AUS SCHWEINFURT

KÖLN, 2012

Berichterstatter: (Gutachter)	Prof. Dr. Joachim Saur Prof. Dr. Fritz M. Neubauer

Tag der mündlichen Prüfung: 08.10.2012

To my beloved son David.

May the spirit of the Enlightenment guide you
through a long, pleasant and cheerful life.

Abstract

Callisto's magnetic field environment and ionosphere are examined using a model for the magnetic fields induced in the satellite's interior and 3D magnetohydrodynamic (MHD) simulations for Callisto's interaction with the Jovian magnetospheric plasma. The induction model is also applied to the other Galilean moons Io, Europa and Ganymede to investigate the inductive responses of the satellites assuming the existence of interior conductive ocean and core layers.

The first part of this thesis includes a thorough study of the frequencies and amplitudes of the temporary variable part of the magnetospheric field i.e., the inducing or primary fields and the strength of the induced or secondary fields originating in the interiors of the satellites. The primary fields are determined by using models for Jupiter's intrinsic field, fields generated by the magnetospheric current sheet and fields caused by Chapman-Ferraro currents at the magnetopause boundary. A Fourier analysis of the magnetic field time series along the Galilean moons' orbits predicted by this composite magnetospheric model yields the frequencies and amplitudes of the primary fields. A second model for the inductive response of a multi-layered conductivity structure based on two separate interior models for each satellite is applied to study the strength of the secondary fields at the surface. The synodic rotation period of Jupiter (~10 h), the orbital periods of the satellites (from 42 h at Io to 400 h at Callisto) and the solar rotation period (642 h) are identified as the primary periodicities for the inducing fields at the Galilean moons. It is further shown that conductive ocean layers at Callisto and the other satellites should generate detectable magnetic signals for several frequencies in the vicinity of the satellites. The inferred strength of the signals at the surface ranges from 16 nT at Callisto to 210 nT for a magma ocean at Io. Possible conductive core layers, however, do not significantly modify the signals outside the satellites.

The interaction of the magnetospheric plasma with the atmosphere and interior of the satellite has been extensively studied for the cases of Io, Europa and Ganymede. The second part of this work represents the first in depth numerical study of Callisto's plasma interaction. A 3D MHD model, taking into account collision, ionization and recombination processes due to the neutral atmosphere of the satellite, is used to examine Callisto's ionosphere and magnetic field environment. In addition to the expected modifications of the magnetospheric plasma flow embodied e.g., by the generation of Alfvén wings and the upstream pileup of the magnetic field, the model results indicate a complex behavior of the plasma flow in Callisto's tail. The model predicts the existence of extended regions where an oppositely directed plasma flow is associated with vertical eddy structures and disturbances of the regions downstream of the Alfvén wings. The plasma densities within the simulation are compared to measured electron density profiles to investigate the underlying reason for the inferred dependence of the generation of an ionosphere on the solar illumination of Callisto's ram side. A parameter study performed for different configurations of the neutral atmosphere shows that an atmosphere primarily confined to the upstream hemisphere of Callisto suitably explains the measured variability of the ionospheric plasma densities. Additional reasons for this variability are varying conditions for the magnetospheric plasma flow, differences in the solar photon flux and differences in the plasma particle transport towards Callisto's flanks depending on the solar illumination geometry. So far, observations of Callisto's airglow yield no direct evidence for the existence of an O_2 atmosphere. The interaction model predicts a disk integrated auroral intensity of ~6 R for earthbound measurements. This value is in agreement with the upper limit of 15 R determined by *Strobel et al.* (2002). The simulation results for several flyby scenarios are compared to magnetic field data taking into account the predicted induced fields. Even though the plasma interaction signatures give rise to ambiguities regarding the secondary field strength, the existence of a conductive interior ocean layer is inevitable in order to explain the measured data. An ocean at a maximum depth of ∼150 km, with a thickness of ∼10 km and a conductivity of sea water (~5 S m^{-1}), which is in agreement with an interior model by *Kuskov and Kronrod* (2005a), yields induced signals within the plausible range suggested by the observations. The hypothesis of an asymmetric neutral atmosphere is consistent with both radio occultation and magnetometer measurements performed by the Galileo spacecraft.

Zusammenfassung

In der vorliegenden Dissertation wird die mögliche Existenz eines unterirdischen Wasserozeans, die Variabilität der Ionosphäre und der Aufbau der Neutralgasatmosphäre sowie die Plasmawechselwirkung des Jupitermondes Kallisto untersucht. Indizien für die Existenz eines Ozeans bei Kallisto ergeben sich aus der Interpretation von Magnetfelddaten der Raumsonde Galileo (siehe z.B. *Khurana et al.* 1998, *Zimmer et al.* 2000). Die gemessenen Magnetfeldstörungen werden Feldern zugeordnet, die aufgrund der zeitlichen Variabilität des magnetosphärischen Hintergrundfeldes in leitfähigen Schichten im Inneren des Mondes induziert werden. Die Existenz eines Wasserozeans mit einem ausreichenden Anteil an gelösten Mineralien wäre eine plausible Erklärung für die Entstehung induzierter Felder bei dem hauptsächlich aus Wassereis bestehenden Mond Kallisto. Das Gesamtmagnetfeld in Kallistos Umgebung entsteht durch die Superposition verschiedener Teilfelder. Diese Felder umfassen das magnetosphärische Hintergrundfeld, mögliche induzierte Felder aus dem Inneren des Mondes und Magnetfelder, die bei der Wechselwirkung Kallistos und seiner Atmosphäre mit dem magnetosphärischen Plasma entstehen. Sowohl induzierte Magnetfelder als auch Magnetfeldstörungen die aufgrund der Wechselwirkung mit dem Hintergrundplasma entstehen, erzeugen zum Teil ähnliche dipolartige Signaturen. Eines der Hauptziele dieser Arbeit ist die Zuordnung der gemessenen Störungen zu möglichen Beiträgen zum Gesamtmagnetfeld und die Verifikation der Existenz induzierter Felder unter Berücksichtigung der Plasmawechselwirkung Kallistos. Mit Hilfe eines Modells, das sowohl eine Beschreibung des magnetosphärischen Feldes, als auch der im Inneren des Mondes induzierten Magnetfelder enthält, können die induzierenden oder primären Anteile des Hintergrundfeldes und der Beitrag der induzierten Felder zum gemessenen Signal vorhergesagt werden. Die Untersuchung der induzierten Feldanteile wurde mit Hilfe des für Kallisto entwickelten Modells auch auf die anderen Galileischen Monde ausgeweitet. Das für die Abschätzung der Magnetfeldstörungen die aufgrund der Plasmawechselwirkung entstehen benötigte magnetohydrodynamische (MHD) Modell ermöglicht zudem eine Untersuchung der von *Kliore et al.* (2002) gemessenen zeitlichen Variabilität der Ionosphäre Kallistos. Das entsprechende Modell gestattet die Analyse der möglichen Ursachen für die gemessenen niedrigen ionosphärischen Plasmadichten im Fall einer sonnenbeschienenen, dem Plasmafluss entgegengesetzt gerichteten Hemisphäre Kallistos. Neben diesen Hauptzielen der Arbeit wird zudem noch die allgemeine Natur der Plasmawechselwirkung bei Kallisto und die Intensität der Aurora Kallistos untersucht.

Das zur Erzeugung induzierter Felder notwendige, zeitlich variable induzierende oder auch primäre Magnetfeld ist im Fall der Galileischen Monde durch das magnetosphärische

Feld Jupiters gegeben. In der vorliegenden Arbeit wird dieses Feld durch verschiedene Teilmodelle beschrieben. Es handelt sich um Modelle für Jupiters intrinsisches Magnetfeld, für das Feld der magnetosphärischen Stromschicht und für die an der Magnetopausengrenzschicht durch Chapman Ferraro Ströme generierten Felder. Aus künstlichen Zeitreihen für das magnetosphärische Feld entlang der Mondbahn werden die vorhandenen Frequenzen und dazugehörigen Amplituden des primären Feldes bestimmt. Die Hauptfrequenzen des Primärfeldes sind durch die synodische Rotationsperiode Jupiters bezüglich der Monde (∼10 h), die Orbitalperiode der Monde (zwischen 42 h für Io und 400 h für Kallisto) und die Rotationsperiode der Sonne (642 h) gegeben. Als weitere Anregungsfrequenzen wurden ganzzahlige Vielfache der zuvor genannten Periodizitäten bestimmt. Mittels eines analytischen Modells für das induzierte oder auch sekundäre Feld eines sphärischen Körpers mit Schichten unterschiedlicher elektrischer Leitfähigkeit kann das an der Oberfläche der Monde messbare induzierte Feld bestimmt werden. Als Grundlage für die Leitfähigkeitsstruktur der Monde werden je zwei gängige Modelle des Mondinneren verwendet, die jeweils die mögliche Existenz eines Wasserozeans oder Magmaozeans (bei Io) berücksichtigen. Die induktive Antwort der Ozeane erzeugt für alle Monde deutlich messbare Magnetfelder bei verschiedenen Anregungsfrequenzen. Der maximale Betrag der entsprechenden Felder liegt bei 16 nT für Kallisto und steigt auf bis zu 210 nT für Io. Die Bestimmung der Beiträge eines leitfähigen Kerns zum sekundären Feld an der Oberfläche zeigt, dass für keinen der Galileischen Monde eine deutliche Änderungen des Gesamtfeldes zu erwarten ist.

Im weiteren Verlauf der Arbeit werden die Wechselwirkung Kallistos mit dem magnetosphärischen Plasma sowie die Ionosphäre und Neutralgasatmosphäre des Mondes untersucht. Während die Plasmawechselwirkung der anderen Galileischen Monde bereits Thema zahlreicher veröffentlichter Studien war, wird in dieser Arbeit das erste detaillierte numerische Modell der Wechselwirkung Kallistos vorgestellt. Im Rahmen der MHD wurde ein Modell formuliert, das den Einfluss der Atmosphäre Kallistos auf das Hintergrundplasma aufgrund von Stößen, Photo- und Stoßionisation sowie dissoziativer Rekombination beschreibt. Die allgemeine Struktur der Modellergebnisse für alle Plasmaparameter weist neben den erwarteten Signaturen der Plasmawechselwirkung, wie z.B. der Entstehung von Alfvénflügeln oder der magnetischen Pileup-Region in Anströmrichtung, zusätzliche komplexe Signaturen in der Schweifregion Kallistos auf. Innerhalb ausgedehnter Bereiche stromabwärts des Mondes fließt das Plasma unerwartet in Richtung Kallistos. Die dazugehörigen Strömungen verursachen sowohl die Ausbildung vertikaler Wirbelstrukturen als auch signifikante Störungen der Alfvénflügel. Ein Vergleich der ionosphärischen Plasmadichten innerhalb des Simulationsgebietes mit den gemessenen Profilen der Elektronendichten von *Kliore et al.* (2002) erlaubt die Untersuchung der Ursachen für die Variabilität der Ionosphäre in Abhängigkeit der Richtung der solaren Einstrahlung. Eine Parameterstudie für verschiedene Geometrien und Zusammensetzungen der Neutralgasatmosphäre ergibt, dass die gemessenen ionosphärischen Dichteschwankungen für verschiedene Positionen der Sonne relativ zur Richtung des anströmenden Plasmas für eine asymmetrische, hauptsächlich auf die Anströmrichtung beschränkte Atmosphäre, in Übereinstimmung mit den Messungen, deutlich erhöht sind. Weitere Ursachen für die beobachteten Dichteschwankungen sind Änderungen der Parameter des Hintergrundplasmas, Variationen der Intensität der solaren Einstrahlung und

der unterschiedlich stark ausgeprägte Transport ionosphärischer Teilchen an die Jupiter zu- und abgewandten Flanken Kallistos für verschiedene Richtungen der solaren Einstrahlung. Eine Modellabschätzung der Intensität der bisher nicht eindeutig nachgewiesenen O_2-Aurora Kallistos ergibt eine Gesamtstrahlung von 6 R für erdgebundene Beobachtungen. Dieses Ergebnis liegt innerhalb des bisher ermittelten oberen Grenzwertes für die Strahlungsintensität von 15 R (*Strobel et al.* 2002). Der Vergleich der Modellergebnisse für das Magnetfeld in Kallistos Umgebung mit den Galileo-Messungen für verschiedene Vorbeiflüge zeigt, dass trotz ähnlicher Signaturen der induzierten und durch Plasmawechselwirkung erzeugten Magnetfelder eine Erklärung der Daten ohne die Berücksichtigung induzierter Felder nicht möglich ist. Ein Wasserozean in 150 km Tiefe unter der Oberfläche, mit einer Ausdehnung von ungefähr 10 km und einer Leitfähigkeit nahe der irdischer Ozeane von 5 S m^{-1}, erzeugt Induktionssignale, die innerhalb der vorgegebenen Grenzen gut mit den Magnetfelddaten übereinstimmen. Ein solcher Ozean wäre zudem konsistent mit gängigen Modellen für Kallistos Inneres (z.B. dem Modell von *Kuskov and Kronrod* 2005a). Die Änderung der Signaturen der Plasmawechselwirkung aufgrund einer asymmetrische Neutralgasverteilung ist ebenfalls konsistent mit den gemessenen Werten für das Magnetfeld.

Contents

1 Introduction

The four Galilean moons, named after their discoverer Galileo Galilei[I], are among the most intensively studied planetary bodies. Io's intensive volcanism, Europa's shallow subsurface ocean and Ganymede's intrinsic magnetic field are features that make these bodies unique compared to most of the other satellites in our solar system. The scientific attention received by the fourth of Jupiter's lovers[II] Callisto to the present day is dwarfed by the long shadow of its sister satellites. Consequently, there are still numerous open questions regarding Callisto, some of which we try to enlighten in the course of this thesis.

One of the main tools scientists use today to study the satellites of our neighbor planets is the analysis of magnetic field data gathered by magnetometers on board various spacecraft visiting those bodies. Surface features such as the giant water plumes at Saturn's satellite Enceladus, the interaction of the satellites and their atmospheres with their plasma environment and, by the analysis of intrinsic induced and dynamo magnetic fields, even their interior structure can all be studied using these data. Based on an analysis of the magnetic field perturbations measured by the Galileo spacecraft near the satellite it was concluded that Callisto, like Europa and possibly Ganymede, possesses an interior liquid water reservoir (*Khurana et al.* 1998, *Neubauer* 1998a, *Kivelson et al.* 1999, *Zimmer et al.* 2000). This presumably conductive ocean layer is exposed to the temporally variable Jovian magnetospheric field at Callisto's position. Eddy currents generated inside the water layer give rise to induced magnetic fields detectable outside the satellite. However, the interaction of Callisto with the surrounding magnetospheric plasma also contributes to the magnetic field perturbations in the vicinity of the satellite. In some cases the plasma interaction can mimic induced field signals giving rise to some ambiguities in the interpretation of the data. The obstacle generating the magnetic field perturbations due to the interaction with the magnetospheric plasma consist not only of Callisto's body itself, but also of the intrinsic field due to the induction effect and both Callisto's neutral atmosphere and ionosphere disturbing the plasma flow due to collisions, mass loading effects and the associated ionospheric conductivities. Therefore, a study for Callisto's plasma interaction and induction signals also needs to include a suitable description of the processes occurring within the satellite's atmosphere. In turn a comparison of the model results to magnetic field and other plasma data possibly yields information about Callisto's atmosphere-ionosphere system.

[I] * 02.15.1564 in Pisa; †01.08.1642

[II] according to Greek mythology

In the present work we deepen previous studies of the induced magnetic fields at Callisto and extend them by applying models for the plasma interaction of Callisto. An analysis of the possible induced fields is given in Chapter 2 of this thesis. Based on models for the magnetospheric background field and a model for the induced field generated within a layered sphere we infer the available amplitudes and frequencies of the inducing fields and predict the associated strength of the induced field at the satellite's surface. The corresponding models developed to analyze Callisto's induction signals were further applied to Io, Europa and Ganymede to obtain a complete picture of the possible induction signals at the Galilean moons. In Chapter 3 we present the first in depth study of Callisto's plasma interaction. This study is based on a 3D magnetohydrodynamic (MHD) model of Callisto's plasma environment using an extended version of the ZEUS-MP single-fluid MHD code (*Hayes et al.* 2006). Next to a general analysis of the plasma interaction processes at Callisto the model capabilities are used to infer information about Callisto's atmosphere-ionosphere system. We analyze several possible reasons for the temporal variability of Callisto's ionosphere observed by *Kliore et al.* (2002) and discuss possible configurations of the neutral atmosphere. Further we give predictions for the intensities of Callisto's O_2 aurora whose existence was not conclusively verified to this date. Finally, we compare our model results to magnetic field data to analyze the plausibility of the assumption of an interior ocean layer generating induced fields, possible implications for Callisto's neutral atmosphere and the general nature of the interaction signatures.

In this chapter we start with a short introduction to the Jovian system. Apart from the properties of Callisto relevant for the models and results presented in this thesis we discuss properties of the other Galilean satellites for comparison and to establish the base for the induced field study in Chapter 2. Additionally, we shortly introduce the Jovian magnetospheric system which defines the ambient conditions for all Galilean satellites. As induction and the plasma interaction effects are both relevant for the interpretation of the results obtained in Chapter 2 and Chapter 3, we also give a general introduction for these two processes in the present chapter.

1.1 The Jovian system

Jupiter and its satellites are often dubbed a miniature solar system embedded in our planetary system. Jupiter itself (Figure 1.1) is the largest of the outer planets' gas giants with a mass of $\sim 1.9 \times 10^{27}$ kg and an equatorial radius (R_J) of 71,492 km. Jupiter orbits the Sun with a perihelion of ~4.95 AU[III] and an aphelion of ~5.46 AU. The planet rotates about itself rather rapidly compared to most of the planets of our solar system, with a period of ~10 h. So far 67 satellites of Jupiter have been discovered. The four Galilean moons Io, Europa, Ganymede and Callisto are, however, by far the most massive bodies in the Jovian system. The following section gives a short overview of the properties of these satellites.

[III] 1 AU $\approx 150 \times 10^6$ km. The distance between the Earth and the Sun.

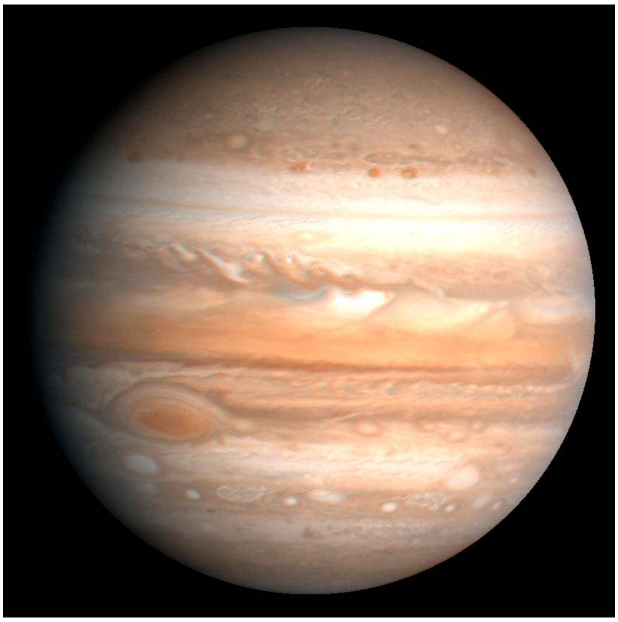

Figure 1.1: *Jupiter view taken by the Cassini spacecraft (Courtesy of NASA / JPL / University of Arizona).*

1.1.1 Properties of the Galilean moons

Io, Europa and Ganymede

The four Galilean moons Io, Europa, Ganymede and Callisto (Figure 1.2) are comparatively large, massive satellites for solar system standards (Table 1.1). Ganymede, in fact, is even the largest of all known satellites. While the two outermost satellites Callisto and Ganymede consist to a large extent (~50 wt%[IV]) of water ice (*Kuskov and Kronrod* 2005b), ice at Europa is primarily confined to a surface layer of ~80 to 170 km thickness (*Anderson et al.* 1998). The innermost satellite Io is essentially depleted of water (*McKinnon* 2007). This general composition of the satellites is also reflected by their mean densities given in Table 1.1.

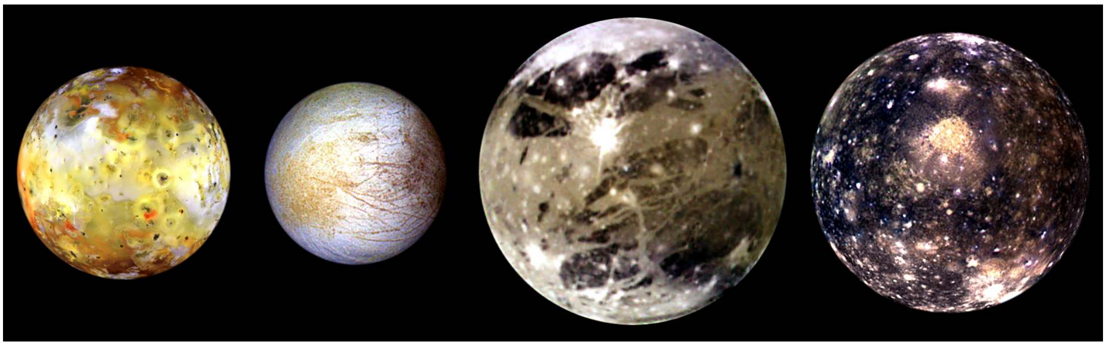

Figure 1.2: *Global images of the Galilean moons (from left right: Io, Europa, Ganymede and Callisto) taken by the Galileo spacecraft (Courtesy of NASA / JPL / DLR).*

[IV] weight percent

	Callisto	**Ganymede**	**Europa**	**Io**	Jupiter
Semi-major axis [R_J]	26.3	15.0	9.4	5.9	5.2 AU
Rotation period [h]	400.6	171.7	85.2	42.5	9.9
Eccentricity	0.007	0.001	0.009	0.004	0.048
Inclination [°]	0.19	0.17	0.47	0.04	1.31
Mean radius [km]	2,410	2,631	1,561	1,822	71,492 (eq)
Mass [kg]	1.1×10^{23}	1.5×10^{23}	4.8×10^{22}	8.9×10^{22}	1.9×10^{27}
Mean density [g cm^{-3}]	1.8	1.9	3.0	3.5	1.3
C/MR^2	0.355	0.315	0.346	0.376	0.254

Table 1.1: *Properties of the Galilean moons and Jupiter after Weiss (2004). For Jupiter the semi-major axis is given in AU and the radius refers to the equatorial value. The values for the normalized moments of inertia (C/MR^2) were given by Anderson et al. (1996, 1998, 2001a,b) for the Galilean moons and Ward and Canup (2006) for Jupiter.*

All of the Galilean moons perform synchronous rotations around Jupiter i.e., their orbital and rotational periods are equal. The orbital paths of the satellites are not only defined by Jupiter's strong gravitational field but are additionally influenced by strong 1:2:4 Laplace resonances between Io, Europa and Ganymede and a weaker 3:7 resonance between Ganymede and Callisto (*Peale et al.* 1979). These resonances, evident in the orbital periods of the satellites, lead to enhanced eccentricities of the satellites' orbits (Table 1.1). Due to these eccentricities all satellites perform a periodical movement inside Jupiter's gravitational field which, in combination with the synchronous rotation, gives rise to strong tidal forces affecting their interiors and surfaces.

These forces are especially prominent at Io where they lead to an extensive tidal heating of the interior and to the most distinct surface volcanism in our solar system. According to several interior models of Io (e.g., *Keszthelyi et al.* 1999, *Zhang* 2003, *Keszthelyi et al.* 2004), tidal forces may hypothetically sustain a semi-liquid or mushy magma ocean layer. However, such a global magma layer is not essentially necessary to create Io's volcanism. At Europa tidal heating is most likely the main energy source which maintains a subsurface liquid water reservoir (*Cassen et al.* 1979). Additionally, tidal forcing may play a role in the generation of Europa's surface features such as ridges and troughs (*Greeley et al.* 2004). Even though Ganymede's surface shows to some extent similar surface structures, these features have an age of ~2 Gyr, much older than at Europa (*Pappalardo et al.* 2004). It is unknown if these structures were created by an ancient subsurface ocean layer. It is also not known whether such a layer is still present in the deep interior of Ganymede today.

The values for the normalized moments of inertia given in Table 1.1 indicate the internal structure of the satellites. For a homogeneous sphere this value approaches C/MR^2 = 0.4. The low value of 0.315 for Ganymede points to a density concentration towards its core. Models for Ganymede's interior (e.g., *Anderson et al.* 1996, *Zhang* 2003, *Kimura et al.* 2009, *Bland et al.* 2009) suggest a clear separation between an outer water ice layer with a thickness of ~1,000 km, a surrounding silicate mantle and a central iron core whose extension is rather uncertain (~500 to 1,000 km). Another evidence for a distinct core layer at Ganymede is its intrinsic magnetic field discovered by the Galileo spacecraft (*Kivelson et al.* 1996), which is likely generated in a central Fe or FeS layer (*Schubert et al.* 2004). Io, in contrast, shows almost no sign of a density concentration towards its center. One reason for this is the absence of water ice in Io's composition. Interior models (e.g., *Anderson et al.* 2001a, *Zhang* 2003, *Keszthelyi et al.* 2004) suggest a rough structuring in a thin lithospheric layer of ~20 to 30 km, a partially molten mantle which probably shows a gradual increase in its density and a gradual decrease of the melt fraction and an inner core of ~500 to 900 km thickness. Europa, finally, is primarily differentiated with an outer water ice shell up to a depth of 80 to 170 km, a chondritic mantle and a central Fe-FeS core with a radius of ~450 to 650 km (e.g., *Anderson et al.* 1998, *Kuskov and Kronrod* 2005a). Besides gravity measurements used, for example, to infer the normalized moments of inertia, electromagnetic sounding using induced fields can provide valuable information about the Galilean moons' interiors (e.g., *Neubauer* 1999, *Saur et al.* 2010). Determining the available signal amplitudes and frequencies for several interior models for all satellites is one of the key goals of the present thesis (Chapter 2).

All Galilean satellites possess tenuous atmospheres (*McGrath et al.* 2004). The primary atmospheric constituent at Io is SO_2, with a mean column density of $\sim 10^{16}$ to 5×10^{16} cm^{-2} (*Lellouch et al.* 2007). The ultimate source of this atmosphere is Io's volcanic activity, even though its generation may involve secondary processes such as sublimation of volcanic material from the surface (*Saur and Strobel* 2004). In contrast, Europa's O_2 atmosphere is generated by sputtering processes sustained by the bombardment of the satellites surface by energetic charged particles (*Ip* 1996, *Saur et al.* 1998). The molecular column densities of this atmosphere is considerably smaller than at Io and, according to *Hall et al.* (1998), ranges between 2×10^{14} to 14×10^{14} cm^{-2}. The same authors report comparable values of 10^{14} to 10^{15} cm^{-2} for the column densities of an O_2 atmosphere at Ganymede.

Callisto

Though Callisto (Figure 1.3) resembles Ganymede in its composition, size and location in the Jovian system, their interior structures show significant differences. Callisto's considerably higher normalized moment of inertia (0.355 with respect to 0.315 at Ganymede, see Table 1.1) indicates that its interior is only partially differentiated (*Anderson et al.* 2001b). The reason for this dichotomy of the two largest Jovian satellites is still not completely understood. One hypothesis by *Barr and Canup* (2010) states that Ganymede and Callisto took different paths in their thermal evolution, due to deviations in the energy input by impacts during the late heavy bombardment. Another possible hint may be the difference in the tidal heating (*Showman and Malhotra* 1997). While Ganymede is affected by Europa and Io due to their 1:2:4 resonance, Callisto only encounters a weak 3:7 resonance with Ganymede.

Whatever the reason for the dichotomy might be, it led to an interior structure of Callisto which is best described by a continuous increase of the rock to ice composition ratio towards the center of the satellite (*Anderson et al.* 2001b). Whether this increase occurs continuously or stepwise is, however, not clear. Typical interior models for Callisto (e.g., *Anderson et al.* 2001b, *Moore and Schubert* 2003, *Zhang* 2003, *Kuskov and Kronrod* 2005a) involve three to six layers with an outer layer of nearly pure water ice which may harbor a sublayer of liquid water, intermediate mantle layers with increasing silicate

Figure 1.3: *Global images of Callisto taken by the Galileo spacecraft (Courtesy of NASA / JPL / Ted Stryk).*

weight fractions and a core layer of pure silicate or iron-silicate mixtures. Valid core radii for Callisto range up to 1,300 km. The state of Callisto's core is unclear. However, the absence of an internal dynamo field and the weak differentiation contradict the assumption of a pure iron core layer. The extension of the outer water ice shell is ~300 km. It may contain a water ocean layer at a depth of ~150 km with a maximum thickness of ~180 km (*Kuskov and Kronrod* 2005a). In spite of the weak tidal heating at Callisto, this liquid layer could be preserved by internal radiogenic heat sources (*Mueller and McKinnon* 1988, *Kuskov and Kronrod* 2005a). The existence of an intrinsic liquid water ocean layer is also supported by magnetic field measurements (*Neubauer* 1998a, *Khurana et al.* 1998, *Kivelson et al.* 1999, *Zimmer et al.* 2000). The analysis of these magnetic signals using models of Callisto's inductive response and, for the first time, its interaction with the magnetospheric plasma is the main motivation for this thesis. In the Chapters 2 and 3 we discuss to which extent Callisto's interior layers contribute to the formation of the measured magnetic perturbations.

In contrast to the other Galilean moons, Callisto at first glance shows no evidence for geologic activity at its surface (*Greeley et al.* 2000, *Moore et al.* 2004). The most prominent features on Callisto's surface are crater structures (see Figure 1.3). Furthermore, Callisto possesses the lowest albedo (0.2) of all Galilean satellites (*Buratti* 1991). This implies that Callisto's surface is comparatively old. There is, however, evidence for a crater degradation process on Callisto (*Moore et al.* 1999). Due to its low albedo, Callisto's maximum surface temperature is the highest of all Galilean moons and reaches values of ~150 K at noon (*Hanel et al.* 1979, *Carlson* 1999, *Moore et al.* 2004). Therefore, sublimation of H_2O occurs where the icy crust is exposed to free space. The remaining nonvolatile components of the ice crust's composition form a thin dark silicate layer. At steep slopes such as crater rims the dust layer may be subject to mass movement, which in turn exposes new icy material. This procedure leads to a degradation of the crater rims and to a overall darkening of Callisto's surface, in spite of the icy nature of the crustal layer below.

In analogy to Europa, sputtering of surface material plays a major role in the generation of Callisto's atmosphere (*Kliore et al.* 2002, *Liang et al.* 2005), even though the amount of magnetospheric energetic particles at Callisto's orbit position is significantly lower (*Moore et al.* 2004). An additional source for the neutral atmosphere are H_2O particles sublimated on the surface. However, so far no successful direct measurements of the expected H_2O and (due to dissociation processes) O_2 atmospheric components are available (*Strobel et al.* 2002). Instead, the Galileo Near-Infrared Mapping Spectrometer (NIMS) revealed the existence of a CO_2 atmosphere at Callisto with a surface density of $\sim 4 \times 10^8$ cm^{-3} (*Carlson* 1999) and a scale height of ~23 km modeled for a surface pressure of 7.5×10^{-9} mbar. The source for this CO_2 atmospheric component is not clear to this date. Another source of information for Callisto's atmosphere are radio occultation measurements of the ionospheric electron densities (*Kliore et al.* 2002). The measured peak densities of ~15,300 and 17,400 cm^{-3} during Galileo's C22 and C23 flybys[V] are remarkably high, compared to the ionospheres of the other Galilean satellites (e.g., 10,000 cm^{-3} at Europa according to *Kliore et al.* 1997). Such high values can not be explained by photo and impact ionization of the CO_2 atmospheric component alone. *Kliore et al.* (2002) propose the existence of an undiscovered O_2 component with a surface density of $\sim 10^{10}$ cm^{-3} to resolve this issue. The C9 radio occultation measurements of Galileo revealed no clear ionosphere signal beyond error bars. *Kliore et al.* (2002) suggest that the solar illumination of Callisto's ram side, encountered during the C22 and C23 flybys but not at C9, might be a necessary condition for the formation of an ionosphere. *Liang et al.* (2005) give a model for the neutral atmosphere which reproduces the above measurements taking into account an additional atmospheric O_2 component with a surface density of 7×10^9 cm^{-3} and a scale height of 30 km. Based on the chemistry in their model they also predict a significant H_2O abundance with a surface density of $\sim 2 \times 10^9$ cm^{-3} and several minor species.

In the course of the present thesis, we simulate the C9, C22 and C23 plasma interaction scenarios to investigate the possible reasons for the differences in the ionospheric densities (Chapter 3). Further, models for a pure CO_2 atmosphere, models additionally considering an O_2 component and models assuming an asymmetric atmosphere generated by sputtering are compared to the electron density and magnetic field data, to infer information about the state of the atmosphere. Both the induction model and the MHD interaction model presented in this thesis depend on the magnetospheric conditions at the location of Callisto and the other Galilean moons. The next section gives a brief introduction to Jupiter's magnetospheric system to establish a base for the upcoming discussions.

[V] For the numbering of the flybys "C" indicates a targeted encounter of Callisto and the appended number denotes the orbit of Galileo around Jupiter.

1.1.2 Jupiter's magnetosphere

While Jupiter as the largest planet in our solar system is still small compared to the Sun, its giant magnetosphere as an entity is the largest object of our solar system. The strength of Jupiter's equatorial surface magnetic field is ~420,000 nT, roughly 14 times stronger than at Earth (e.g., *Acuna and Ness* 1976, *Connerney et al.* 1998, *Khurana et al.* 2004). The absolute strength of the field given by the magnetic moment is even 20,000 times larger than the terrestrial one (*Kivelson and Russell* 1995). The field rotates rapidly with the planet's rotational period of 9 h 55 min. The magnetic axis is tilted ~9.6° with respect to the rotational axis towards the right handed System III eastern longitude of ~160° (200° western longitude, also see Figure 1.4). For definition of the System III coordinate system see e.g., the work of *Dessler* (2002) or *Seidelmann and Divine* (1977).

The magnetosphere is primarily populated by plasma produced by charge exchange ionization of neutral particles expelled by Io's volcanoes (e.g., *Bagenal and Sullivan* 1981, *Khurana et al.* 2004). Roughly 1 t s^{-1} of plasma is inserted into the magnetospheric system by Io. Compared to other plasma supplies, such as the solar wind (100 kg s^{-1}) sputtering from the icy moons' surfaces (20 kg s^{-1}) and the Jovian ionosphere (20 kg s^{-1}), Io is by far the most important plasma source (*Khurana et al.* 2004). Consequently, the plasma mainly consists of SO_2 as well as related ion species and electrons in a quasi neutral state (*Krupp et al.* 2004). The freshly produced plasma is electromagnetically

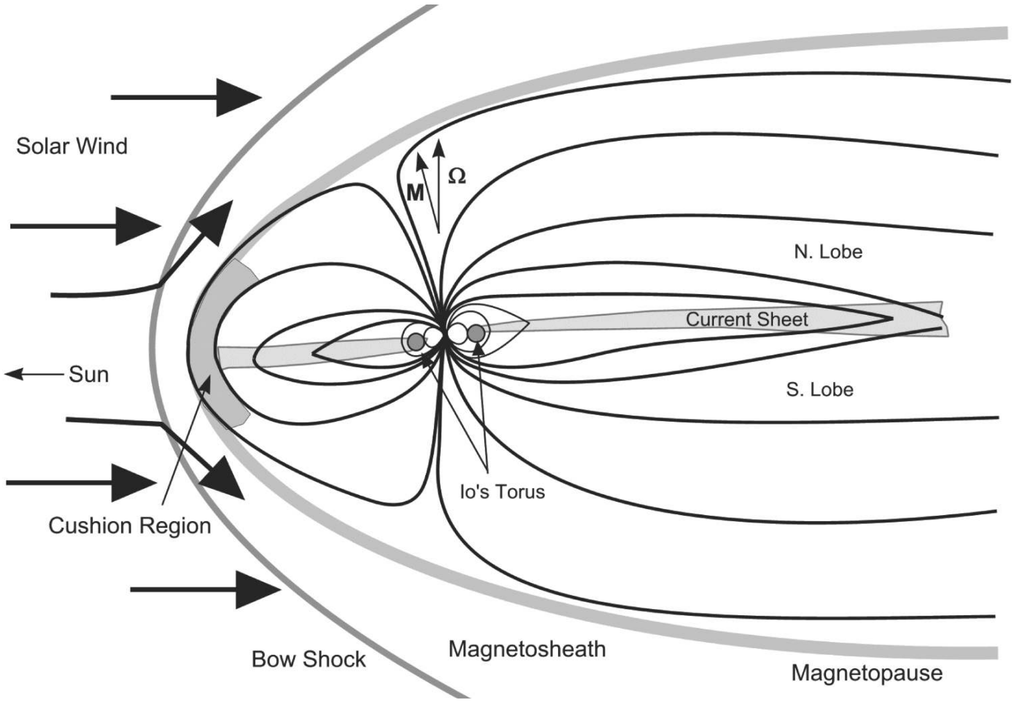

Figure 1.4: *Sketch for the noon-midnight meridian of the Jovian magnetosphere after Khurana et al. (2004). The angle between the vector denoted* M *which represents Jupiter's magnetic axis and the rotational axis given by* Ω *indicates the tilt of the magnetosphere. Black lines indicate the field lines of the magnetospheric field. For the significance of the annotated regions not discussed within this section the reader is referred to the original publication.*

accelerated by Jupiter's magnetic field. In the inner magnetosphere (up to ~10 R_J) the plasma velocities nearly reach the rotational speed of Jupiter. Initially, the plasma is mainly confined to a torus structure near Io, inclined by the tilt of the Jovian field with respect to the plane of the satellites' orbits (see Figure 1.4). Interchange processes induced by centrifugal forces drive the plasma outwards in the horizontal direction. Additionally, electromagnetic mirror forces confine the plasma vertically to regions near the magnetic equator. These processes generate a plasma or current sheet layer with a vertical half thickness of ~2 to 3 R_J (*Khurana* 1997), stretching throughout the entire magnetosphere (For the generation of the plasma sheet see *Khurana et al.* 2004, *Krupp et al.* 2004, and references therein). The magnetospheric plasma flow generates its own, so called current sheet magnetic field which leads to a horizontal stretching of the originally quasi-dipolar field lines in the middle magnetosphere i.e., between 10 and 40 R_J, as indicated in Figure 1.4 (also see e.g., *Connerney et al.* 1981, *Behannon et al.* 1981, *Khurana and Kivelson* 1993, *Khurana* 1997). In the region beyond ~20 R_J the plasma is significantly decelerated below corotational speed due to the inertial corotation lag (*Hill* 1979, 2001). The slow down of the plasma additionally generates a bending or sweep back of the field lines in the azimuthal direction (*Khurana and Kivelson* 1993).

Because of the tilt between the magnetic equator and the orbital plane and due to the rapid rotation of the Jovian magnetospheric field and the current sheet with respect to the satellite's orbital period, Callisto is repeatedly exposed to different magnetospheric regimes. The satellite encounters conditions above and below the current sheet, where the surrounding magnetic field points primarily towards or away from Jupiter and the plasma density is relatively low. During current sheet crossings the plasma density at Callisto increases and the magnetic field points in the vertical direction. However, all of the actual flybys of Galileo at Callisto we consider in the course of this thesis took place away from the current sheets center.

The magnetosphere's extension is confined by the magnetopause boundary depicted in Figure 1.4 (e.g., *Engle* 1992, *Khurana et al.* 2004). In this region the magnetic pressure of the Jovian magnetospheric field and the ram pressure of the solar wind cancel each other. Depending on the current solar wind conditions the location of the magnetopause subsolar point can vary approximately from 45 to 100 R_J (*Joy et al.* 2002). The Galilean satellites are at all times located inside the Jovian magnetosphere. The downstream tail of the magnetosphere eventually extends beyond the orbit of Saturn at ~9.5 AU (*Khurana et al.* 2004). Inside the magnetopause boundary layer a Chapman-Ferraro current system generates an additional contribution to the magnetic field (*Chapman and Ferraro* 1930). This contribution generates a compression of the magnetic field lines on the solar wind ram side and an extension downstream.

The rotating Jovian magnetosphere is both the source for possible induction signals and for magnetic perturbations due to the plasma interaction at the Galilean moons. In Section 1.2 we give an introduction to both of these effects relevant for the further discussions within this thesis.

1.2 Induction signals and the plasma interaction of the Galilean moons

The magnetic field in the vicinity of Callisto and the other Galilean satellites shows significant perturbations with respect to the surrounding magnetospheric field. There are two main possible sources for those perturbations: First, magnetic fields generated in the interior of the satellite could contribute to the measured fields. These fields can originate from dynamo generation processes inside the satellites' core layers or from induced fields generated inside conductive interior layers. Secondly, the interaction between the impinging magnetospheric plasma and the satellite's surface and atmosphere-ionosphere system generates exterior magnetic field structures which in some cases can mimic the essentially dipolar interior fields. We start this section with a discussion of the potential induced interior fields which led to the hypothesis of the existence of interior ocean layers inside all Galilean satellites.

1.2.1 Induced fields: the ocean hypothesis

The basic concept of the induction effect is that according to Maxwell's equations (see Appendix A.1) a temporally variable magnetic field creates currents inside a electrically conductive body (e.g., *Parkinson* 1983, *Schmucker* 1985, *Olsen* 1999). For Callisto as well as for the other Galilean moons the variable magnetic field is provided by Jupiter's magnetosphere (*Neubauer* 1999, *Kivelson et al.* 1999, *Saur et al.* 2010). The tilt of the magnetospheric field with respect to the satellites' orbits and the fast rotation of the field structure leads to periodic variations of the background or primary field at the satellites' locations. On the scale of the satellites' sizes this variable field is primarily homogeneous. The strength of the eddy shaped currents generated in a conductive interior of a satellite depends on the amplitude of the primary field and on the distribution of the conductivities. The penetration or skin depth δ i.e., the depth at which the primary field generating the currents is reduced by a factor of e, defined by

$$\delta = \sqrt{\frac{2}{\sigma \mu_0 \omega}}, \tag{1.1}$$

also depends on the conductivity σ and, additionally, on the frequency of the primary field oscillations ω. Equation (1.1) shows that low frequency inducing signals are able to penetrate deeper into the conductive interior. The induced currents themselves, in turn, generate induced or secondary magnetic fields. In the case of a spherical conductivity distribution these fields have, to first order, a dipolar character (*Parkinson* 1983). This dipole is directed in opposite direction to the primary field and follows its temporal variations with a certain phase lag ϕ. The strength of the internal secondary field B_{sec} is commonly expressed in form of an relative amplitude A with respect to the external primary field B_{pri} i.e., $A = B_{\mathrm{sec}}/B_{\mathrm{pri}}$. For a perfectly conductive interior of a satellite A approaches unity, ϕ approaches zero and the secondary fields cancel the primary field at the surface.

At Callisto magnetic field perturbations which may be attributed to induced fields were measured during most of the flybys of Galileo at the satellite[VI]. Figure 1.5 shows the magnetic field data of the C3 and C9 flybys given in CphiO coordinates. For this Callisto-centric Cartesian coordinate system x points in the direction of rigid corotation, y points toward Jupiter and the z-axis is aligned with the Jovian rotational axis. Figure 1.5 additionally shows a data comparison by *Zimmer et al.* (2000) for several induced field models assuming different amplitudes A. The general structure of the measured magnetic field perturbations is fit remarkably well for models with $A \approx 1$. Note that the given values of $A = 1.35$ and $A = 1.75$ correspond to models which account for a conductive ionosphere of Callisto. In analogy to the fields induced in the interior, a substantial ionospheric layer can produce similar secondary fields which increase the measured relative amplitude. Further, based on the two flybys shown in Figure 1.5 an internal dynamo as a source for the perturbations can be ruled out. According to *Zimmer et al.* (2000), for the given C3 and C9 flyby geometries an intrinsic dynamo field would not generate fields pointing into different directions as visible in the B_y component of Figure 1.5. An induced dipolar field, in contrast, does change its direction due to the different orientations of the primary field that Callisto encountered for both flybys. On the time scale of the Galileo mission (8 years in orbit) a pole reversal of an intrinsic dynamo field would be highly unlikely. Additionally, interior models of Callisto could hardly explain the existence of an internal dynamo for the proposed state of the core (e.g., *Kuskov and Kronrod* 2005a).

For the generation of the suggested induced fields a conductive layer needs to be present inside Callisto. The main constituents of the interior i.e., ices with an increasing contribution of silicates with depth, possess relatively low conductivity values, insufficient for the generation of induced fields with the observed strength. However, already a relatively thin water layer, liquefied by internal radiogenic heat sources as proposed for example by *Kuskov and Kronrod* (2005a), could generate substantial induced fields. Though the existence of other conductive sources such as iron rich layers cannot be completely ruled out, a water ocean layer is, from the geological standpoint, the most probable explanation for the observed perturbations. However, the results by *Zimmer et al.* (2000) allow no definitive conclusions about the depth, thickness and conductivity of the ocean.

Perturbation signatures similar to the ones mentioned above have been detected for all other Galilean moons. For Europa several induction and combined plasma interaction and induction models (e.g., *Schilling et al.* 2007, 2008) successfully proved the existence of an ocean layer in a depth of ~10 km and with a thickness of ~25 to 100 km for a proposed ocean conductivity above 0.5 S m^{-1}, close to the conductivity of terrestrial ocean water. For Io a recent work by *Khurana et al.* (2011) claims the discovery of an interior magma ocean layer. For Ganymede so far no conclusive interpretation of the measured magnetic field perturbations was reached. The possible existence of an ocean at Ganymede might finally be resolved by the JUICE[VII] mission which includes an orbiter around this satellite.

There is one caveat concerning the interpretation of the magnetic data at Callisto. So far the plasma interaction of this satellite was not adequately considered. Determining this contribution to the measured fields is one of the goals of this thesis. The next section gives an introduction to the concept of the plasma interaction at Callisto and its siblings.

[VI] eight in total dubbed C3, C9, C10, C20, C21, C22, C23 and C30

[VII] JUpiter ICy moons Explorer, see `http://sci.esa.int/juice`

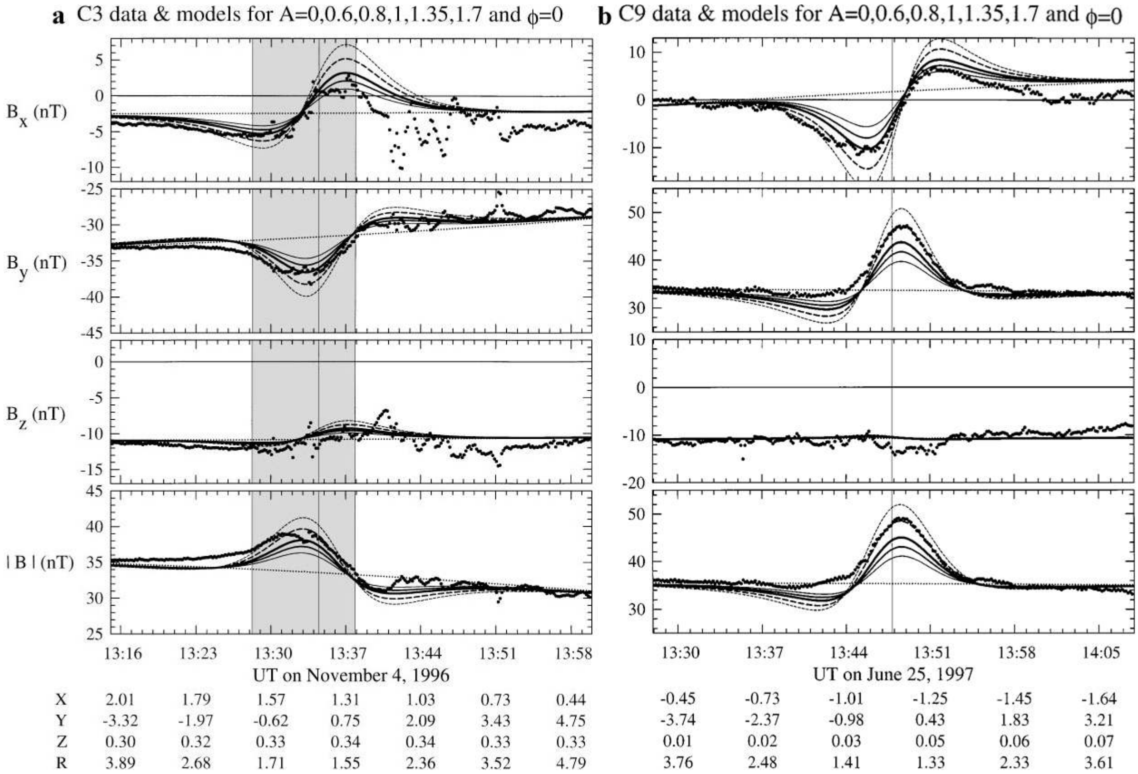

Figure 1.5: *Magnetic field data for the C3 and C9 Galileo flybys as well as model results for several relative amplitudes A of the induced field after Zimmer et al. (2000). Thick dots display the measured data. The modeled fields are shown for the cases: A = 0.6 (thinnest solid curve), A = 0.8 (solid curve of intermediate thickness), A = 1 (thickest solid curve), A = 1.35 (thick dashed curve), and A = 1.7 (thin dashed curve). The assumed phase lag for all models is $\phi = 0$. The Jovian magnetospheric field is indicated by the thin dotted curve. The values below give the time labels, CphiO coordinates normalized to Callisto's radius and the normalized distance to the satellites center. The shaded region indicates a crossing of the geometrical wake of Callisto*

1.2.2 Plasma interaction scenarios

The nature of the interaction between the Jovian magnetospheric plasma flow and the satellites exposed to this flow has been extensively studied, especially in the case of Io (e.g., *Piddington and Drake* 1968, *Goldreich and Lynden-Bell* 1969, *Goertz and Deift* 1973, *Neubauer* 1980, *Neubauer* 1998b, *Kivelson et al.* 2004). A suitable theoretical framework to describe this interaction is the magnetohydrodynamic (MHD) approach (e.g., *Kivelson and Russell* 1995, *Baumjohann and Treumann* 1996). MHD theory treats the plasma as a fluid. Therefore, the movement of individual particles including, for example, the gyration of the plasma ions and electrons is neglected. This approach can be justified if the characteristic spatial and temporal scales of the flow are large compared to the scales of the kinetic processes. The macroscopic scales for the interaction are the satellite's radius R and the plasma convection time τ_p. These scales should be large compared to the gyro radii $r_{g,i}$ and periods $\tau_{g,i}$ of the plasma ions to justify the fluid approach.

The respective values for the Galilean moons listed in Table 1.2 indicate that a MHD description of Callisto's interaction is justified only when the satellite is located outside the current sheet (see values for $r_{g,i}$ and $\tau_{g,i}$ given in brackets), mainly due to the increased magnetospheric background field B_0. All cases of Callisto's interaction considered in the present thesis fall into this category. However, one needs to bear in mind that kinetic aspects of the plasma have more influence at Callisto than at the other satellites. Further, only stationary interaction scenarios are considered in the discussion below and for the models presented in this thesis. This is justified as the plasma convection time τ_p is lower than the time scale of Callisto's motion relative to the magnetospheric field, which lies in the order of tens of minutes to hours. It should, however, be noted that rapid fluctuations in the magnetospheric conditions frequently occur at Callisto. These small scale fluctuations are generally not predictable and therefore need to be neglected here.

All Galilean moons are exposed to a continuous flow of magnetospheric plasma which impinges on their trailing side due to the fast magnetospheric rotation with respect to the satellite's orbital velocities. There are two main concepts for the description of the interaction process within the MHD-framework (*Saur et al.* 2004): First, the interaction can be described by considering the perturbations of the plasma flow and the magnetic field (B, v picture), which generate a current system in the vicinity of the satellite. Secondly, currents and the associated electric fields generated by the interaction may alternatively be considered as the source of the magnetic disturbances (E, j picture). Essentially, both approaches are suitable to describe the nature of the interaction.

The drivers of the interaction are the deceleration of the plasma flow equivalently by electron and ion neutral collisions and by mass loading due to ionization processes within the satellite's atmosphere (*Neubauer* 1998b). In the ideal MHD approach, valid outside of the satellite's conductive ionospheric region, the magnetic field is frozen in to the plasma (e.g., *Kivelson and Russell* 1995, *Baumjohann and Treumann* 1996, also note Equation 1.4 below). Therefore, in the B, v picture the deceleration of the flow leads to an upstream

	Callisto	**Ganymede**	**Europa**	**Io**
B_0, Jovian magnetic field [nT]	4 (42)	64 (113)	370 (460)	1720 (2080)
v_0, relative velocity [km s^{-1}]	192 (122-272)	139 (84-152)	76 (56-86)	57 (53-57)
n_i, ion number density [cm^{-3}]	0.10 (0.01-0.5)	4 (1-8)	130 (12-170)	1920 (960-2900)
m_i, average ion mass [amu]	16 (2)	14 (2)	18.5 (17)	22 (19)
p, total pressure [nPa]	0.38 (0.39)	3.8 (3.9)	17 (26)	34 (54)
R, mean radius [km]	2410	2631	1561	1822
$r_{g,i}$, ion gyro radius [km]	530 (34)	36 (13)	8 (12)	1.8 (1.6)
τ_p, plasma convection time [s]	415	936	552	5460
$\tau_{g,i}$, ion gyro period [s]	262 (3)	14 (1)	3 (2)	0.8 (0.6)
M_A, Alfvén Mach number	2.8 (0.02-8.5)	0.73 (0.05-1.1)	0.47 (0.08-0.59)	0.31 (0.16-0.39)
M_S, sonic Mach number	0.4 (0.03-1.2)	0.5 (0.06-0.8)	0.9 (0.16-1.1)	2.0 (1.0-2.1)
β, plasma beta	64 (0.6)	2.4 (0.8)	0.32	0.04

Table 1.2: *Properties of the plasma flow at Callisto and the other Galilean moons after Kivelson et al. (2004). The given values refer to conditions at the magnetic equatorial plane i.e., inside the current sheet. Values in brackets correspond to conditions in the lobe regions outside the current sheet, or to minimum and maximum values for v_0, n_i, M_A and M_S. The values for τ_p were adapted from Neubauer (1998b). The gyro periods were calculated using: $\tau_{g,i} = \frac{2\pi m_i}{B_0 q}$, where q is equal to the elementary charge.*

pile up of the magnetic field lines and to an enhanced magnetic field magnitude. Away from the atmosphere the same magnetic field lines continue to move with their original velocity. This leads to a draping of the field lines around the satellite as depicted in the side view in Figure 1.6. Perpendicular to the magnetic field lines and the direction of the incident plasma the flow is diverted around the obstacle. The plasma velocity increases above the background value v_0 at these flanks. Behind the satellite the plasma flow is accelerated to its original speed due to the relaxation of the magnetic field lines caused by the magnetic tension. In this region the magnitude of the magnetic field decreases.

The flow pattern along the magnetic field lines is dominated by standing shear Alfvén waves which primarily propagate along this direction (e.g., *Kivelson and Russell* 1995, *Baumjohann and Treumann* 1996). These transverse waves are characterized by consecutive disturbances in the magnetic field and the velocity. Alfvén waves are able to transport energy and momentum along the magnetic field lines. Their wave speed is determined by the magnetic field $\mathbf{B}_0$ and the mass density ρ of the plasma:

$$\mathbf{v}_A = \frac{\mathbf{B}_0}{\sqrt{\mu_0 \rho}}. \tag{1.2}$$

The actual direction of the Alfvén wave propagation is defined by the sum of the Alfvén velocity parallel and anti-parallel to the undisturbed magnetic field $\mathbf{B}_0$ and the incident plasma velocity $\mathbf{v}_0$ (*Neubauer* 1980):

$$C_A^{\pm}: \qquad \mathbf{v}_A^{\pm} = \mathbf{v}_0 \pm \mathbf{v}_A. \tag{1.3}$$

The cylindrical regions starting from the cross section of the satellite (including its atmosphere) along the two Alfvén characteristics $C_A^{\pm}$ are called Alfvén wings. Their direction is indicated by thin solid lines in Figure 1.6. Inside the wings the plasma flow is significantly slowed down and the magnetic field is bend towards the direction of $C_A^{\pm}$, while its magnitude remains unchanged.

In the view of the E, j picture, the electric field

$$\mathbf{E}_0 = -\mathbf{v}_0 \times \mathbf{B}_0 \tag{1.4}$$

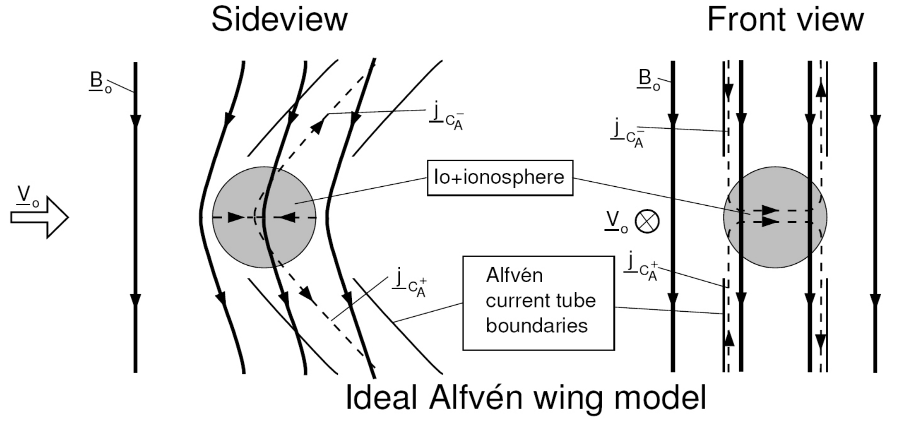

__Figure 1.6:__ Sketch of Io's plasma interaction for a side view and a view along the flow direction after Saur (2004). The magnetic field structure is indicated by solid lines with arrows. The current system is shown by dashed lines. The Alfvén wings are depicted by thin solid lines.

of the plasma flow in the rest frame of the satellite, drives a current perpendicular to $\mathbf{B}_0$ inside the conductive ionosphere of the satellite (see dashed lines in the front view of Figure 1.6). This current leads to a charge separation towards the two hemispheres of its direction and to an electric field whose Lorentz forces slow down the plasma flow and perturb the magnetic field. Away from the satellite the conductivities perpendicular to $\mathbf{B}_0$ are low but the conductivity along the field lines is high everywhere. Therefore, the current is continued along the magnetic field lines or, more precisely, the Alfvén characteristics. The field lines guide the currents towards Jupiter's ionosphere where the current system is closed. The carrier for the currents are, in fact, the Alfvén waves described above for the B, v picture. Apart from shear Alfvén waves, compressional slow and fast mode magnetohydrodynamic waves are generated by the plasma interaction. Slow mode waves can also generate wing structures along their characteristics (*Neubauer* 1998b). However, the perturbations associated with those waves are generally much weaker.

The interaction process described above is only valid for subalfvénic flow velocities i.e., in terms of the Alfvén Mach number, for $M_A = v_0/v_A < 1$. Superalfvénic flows generate shock boundaries upstream of the obstacle, preventing the generation of Alfvén wing structures. While the flow at Io, Europa and Ganymede is primarily subalfvénic, Callisto repeatedly encounters superalfvénic conditions while moving through the center of the current sheet (see Table 1.2). Outside the current sheet the plasma conditions at Callisto also show distinct deviations compared to the other interaction scenarios. The magnitude of the magnetic field B_0, the density ρ and the plasma pressure p are significantly lower in these regions. On the other hand, the flow velocities v_0 are considerably higher. Additionally, the plasma parameters at Callisto are highly variable. Therefore, various interaction scenarios with different interaction strengths and geometries are possible for this satellite.

Fields induced in Callisto's interior change the overall pattern of the interaction. Figure 1.7 shows the deviation of the Alfvén wing structures caused by a dipolar induction field discussed by *Neubauer* (1999). The wing cross sections are reduced and the wings are shifted with respect to the satellite (Figure 1.7A and 1.7C). The shape of the cross section in these cases is approximately cylindrical. Also, the maximum current which can flow through the wings is reduced. During current sheet crossings (Figure 1.7B and 1.7D) the induced field vanishes as the time variable primary fields approach their zero-crossings and the wings remain unaffected. This is, however, only the case if the flow retains its subalfvénic nature. As the magnetic signatures of Callisto's plasma interaction depend on the orientation of the Jovian background field they are themselves temporally variable. Therefore, they contribute to the induction effect which in turn modifies the interaction field patterns. An entirely self-consistent formulation for a model analyzing the magnetic perturbations needs to include this feedback processes (*Neubauer* 1999). The only interaction model accounting for this feedback was given for Europa by *Schilling et al.* (2007, 2008). Though the Callisto MHD model introduced in Chapter 3 closely follows the formulation of these authors, the above feedback mechanism is not taken into account for the results presented in this thesis. Still, the presented model gives the first numerical 3D MHD description for Callisto plasma and magnetic field environment. Possible induced signals are considered by using a separate model for the primary and secondary fields at the Galilean satellites, introduced in the following chapter.

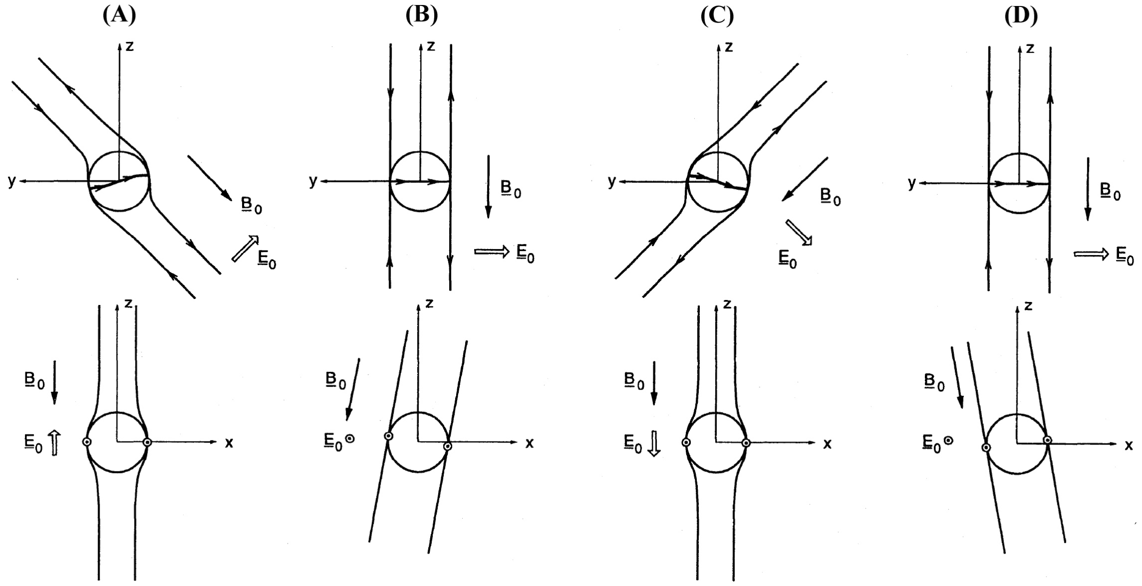

Figure 1.7: *Callisto's Alfvén wing pattern considering internal induced fields after Neubauer (1999). The x-coordinate indicates the direction of the plasma flow. y is directed towards Jupiter and z points in the direction of the Jovian rotational axis. (A) displays conditions at northern magnetic latitudes and (C) the corresponding case below the magnetic equator (below the current sheet). (B) and (D) display the geometry during current sheet crossings, if the condition $M_A < 1$ is still fulfilled. $\underline{B}_0$ and $\underline{E}_0$ indicate the direction of the undisturbed magnetic and electric fields.*

2 Induction signals of the Galilean moons

In this chapter we analyze the possible inductive response of the interior of Callisto. Additionally, the established procedure is applied to Ganymede, Europa and Io. In a first step, we present a model for the secondary, induced fields generated for a spherical conductivity distribution consisting of an arbitrary number of interior shells. Secondly, several interior models for all Galilean satellites are outlined. They define the conductivity structure required as an input for the secondary field model. In a third step, models for the magnetospheric field of Jupiter i.e., the primary or inducing field are specified. Based on these models we infer various amplitudes and frequencies of the Jovian field at the orbits of the satellites. The obtained primary field amplitudes and frequencies are used to predict the associated amplitudes and phase shifts of the induced fields at all Galilean moons, based on the secondary field model. The procedures and results outlined in this chapter were in parts published by *Seufert et al.* (2011).

2.1 Observations and previous models

Distinct magnetic perturbations were measured in the vicinity of all Galilean satellites. These measurements were recorded by the magnetometer on board the Galileo spacecraft (*Kivelson et al.* 1992) and can be obtained from the Planetary Data System[I] provided by NASA. At Callisto and Europa magnetic field anomalies were to some extent attributed to induced fields (*Neubauer* 1998a, *Khurana et al.* 1998, *Kivelson et al.* 1999). In analogy to similar models at Earth (e.g., *Lahiri and Price* 1939, *Parkinson* 1983, *Olsen* 1999, *Constable and Constable* 2004), several authors modeled the characteristics of those fields for Callisto (*Zimmer et al.* 2000) and Europa (*Kuramoto et al.* 1998, *Zimmer et al.* 2000, *Schilling et al.* 2008). Recently, *Khurana et al.* (2011) modeled the magnetic field environment at Io taking into account induction effects by a potential internal magma ocean. Ganymede possibly also shows signatures of induced magnetic fields. However, Ganymede's internal dynamo field gives rise to some ambiguities regarding the interpretation of the observed magnetic field as outlined by *Kivelson et al.* (2002). In addition, several summaries of induced magnetic field studies are available in the literature (e.g., *Jia et al.* 2009, *Saur et al.* 2010).

[I] `http://pds.nasa.gov`

Most of the above induction models consider simple one or two layer structures of the satellites' interiors. Therefore, they potentially neglect geologic restraints which can be taken into account by assuming more complex multi-layer interior models. Additionally, most authors focus on the main primary field amplitudes and frequencies, such as the variations due to Jupiter's internal dipole or the current sheet field in the case of Callisto. Low frequency contributions from the primary signals, which potentially allow a deep sounding of the interior, are neglected in most of the previous surveys. We present the first thorough study of all available primary signal contributions at the Galilean moons, taking into account realistic multi-layer interior models. While the focus of the present thesis lies on Callisto, the models below are also applied to the other Galilean satellites. Section 2.2 introduces the model used to determine the induced field signals at all satellites.

2.2 Induction model

2.2.1 Theory

According to Maxwell's equations (see Appendix A.1), temporally variable magnetic fields induce electric fields and therefore currents inside an electric conductor. Those currents in turn generate magnetic fields which act against the fields outside the conductor. By combining Ohm's, Faraday's, Ampère's law and Gauss's law for magnetism, the following diffusion equation can be derived:

$$\frac{\partial \mathbf{B}}{\partial t} = -\nabla \times \left(\frac{1}{\sigma\mu} (\nabla \times \mathbf{B}) \right). \tag{2.1}$$

It describes the spatial and temporal evolution of the magnetic field **B** inside a medium with an electric conductivity of σ. The displacement currents in Ampère's law are neglected here as the conduction currents are considerably larger for the relevant materials and appropriate time scales for the induction process at the Galilean moons (*Saur et al.* 2010). Further, for the diamagnetic and paramagnetic materials expected in the interiors of the satellites which possess a magnetic susceptibility of $\chi_m \approx 0$, μ can be assumed to be the vacuum permeability μ_0. Also note that possible tidal motions inside the liquid or semi-liquid layers of the Galilean moons are neglected here. If we consider regions with a spatially constant conductivity, Equation (2.1) simplifies to:

$$\frac{\partial \mathbf{B}}{\partial t} = \frac{1}{\sigma\mu_0} \Delta \mathbf{B}. \tag{2.2}$$

We now follow the approach of *Parkinson* (1983) to find solutions for Equation (2.2) for a spherical distribution of σ within an arbitrary number ($s = 1$ to S) of shells. The conductivity inside the shells σ_s is assumed to be constant, so that Equation (2.2) is valid for each layer. The background field $\mathbf{B}_0$ which drives the induction, can be decomposed into its stationary contributions $\mathbf{B}_{0,\text{stat}}$ and time-variable contributions $\mathbf{B}_{\text{pri},n}$ for N different frequencies ω_n. It can be expressed by a Fourier decomposition of the form:

$$\mathbf{B}_0 = \mathbf{B}_{0,\text{stat}} + \mathbf{B}_{\text{pri}} = \mathbf{B}_{0,\text{stat}} + \sum_{n=1}^{N} \mathbf{B}_{\text{pri},n} e^{-i\omega_n t}. \tag{2.3}$$

Since Equation (2.2) is linear in $\mathbf{B}$, we can determine separate solutions for each time-dependent component (for each ω_n) of the inducing or primary field $\mathbf{B}_{\mathrm{pri}}$. To determine the fields inside ($\mathbf{B}_{\mathrm{int}}$) and outside ($\mathbf{B}_{\mathrm{ext}}$) the satellite different approaches must be applied. If the plasma currents outside the satellite are neglected, the magnetic field in this region can be expressed using a scalar potential $U_{\mathrm{ext},n}$:

$$\mathbf{B}_{\mathrm{ext},n} = -\nabla U_{\mathrm{ext},n} = -\nabla\left(\mathrm{R}\left[B_{\mathrm{pri},n}\left(\frac{r}{\mathrm{R}}\right)^{l} + B_{\mathrm{sec},n}\left(\frac{\mathrm{R}}{r}\right)^{l+1}\right] S_l^m e^{-i\omega_n t}\right). \tag{2.4}$$

Here R is the radius of the satellite and l and m the degree and order of the spherical harmonics $S_l^m(\theta, \Phi)$ characterizing the potential. $U_{\mathrm{ext},n}$ includes complex coefficients of both the primary field $B_{\mathrm{pri},n}$ and the induced secondary field $B_{\mathrm{sec},n}$. For the field inside the conducting sphere (where the current density is: $\mathbf{j} \neq 0$) we need to use a vector potential $\mathbf{A}_{\mathrm{int},n}$, which can be separated in a toroidal part T and a poloidal part P:

$$\mathbf{B}_{\mathrm{int},n} = \nabla \times \mathbf{A}_{\mathrm{int},n} = \nabla \times (T\mathbf{r} + \nabla P \times \mathbf{r})\,. \tag{2.5}$$

The toroidal part T of this potential can be neglected as it has no radial component and therefore can neither be induced by external fields nor be detected outside the sphere (see *Parkinson* 1983). For a spherically symmetric conductivity distribution $\sigma(r)$ the poloidal part P can be written using a separation of variables:

$$P = \gamma F(r) S_l^m(\theta, \Phi) e^{-i\omega_n t}. \tag{2.6}$$

Here F is a function of r, and γ an additional constant both of which need to be determined. The magnetic field $\mathbf{B}_{\mathrm{int},n}$, which follows from P, has to solve the diffusion equation (2.2). By applying Equation (2.2) to Equation (2.5) and rewriting the resulting expression with the help of the Legendre equation (e.g., *Abramowitz and Stegun* 1964) one can show that F has to solve the following equation:

$$\frac{d^2F}{dr^2} + \frac{2}{r}\frac{dF}{dr} - \left(k^2 + \frac{l^2 + l}{r^2}\right) F = 0, \tag{2.7}$$

where the wave number k is defined by $k_{n,s}^2 = -i\omega_n \mu_0 \sigma_s$. Equation (2.7) is the modified spherical Bessel equation which has two independent solutions:

$$F_1(r, k) = \sqrt{\frac{\pi}{2rk}} I_{l+\frac{1}{2}}(rk) \tag{2.8}$$

and

$$F_2(r, k) = \sqrt{\frac{\pi}{2rk}} K_{l+\frac{1}{2}}(rk). \tag{2.9}$$

These are the spherical modified Bessel functions of the first and second kind (e.g., *Parkinson* 1983, *Abramowitz and Stegun* 1964, *Riley et al.* 2006). They depend on the product of r and the complex wave number k. Solution F_2 approaches infinity as r approaches zero. We now consider the case of a homogeneous sphere and therefore assume $F = F_1$ to be the physically valid solution of Equation (2.7).

The constant γ in Equation (2.6) can be determined by equating the components arising from Equations (2.5) and (2.4) at the surface ($r = \mathrm{R}$). This procedure yields the constants: $\gamma_r = \mathrm{R}B_{\mathrm{sec},n}/(lF(\mathrm{R}k))$ and $\gamma_{\theta,\Phi} = -B_{\mathrm{sec},n}/F'(\mathrm{R}k)$. Here F' denotes the derivative of F with respect to r. Finally, the following expressions for the secondary field outside and inside the satellite can be obtained from Equations (2.5) and (2.4):

Magnetic field outside the satellite ($r > \mathrm{R}$):

$$B_{\mathrm{ext},r} = \sum_n B_{\mathrm{sec},n}(l+1)\left(\frac{\mathrm{R}}{r}\right)^{l+2} S_l^m e^{-i\omega_n t} \tag{2.10}$$

$$B_{\mathrm{ext},\theta} = -\sum_n B_{\mathrm{sec},n}\left(\frac{\mathrm{R}}{r}\right)^{l+2} \frac{\partial S_l^m}{\partial \theta} e^{-i\omega_n t} \tag{2.11}$$

$$B_{\mathrm{ext},\Phi} = -\sum_n B_{\mathrm{sec},n}\frac{1}{\sin\theta}\left(\frac{\mathrm{R}}{r}\right)^{l+2} \frac{\partial S_l^m}{\partial \Phi} e^{-i\omega_n t}. \tag{2.12}$$

Magnetic field in the interior ($r < \mathrm{R}$):

$$B_{\mathrm{int},r} = \sum_n B_{\mathrm{sec},n}\frac{\mathrm{R}}{r}\frac{F(rk_{n,s})}{F(\mathrm{R}k_{n,s})}(l+1) S_l^m e^{-i\omega_n t} \tag{2.13}$$

$$B_{\mathrm{int},\theta} = -\sum_n B_{\mathrm{sec},n}\frac{\mathrm{R}}{r}\frac{F'(rk_{n,s})}{F'(\mathrm{R}k_{n,s})}\frac{\partial S_l^m}{\partial \theta} e^{-i\omega_n t} \tag{2.14}$$

$$B_{\mathrm{int},\Phi} = -\sum_n B_{\mathrm{sec},n}\frac{\mathrm{R}}{r\sin\theta}\frac{F'(rk_{n,s})}{F'(\mathrm{R}k_{n,s})}\frac{\partial S_l^m}{\partial \Phi} e^{-i\omega_n t}. \tag{2.15}$$

The equations above also describe the shape of the induced fields. For $l = 1$ i.e., for a homogeneous primary field, the secondary field resembles an interior dipole which points in the opposite direction of $\mathbf{B}_{\mathrm{pri},n}$. Note that the poles of the spherical coordinate system used above are aligned with this direction. The absolute values for the secondary field $B_{\mathrm{sec},n}$ are the last unknown factors in Equations (2.10) to (2.15). For the homogeneous sphere considered at this stage of the discussion, they can be obtained by solving the system of equations arising by equating two associated components of the interior field and the exterior field including $B_{\mathrm{pri},n}$. This procedure yields an expression for the strength of the secondary field with respect to the amplitude of the primary field i.e., $B_{\mathrm{sec},n}/B_{\mathrm{pri},n}$:

$$\frac{B_{\mathrm{sec},n}}{B_{\mathrm{pri},n}} = \frac{l}{l+1}\left(\frac{\frac{F'(\mathrm{R}k)}{F(\mathrm{R}k)} - (l+1)}{\frac{F'(\mathrm{R}k)}{F(\mathrm{R}k)} + l}\right) = \frac{l}{l+1}A_n e^{i\phi_n}, \tag{2.16}$$

where A_n is the relative amplitude of the secondary field with respect to the primary field. The maximum possible amplitude is $A_n = 1$. In this case the sphere acts as a perfect conductor. ϕ_n is the phase shift of the secondary signal with respect to the primary field.

It should be noted, that the primary signal can be seen as a diffusion-wave penetrating the interior. This wave is damped by the conductive media inside the satellite. The depth at which the amplitude of the wave has decreased by a factor of e is the skin depth δ introduced in Section 1.2.1. It depends on the conductivity of each separate layer σ_s and on the frequency of the propagating wave ω_n. According to Equation (1.1), low frequency signals penetrate the conductive layers more efficiently and possibly yield information about the deep interior of the satellite.

2.2.2 Model for the secondary fields

We now consider the case of a sphere differentiated into S layers with arbitrary conductivites σ_s and radii r_s (see Figure 2.1). The relative amplitude A_n and phase shift ϕ_n of the secondary field can be obtained by successively solving a system of equations arising from equating two associated components of the magnetic field at each shell boundary r_s (*Parkinson* 1983).

In this case the general solution of Equation (2.7) reads:

$$F_{n,s} = C_s F_1(rk_{n,s}) + D_s F_2(rk_{n,s}). \tag{2.17}$$

For the innermost layer $D_s = 0$ must still be valid as F_2 approaches infinity at $r = 0$. This gives rise to $2S - 1$ constants to be determined. A solution for this problem can be given by the following recursive formula:

$$\frac{B_{\mathrm{sec},n}}{B_{\mathrm{pri},n}} = \frac{l}{l+1} \frac{\frac{F_1'(\mathrm{R}k_{n,S})}{F_1(\mathrm{R}k_{n,S})} - (l+1) + \frac{D_{S-1}}{C_{S-1}} \frac{F_2(\mathrm{R}k_{n,S})}{F_1(\mathrm{R}k_{n,S})} \left[\frac{F_2'(\mathrm{R}k_{n,S})}{F_2(\mathrm{R}k_{n,S})} - (l+1)\right]}{\frac{F_1'(\mathrm{R}k_{n,S})}{F_1(\mathrm{R}k_{n,S})} + l + \frac{D_{S-1}}{C_{S-1}} \frac{F_2(\mathrm{R}k_{n,S})}{F_1(\mathrm{R}k_{n,S})} \left[\frac{F_2'(\mathrm{R}k_{n,S})}{F_2(\mathrm{R}k_{n,S})} + l\right]} \tag{2.18}$$

$$\frac{D_s}{C_s} = \frac{F_1(r_{s-1}k_{n,s})}{F_2(r_{s-1}k_{n,s})} \cdot \frac{\left(\frac{F_1'(r_{s-1}k_{n,s})}{F_1(r_{s-1}k_{n,s})} - \frac{F_1'(r_{s-1}k_{n,s-1})}{F_1(r_{s-1}k_{n,s-1})} + \frac{D_{s-1}}{C_{s-1}} \frac{F_2(r_{s-1}k_{n,s-1})}{F_1(r_{s-1}k_{n,s-1})} \left[\frac{F_1'(r_{s-1}k_{n,s})}{F_1(r_{s-1}k_{n,s})} - \frac{F_2'(r_{s-1}k_{n,s-1})}{F_2(r_{s-1}k_{n,s-1})}\right]\right)}{\left(\frac{F_1'(r_{s-1}k_{n,s-1})}{F_1(r_{s-1}k_{n,s-1})} - \frac{F_2'(r_{s-1}k_{n,s})}{F_2(r_{s-1}k_{n,s})} + \frac{D_{s-1}}{C_{s-1}} \frac{F_2(r_{s-1}k_{n,s-1})}{F_1(r_{s-1}k_{n,s-1})} \left[\frac{F_2'(r_{s-1}k_{n,s-1})}{F_2(r_{s-1}k_{n,s-1})} - \frac{F_2'(r_{s-1}k_{n,s})}{F_2(r_{s-1}k_{n,s})}\right]\right)} \tag{2.19}$$

$$\frac{D_2}{C_2} = \frac{F_1(r_1k_{n,2})}{F_2(r_1k_{n,2})} \left(\frac{\frac{F_1'(r_1k_{n,2})}{F_1(r_1k_{n,2})} - \frac{F_1'(r_1k_{n,1})}{F_1(r_1k_{n,1})}}{\frac{F_1'(r_1k_{n,1})}{F_1(r_1k_{n,1})} - \frac{F_2'(r_1k_{n,2})}{F_2(r_1k_{n,2})}} \right). \tag{2.20}$$

Here Equation (2.18) represents the boundary condition at the surface, (2.20) at the innermost shell and (2.19) at each shell in between. A_n and ϕ_n can be calculated from this equations, in analogy to Equation (2.16). These two values now fully depend on the interior conductivity structure. In order to determine possible values for A_n and ϕ_n for Callisto and the other Galilean satellites, we use geophysical models for the satellites interior. The respective models are presented in the following section.

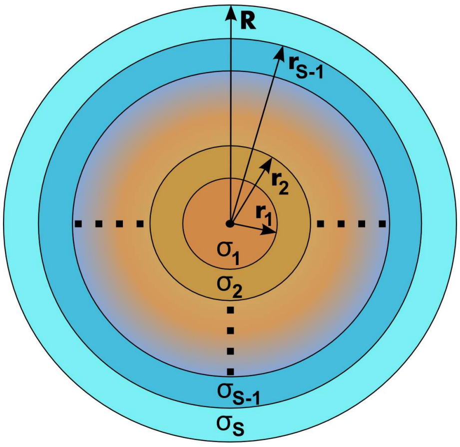

Figure 2.1: *Concept of a spherical conductivity distribution for S shells.*

2.2.3 Interior models

To reflect the uncertainties in the present knowledge about the Galilean moons' interiors two models were selected for each satellite. First, we consider models which explicitly assume the existence of ocean layers. Models including a subsurface water ocean were given by *Kuskov and Kronrod* (2005a) for Callisto (Table 2.1) and Europa (Table 2.5) and by *Kimura et al.* (2009) for Ganymede (Table 2.3). For Io, a model considering the presence of a magma ocean layer (Table 2.7) was presented by *Keszthelyi et al.* (1999). Secondly, a set of three layer models (consisting of crust, mantle and core) was given by *Zhang* (2003) for all Galilean satellites (Tables 2.2, 2.4, 2.6 and 2.8). These models are based on common physical assumptions, which gives the opportunity to directly compare the results obtained for different satellites. Although these models do not explicitly include ocean layers, we assume an enhanced conductivity for parts of one layer for each model. The differences between the two sets of models are used to discuss the effect different features, like a smaller ice shell thickness at Europa or a larger depth of the ocean layer at Ganymede, have on the induction signals. A further description of the above models is given in Section 2.3.2 in context of the resulting secondary magnetic field signatures.

So far, there is almost no scientific information available for the electrical conductivities of materials under the physical conditions present inside the Galilean moons. We estimated these values based on various sources in the literature. The densities of the layers given in Tables 2.1 to 2.8 are used as a proxy for the state of the material. Other factors like the temperature were not available for all models and were not included in the estimation. We preferentially use values which have been given for the interior of the Earth. Table 2.9 lists the assumed materials, the estimated conductivities and the respective references. The conductivities of the materials involved in the induction process constitute the major uncertainty of our approach.

In order to test the implications of different ocean configurations, the ocean thickness and conductivity for each model is varied within a plausible range indicated in the Tables 2.1 to 2.8. For Callisto, Io and the *Kimura et al.* (2009) Ganymede model the outer crustal

	h [km]	σ [S m^{-1}]	ρ [g cm^{-3}]	Ref.
Crust	150	10^{-6}	1	(6)
Ocean	0 - 450	0.01-100	1	(7)
Mantle 1	450 - 0	10^{-6}	2	(11)
Mantle 2	300	10^{-5}	2.15	(11)
Mantle 3	910	10^{-4}	2.43	(11)
Core	600.3	10^{-2}	3.15	(3)

***Table 2.1:** Callisto model adapted from Kuskov and Kronrod (2005a). The last column denotes the references for the sources of literature for the conductivity (see Table 2.9). The thicknesses of the ocean and the mantle are varied, respectively.*

	h [km]	σ [S m^{-1}]	ρ [g cm^{-3}]	Ref.
Crust	200	10^{-6}	1	(6)
Ocean	0-1,000	0.01-100	1	(7)
Mantle	1,439-439	10^{-5}	2.15	(11)
Core	771.3	5	4.5	(4)

***Table 2.2:** Callisto model adapted from Zhang (2003). References correspond to the literature given in Table 2.9. The thicknesses of the ocean and the mantle are varied, respectively.*

	h [km]	σ [S m^{-1}]	ρ [g cm^{-3}]	Ref.
Crust	150	10^{-6}	1	(6)
Ocean	500-0	0.01-100	1	(7)
Icy mantle	350-850	10^{-6}	1.8	(11)
Mantle	650	10^{-5}	3.5	(8)
Core	981.2	10^{5}	8	(5)

***Table 2.3:** Ganymede model adapted from Kimura et al. (2009). References correspond to the literature given in Table 2.9. The thicknesses of the ocean and the icy mantle are varied, respectively.*

	h [km]	σ [S m^{-1}]	ρ [g cm^{-3}]	Ref.
Crust	785-0	10^{-6}	1	(6)
Ocean	0-785	0.01-100	1	(7)
Mantle	1,136	10^{-5}	3.1	(10)
Core	710.2	10^{5}	8	(5)

***Table 2.4:** Ganymede model adapted from Zhang (2003). References correspond to the literature given in Table 2.9. The thicknesses of the ocean and the crust are varied, respectively.*

	h [km]	σ [S m^{-1}]	ρ [g cm^{-3}]	Ref.
Crust	150 - 0	2.1×10^{-6}	1	(6)
Ocean	0 - 150	0.01 - 100	1	(7)
Mantle	855	10^{-6}	3.6	(8)
FeS core	560	5	4.7	(9)

***Table 2.5:** Europa model adapted from Kuskov and Kronrod (2005a). References correspond to the literature given in Table 2.9. The thicknesses of the ocean and the crust are varied, respectively.*

	h [km]	σ [S m^{-1}]	ρ [g cm^{-3}]	Ref.
Crust	100 - 0	10^{-6}	1	(6)
Ocean	0 - 100	0.01 - 100	1	(7)
Mantle	865	10^{-5}	3.13	(10)
Fe core	596	10^{5}	8	(5)

***Table 2.6:** Europa model adapted from Zhang (2003). References correspond to the literature given in Table 2.9. The thicknesses of the ocean and the crust are varied, respectively.*

	h [km]	σ [S m^{-1}]	ρ [g cm^{-3}]	Ref.
Crust	25	10^{-4}	2.8	(1)
Magma	0 - 250	10^{-3} - 15	2.9	(2)
Mantle	996 - 1,246	10^{-2}	3.1	(3)
FeS core	550.6	5	5.15	(4)

***Table 2.7:** Io model adapted from Keszthelyi et al. (1999). References correspond to the literature given in Table 2.9. The thicknesses of the magma ocean and the mantle are varied, respectively.*

	h [km]	σ [S m^{-1}]	ρ [g cm^{-3}]	Ref.
Crust	120	10^{-4}	2.8	(1)
Magma	0 - 500	10^{-3} - 15	2.9	(2)
Mantle	636 - 1,136	10^{-2}	3.66	(3)
Fe core	565.6	10^{5}	8	(5)

***Table 2.8:** Io model adapted from Zhang (2003). References correspond to the literature given in Table 2.9. The thicknesses of the magma ocean and the mantle are varied, respectively.*

Ref.	ρ [g cm^{-3}]	σ [S m^{-1}]	Analogue	Source
			Silicate	
(1)	2.8	10^{-3} - 10^{-5}	Dry silicate	*Beblo et al.* (1985)
(2)	2.9	10^{-3} - 15	Dry magma	*Waff and Weill* (1975),*Beblo et al.* (1985)
(3)	3.1	10^{-2}	Partially molten gabbro	*Maumus et al.* (2005)
(8)	3.5-3.7	10^{-4} - 10^{-10}	Chondrites	*Parthasarathy and Sharma* (2004)
(10)	3.2-3.4	10^{-4} - 10^{-8}	Chondrites	*Parthasarathy and Sharma* (2004)
			Iron rich material	
(4)	5.15	2 - 8	Lower Earth mantle	*Dobson and Brodholt* (2000)
(5)	10	3×10^5	Outer Earth core	*Stacey* (1992)
(9)	5	5	Lower Earth mantle	*Stacey* (1992)
			Ice and water	
(6)	1	10^{-6}	H_2O ice	*Beblo et al.* (1985)
(7)	1	0.01 - 100	Saline water	*Beblo et al.* (1985)
(11)	2-3	10^{-4} - 10^{-6}	Silicate + 41% water ice	*Grimm et al.* (2007)

Table 2.9: *Sources of literature for the conductivity of the materials assumed in the adapted interior models of the Galilean moons. The index given in the first column refers to the indexes in the tables for the interior models (Tables 2.1 to 2.8). Column 4 denotes the material from the literature which we use as an analog for the present material.*

layer is kept fixed and the thickness of the mantle layer below the ocean is reduced for increasing water layer extensions. At Europa and for the *Zhang* (2003) Ganymede model the thickness of the crust is reduced while the mantle thickness is kept fixed. The values for all other layers including the thickness of the core are kept fixed.

Results for other well established interior models such as *Schubert et al.* (2004) or *Sohl et al.* (2002) for Callisto and Ganymede and *Schubert et al.* (2009) for Europa, were found to be very similar to the results for the first set of models mentioned above. Therefore, these models and the respective secondary field properties are not explicitly presented in this thesis. However, some of the few notable differences are mentioned in Section 2.3.2.

2.2.4 Magnetosphere model

A global model for the Jovian magnetospheric field needs to account for field contributions generated by several magnetospheric processes. The primary field model presented in this section includes the three major field sources of the magnetosphere: the Jovian internal field, the magnetospheric current sheet and the magnetopause boundary layer. The respective field contributions are incorporated by using separate sub-models. Therefore, the inducing fields generated by the different contributions to the magnetospheric field can be distinguished. The total magnetospheric field can be obtained by a superposition of the separately modeled fields. Note that the System III spherical coordinate system (e.g. *Dessler* 2002, *Seidelmann and Divine* 1977) is used in the following sections, except for the model of the Jovian current sheet magnetic field.

2.2.4.1 Jupiter's internal field

Jupiter's intrinsic dynamo field $\mathbf{B}_{0,\mathrm{int}}$ can be described by a scalar potential (e.g., *Chapman and Bartels* 1940, *Parkinson* 1983)

$$U_{0,\mathrm{int}} = \mathrm{R}_J \sum_{l=1}^{\infty} \left(\frac{\mathrm{R}_J}{r}\right)^{l+1} \sum_{m=0}^{l} P_l^m(\cos\theta)\left[g_l^m \cos(m\Phi) + h_l^m \sin(m\Phi)\right], \tag{2.21}$$

where R_J denotes the radius of Jupiter (71,492 km), P_l^m are the Schmidt-normalized Legendre functions of degree l and order m and g_l^m and h_l^m are the Schmidt coefficients of the field. The respective spherical coordinate system is defined by the radial distance to Jupiter r, the co-latitude θ and the longitude Φ. The magnetic field for this potential follows from:

$$\mathbf{B}_{0,\mathrm{int}} = -\nabla U_{0,\mathrm{int}}. \tag{2.22}$$

At Jupiter the coefficients g_l^m and h_l^m were derived from spacecraft magnetometer data by several authors (for a summary of available models see *Khurana et al.* 2004). In the present thesis, the so called VIP4 model put forward by *Connerney et al.* (1998) is applied. The coefficients of this model were fit to Pioneer and Voyager data and observations for the location of Io's footprint in the Jovian auroral oval. For the analysis presented here, coefficients up to $m, l = 3$ i.e., dipole, quadrupole and octopole coefficients are considered (see Table 2.10). Higher order coefficients are neglected as they are too uncertain and insignificant at the satellites' positions.

g_1^0	g_1^1	g_2^0	g_2^1	g_2^2	g_3^0	g_3^1	g_3^2	g_3^3
4.205	-0.659	-0.051	-0.619	0.497	-0.016	0.520	0.244	-0.176
	h_1^1		h_2^1	h_2^2		h_3^1	h_3^2	h_3^3
	0.250		-0.361	0.053		-0.088	0.408	-0.316

Table 2.10: *Spherical harmonic coefficients g_l^m and h_l^m in Gauss for the VIP4 model after Connerney et al. (1998).*

2.2.4.2 Current sheet field

The flow of charged particles within the Jovian magnetosphere generates its own magnetic field structure rotating nearly synchronously with the intrinsic Jovian field (see Section 1.1.2). *Khurana* (1997) modeled this current sheet field $\mathbf{B}_{0,cs}$ using an Euler potential description of the following form:

$$\mathbf{B}_{0,cs} = \nabla f(\rho, \Phi, z) \times \nabla g(\rho, \Phi, z), \tag{2.23}$$

with

$$\begin{aligned} f = &-C_1 \rho \left[\tanh\left(\frac{r_{01}}{r}\right)\right]^{a_1} \ln\left[\cosh\left(\frac{z - z_{cs}}{D_1}\right)\right] \\ &+ \int \rho \left\{ C_2 \left[\tanh\left(\frac{\rho_{02}}{\rho}\right)\right]^{a_2} + C_3 \left[\tanh\left(\frac{\rho_{03}}{\rho}\right)\right]^{a_3} + C_4 \right\} \mathrm{d}\rho \end{aligned} \tag{2.24}$$

and

$$g = \Phi + p\left[1 + q \tanh^2\left(\frac{z - z_{cs}}{D_2}\right)\right]\rho. \tag{2.25}$$

The cylindrical coordinate system used in this expression (ρ, Φ and z) is defined relative to the magnetic equator. z_{cs} is the current sheet's distance from the magnetic equator given by:

$$z_{cs} = \rho \tan(9.6^\circ)\left[\frac{x_0}{x} \tanh\left(\frac{x}{x_0}\right) \cos(\Phi - \delta) - \cos(\Phi - \pi)\right], \tag{2.26}$$

with

$$\delta = \pi - \frac{\Omega_J \rho_0}{v_0} \ln\left[\cosh\left(\frac{\rho}{\rho_0}\right)\right]. \tag{2.27}$$

Table 2.11 lists the free parameters in the above expressions defining the overall current sheet structure and the respective values for the so called common model given by *Khurana* (1997). These values represent the best fit of the model field to multiple sets of magnetometer data. Note, that the modeled current sheet field needs to be transformed from the cylindrical coordinate system to the spherical System III coordinates used for the other models.

C_1	C_2	C_3	C_4	a_1	a_2	a_3	D_1 [R_J]
80.3	690.4	101.3	-1.7	2.49	1.80	2.64	2.01

D_2 [R_J]	r_{01} [R_J]	ρ_0 [R_J]	ρ_{02} [R_J]	ρ_{03} [R_J]	x_0 [R_J]	p	q
13.27	38.0	33.2	2.14	12.5	-33.5	6.26×10^{-3}	0.35

Table 2.11: *Parameters of the current sheet model defined by the Equations* (2.23) *to* (2.27) *and values for the common model by Khurana (1997).*

Preceding the work of *Khurana* (1997), *Connerney et al.* (1981) presented a vector potential model for the Jovian current sheet. This model was used by *Engle* (1992) to estimate the magnetopause standoff distance required by the model presented in Section 2.2.4.3. To retain a self consistent model for the magnetopause field, we consequently apply the

Connerney et al. (1981) model to estimate the position of the magnetopause. Although we analyzed the field amplitudes and frequencies predicted by the *Connerney et al.* (1981) model, the respective results are not presented in this thesis. Instead we focus on the more elaborated model by *Khurana* (1997). Because the model results for the current sheet and the magnetopause fields are analyzed separately, there is no inconsistency in using different approaches for the current sheet contributions.

2.2.4.3 Magnetopause field

The magnetopause is the boundary layer defined by the pressure equilibrium between the solar wind and the magnetosphere. Chapman-Ferraro currents flowing at this boundary generate magnetic fields contributing to the primary field at the satellites. *Engle and Beard* (1980) and *Engle* (1992) derived a global model for these fields by calculating the surface of the boundary layer. They use a magnetospheric model including the *Connerney et al.* (1981) current sheet model and the dipole field of Jupiter. The calculated surface is used to fit coefficients of a scalar potential $U_{0,mp}$ describing the magnetopause field $\mathbf{B}_{0,mp}$:

$$\mathbf{B}_{0,mp}(r,\theta,\Phi) = -C_n \nabla U_{0,mp}(r,\theta,\Phi), \tag{2.28}$$

with

$$U_{0,mp} = \sum_l \left(\frac{r}{R_{ss}}\right)^l \sum_{m=0}^{l} G_l^m P_l^m(\cos\theta)\cos(m\Phi). \tag{2.29}$$

R_{ss} denotes the location of the magnetopause subsolar point. The normalization constant C_n is the magnetospheric field strength at R_{ss} predicted by the internal field model and the *Connerney et al.* (1981) current sheet model. The coordinate system is defined in analogy to the system used in Section 2.2.4.1. The model coefficients G_l^m were calculated for various orientations of the magnetic axis of Jupiter. *Engle* (1992) gives coefficients for $\alpha = 0°$ (tilted toward the Sun), $\alpha = 180°$ (tilted away from the Sun) and $\alpha = 90°$ (no tilt). *Bode* (1994) derived a functional expression for G_l^m describing arbitrary tilt configurations. As the primary fields calculated for these models show only negligible differences, only results for the $\alpha = 90°$ model (see Table 2.12) are presented in this thesis.

G_1^0	G_2^1	G_3^0	G_3^2	G_4^1	G_4^3	G_5^0	G_5^2	G_5^4	G_6^1
0.639	0.3476	0.0157	0.0817	0.0194	0.0059	-0.0189	-0.0172	-0.0145	-0.0115

G_6^3	G_6^5	G_7^0	G_7^2	G_7^4	G_7^6	G_8^1	G_8^3	G_8^5	G_8^7
-0.0209	-0.0166	0.0065	0.0008	-0.0115	-0.0093	0.0001	0.0040	-0.0019	-0.0030

Table 2.12: *Coefficients up to* $l = 8$ *for the Engle (1992) no tilt model in Gauss units. Coefficients not listed are equal to zero.*

By adjusting C_n, the above model can be scaled to different magnetopause standoff distances R_{ss} representing changing solar wind conditions. Both variable and stationary solar wind conditions are considered here to infer the primary fields generated at the magnetopause. The default subsolar point distance for stationary conditions was defined close to the average value at $R_{ss} = 60\ \mathrm{R}_J$. Section 2.2.4.4 outlines the derivation for the values used for R_{ss}.

2.2.4.4 Variability of the magnetopause

Variabilities in the solar wind conditions lead to fluctuations of the magnetopause position. The associated variations of the magnetopause field are a possible source for primary fields generating induction signatures. The *Engle* (1992) model can be scaled to varying magnetopause distances to simulate these primary field contributions. Based on a study of Voyager data by *Huddleston et al.* (1998), *Alexeev and Belenkaya* (2005) gave an empirical fit of the magnetopause position R_{ss} with respect to the pressure of the solar wind p_{sw}:

$$R_{ss} = \frac{35.5\mathrm{R}_J}{p_{sw}^{0.22}\,[\mathrm{nPa}]}. \tag{2.30}$$

Solar wind velocity v_{sw} and density ρ_{sw} data collected by the Ulysses spacecraft are provided by the Planetary Data System. The solar wind ram pressure $p_{sw} = \rho_{sw} v_{sw}^2$ calculated from these data yields time series for the approximate positions of R_{ss} by applying Equation (2.30). The data sets were recorded in the vicinity of Jupiter's orbit at 5.0 AU to 5.5 AU. Since the absolute timing of the solar wind fluctuations is irrelevant for the present analysis, the data was not spatially extrapolated to the exact position of Jupiter. The data processing included an averaging over 0.125 h for Ulysses data sets of the years 1992, 1997 to 1999 and 2003 to 2005. The strongest variations were encountered during the second half of 1992. Therefore, only results for magnetic fluctuations predicted for this time series are presented in this thesis.

The velocity and R_{ss} variations for the 1992 time series are shown in Figure 2.2. A distinct periodicity with the solar rotation period of ~27 days is visible in the v_{sw} data. This periodicity is less obvious in the resulting values for R_{ss}. The reason for this is, that the density does not show such a clear periodicity but varies over a much greater range. The magnetopause subsolar point distances span between 40 and 100 Jovian radii with an average of ~70 R_J. These values lie in the typical range for R_{ss} at Jupiter (*Huddleston et al.* 1998). The short-lived peaks exceeding distances of 100 R_J might be unrealistic but have no significance for our analysis. They only cause a slight decrease of the weak magnetopause field near the satellites for these R_{ss} distances.

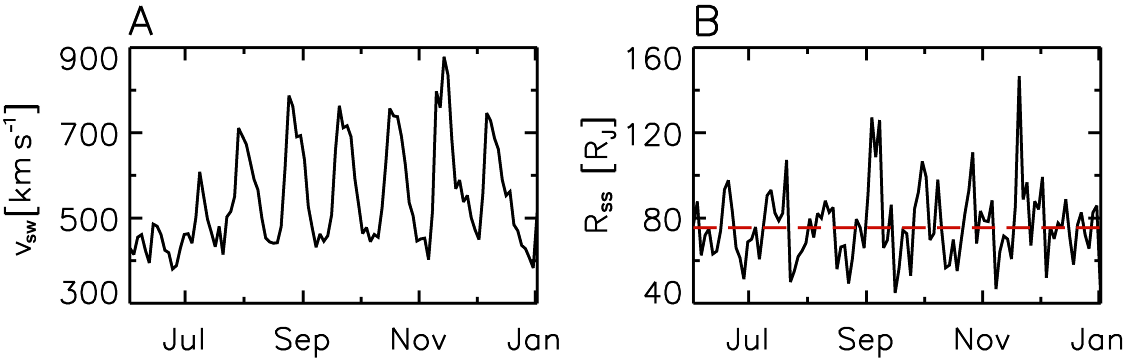

Figure 2.2: Values for (A) the solar wind velocity v_{sw} and (B) the magnetopause standoff distance R_{ss} for the Ulysses data set recorded in the second half of 1992. The average value for R_{ss} is close to 70 R_J (dashed red line).

2.3 Results

The sequence of models presented in the previous section can be used to predict the induced fields at the Galilean moons. In Section 2.3.1, we infer different amplitudes $B_{\mathrm{pri},n}$ and periodicities $T_n = 2\pi/\omega_n$ of the primary field predicted by the magnetosphere model. Section 2.3.2 gives a discussion for the secondary fields $B_{\mathrm{sec},n}$ triggered for several primary signal frequencies based on two separate interior models for each satellite.

2.3.1 Primary fields

2.3.1.1 The magnetospheric field at the Galilean moons

The magnetic field at the position of the Galilean moons can be obtained from a superposition of the three magnetospheric sub-models introduced in Section 2.2.4. Figure 2.3A shows the field lines for a superposition of the VIP4 internal field model and the *Khurana* (1997) current sheet model. Due to the fast rotation (every ~10 h) of the magnetosphere the magnetic equator (blue dotted line) repeatedly crosses the satellites' orbital positions (red dotted line) causing varying magnetic field conditions. The structure of the magnetopause field depicted in Figure 2.3B generates additional magnetic field variations between orbital locations close to the subsolar point and in the Jovian magnetotail. Note, that the magnetopause model is presented separately in Figure 2.3 as it is not consistent with the *Khurana* (1997) model (see Section 2.2.4.2). Instead the field lines were obtained by applying the *Connerney et al.* (1981) current sheet model.

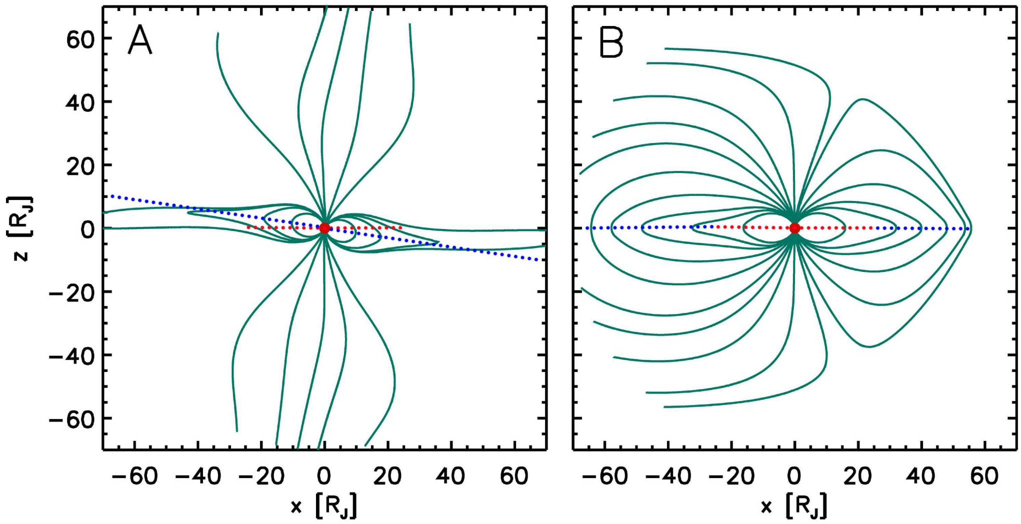

Figure 2.3: *Magnetic field lines for a superposition of (A) the Connerney et al. (1998) VIP4 and the Khurana (1997) current sheet models and (B) the VIP4, Connerney et al. (1981) current sheet and the Engle (1992) no tilt models. The satellites orbital plane up to the position of Callisto is indicated by red dotted lines, the magnetic equator by blue dotted lines. The Jovian dipole is tilted towards the Sun in the positive x direction (A) and perpendicular to the Sun in the y direction (B), respectively.*

The resulting magnetic field components in System III coordinates (e.g. *Dessler* 2002, *Seidelmann and Divine* 1977) are shown in Figures 2.4A/B for Callisto, 2.4C/D for Ganymede, 2.4E/F for Europa and 2.4G/H for Io. Stationary magnetopause conditions are used here (with $R_{ss} = 60\ \mathrm{R}_J$) and the inclinations and eccentricities of the orbits (see Table 1.1) have been taken into account. For one synodic rotation of Jupiter with respect to each satellite (left panels in Figure 2.4) B_θ is approximately constant at a certain background level. At Io, Europa and Ganymede B_r and B_Φ generally contribute less to the total field. These two components repeatedly change their sign and are approximately in anti-phase. Figure 2.5 shows that this behavior leads to a nearly elliptical polarization of the field along the satellites' orbits. At Callisto the field even approaches a linear polarization. The period of these dominant field fluctuations matches the synodic rotation period. They are generated due to the tilt of the magnetic axis and constitute the main contribution to the inducing primary field. B_r is strongest near maximum magnetic latitudes i.e., when the tilt of the magnetic axis points in direction of the satellite at $\lambda_{III} \approx 200°$. Small longitudinal deviations arise due to the orbit eccentricities and inclinations. At Callisto and to a lesser extent at Ganymede the field points nearly in the direction of Jupiter (r-direction) when the satellite is located outside the current sheet. The current sheet also leads to a hinging and sweep back of the field lines at Callisto (*Khurana* 1997) which changes the shape of the B_Φ component compared to the other satellites. Variations in B_θ are much weaker than for the other components. However, long period fluctuations not present for B_r and B_Φ arise, depicted in the right panels of Figure 2.4 for a single orbit of the satellites. The corresponding periods are the orbital periods of the Galilean moons. These variations are primarily caused by the shape of the magnetopause for Callisto and by the orbital eccentricity for Io and Europa. At Ganymede both effects contribute equally to the B_θ fluctuations.

In Section 2.3.1.2 we present results of a Fourier analysis of the presented time series, which allows us to infer the corresponding amplitudes and the exact periods of the field fluctuations mentioned above. The spectral analysis also proves the existence of additional low and high frequency primary signals.

2.3.1.2 Spectral analysis

Separate spectral analyses are used for the magnetic field time series given by all magnetospheric sub-models presented in Section 2.2.4. The magnetopause model was used to generate time series both for stationary (using several values of R_{ss}) and temporally variable solar wind conditions using Ulysses solar wind data (see Section 2.2.4.4). Further, circular, eccentric and inclined satellite trajectories were used as input for each model to identify contributions generated due to the shape of the orbits. The time series span the duration of 1,000 Jovian rotations (~10,000 h) and are sampled with 50,000 data points. For the case of variable magnetopause positions the time series is synchronized with the 0.125 h averaged Ulysses data which spans 5,170 h sampled by 41,000 data points.

A Fast Fourier Transform (FFT) analysis of these generic time series yields the amplitudes and periods for the primary fields summarized in Table 2.13. Only values for significant amplitudes (arbitrarily defined as $B_{\mathrm{pri},n} > 0.2$ nT) are listed. For clarification and com-

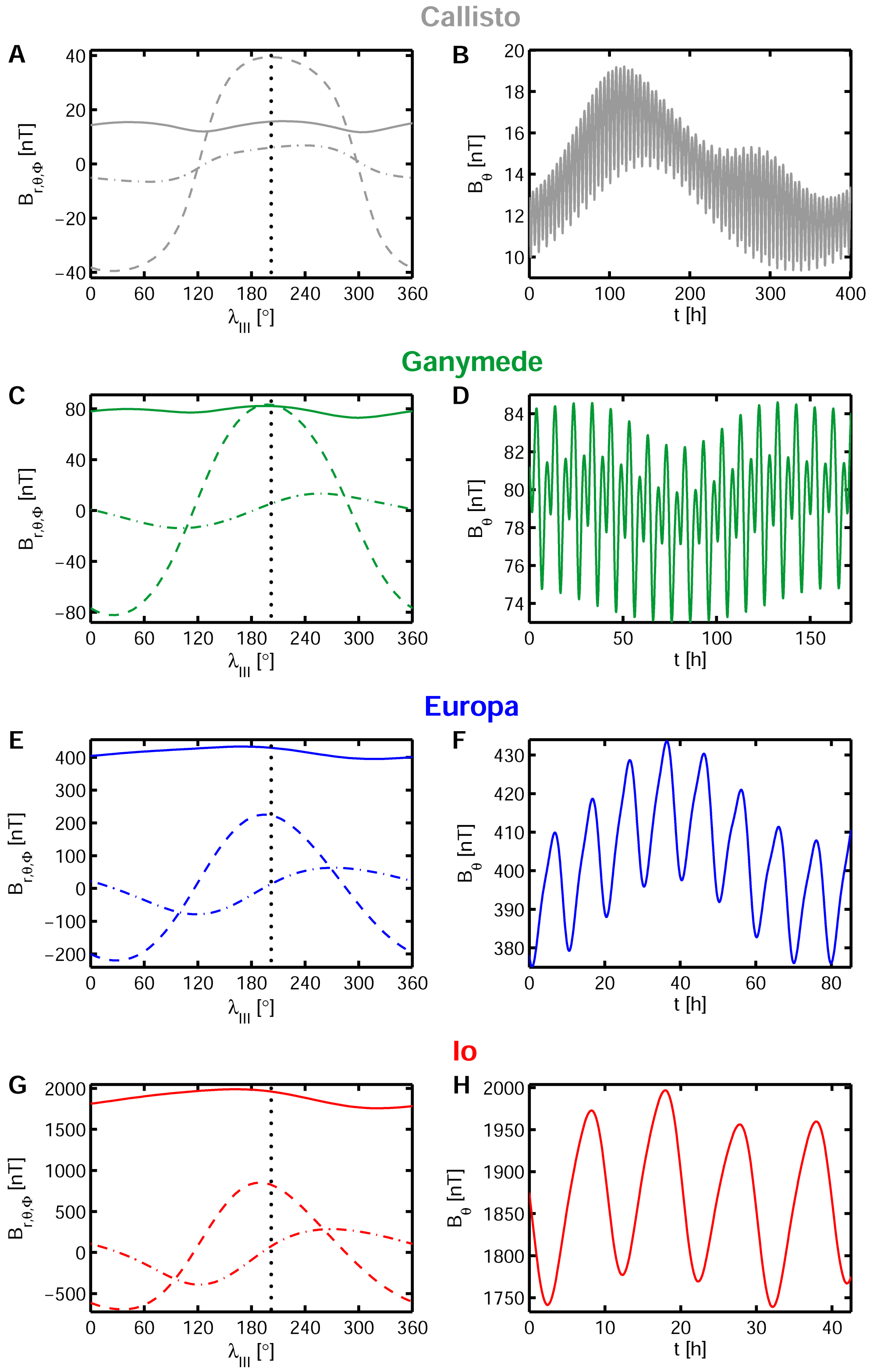

__Figure 2.4:__ Time series for the magnetospheric field at the Galilean satellites. (A), (C), (E) and (G) show the B_r (dashed lines), B_θ (solid lines) and B_Φ (dash-dotted lines) magnetic components (System III coordinates) for one synodic Jovian rotation i.e., for 360° in λ_{III} longitude. The black dotted line indicates the maximum northern magnetic latitude at $\lambda_{III} \approx 200°$. (B), (D), (F) and (H) show the variations of B_θ for one satellite orbit.

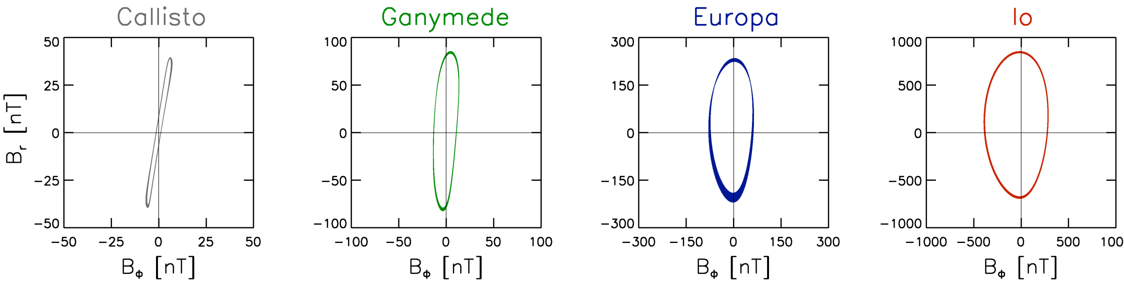

Figure 2.5: *B_r vs. B_Φ along the satellites' orbits. The field is elliptically polarized. Eccentricity and inclination of the orbits lead to a broadening of the lines.*

parison, Figure 2.6 shows amplitude spectra corresponding to the time series presented in Figure 2.4 i.e., to a superposition of all magnetosphere sub-models. Differences in the absolute amplitudes in Figure 2.4 and Table 2.6 occur due to enhanced spectral leakage in the total model FFT. The spectra mainly consist of different delta peaks at various frequencies which can not be resolved adequately at the same time. To suppress spectral leakage the FFT analysis was carried out for slightly different lengths of our generic time series until the maximum amplitude value was reached for an individual peak.

The values in Table 2.6 prove the conclusion that the major primary signals can be found in the B_r and B_Φ components at the synodic Jovian rotation period. The exact periods are 12.95 h for Io, 11.23 h for Europa, 10.53 h for Ganymede and 10.18 h for Callisto. The dominant B_r amplitudes are generated by the Jovian dipole and the current sheet. They reach up to 750 nT at Io, 215 nT at Europa and ~85 nT at Ganymede. Although the dipolar field contribution is almost negligible at Callisto, the current sheet field increases the corresponding amplitudes up to ~40 nT. B_Φ provides additional primary signals at this frequency of 370 nT at Io, 105 nT at Europa, 30 nT at Ganymede and 10 nT at Callisto. In B_θ the Jovian quadrupole field generates similar signatures with relatively low amplitudes of 100 nT at Io, 16 nT at Europa, 2.5 nT at Ganymede and only 0.3 nT at Callisto.

Short period primary signals with 1/2 and 1/3 of the synodic rotation period are evident in Figure 2.6 both in B_r and B_Φ. The B_r amplitudes of these signals drop rapidly from 108 nT and 16 nT at Io to ~17 nT and 2.8 nT at Europa and 2.6 nT and 3.3 nT at Ganymede. The primary sources for these fluctuations are the Jovian quadrupole and octopole fields. At Callisto the only significant short period contribution of 6 nT is caused by the current sheet structure. Some rather weak inducing fields of 1/2 of the synodic Jovian rotation period can also be found in B_θ. Every magnetic component provides at least two short period ($<$ 13 h) inducing signals for each satellite. If the interior of the satellites is sufficiently conductive the amplitude of most of these signals should be large enough to provide measurable induced signals at multiple frequencies.

The inclinations and eccentricities of the satellites' orbits and the change in distance with respect to the magnetopause cause inducing signals with the satellites' orbital periods. The corresponding periods are: 42.45 h for Io, 85.22 h for Europa, 171.70 h for Ganymede and 400.55 h for Callisto. The orbital inclination causes inducing signals predominantly in the B_r component. Except for a 10 nT signal at Europa these signals are rather weak (2.9 nT at Io, 1.7 nT at Ganymede and only 0.7 nT at Callisto). However, the or-

	Callisto		Ganymede		Europa		Io		Source
	T_n[h]	$B_{\mathrm{pri},n}$[nT]	T_n[h]	$B_{\mathrm{pri},n}$[nT]	T_n[h]	$B_{\mathrm{pri},n}$[nT]	T_n[h]	$B_{\mathrm{pri},n}$[nT]	
B_r	3.39	5.9	3.51	3.3	3.74	1.2			Current sheet
					3.74	1.6	4.32	16.1	Octopole
	5.09	0.3	5.27	2.6	5.62	16.8	6.48	107.9	Quadrupole
	10.18	7.7	10.53	41.9	11.23	170.8	12.95	698.9	Dipole
	10.18	36.1	10.53	43.9	11.23	45.8	12.95	50.9	Current sheet
	400.55	0.7	171.70	1.7	85.22	10.5	42.45	2.9	Inclination
B_Φ					3.74	1.2	4.32	12.1	Octopole
	5.09	0.2	5.27	1.7	5.62	11.2	6.48	71.9	Quadrupole
	10.18	3.9	10.53	20.9	11.23	85.4	12.95	344.9	Dipole
	10.18	6.9	10.53	9.7	11.23	19.1	12.95	32.5	Current sheet
B_θ					5.62	1.3	6.48	13.0	Octopole
	5.09	1.9	5.27	3.0	5.62	2.2	6.48	0.9	Current sheet
	10.18	0.3	10.53	2.5	11.23	16.0	12.95	103.1	Quadrupole
	400.55	0.5	171.70	1.0	85.22	15.8	42.45	26.1	Eccentricity
	400.55	2.5	171.70	1.5	85.22	0.9	42.45	0.6	Magnetopause
	641.90	1.2	641.90	1.2	641.90	1.1	641.90	1.1	MP variability
$\lvert B_p\rvert$		400		150		300		730	Plasma fields

Table 2.13: *Primary signal amplitudes $B_{pri,n}$ and periods T_n for all magnetic components in System III coordinates. The last column indicates the source of the predicted magnetic variability. The bottom row shows the maximal plasma interaction fields for comparison.*

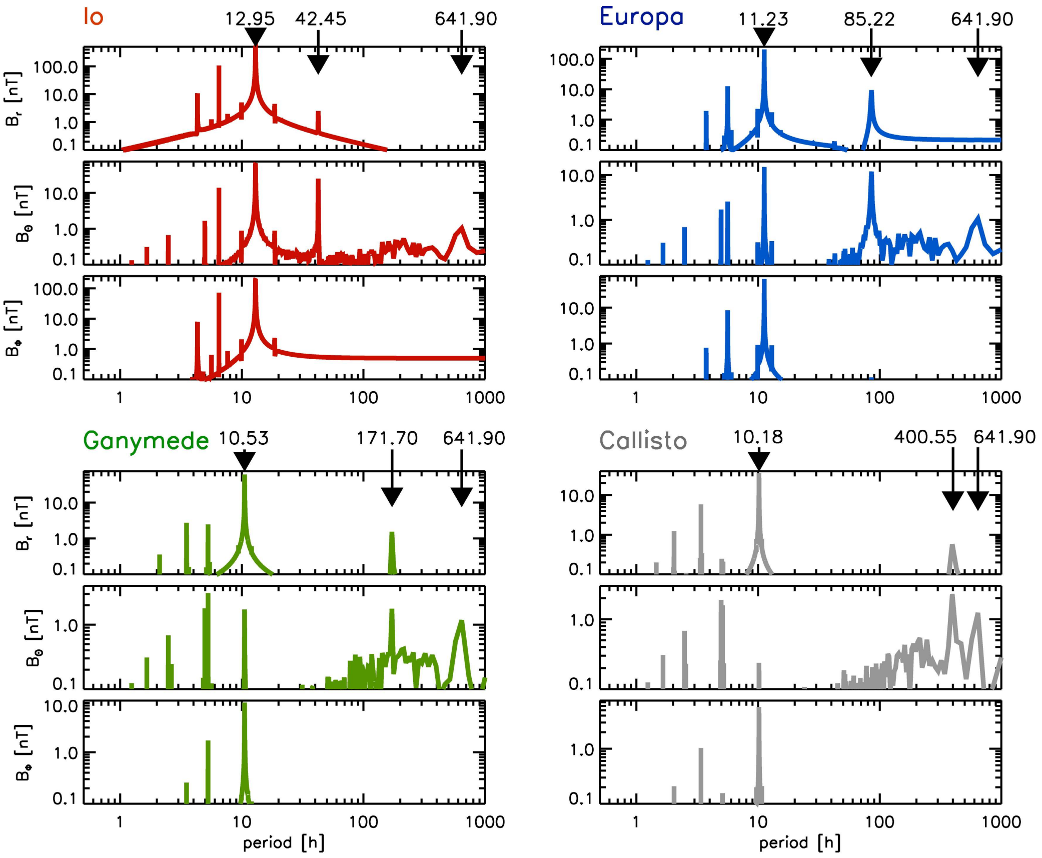

Figure 2.6: *Primary field amplitude spectra for Callisto, Ganymede, Europa and Io. Arrows indicate the synodical, orbital and solar rotation period (from left to right). Note that the scale of the y-axis varies from panel to panel. The displayed amplitudes may differ from the more precise values given in Table 2.13 due to losses by spectral leakage.*

bital eccentricities and the magnetopause field cause additional periodic signals in the B_θ component. The amplitudes of these contributions add up to a maximum of ~27 nT at Io ~17 nT at Europa and ~2.5 nT at Ganymede. At Callisto the amplitude of this signal is almost entirely determined by the position of the magnetopause. For a magnetopause standoff distance of R_{ss} = 60 R$_J$ we predict a signal of ~3 nT.

The strength of this magnetopause field B_θ peak depends on the strength of the solar wind. Figure 2.7 shows the dependency of the peak value on the subsolar point standoff distance in the magnetopause model. Strong solar wind conditions (R_{ss} = 40 R$_J$) lead to increased amplitudes of ~6 nT for Callisto and ~4 nT at Ganymede. These long period inducing signals are of special interest as they penetrate deeper into the satellites' bodies (according to Equation 1.1).

The temporal variability of the magnetopause gives rise to a third set of field periodicities. The spectra in Figure 2.6 show peaks arising at the solar rotation period of 641.9 h. At Callisto and Ganymede this feature is clearly visible with an amplitude of 1.2 nT. For Io and Europa the peaks are of about the same strength but small relative to other B_θ fluctuations. The reason for this similar peak amplitude at all satellites is that the solar rotation period is longer than the orbital periods. Averaged over multiple orbits all satellites can be assumed to be approximately at the location of Jupiter. They therefore experience roughly the same variations regardless of their orbital distance. These very long period inducing signals are again quite weak and will be rather difficult to measure. However, they pose the opportunity to sound very deeply into the satellites' interiors.

The main factors reducing the detectability of the signals presented above are the plasma interaction fields generated in the vicinities of the satellites. Models for the interaction signatures at Callisto are presented in Chapter 3 of this thesis. To allow a rough comparison between the interaction and primary field strengths at this stage of the discussion, estimates for the maximum interaction fields near the satellites are given in the last row of Table 2.13. They were obtained by using the following expression for the maximum total

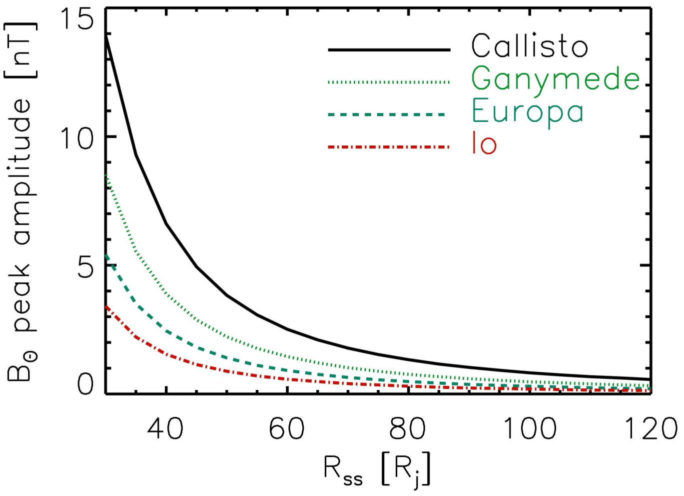

Figure 2.7: *Peak amplitude of the magnetopause field's B_θ component at the orbital period as a function of the subsolar point distance R_{ss}.*

current in both Alfvén wings after *Neubauer* (1980), *Neubauer* (1998b) and *Saur* (2004):

$$I = 8v_0 B_0 \mathrm{R}\Sigma_A \overbrace{\frac{\Sigma_P}{\Sigma_P + 2\Sigma_A}}^{\alpha}, \tag{2.31}$$

where we assume the plasma velocity v_0 to be perpendicular to the magnetic field. The values in Table 2.13 are calculated for the maximum current $I_{\max}$ i.e., in the limit of an infinite ionospheric Pedersen conductance Σ_P ($\alpha = 1$) and for maximum values of the velocity v_0, the background magnetic field B_0 and the Alfvén conductance Σ_A given by *Kivelson et al.* (2004). The magnetic field due to the plasma interaction, B_p, follows from the current flowing through the satellites' ionospheres (with an assumed ionospheric extension of 300 km):

$$\oint B_p \mathrm{d}x = \mu_0 I_{\max} \Rightarrow B_p = \mu_0 \frac{I_{\max}}{\pi(\mathrm{R} + 300\,\mathrm{km})}. \tag{2.32}$$

The interaction signal strength given in Table 2.13 should be taken as a crude estimate of the maximum possible plasma fields occurring in addition to the secondary fields discussed in Section 2.3.2. Examples for field perturbations of this strength (700 nT at Io and 300 nT for Europa) are the I0 (*Kivelson et al.* 1996) and the E12 (*Kivelson et al.* 2000) flybys of the Galileo spacecraft. Most of the time, however, the plasma interaction is much weaker. While the values in Table 2.13 (as well as the I0 and E12 flybys) correspond to situations when the satellites are in the center of the current sheet, the interaction strength significantly diminishes as the satellites move away from this center.

One reason for this dependence is the Alfvén conductance which decreases by a factor of up to 1/2 for Io, 1/5 for Europa, 1/10 for Ganymede and 1/250 for Callisto (*Kivelson et al.* 2004) with distance from the sheet's center. The plasma interaction field B_p decreases accordingly. Additionally, the factor α in Equation (2.31) generally decreases as the ionospheric conductance Σ_P weakens with distance to the current sheet. The reason for this is that Σ_P depends on the ionospheric plasma density, which is controlled by the density of the magnetospheric plasma. Lower values for Σ_P due to variations of the distance from the center of the current sheet can weaken the interaction strength α in some cases about the same degree given above for the Alfvén conductance. Therefore, the analysis of induced fields in the satellites' vicinities is much easier in situations when the distance to the current sheet center is large. Another factor that supports the separation of interaction fields and induced fields is the different temporal dependency of induced fields and interaction fields. While the induced fields periodically change their sign, the steady flow of plasma within the magnetosphere leads to interaction fields which only change in strength but usually not in sign. In summary, it is important to consider the plasma interaction effects for induction studies at all satellites. Within this thesis we present the first attempts to model the measured perturbation fields at Callisto considering both plasma interaction and induced magnetic fields in Section 3.3.3.

After this thorough discussion of the available primary field signals, we determine the secondary fields at the Galilean moons generated by this signals in the following section.

2.3.2 Secondary fields

According to the results for the primary field, three classes of periodicities are present at the Galilean moons: the synodic rotation period of Jupiter, the satellites' orbital periods and the solar rotation period. For each of these frequencies we apply the induction model given by Equations (2.18) to (2.20) to the two interior models introduced in Section 2.2.3 for each satellite.

The resulting secondary field amplitudes A_n (in %) are displayed in contour line plots covering plausible ocean thickness and conductivity ranges (Figures 2.8, 2.10, 2.12 and 2.14). In the following discussions regions near the lower right corner of these plots are denominated as strong and regions near the upper left corner as weak ocean cases. The resolving power the induction method provides for the satellite's core is determined by the amplitude difference (denoted ΔA in Figures 2.8 to 2.14) between the present model and the same model with an unconductive core i.e., with a core conductivity of 10^{-9} S m^{-1} (not exactly zero for numerical reasons). This difference gives the core contribution to the total signal in percent. It is displayed by color contours, where white and yellow colors indicate negative values for ΔA_n or regions where A_n decreases due to higher core conductivities. Note that the color contours and the black isolines denote two different quantities independently plotted in Figures 2.8 to 2.14. The phase shift of the secondary signals is displayed in a similar way in Figures 2.9, 2.11, 2.13 and 2.15.

Multiplication of the values for A_n and the primary field amplitudes $B_{\mathrm{pri},n}$ derived in Section 2.3.1.2, yields the secondary field strength measurable at the satellite's surface. A spacecraft at a distance r would measure signals decreased by the factor $(r/\mathrm{R})^3$ for the dipole fields generated by the locally homogeneous primary fields considered here.

2.3.2.1 Io

Despite the results of *Khurana et al.* (2011) there is no conclusive evidence for a global magma ocean at Io yet. However, *Keszthelyi et al.* (1999) state that a mushy magma ocean in contrast to a solid interior is consistent with the very high temperature silicate lavas and ultramafic volcanism observed at Io. The model by *Keszthelyi et al.* (1999) is adapted here assuming a FeS core of medium conductivity, a relatively conductive partially molten mantle and an up to 250 km thick magma ocean beneath a thin crust (see Table 2.7). The three layer Io model by *Zhang* (2003) was extended by substituting the upper part of the mantle with a magma ocean layer (Table 2.8). This extension may not be consistent with the original model, especially for thick magma ocean layers. Therefore, results for these cases should be taken as a crude estimate for the induction at Io. Figure 2.8 shows the resulting relative amplitudes A_n for both models. To assess the significance of these figures, it is interesting to note that, for large conductivities and small thicknesses of the magma ocean, the amplitude isolines become straight and follow lines of constant magma ocean conductance ($A_n \propto \sigma h$).

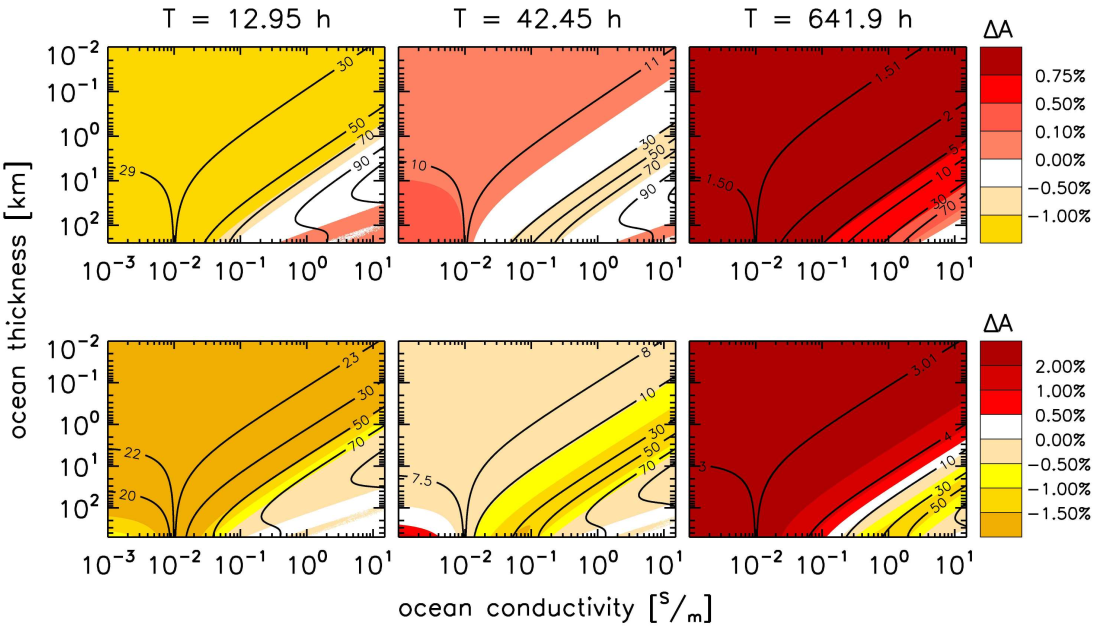

Figure 2.8: Amplitudes of the secondary field A_n with respect to the primary field for the Io-Keszthelyi et al. (1999) (upper panel) and -Zhang (2003) models (lower panel). Three primary field periods T_n and various magma ocean thicknesses and conductivities are considered. Isolines: induced amplitude in % of the primary field strength. Color encoded: differences ΔA_n for the induced amplitudes of interior models with and without a conductive core in % of the primary field strength. White and yellow areas indicate negative values caused by the mutual induction between ocean and core.

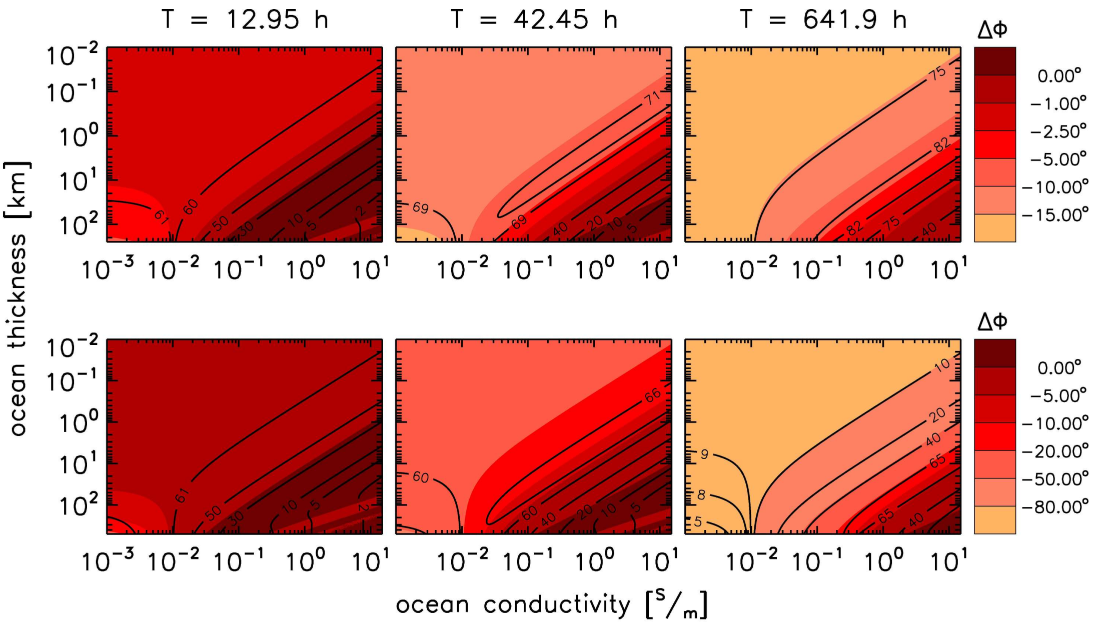

***Figure 2.9:** Phase shift of the secondary field with respect to the primary field for the Io-Keszthelyi et al. (1999) model (upper panel) and the Io-Zhang (2003) model (lower panel) for three primary field periods T_n and various magma ocean thicknesses and conductivities. Isolines: phase shift in degrees. Color encoded: differences for the phase shifts $\Delta\phi_n$ of interior models with and without a conductive core in degrees.*

Observability of the magma ocean

For both models the isolines in Figure 2.8 show that for the synodic rotation period as well as the orbital period amplitudes near 90% are possible for the strong magma ocean case ($\sigma > 1$ S m^{-1}, $h > 5$ km). In this case Io nearly acts as a perfect conductor. For the solar rotation period the maximum amplitude is ~60%. For weaker magma oceans the conductivity of the partially molten mantle prevents the amplitude to drop to zero. To obtain the actual contribution by the magma ocean to the total signal one needs to subtract the signal remaining in the case of a weak magma ocean. This gives a contribution by the magma ocean of ~65% to 80% depending on the period. At Io the partially molten mantle contributes significantly to the total signal. We determine the secondary signal for mantle conductivities of 10^{-4} S m^{-1} and 10^{-2} S m^{-1} and find an increase of up to 20% to 25% for a period of 12.95 h for both models. It should be noted that at 10^{-2} S m^{-1} the conductivity of the magma ocean drops below that of the mantle beneath. In Figure 2.8 this causes a convergence of the isolines at 10^{-2} S m^{-1} and a reversal in the direction of the lines for smaller conductivities. The *Zhang* (2003) model gives amplitudes which are ~7% weaker than those obtained with the *Keszthelyi et al.* (1999) model. This is a result of the higher crustal thickness in this model. An increased distance to the conducting layer results in a significant decrease of the measurable signal. Due to the strong primary signals at Io even a relatively weak magma ocean configuration produces significant signals at the surface of Io in the orbital and synodical frequency range. For the strong magma ocean case ($\sigma > 1$ S m^{-1}, $h > 5$ km) we predict signals of up to 210 nT at a period of 12.95 h and 14 nT at 42.95 h occurring at the surface of Io. The amplitude for the solar rotation period is quite weak (up to 0.4 nT). The strong plasma interaction field at Io, however, will make it very difficult to extract even the strongest induction signals from single flyby measurements (e.g., *Kivelson et al.* 2001, *Saur et al.* 2002).

Observability of the core

The amplitude difference between the original model and the corresponding non-conductive core model is indicated by the color plot in Figure 2.8. At first glance, it is intriguing why this difference becomes negative (white and yellow areas in Figure 2.8). This is possible due to mutual induction occurring between the core and the magma ocean, as discussed in Section 2.3.2.5. The core influence for both models of Io at all periods varies between -1.8% to 2.5%. Multiplication with the primary field amplitude for a period of 12.95 h (Section 2.3.1.2) yields a surface core field strength of ~5 nT. For the 42.95 h period the signal strength would be only 0.2 nT. The maximum difference for all T_n occurs in the range of weak magma oceans for the solar rotation period. However, the corresponding secondary field is very weak ($<$ 0.01 nT). A conductive core is not detectable if a strong magma ocean almost completely shields the core from the primary field. However, mutual induction may in some cases (dark yellow in Figure 2.8) allow for some contribution of a conductive core to the total signal even in the presence of a rather strong ocean.

Phase information

The phase shift of the secondary field with respect to the primary field yields additional information for induction studies. A comparison of the panels of Figures 2.8 and 2.9

shows, that while the amplitude rises monotonously toward the lower right corner of the displayed parameter space, the values for the phase shift reach a maximum value somewhere between the strong and the weak ocean case. Not so obvious but equally important are the different gradients of the isolines in some parts of the parameter space of Figures 2.8 and 2.9. Two different internal configurations showing exactly the same amplitude of the induced field (lying on the same isoline in Figure 2.8) may lead to different phase shifts and could possibly be distinguished. Figure 2.9 shows that strong magma ocean configurations ($\sigma > 1$ S m^{-1}, $h > 5$ km) suppress the phase shift almost completely. However, weaker magma oceans yield a significant phase shift of up to 70°. The timing of the observed induction signal is therefore another indicator for the internal conductivity of the satellite. The differences for the phase again show that a strong magma ocean shields the core. The maximum phase difference occurs for weak magma oceans and is only significant (> 10°) for the orbital and solar rotation periods.

2.3.2.2 Europa

Europa's ocean is thought to lie beneath a relatively thin layer of ice (e.g., *Pappalardo et al.* 1999). It is expected to be directly connected to the rocky mantle which may be one source of heat to keep it liquid (e.g., *Schubert et al.* 2009). The models for Europa used in this study were given by *Kuskov and Kronrod* (2005a) (Table 2.5) and *Zhang* (2003) (Table 2.6). Both are four layer models including a FeS- or Fe-core, a silicate mantle and a liquid ocean beneath an icy crust with differences in the ice shell thickness and core conductivity. The results are presented in the Figures 2.10 and 2.11.

Observability of the ocean

Both interior models show that a strong ocean ($\sigma > 1$ S m^{-1}, $h > 10$ km) induces signals which almost reach the primary field strength (80% to 90%) for all periods. According to our results of Section 2.3.1.2 such an ocean would produce signals at Europa's surface of 80 nT at 11.23 h, 6 nT at 85.22 h and 0.5 nT at a period of 641.9 h. The results for both models are almost indistinguishable. Obviously the slightly smaller ice shell thickness and the larger core conductivity of the *Zhang* (2003) model have no major influence. The nearly unconductive mantle layer does not affect the strength of the total signal. Up to a mantle conductivity of $\sim 10^{-3}$ S m^{-1} its influence lies beneath 1% of the primary signal. Our model predicts, however, significant signals of ~50% even for moderate ocean parameters of $h \approx 1$ km and $\sigma \approx 5$ S m^{-1}. In agreement with results from other authors (e.g., *Zimmer et al.* 2000, *Schilling et al.* 2007) we conclude that the large induction signals observed at Europa might very well be the result of a liquid ocean. There are still many unknown parameters of the ocean like its depth, its extension, its salinity and so on. This information may be gained by obtaining magnetic field data of sufficient accuracy to be analyzed for multiple inducing frequencies. The measured amplitude for a single frequency can be explained by models with various ocean thicknesses h and conductivities σ (represented by isolines in Figure 2.10). The amplitudes depend non-linearly on the interior conductivity parameters. Therefore, with amplitude information for multiple frequencies, all interior models which cannot explain these values can be simultaneously ruled out. Information for each single frequency therefore narrows the

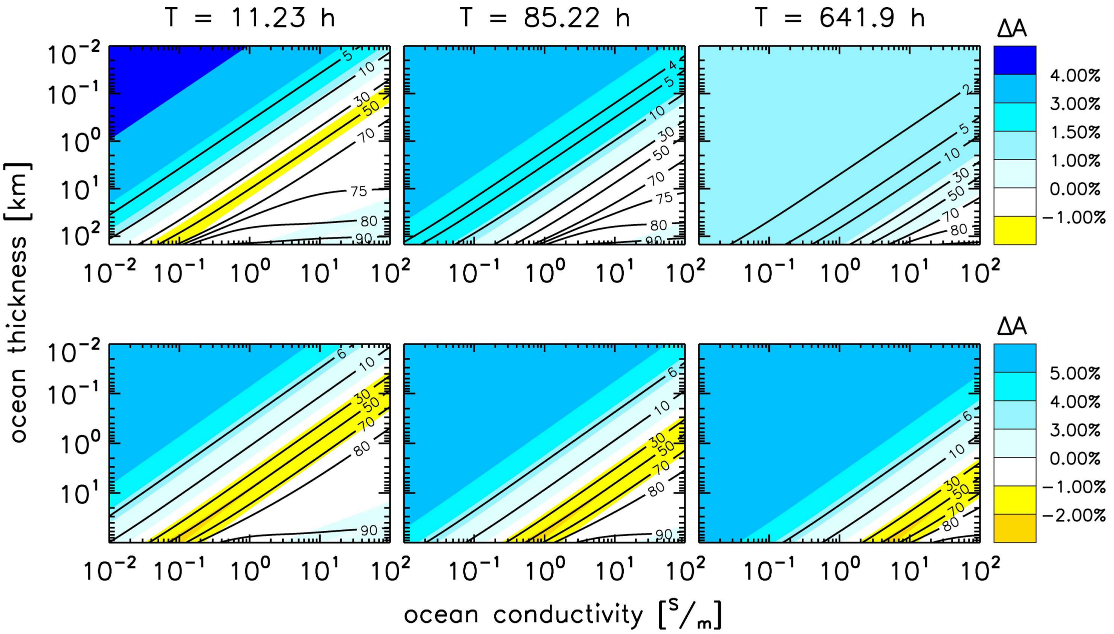

Figure 2.10: *Relative amplitudes A_n in % for the Europa-Kuskov and Kronrod (2005a) (upper row) and -Zhang (2003) models (lower row). Refer to Figure 2.8 for further explanations.*

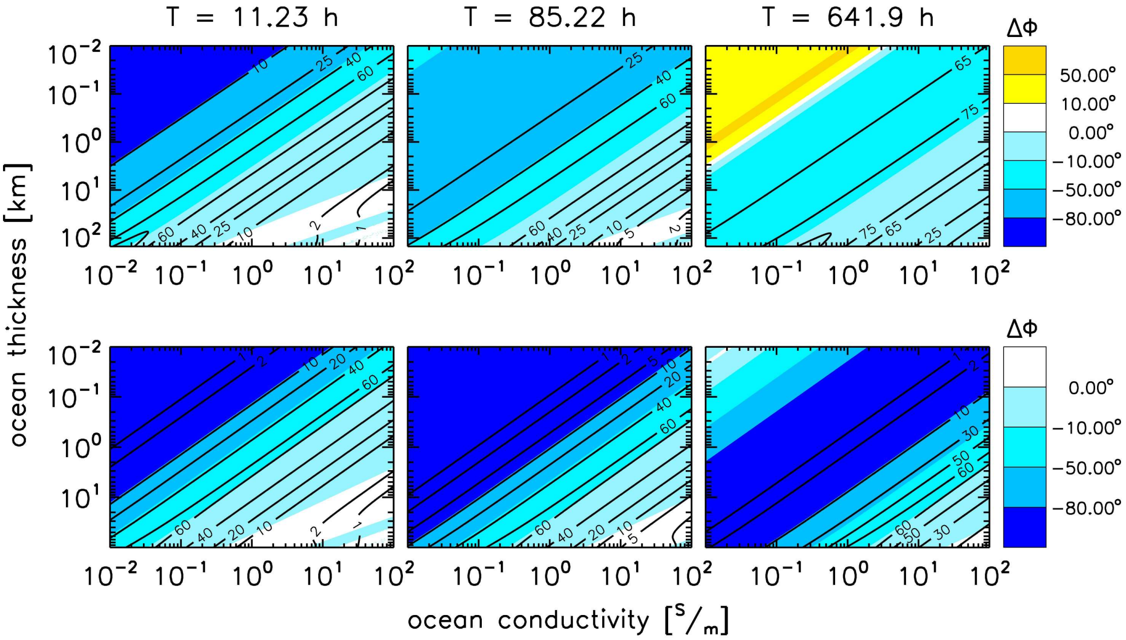

Figure 2.11: *Phase shift ϕ_n in degrees for the Europa-Kuskov and Kronrod (2005a) (upper row) and -Zhang (2003) models (lower row). Refer to Figure 2.9 for further explanations.*

valid parameter range for σ and h. Our results show that multi-frequency measurements at Europa should be possible at all three presented frequencies.

Observability of the core

In the absence of a conductive ocean ($\sigma < 1$ S m^{-1}, $h < 1$ km) the secondary field strength drops to ~5% of the primary field for the *Zhang* (2003) model and 1.4% to 4% (depending on the frequency) for the *Kuskov and Kronrod* (2005a) model. The residuals are signals induced in the core. Although their relative values are larger than at Io, the lower primary field amplitudes give rise to about the same secondary field strength at the surface of 5 nT at a period of 11.23 h. For a period of 85.22 h the signal strength is ~0.4 nT. The major limiting factor for the detection of these signals is the strong damping by Europa's ocean. There is, however, a certain parameter range of σ and h (yellow in Figure 2.10) where the mutual induction effect allows for a core signal of 1% to 2% in the presence of the ocean. If an ocean is clearly visible in the signal for multiple frequencies but one frequency lacks these 1% to 2% of the predicted signal strength this could be interpreted as the contribution of a conductive core due to mutual induction. This fact could be exploited to detect the core in future measurements. For example, with an iron core like in the *Zhang* (2003) model a contribution of ~2 nT to the total signal at a period of 11.23 h is reached for ocean parameters inside the yellow colored region of Figure 2.10 (lower panel). We therefore conclude that it might be possible to detect a conductive core at Europa with the induction method though the signal is likely rather small.

Phase information

The phase shift for strong ocean cases at Europa ($\sigma > 1$ S m^{-1}, $h > 10$ km) is small for the synodical and orbital inducing frequencies (see Figure 2.11). It is, however, ~10° to 20° larger for the solar rotation period. When we compare both interior models we see that the higher core conductivity of the *Zhang* (2003) model leads to a much smaller phase shift for weak oceans ($\sigma < 1$ S m^{-1}, $h < 1$ km). The difference in the phase shift in the case of a non-conductive core is also large in the absence of a conductive ocean (see color contours at the top left corners in all panels of Figure 2.11).

2.3.2.3 Ganymede

For the analysis of Ganymede's secondary fields we adapt models by *Kimura et al.* (2009) and *Zhang* (2003) summarized in Tables 2.3 and 2.4. The model of *Kimura et al.* (2009) consists of five layers with an ocean located between the icy crust and a lower mantle ice layer. It is based on numerical simulations of the thermal history of Ganymede. The model predicts a phase transition from ice I to ice III, ice V and ice VI through the first 900 km of the satellite. The high pressure (III, V and VI) ices are treated as a single layer with a homogeneous conductivity here. The thicknesses of the silicate layer below the ice and the innermost core layer vary between 900 to 1,100 km and 834 to 634 km, respectively, depending on the core density. Although the *Zhang* (2003) four layer model is probably too simple to realistically describe Ganymede's interior, it is considered here to allow for a comparison with the other satellites. The model consists of an iron core, a rocky mantle and an icy crust at the bottom of which we include Ganymede's ocean.

Please note that the assumption that the ocean lies deep inside the interior and has contact to the rocky mantle is not very realistic. However, this setup allows us to investigate at which depth the ocean produces a significant signal. Also the range for the thickness of the ocean may be greatly exaggerated. In this section we further refer to a model by *Schubert et al.* (2004) which is not explicitly presented here.

Observability of the ocean

The amplitude structures for both Ganymede models look quite different (isolines in Figure 2.12). For the *Kimura et al.* (2009) model the top of the ocean is relatively close to the surface. This causes large induced amplitudes of ~80% even for average values for the conductivity ($\sigma > 0.1$ S m^{-1}) and thickness ($h > 0.1$ km) of the ocean. The mantle contributes less than 1% to these signals for conductivities lower than 10^{-3} S m^{-1}. The corresponding secondary field strength at the surface is ~32 nT for a period of 10.53 h, 0.6 nT for 171.7 h and 0.5 nT for 641.9 h. For the *Zhang* (2003) model the relative amplitudes are considerably smaller (up to ~50% less), except for large values of h (> 100 km). The reason for this is that the upper boundary of the ocean lies deep inside the satellite for thin ocean layers. As the lower boundary is kept fixed, the ocean is close to the surface only for large ocean thicknesses. We conclude that an ocean which lies deep in the interior of Ganymede generates significantly weaker induction signals. For realistic ocean depths of ~150 km (e.g., *Spohn and Schubert* 2003) this effect should be rather small. One should, however, keep in mind that the detectability of all oceans presented in this study crucially depends on the depth of its upper boundary.

Observability of the core

The internal dynamo field discovered at Ganymede by *Kivelson et al.* (1996) indicates the existence of a layer of molten iron in the core region of the satellite. Additional information about Ganymede's core might be gained from an analysis of induction signals caused by different periods of the time varying external magnetic field. The core's contribution to the total field induced by the primary field (neglecting Ganymede's internal field) in absence of an ocean on Ganymede is ~5% of the primary field for the *Kimura et al.* (2009) model and ~2% for the *Zhang* (2003) model, where the core radius is ~300 km smaller. The Ganymede model given by *Schubert et al.* (2004), whose results are otherwise similar to the *Kimura et al.* (2009) model, also shows less distinct core signals of ~2.7% due to its smaller core radius. Without a conductive ocean the resulting secondary field at the surface has a strength of ~2 nT at a period of 10.53 h for the *Kimura et al.* (2009) model. The signal induced in the core easily becomes obscured by the overlying ocean. The mutual induction effect gives rise to core signals of up to 0.8 nT in some cases (yellow regions in Figure 2.12). This signal strength is, however, very likely too small to allow for a reliable detection of the core especially in the presence of plasma interaction fields.

Phase information

The phase information gives a similar picture for both models (Figure 2.13). A strong ocean configuration ($\sigma > 10$ S m^{-1}, $h > 10$ km) suppresses the phase shift. The same applies for the case of weak ocean configurations where the remaining signal represents the influence of the core. Therefore, a weak signal with little phase shift could be inter-

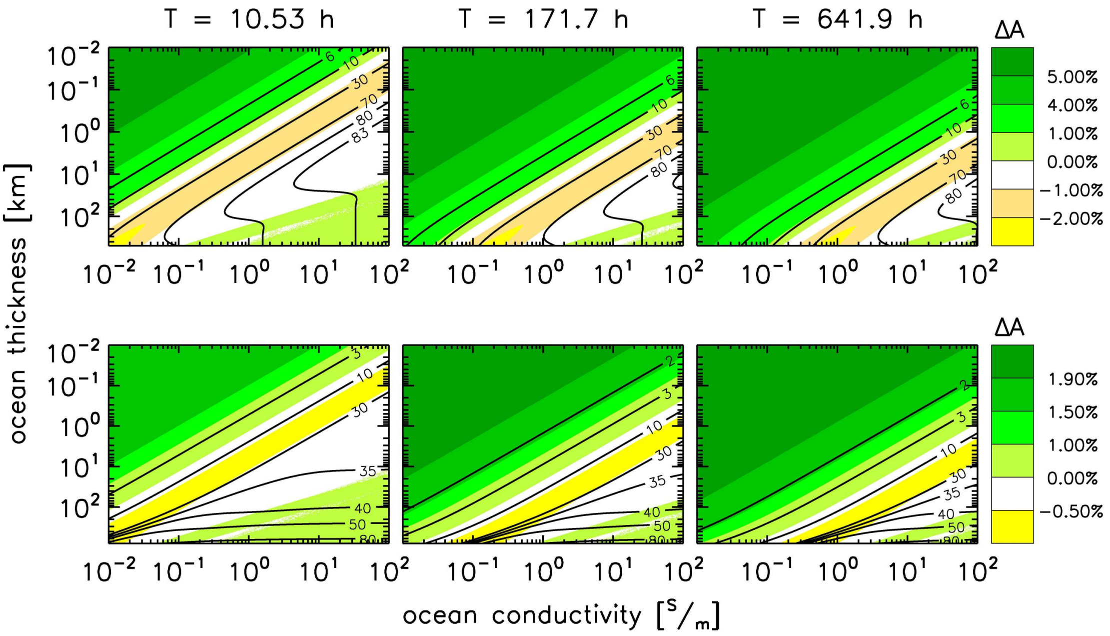

Figure 2.12: *Relative amplitudes A_n in % for the Ganymede-Kimura et al. (2009) (upper row) and -Zhang (2003) models (lower row). Refer to Figure 2.8 for further explanations.*

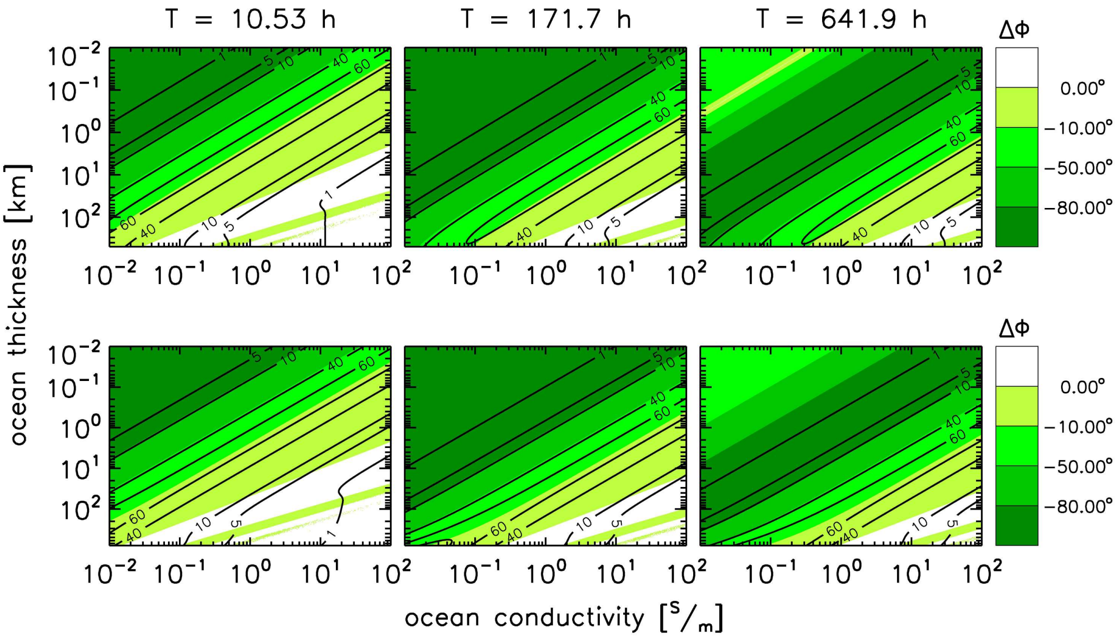

Figure 2.13: *Phase shift ϕ_n in degrees for the Ganymede-Kimura et al. (2009) (upper row) and -Zhang (2003) models (lower row). Refer to Figure 2.9 for further explanations.*

preted as a signal of the core alone while a strong signal without phase lag indicates a significant contribution of an ocean. The parameter regime with the biggest phase shift seems to coincide with the regime where mutual induction plays a role. In summary it seems promising to include the phase information in analysis of real data at Ganymede.

2.3.2.4 Callisto

Callisto's only partially differentiated interior (*Anderson et al.* 2001b) can be addressed by adapting the model of *Kuskov and Kronrod* (2005a) as a six layer representation (Table 2.1) with increasing conductivities toward the center. The ocean is assumed to lie beneath an icy crust and above a mantle divided in three sub layers. Callisto does not possess a core with a significant amount of iron in this model so that its conductivity is rather low. Multilayer Callisto models by *Sohl et al.* (2002) constrained by Galileo gravity measurements discuss different core compositions and densities, such as pure olivine-type rocks with 3,300 kg m^{-3} and a mixture of 50 wt% iron and 50 wt% olivine. In these models the outermost icy shell with a thickness of 660 km includes a phase transition from ice I to ice VI. The layer beneath consists of hydrated silicates or a rock-ice mixture with a shell thickness of 1,150 to 1,300 km depending on the core density.

The results we infer for the *Sohl et al.* (2002) models are quite similar to the ones presented for the *Kuskov and Kronrod* (2005a) model in this section. The only notable difference comes from a slightly larger crust i.e., ice I layer thickness of ~180 km. Therefore, we choose not to present results for the *Sohl et al.* (2002) Callisto model. This model consists of four layers with a larger crustal thickness and a larger core density than the *Kuskov and Kronrod* (2005a) model. We adapt this fact by increasing the core conductivity. The assumption of an ocean located deep in the interior in direct contact to the mantle and the large range of ocean thicknesses are hardly realistic. Therefore, this model should not be used as a stand alone case, but only for comparison with the more realistic *Kuskov and Kronrod* (2005a) model and the other *Zhang* (2003) models. The results are shown in Figures 2.14 and 2.15.

Observability of the ocean

Figure 2.14 shows a distinct signal of up to 80% for the synodic rotation period even for average conductivities ($\sigma > 1$ S m^{-1}) and thicknesses ($h > 1$ km) for both models. The *Sohl et al.* (2002) model (not depicted here) gives similar results except for a 2% to 4% smaller amplitude for strong ocean configurations. This is due to the larger crustal thickness assumed in this model. The contribution of the mantle layers to these values is less than 1% as long as their conductivities are lower than 10^{-4} S m^{-1}. Taking into account the results of Section 2.3.1.2, the strength of the secondary field for the 10.18 h period is 16 nT at the surface of Callisto. The rotation period of Callisto is comparable to the solar rotation period. For both frequencies a signal of 70% to 80% can be expected for strong ocean cases ($\sigma > 10$ S m^{-1}, $h > 10$ km). The corresponding secondary field strengths are 0.9 nT for 400.55 h and 0.4 nT for a period of 641.9 h. To apply the multi-frequency approach at Callisto it is necessary to measure the magnetic field in the vicinity of the satellite very precisely and to determine the contribution from the plasma interaction.

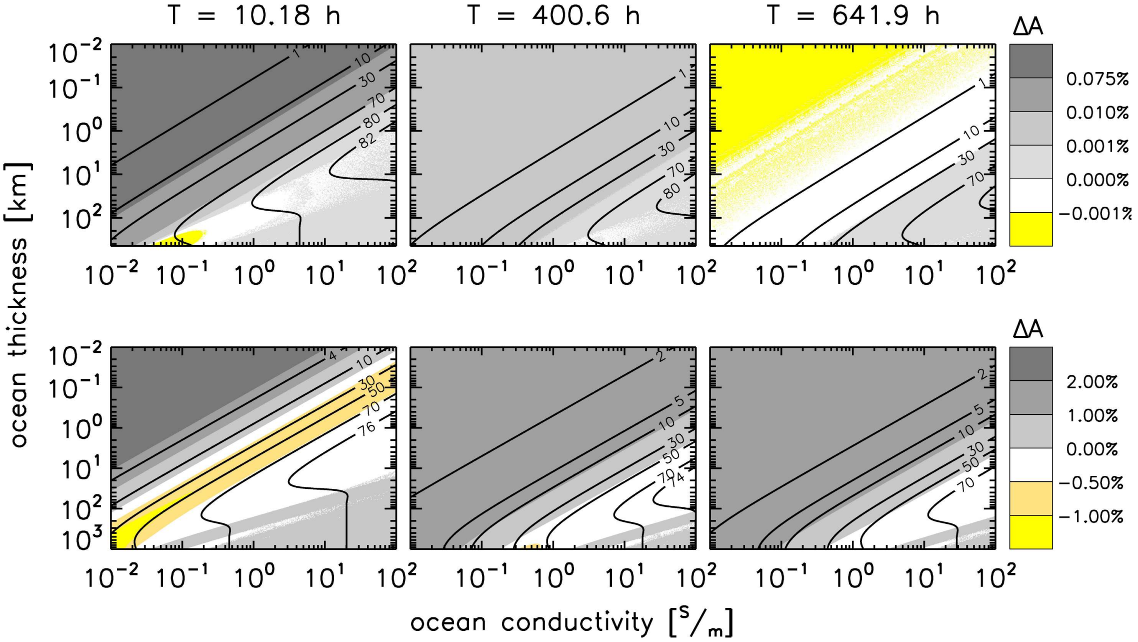

Figure 2.14: *Relative amplitudes A_n in % for the Callisto-Kuskov and Kronrod (2005a) (upper row) and -Zhang (2003) models (lower row). Refer to Figure 2.8 for further explanations.*

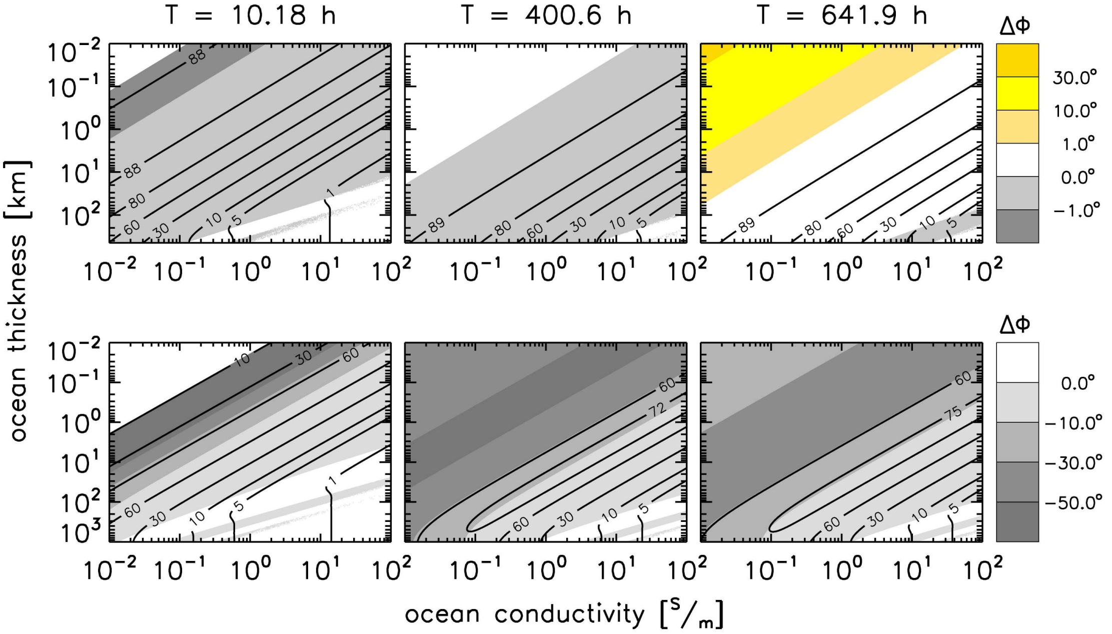

Figure 2.15: *Phase shift ϕ_n in degrees for the Callisto-Kuskov and Kronrod (2005a) (upper row) and -Zhang (2003) models (lower row). Refer to Figure 2.9 for further explanations.*

Observability of the core

The rather non-conductive core adapted for the *Kuskov and Kronrod* (2005a) model generates signals which have almost no influence on the total induction signal and will certainly not be detectable. The situation looks somewhat better for the *Zhang* (2003) model. However, contributions of 1% (with mutual induction, yellow regions in Figure 2.14) to 2% (without a conductive ocean) only yield a secondary field strength at the surface of 0.2 to 0.4 nT at a period of 10.18 h. We conclude that it is not possible to gain information about Callisto's core from induction measurements at any frequency.

Phase information

The model results for Callisto show that a strong ocean ($\sigma > 10$ S m^{-1}, $h > 10$ km) suppresses a phase shift of the signal. For a non-conductive ocean the weak overall conductivity of the *Kuskov and Kronrod* (2005a) model leads to a phase lag of nearly 90°. The larger core conductivity of the *Zhang* (2003) model on the other hand suppresses the phase shift to some degree. Therefore, if there were no ocean on Callisto one could possibly gain information about the core from the phase shift.

2.3.2.5 Mutual induction

Throughout this section we repeatedly mentioned the effect of mutual induction. When we subtract the amplitude results of models with a weak core conductivity from our original models we get negative values for certain ocean thicknesses and conductivities. This means that a less conductive core can lead to a larger induction signal than a highly conductive core if a conductive ocean is present. The reason for this is as follows. The time-variable primary field ((1) in Figure 2.16) induces a field inside the satellite's core ((3) in Figure 2.16). This field in turn is part of the total field the conductive ocean (blue layer in Figure 2.16) experiences. However, the field induced in the core tries to act against the primary field and therefore has an opposite sign. It induces a magnetic field inside the ocean which leads to a decrease of the total induction signal outside the satellite ((4) and (4') in Figure 2.16).

The mutual induction between the core and the ocean is completely included in the theoretical description of Section 2.2. It is only significant when the ocean layer is not conductive enough or too thin to completely shield the underlying material from the primary field. On the other hand it needs to be conductive enough to allow for induction from the core signal. That is why we see this effect in an intermediate parameter region in the Figures 2.8 to 2.14 presented above (white and yellow regions). Generally all fields induced at the satellites in turn induce magnetic fields in all conductive layers.

2.3.2.6 Satellite measurements

Magnetometer data of the Galileo spacecraft are, so far, the only sources for induction measurements at the Galilean moons. Only a few flybys exist which provide measurements in the vicinity of the satellites for a short period of time. It is very difficult to ade-

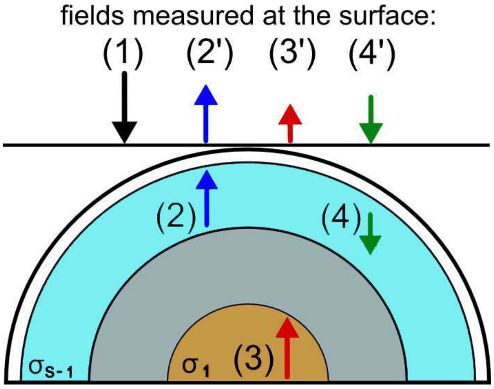

Figure 2.16: *Concept of the mutual induction effect at a satellite with two conductive layers (e.g., a conductive ocean σ_{S-1} and core σ_1). Black arrow: primary field (1), blue arrow: secondary ocean field (2) induced by (1), red arrow: secondary core field (3) induced by (1), green arrow: ocean field (4) induced by (3). (2'), (3') and (4') represent the induced fields as they would be measured at the surface of the satellite. For suitable internal structures (3') becomes smaller than (4') and the mutual induction reduces the total signal.*

quately separate magnetic fields from plasma interaction effects in these data. Therefore, those measurements are not well suited for multi-frequency induction analysis. Additional magnetometer measurements by future Jupiter system missions are therefore necessary to apply the multi-frequency induction method.

For multi-frequency induction studies it is preferable to use magnetometer data from a spacecraft orbiting the satellite rather than just flyby data. An orbiter could perform continuous measurements over a time of several excitation periods and thus provide an excellent temporal coverage. The optimal geometry for such orbits would be a low polar orbit. A coverage of the whole satellite surface can be achieved by the rotation of the orbit in the east-west direction. As the secondary field strength decreases by r^{-3} with distance to the surface, it is crucial to keep the orbits as low as possible. In addition, the internal field ”seen” from a low polar orbit will contain only small plasma magnetic fields from the thin shell between the orbital envelope and the surface. To gain information about the secondary field contributions at Ganymede it is necessary to determine the moments of the internal field. As the internal field is expected to be temporally constant throughout the orbiting phase, it should be relatively straightforward to obtain its strength.

When the data is acquired during flybys the best geometry for the measurements also is low polar flyby. In this case it is more difficult to filter out the plasma interaction field. Precise modeling of each flyby is necessary to apply induction techniques. Finally it is of course necessary to obtain a good absolute accuracy as well as good long term stability of the magnetometer. The challenge for the magnetometer and mission engineers will therefore be to enable measurements with suitable precision (~0.1 to 1 nT according to the results in this thesis).

The next opportunity to study induced fields in the Jovian system may be provided by the JUICE mission recently approved by the European Space Agency (ESA). This mission presumably includes an orbiter around Ganymede and multiple flybys at the other Galilean moons. JUICE will presumably arrive at Jupiter in 2030.

2.3.3 Conclusions

We used models for the Jovian magnetospheric field, the internal conductivity structure and the induced fields in a multi-layered sphere to infer the primary and secondary magnetic fields in the vicinity of the Galilean moons.

For the primary field we proved the existence of three main classes of periodicities: the synodic Jovian rotation period with respect to the satellites and fractions of these periods, the satellites' orbital periods and the solar rotation period. Although the strongest signals are available for the synodic rotation period, the signal amplitudes at several different periods are generally large enough to allow for multi-frequency induction studies at all satellites. Further, the derived long periodic signals may provide the opportunity for a deep sounding of the satellites' interiors. The complete set of available primary field periodicities and amplitudes were summarized in Table 2.13.

In a second step the relative amplitudes and phase shifts of the secondary fields at all Galilean satellites were determined for the three major primary field periods and two separate interior models. The secondary field contributions of possible conductive ocean layers should be measurable at several of the presented frequencies for all satellites. Additional induced signals from the interior core layers are generally very weak. The presence of conductive ocean layers effectively shields the deep interior from the penetrating primary field signals. However, mutual induction between the core and ocean layers may provide induced field signals even in the presence of distinct ocean layers. Still, measurements for the induced fields will most likely not allow to infer information about the state of the satellites cores. Table 2.14 briefly summarizes the predicted secondary field strengths $B_{\mathrm{sec},n}$ generated by the core and ocean layers. Note that these values refer to the field strength at the equator of the induced dipole for all satellites (Equations (2.10) to (2.12)).

	Callisto	**Ganymede**	**Europa**	**Io**
Ocean signal (synodic rot. period)	16	32	80	210
Ocean signal (orbital rot. period)	0.9	0.6	6	14
Ocean signal (solar rot. period)	0.4	0.5	0.5	0.4
Core signal (synodic rot. period)	0.4	2 (0.8)	5 (2)	0 (5)

Table 2.14: *Summary for the predicted secondary field strengths $B_{sec,n}$ (in nT) generated by conductive ocean and core layers. The given values represent the field strength at the equator of the induced dipole at the surface of the Galilean satellites. Values for the core signals refer to cases where no conductive ocean layer is present or where mutual induction occurs (values in brackets).*

To apply a multi-frequency approach using real magnetic data suitable measurements are necessary. To obtain a sufficient strength of the secondary signal, it would be preferable to perform precise magnetic measurements with a spacecraft on a low polar orbit. The scientific value of these data is significant as it may allow the confirmation of liquid water and the characterization of the corresponding reservoirs at the Galilean moons. Therefore, induction studies potentially yield unprecedented implications regarding the origin of life and the formation of our Solar System.

3 Callisto's plasma interaction

The possible induction signals at Callisto derived in Chapter 2 theoretically allow to infer information about the satellite's interior from magnetometer measurements. However, the additional magnetic perturbations caused by the satellite's plasma interaction potentially lead to ambiguities regarding the amplitude and phase shift of the induced field. It is therefore necessary to distinguish both contributions to the measured signal as precisely as possible. The interaction process is generally non-linear in its nature. Therefore, analytical models can only be formulated for very specific cases. Especially at Callisto, where the parameters of the ambient plasma flow and the general geometry of the plasma interaction are subject to large variabilities, numerical models provide the only reasonable means to determine the interaction signatures. Suitable descriptions of the collision, mass loading and loss processes due to the satellite's neutral atmosphere are crucial components for realistic plasma interaction models. In turn, a model which yields a reasonable magnetic field or plasma data fit for different ambient plasma conditions may provide constrains for the nature of the satellite's atmospheric system. Therefore, apart from the induced fields, Callisto's atmosphere and ionosphere are the primary targets for the present analysis.

In contrast to Chapter 2 where we primarily used the jovicentric System III coordinates, most of the definitions, data and results presented within this chapter are given with respect to the CphiO coordinate system. This right-handed Cartesian coordinate system is defined with its origin at the center of the moon, the x-axis pointing in the direction of rigid corotation, the y-axis directed towards Jupiter and the z-axis parallel to Jupiter's rotational axis. Most of the distances given in this chapter are measured in Callisto radii (R_C = 2410 km). Before we introduce our MHD model for Callisto's plasma interaction, we first summarize available observations and models which provide valuable constrains for the interaction model setup.

3.1 Observations and previous models

To date, no numerical models for Callisto's plasma interaction were presented in peer review literature. However, a vast amount of numerical and analytical models have been established to analyze the interaction at the other satellites of Jupiter and Saturn (e.g., *Neubauer* 1998b, *Saur et al.* 1999, *Liu et al.* 2000, *Simon et al.* 2006, *Jia et al.* 2008, *Kriegel et al.* 2009). The MHD model presented in the following sections was formulated using similar approaches as the models given by *Schilling* (2006) for Europa, *Jacobsen*

(2011) for Io and *Backes* (2004) for Titan. It should be noted that, in spite of the similarities regarding the induction signals encountered at Europa, Titan's plasma interaction more closely resembles the conditions at Callisto. This similarity is reflected, for example, by the rather low magnitude of the magnetospheric background field at Callisto and Titan of ~40 nT and ~5 nT, by the comparable plasma densities of ~0.1 cm^{-3} and by the overall high variability of the ambient plasma conditions at both satellites (compare e.g., Table 1.2 and Table 2.2 given by *Backes* 2004).

The Galileo mission provided magnetic field measurements for seven flybys in the vicinity of Callisto dubbed C3, C9, C10, C21, C22, C23 and C30. Besides several studies discussing Callisto's internal field contributions using C3, C9 and C10 flyby data (*Khurana et al.* 1997, *Kivelson et al.* 1999, *Zimmer et al.* 2000, *Kivelson* 2004), most of the data sets have not been published in the literature. However, the data for all flybys are freely available at the Planetary Data System. We present the C3, C9, C10 and C22 magnetometer data sets along with our results in Section 3.3.3 and the remaining C21, C23 and C30 data in Appendix A.2. The trajectories of the flybys are also given in the respective sections. Further basic information for each Galileo encounter are summarized in Table 3.1. Unfortunately, no magnetometer data was recorded during the C20 Galileo orbit. Therefore, no discussion for this flyby is given in the course of this thesis. With exception of the C9 flyby, Galileo always approached Callisto in the downstream wake region close to the satellite's equatorial plane. The minimum distance to the surface for all flybys was reached during the C30 encounter. Still, all flybys reached minimum altitudes below one Callisto radius. In addition to the recorded magnetometer data indicated by the index M in the last column of Table 3.1, solar occultation measurements of Callisto's ionospheric electron densities (I) and observations of the background plasma conditions (P) were performed by Galileo. A summary of the respective data relevant for the interaction model is given in the following sections.

Flyby	Date	$\lambda_{\rm III}$ [°]	z_{cs} [R$_J$]	$\alpha_\odot$ [°]	Altitude [km]	Geometry	Meas.
C3	1996-Nov-04	242.9	3.24	110.0	1,135.9	Cent. Wake	M, P
C9	1997-Jun-25	59.9	-3.52	83.0	418.1	Upstream	M, I, P
C10	1997-Sep-17	335.9	-2.45	75.5	535.3	Cent. Wake	M, P
C20	1999-May-05	153.3	2.93	267.5	1,321.4	Wake	I
C21	1999-Jun-30	316.1	-1.87	26.1	1,048.1	Wake	M, P
C22	1999-Aug-14	26.8	-4.31	272.0	2,299.3	Wake	M, I, P
C23	1999-Sep-16	278.8	1.08	268.8	1,052.4	Wake	M, I, P
C30	2001-May-25	76.2	3.50	197.5	131.91	Downstream	M, P

Table 3.1: *Summary of all Galileo flybys at Callisto. λ_{III} and $\alpha_\odot$ denote the System III western longitude and the solar phase angle measured counterclockwise from the Sun-Jupiter anti-solar line. z_{cs} is the height above or below (negative values) the current sheet, obtained by applying Function* (2.26) *of the current sheet model. All values correspond to the situation at the closest approach of Galileo at Callisto. The last column indicates if magnetometer (M), radio occultation (I) or plasma parameter measurements (P) are available for the respective flyby.*

3.1.1 Atmosphere and ionosphere

Kliore et al. (2002) present ionospheric electron density profiles recorded during eight radio occultation measurements at four Galileo encounters of Callisto (see Figure 3.1). Six out of these eight measurements show peak densities which exceed the associated error bars indicating the presence of an ionospheric electron layer. The peak values reach 5,100 ± 3,300 cm^{-3} for C20, 15,300 ± 2,300 cm^{-3} for C22 and 17,400 ± 1,500 cm^{-3} for the C23 flyby. For C9 no distinct electron peak densities were inferred. Despite of the limited amount of available data and the uncertainties therein, *Kliore et al.* (2002) note that a necessary condition for the formation of an ionosphere might be that the impinging plasma and the solar radiation both affect the same hemisphere of Callisto. These conditions were encountered during C20, C22 and C23 but not for C9. This fact could imply that sputtering by energetic plasma particles is the dominant generation process of the atmosphere. This process leads to increased atmospheric densities at the upstream hemisphere of the satellite. Consequently, if photo ionization is the dominant process for the generation of the ionospheric particles no significant ionospheric layers forms if the upstream hemisphere is not sunlit. We revisit this hypothesis in Section 3.3.2 where we discuss the nature of Callisto's ionosphere as predicted by our MHD model.

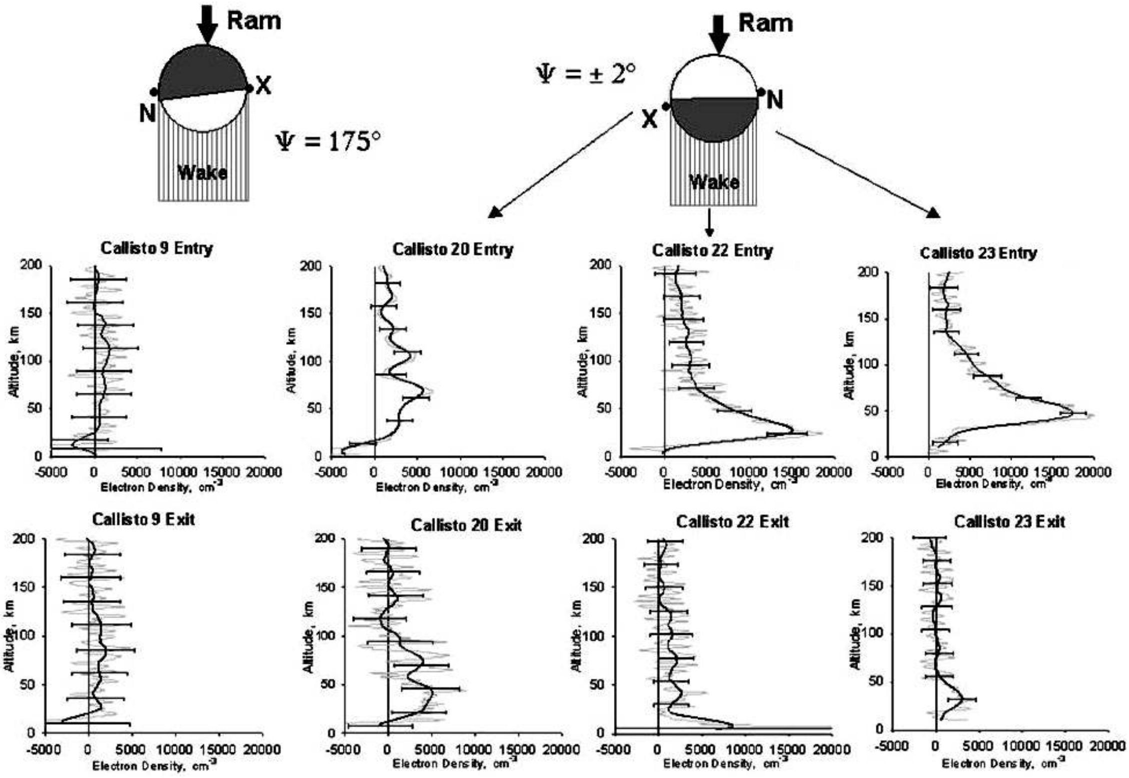

Figure 3.1: Electron density profiles of Callisto's ionosphere inferred from radio occultation measurements after Kliore et al. (2002). Two measurements denoted "Entry" (N) and "Exit" (X) are given for each flyby. Solid black lines show smoothed versions of the unsmoothed gray profiles. The solar zenith angle Ψ is related to the solar phase angle $\alpha_{\odot}$ used in this thesis by $\Psi = 270° - \alpha_{\odot}$. The upper sketches indicate the geometry of the solar irradiation for the respective flybys. Dark areas indicate the shadow region.

The measured ionospheric densities allow conclusions for the surface density and scale height of Callisto's neutral atmosphere. *Carlson* (1999) discovered a CO_2 atmospheric component at Callisto by performing an off-limb scan with the Galileo Near Infrared Mapping Spectrometer (NIMS) during the C10 encounter. The inferred surface density is 4×10^8 cm^{-3} with an atmospheric scale height of 23 km derived for an assumed surface pressure of 7.5×10^{-9} mbar. According to *Kliore et al.* (2002) these neutral atmospheric densities are too low to explain the measured ionospheric peak densities. Instead, in analogy to Europa and Ganymede, an undiscovered O_2 atmosphere with a surface density of 10^{10} to 3×10^{10} cm^{-3} and a scale height of 15 to 25 km could explain the measured electron densities considering both electron impact and photo ionization processes. The chemistry of such a combined CO_2 and O_2 atmosphere has been modeled by *Liang et al.* (2005) taking into account the results from the radio occultation measurements. In this thesis we adapt their model values for the O_2 atmospheric surface density of 7×10^9 cm^{-3} and scale height of 23 km.

Unfortunately, all attempts to prove the existence of Callisto's O_2 atmosphere failed to this date. *Strobel et al.* (2002), however, obtained upper limits for the abundances of O_2, CO, C and O which were also taken into account for the *Liang et al.* (2005) model. For our plasma interaction model we consider different setups assuming the presence of a pure CO_2 or a combined CO_2 and O_2 atmosphere.

3.1.2 Plasma environment

The densities, velocities and thermal characteristics of the magnetospheric plasma particles near Callisto can be deduced from recordings by the Galileo Plasma Subsystem (PLS, see *Frank and Paterson* 2002 for values at orbits encountering Callisto) and Plasma Wave Subsystem (PWS, see *Gurnett et al.* 1997, 2000) instruments. Due to the high uncertainties in the derived values no decisive parameters for the ambient plasma flow were published for the flybys at Callisto so far. However, *Bagenal and Delamere* (2011) give a model for the plasma parameters throughout the Jovian magnetosphere based on statistics inferred from the above measurements. Their functional description of the radial plasma density distribution in the magnetic equatorial plane yields a value of $n_{0,\mathrm{eq}} = 0.153$ cm^{-3} at the position of Callisto. The background plasma densities n_0 for different heights z_{cs} of Callisto with respect to the center of the current sheet (see Table 3.1 and Equation 2.26) can be obtained from:

$$n_0(z_{cs}) = n_{0,\mathrm{eq}} e^{-z_{cs}/H_{cs}}, \tag{3.1}$$

where the scale height of the current sheet at Callisto's orbit is given by $H_{cs} = 3.65$ R$_J$. The thermal ion temperature T_i of the plasma near Callisto is given in Figure 3 of *Bagenal and Delamere* (2011). We adapt a value of $k_B T_i = 635$ eV. This value lies close to the value for the electron temperature of $k_B T_e = 500$ eV given by *Kivelson et al.* (2004). We can therefore assume, that the mean temperatures of the plasma electrons and ions are approximately equal. Note, however, that *Kivelson et al.* (2004) suggest rather low ion temperatures of 10 to 100 eV in contrast to the value for T_i used in this thesis. Assuming a plasma temperature of $T_0 = T_i = T_e$ and ideal gas conditions the total internal energy density e_0 and the total plasma pressure p_0 are given by:

$$e_0 = \frac{3}{2}p_0 = \frac{3}{2}n_0 k_B 2T_0. \tag{3.2}$$

The actual energy distribution of the plasma can be described by assuming several ion and electron populations within different energy regimes. The scale height H_{cs} for the thermal or low energy plasma populations is smaller than for the high temperature or energetic particles (above 10 keV). The average temperature therefore increases with distance from the current sheet center (*Kivelson et al.* 2004). This fact is not incorporated in the above formulation for the plasma temperature. Additionally, the velocity distributions of the ions are generally not purely Maxwellian as assumed by *Bagenal and Delamere* (2011) but show a significant tail at supra-thermal energies. Therefore, the uncertainty in the value of T_0 is about a factor of two according to *Bagenal and Delamere* (2011).

At Callisto the energetic ions contribute ~95% (0.37 nPa) to the total pressure of 0.38 to 0.39 nPa (*Kivelson et al.* 2004). Therefore, the above assumption of a total pressure which simply follows the temperature of the thermal ions leads to a considerable underestimation of the actual values for p_0. In our MHD framework used to model Callisto's plasma interaction, we do not discriminate between thermal and supra-thermal ions. Therefore, we need to assume average values for the pressure, which in turn leads to an underestimation of the plasma beta

$$\beta = \frac{2\mu_0 p_0}{B_0^2} \tag{3.3}$$

i.e., of the effective role of the thermal pressure with respect to the magnetic pressure. Typical values for this parameter at Callisto would be $\beta \approx 0.6$ to 64 (*Kivelson et al.* 2004) whereas above assumptions for the total pressure yield values on the order of 0.01. This issue can not be resolved self consistently within our formulation for Callisto's plasma interaction. We therefore primarily use artificially increased values (by a factor of 100) for e_0 and perform several comparative simulations using $k_B T_i = 635$ eV. The effect of the artificially increased total pressure is discussed along with our results for this chapter. However, one should keep in mind that energetic particles which need to be treated by the means of kinetic theory instead of MHD can contribute significantly to the energy balance at Callisto.

The azimuthal velocity of the plasma at Callisto can to first order be assumed to be close to the corotational speed of 192 km s^{-1} (see Table 1.2). However, relatively large deviations from this average value are possible. Furthermore, *Bagenal and Delamere* (2011) give values for a possible radially outward velocity component of up to 50 km s^{-1}. However, most of our simulation setups assume a perfectly corotating ambient plasma.

In addition to this model description for the plasma parameters, we were provided with the actual measurements (Fran Bagenal, personal communication) which were used in the work of *Bagenal and Delamere* (2011). The respective values for the density, velocity and total pressure for the times closest to the Callisto approach for each Galileo flyby are summarized in Table 3.2. The measurements indicate that, in addition to the variabilities of the plasma density and temperature, all velocity components are subject to significant fluctuations at Callisto. However, unrealistic values such as a reversed azimuthal velocity

v_ϕ for C23 raise doubts about the significance of the inferred data. Although no error bars were given for those values we must consider them to be rather uncertain. Therefore, we primarily use the model based values discussed above for our simulations of the Galileo flybys, even though some numerical experiments were also performed using the measured plasma parameters.

Flyby	t(C/A) [UTC]	t(M) [UTC]	n_0 [cm^{-3}]	T_i [eV]	v_r [km s^{-1}]	v_ϕ [km s^{-1}]	v_θ [km s^{-1}]
C3	13:34:28	14:22:24	0.12	111	-86.6	256	43.4
C9	13:47:50	15:00:22	0.10	516	-61.6	164	72.8
C10	00:18:55	23:36:42	0.04	964	11.3	332	-6.55
C21	07:46:50	06:49:55	0.18	2,670	-88.6	72.5	-6.73
C22	08:30:52	07:21:46	0.03	1,030	35.5	340	31.0
C23	17:27:02	17:19:51	0.05	762	-239	-152	-121
C30	11:23:58	09:37:00	0.05	610	243	122	28.7

Table 3.2: *Density n_0, ion temperature T_i and velocity components v_r, v_ϕ and v_θ (System III coordinates) of the background plasma for all Callisto flybys of Galileo, provided by Fran Bagenal. t(C/A) denotes the actual time of the closest approach and t(M) the specified time for the temporally interpolated plasma measurements. The corresponding dates for t(C/A) and t(M) are given in Table 3.1. For C10 t(M) refers to the previous day.*

3.1.3 Additional measurements

Several additional measurements relevant for Callisto which we do not consider in the further discussion of this chapter shall now be briefly summarized.

Grün et al. (1998) report Galileo measurements of electromagnetically coupled dust during the C3 flyby at Callisto. Near the closest approach they found a slight increase in the dust count rate, indicating a population of dust particles generated at Callisto. However, no values for the density and velocities of those particles could be obtained. Further, our MHD model is not capable of considering these charged dust particles. Therefore, we do not take into account these observations.

The existence of equatorial electron beams associated with Callisto was reported by *Mauk and Saur* (2007) for the C3 and C9 encounters of Galileo. These beams observed in wake region are potentially generated by Callisto's plasma interaction. They should be associated with a brightening within Jupiter's auroral regions which are connected to the generation region of the beams along magnetic field lines. In analogy to Io, Europa and Ganymede, Callisto's plasma interaction generates an auroral footprint. However, the auroral regions mapping to the position of Callisto coincide with Jupiter's main auroral oval most of the time. Still, *Clarke et al.* (2011) reported the observation of this footprint within Jupiter's aurora for a rare case when it was not completely hidden within the main oval. Although we do not present results for the energy transfer from the plasma interaction region into Jupiter's aurora predictions for the intensity of Callisto's auroral spot are generally possible using the model presented in the following sections.

3.2 Model description

Within the limits discussed in Chapter 1.2.2 Callisto's plasma interaction can be treated using the theoretical framework of magnetohydrodynamics. MHD theory describes the temporal and spatial evolution of the macroscopic plasma properties such as the density, bulk velocity, magnetic field and internal energy or temperature. The behavior of individual particles is neglected within this fluid approach. On the one hand, this presents an approximation to the actual evolution of the plasma flow. On the other hand, the MHD approach allows a realistic and at the same time convenient numerical treatment of the plasma interaction problem. The key point for the numerical formulation of a satellite-magnetosphere interaction is the implementation of the obstacle i.e., of physical effects caused by the satellite's neutral atmosphere as well as the surface and interior. We now introduce the basic MHD equations and present our theoretical and numerical implementation of Callisto.

3.2.1 Theory

The behavior of a plasma can be precisely described by the evolution of its particle distribution function $f_s(\mathbf{r}, \mathbf{u}_s, t)$ in phase space (e.g., *Baumjohann and Treumann* 1996, *Schunk and Nagy* 2000, *Bellan* 2006). f_s represents the number of particles for a plasma species s (electrons or ions) that populate a volume d^3r about $\mathbf{r}$ and additionally possess a velocity $\mathbf{u}_s$ within a velocity-space volume of d^3u_s at a given time t. An example for f_s is the drifting Maxwellian distribution function which is valid for collision-dominated plasmas. In kinetic theory the evolution of f_s is characterized by the Boltzmann equation:

$$\frac{\partial f_s}{\partial t} + \mathbf{u}_s \cdot \nabla_r f_s + \mathbf{a}_s \cdot \nabla_u f_s = \frac{\delta f_s}{\delta t}. \tag{3.4}$$

Here $\delta f_s / \delta t$ represents the effect of collisions as well as ionization and recombination processes. Further,

$$\mathbf{a}_s = \mathbf{G} + \frac{q_s}{m_s} (\mathbf{E} + \mathbf{u}_s \times \mathbf{B}) \tag{3.5}$$

is the acceleration of the particles. $\mathbf{a}_s$ comprises all forces acting on the particles with a charge of q_s and a mass of m_s, such as the gravitational force $m_s\mathbf{G}$ and the Lorentz force introduced by the second term on the right hand side of Expression (3.5). Note that we neglect the gravitational force in the following discussions and within our model as it is generally weak compared to the Lorenz force term.

Equation (3.4) can be simplified if we neglect the collision term i.e., by setting $\delta f_s / \delta t = 0$. The corresponding equation is then called Vlasov equation. The macroscopic quantities describing the plasma flow can be obtained from Equation (3.4) or the Vlasov equation by multiplying with different powers i of the velocity $\mathbf{u}_s^i$ and performing a three dimensional integration over velocity space. This procedure is called "taking the i-th moment" of the distribution function. The zero order moment yields an expression for the temporal and spatial evolution of the mass density ρ_s or number density n_s. The first and second order moments describe the average velocity $\mathbf{v}_s$ and the internal energy density e_s, temperature

T_s or pressure p_s for the species s. The last three quantities can be used equivalently by noting that $p_s = 2/3e_s = n_s k_B T_s$.

In each equation arising from the outlined procedure an additional higher order quantity appears whose evolution needs to be determined by taking the next higher order moment of Equation (3.4). Therefore, it is necessary to close the system of equations by introducing assumptions for one of these quantities. For example, when we assume adiabatic conditions, we can use the relation $p_s \sim \rho_s^\gamma$ with the adiabatic index γ to close the system of equations without explicitly solving an equation for the evolution of the internal energy. Additionally, the Lorenz force term in Equation (3.5) introduces electric fields $\mathbf{E}$ and magnetic fields $\mathbf{B}$ into the system of equations. Their evolution must be described by solving Maxwell's equations (see Appendix A.1) along with the derived fluid equations. The displacement currents in Maxwell's equations can be neglected as the velocities of the particles and waves involved the plasma interaction process are generally much smaller than the speed of light.

We now assume the presence of different neutral particle species denoted by the index ns which affect the plasma by ion- and electron-neutral collisions represented by the collision frequencies $\nu_{s,ns}$ as well as mass loading due to ionization processes represented by the production rate $P_{s,ns}$. Further, we account for the loss of plasma particles due to recombination processes with a loss rate L_s. Collisions between the plasma particles of different species (s and s') are given by the collision frequencies $\nu_{s,s'}$. We neglect the heat flux Q arising in the energy equation to close the system of equations. The final set of macroscopic equations for a plasma particle species s derived from Equation (3.4) then reads (e.g., *Neubauer* 1998b, *Schunk and Nagy* 2000):

$$\frac{\partial \rho_s}{\partial t} + \nabla \cdot (\rho_s \mathbf{v}_s) = m_s \overbrace{\left(\sum_{ns} P_{s,ns} - L_s \right)}^{\frac{\delta n_s}{\delta t}}, \tag{3.6}$$

$$\begin{aligned} \frac{\partial \mathbf{v}_s}{\partial t} + \mathbf{v}_s \cdot \nabla \mathbf{v}_s = {} & \frac{q_s}{m_s} (\mathbf{E} + \mathbf{v}_s \times \mathbf{B}) - \frac{1}{\rho_s} \nabla p_s \\ & \underbrace{- \sum_{ns} \left(\nu_{s,ns} + \frac{P_{s,ns}}{n_s} \right) (\mathbf{v}_s - \mathbf{v}_{ns}) - \sum_{s'} \nu_{s,s'} (\mathbf{v}_s - \mathbf{v}_{s'})}_{\frac{\delta \mathbf{v}_s}{\delta t}}, \end{aligned} \tag{3.7}$$

$$\begin{aligned} \frac{\partial e_s}{\partial t} + \nabla \cdot (e_s \mathbf{v}_s) = {} & -p_s \nabla \cdot \mathrm{v}_s - \frac{1}{2} m_s v_s^2 \frac{\delta n_s}{\delta t} - \mathbf{v}_s \rho_s \frac{\delta \mathbf{v}_s}{\delta t} \\ & + \sum_{ns} \nu_{s,ns} \frac{\rho_s}{m_s + m_{ns}} \left(3k_B (T_{ns} - T_s) + m_{ns} (\mathbf{v}_s - \mathbf{v}_{ns})^2 \right) \\ & + \sum_{ns} \left(\frac{1}{2} m_{ns} \mathbf{v}_{ns}^2 + \frac{3}{2} k_B T_{ns} \right) P_{s,ns} - \left(\frac{1}{2} m_s \mathbf{v}_s^2 + \frac{3}{2} k_B T_s \right) L_s. \end{aligned} \tag{3.8}$$

Equations (3.6), (3.7) and (3.8) are the continuity, momentum and energy equation for the multi-fluid approach. In the energy equation (3.8) the mass m_{ns}, temperature T_{ns} and velocity $\mathbf{v}_{ns}$ of the neutral species appear in terms that describe the heating and cooling due to heat conduction and inelastic collisions with the neutral particles. Further, the terms braced in the continuity and momentum equation also affect the evolution of the internal energy. They describe the energy loading and loss due to converted neutral and plasma particles as well as the change of momentum due to collisions.

Let us now consider a plasma that consists of a singly charged ion (index i) and an electron species (index e). Above equations can be further simplified if we assume that on large spatial scales (larger than the Debye length) the plasma acts as a single, quasi-neutral fluid. In other words, the number density of the ions and electrons are assumed to be approximately equal everywhere ($n = n_i = n_e$). In this case the evolution of the plasma can be formulated using the bulk variables:

$$
\begin{aligned}
m &= m_i + m_e \approx m_i, && (3.9)\\
n &= \frac{m_i n_i + m_e n_e}{m_i + m_e}, && (3.10)\\
\rho &= \rho_i + \rho_e, && (3.11)\\
\mathbf{v} &= \frac{m_i n_i \mathbf{v}_i + m_e n_e \mathbf{v}_e}{m_i n_i + m_e n_e}, && (3.12)
\end{aligned}
$$

and

$$
e = \frac{3}{2} p = \frac{3}{2}(p_i + p_e). \qquad (3.13)
$$

If collisions, production and loss terms are neglected, as in the Vlasov equation, Equations (3.6) to (3.8) for the electrons and ions and Maxwell's equations can be combined to:

$$
\begin{aligned}
\frac{\partial \rho}{\partial t} + \nabla \cdot (\rho \mathbf{v}) &= 0, && (3.14)\\
\rho \left(\frac{\partial \mathbf{v}}{\partial t} + \mathbf{v} \cdot \nabla \mathbf{v} \right) &= -\nabla p + \frac{1}{\mu_0} (\nabla \times \mathbf{B}) \times \mathbf{B}, && (3.15)\\
\frac{\partial e}{\partial t} + \nabla \cdot (e \mathbf{v}) &= -p \nabla \cdot \mathbf{v}, && (3.16)\\
\frac{\partial \mathbf{B}}{\partial t} &= \nabla \times (\mathbf{v} \times \mathbf{B}) \,. && (3.17)
\end{aligned}
$$

These are the ideal single fluid MHD equations which are the base for our description of Callisto's plasma interaction. The total pressure p is assumed to be isotropic in the above expressions. In the induction equation we do not account for the Hall term which decouples the ion and electron motions on ion inertial scales. In this case the plasma is essentially frozen into the flux of the electrons instead of the total plasma motion. For a numerical approach a self consistent Hall-MHD formulation would require vast computational resources. This is the main reason why we can not take this term into account for our simulations. Note that in analogy to Io (*Saur et al.* 1999) and other than for Europa (*Schilling* 2006), neglecting the Hall term is generally not justified due to the large Hall conductivities encountered at Callisto (see e.g., Table 21.1 in *Kivelson et al.* 2004). The Hall term may therefore slightly change the nature of Callisto's interaction with respect to the results presented in this thesis. We discuss the associated potential implications along with our results in Sections 3.3.2.4 and 3.3.3.

In order to account for Callisto's neutral atmosphere the additional terms which appear in the multi-fluid Equations (3.6) to (3.8) given above also need to be included in the single fluid formulation. The full set of equations is given in the next section along with the discussion of our aeronomic formulation for the production, loss and collision terms.

3.2.2 Model equations

The base of our numerical implementation is the so called ZEUS code developed by *Stone and Norman* (1992a,b) and *Stone et al.* (1992). The current massive parallel version of this MHD code (ZEUS-MP version 2.1.2, see *Hayes et al.* 2006) solves Equations (3.14) to (3.17) on a three dimensional grid. To account for the influence of Callisto's neutral atmosphere we use an extended version of these equations which can be derived from the multi-fluid equations (3.6) to (3.8):

$$\frac{\partial \rho}{\partial t} + \nabla \cdot (\rho \mathbf{v}) = \sum_{ns} m_{ns} \left(P_{ns} - L_{ns} \right), \tag{3.18}$$

$$\rho \left(\frac{\partial \mathbf{v}}{\partial t} + \mathbf{v} \cdot \nabla \mathbf{v} \right) = -\nabla p + \frac{1}{\mu_0} (\nabla \times \mathbf{B}) \times \mathbf{B} - \sum_{ns} m_{ns} P_{ns} \mathbf{v} - \left(\frac{m_e}{m_i} \nu_{e,ns} + \nu_{i,ns} \right) \rho \mathbf{v}, \tag{3.19}$$

$$\begin{aligned} \frac{\partial e}{\partial t} + \nabla \cdot (e \mathbf{v}) = & -p \nabla \cdot \mathbf{v} + \frac{3}{2} n k_B \sum_{ns} \nu_{i,ns} \left(T_{ns} - T \right) + \frac{3}{2} k_B \sum_{ns} P_{ns} T_{ns} \\ & - \frac{3}{2} k_B T \sum_{ns} L_{ns} + \frac{1}{2} \rho v^2 \sum_{ns} \left(\frac{P_{ns}}{n} + \nu_{i,ns} + \frac{m_e}{m_i} \nu_{e,ns} \right), \end{aligned} \tag{3.20}$$

$$\frac{\partial \mathbf{B}}{\partial t} = \nabla \times \left(\mathbf{v} \times \mathbf{B} - \frac{m_e}{n q_e^2} \mathbf{j} \sum_{ns} \left(\nu_{e,ns} + \frac{m_e}{m_i} \nu_{i,ns} \right) - \frac{m_e}{n^2 q_e^2} \mathbf{j} \sum_{ns} L_{ns} \right). \tag{3.21}$$

As a further constrain, Gauss's law for magnetism ($\nabla \cdot \mathbf{B} = 0$) must be valid everywhere.

In the induction equation (3.21) additional diffusion terms appear due to the collision and loss terms in the continuity and momentum equations needed to derive the formulation above. These terms dominate where the neutral gas densities are large. In the respective regions of Callisto's atmosphere the magnetic field is no longer completely frozen into the decelerated plasma and is mainly transported by diffusion instead. As stated in Section 3.2.1 the Hall term is neglected in the induction equation.

While the ion-electron collision terms cancel in the derivation of the momentum equation (3.19), they appear as Joule heating terms in the energy equation (3.20). However, the respective terms are small compared to the influence of the neutral collisions for the relatively dens atmosphere of Callisto. Therefore, they are negligible for our purposes. The same holds for two additional terms in the energy equation which include the current density **j** (see e.g., the model description of *Backes* 2004). The remaining terms on the right hand side of Equation (3.20) are the adiabatic change of pressure, the temperature coupling with the neutral gas, the change of energy due to particle production and loss processes as well as the Joule heating due to collisions with neutrals. Note that we do not account for heat conduction terms which are especially relevant for the internal energy budget of the electrons. We compensate this deficiency in our formulation of the impact ionization process given in Section 3.2.2.3. Further, both for the energy (3.20) and momentum equation (3.19) the neutral gas velocity is assumed to be small with respect to the plasma velocity. Apart from the collision and production terms which act in a similar way in the momentum equation (*Neubauer* 1998b), an additional frictional term proportional to **j** was neglected here. The remaining production, loss and the collision terms in the above equations still adequately describe the impact of Callisto's neutral atmosphere on the plasma flow. The plasma is considered to primarily consist of O^+ particles which matches the average ion mass at Callisto (see Table 1.2 or *Kivelson et al.* 2004).

For the density of the atmospheric species we assume an exponentially decreasing profile depending on the radial distance to the surface $r - R_C$ defined by:

$$n_{ns} = \frac{n_{ns,0}}{H_{\mathrm{rel}}} e^{-(r-R_C)/(H_{ns}H_{\mathrm{rel}})}, \tag{3.22}$$

where $n_{ns,0}$ is the surface density, $R_C = 2410$ km the radius of Callisto and H_{ns} the scale height of the CO_2 or O_2 atmosphere. The respective values used for the following analysis are $n_{CO_2,0} = 4 \times 10^8$ cm^{-3}, $n_{O_2,0} = 7 \times 10^9$ cm^{-3} and $H_{CO_2} = H_{O_2} = 23$ km (see Section 3.1.1). H_{rel} is a scaling factor introduced due to the limited maximum resolution available for our model setup (see Section 3.2.4). Values of $H_{\mathrm{rel}} > 1$ in Equation (3.22) give less steeper profiles but retain the total particle content of the atmosphere. For all simulations discussed within this thesis we use a value of $H_{\mathrm{rel}} = 10$ for both atmospheric species. The resulting neutral density setup for CO_2 is exemplarily shown in the left panel of Figure 3.2. Due to the finite grid resolution the maximum values for the density are slightly smaller than the analytical value for CO_2 which is 4×10^7 cm^{-3} for $H_{\mathrm{rel}} = 10$.

For the comparison of the ionospheric densities generated within our model with the *Kliore et al.* (2002) results (Section 3.3.2) we performed additional simulations where we

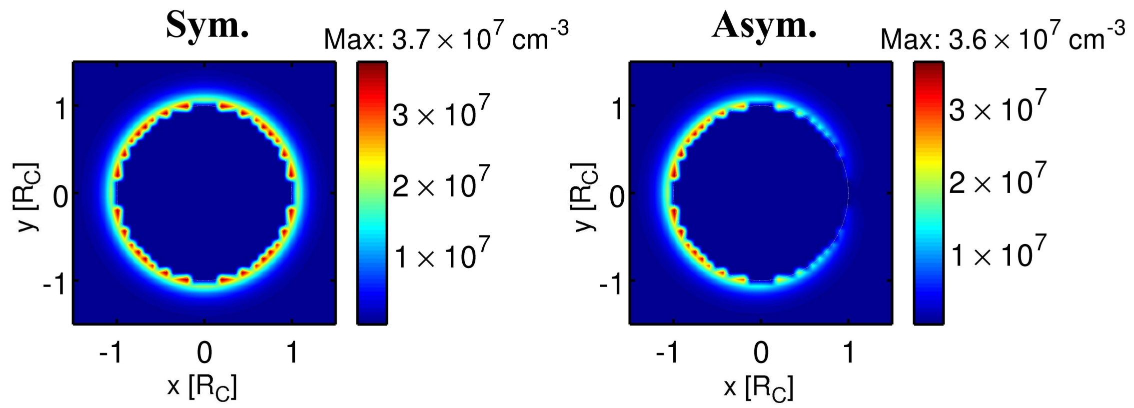

Figure 3.2: *CO_2 neutral densities in cm^{-3} for a symmetric (left) and an asymmetric (right) neutral density setup in our MHD model for a scaling factor of $H_{rel} = 10$. Both atmospheres are rotationally symmetric with respect to the x-axis.*

assume an asymmetric atmosphere with decreasing neutral densities towards the downstream hemisphere of Callisto. Equation (3.22) is multiplied by a factor $\cos(\psi/2)$ in this case, where ψ is the angle between the position vector and the unity vector in the negative x-direction. The resulting density distribution (right panel in Figure 3.2) represents just a simple test case for an atmosphere which is primarily generated by sputtering of surface particles. It must be noted that the above cosine function implies that the atmospheric densities reach zero in the tail region of Callisto. Albeit this condition is certainly not realistic it has no significant implications on the results presented in the following sections. Realistic models for the generation of Callisto's atmosphere are not available in the literature so far. We therefore refrain from applying more sophisticated models for an asymmetric atmosphere as given, for example, by *Pospieszalska and Johnson* (1989) and *Saur et al.* (1998) for Europa.

To account for the micro-physical processes relevant for the plasma interaction, we need a suitable aeronomic formulation for P_{ns}, L_{ns}, $\nu_{i,ns}$ and $\nu_{e,ns}$. There are two major sources for ionized particles from Callisto's neutral atmosphere. First, the solar irradiation leads to a dissociation of neutral particles. Secondly, the impinging plasma electrons interact with the neutral particles and eventually ionize them. The production rate in the continuity equation (3.18), the momentum equation (3.19) and the energy equation (3.20) therefore reads:

$$P = \sum_{ns} P_{ns} = \sum_{\mathrm{CO_2,O_2}} \left(P_{\mathrm{imp},ns} + P_{\mathrm{pho},ns}\right), \tag{3.23}$$

where $P_{\mathrm{pho},ns}$ is the photo ionization rate and $P_{\mathrm{imp},ns}$ is the impact ionization rate for the CO_2 and O_2 particles.

3.2.2.1 Photo ionization

The solar extreme ultraviolet radiation (EUV) is a significant energy source for the ionization of neutral atmospheric particles at Callisto. Photons in these wavelength regions can effectively eject electrons from neutral atoms or molecules. We determine the intensity of the solar photon flux $I(\lambda_i, t)$ at the time t by applying the so called EUVAC Solar Flux Model which covers 37 wavelength intervals λ_i, in a range of 5 to 105 nm (*Richards et al.* 1994, *Schunk and Nagy* 2000). The respective flux needs to be extrapolated to the position of Jupiter which gives:

$$I(\lambda_i, t) = \frac{1AU^2}{d_{JS}^2(t)} F(\lambda_i) \left[1 + A(\lambda_i)\left\{P(t) - 80\right\}\right], \tag{3.24}$$

where $d_{JS}(t)$ is the distance between Jupiter and the Sun in AU, $F(\lambda_i)$ is the modified reference flux for a specific wavelength and $A(\lambda_i)$ is a scaling factor. The values of A and F for the EUVAC model are given by *Schunk and Nagy* (2000) for each interval λ_i. Further,

$$P(t) = \frac{1}{2}\left(F10.7 + F10.7A\right) \tag{3.25}$$

is the mean value of the adjusted solar flux $F10.7$[I] and the adjusted solar flux averaged over ±40 days (81 days in total) denoted by $F10.7A$, both given in W m^{-2} s. Galileo

---

[I] F10.7 denotes the index for the solar radio flux at a wavelength of 10.7 cm.

spacecraft ephemeris data provide the distance between Jupiter and the Sun for the flyby scenarios discussed in this thesis. The time variable value P is determined from freely available data recorded by the radio telescope at the Dominion Astrophysical Observatory in Penticton, Canada[II]. The respective values for the time of each flyby and default values used for test cases are listed in Table 3.3. Note that variations due to the solar cycle e.g., between the C9 and C22 cases, are fully included within this model formulation.

The photo ionization rate can be determined from $I(\lambda_i, t)$ using the expression:

$$P_{\text{pho},ns} = n_{ns} \sum_{i=1}^{37} \sigma_{\text{ion},ns}(\lambda_i) I(\lambda_i, t) e^{-\tau(ns,\lambda_i,t,\mathbf{r})}, \tag{3.26}$$

where the ionization cross sections $\sigma_{\text{ion},ns}$ for each wavelength interval and both neutral species are given by *Schunk and Nagy* (2000). The optical thickness τ is defined by:

$$\tau = \int_r^\infty \sum_{ns} n_{ns}(l) \sigma_{\text{abs},ns}(\lambda_i) \mathrm{d}l, \tag{3.27}$$

with the particles' absorption cross sections $\sigma_{\text{abs},ns}$ (again given by *Schunk and Nagy* 2000) and an integration from arbitrary locations along the line of sight l towards the Sun. We determine τ by applying the trapezoidal rule to numerically integrate from each point in the atmosphere along a line towards the Sun defined by the solar phase angles $\alpha_\odot$ given in Table 3.1.

The corresponding maximum value of τ for all wavelengths at the subsolar point near Callisto's surface is ~0.6 (for $i = 21$, see Figure 3.3). At this point Callisto's atmosphere is still optically thin ($\tau < 1$). If we assume our default conditions for the solar radiation, the production rates at the subsolar point are $P_{\text{pho,CO}_2} = 18$ cm^{-3} s^{-1} and $P_{\text{pho,O}_2} = 213$ cm^{-3} s^{-1} (Figure 3.4). Note that in our simulations the actual production rates are lower by a factor of about $1/H_{\text{rel}} = 1/10$. However, τ exceeds one at Callisto's flanks with respect to the location of the Sun, as displayed in Figures 3.5 and 3.6. The maximum for the production rates at the flanks ($x \approx 0$ in Figure 3.5) is shifted by ~0.2 R$_C$ towards the Sun. Along the y-direction the maximum is also slightly shifted away from the surface (~0.01 R$_C$). These shifts coincide approximately with the point where the atmosphere becomes optically thick. Before we continue our introduction of the aeronomic processes with the electron impact ionization, we now shortly discuss the differences between the ambient plasma particles and the newly ionized ionospheric plasma.

	C3	C9	C10	C21	C22	C23	C30	Default
d_{JS}	5.15	5.07	5.05	4.95	4.95	4.96	5.10	5.00
F10.7	67.8	74.1	94.0	216.5	131.5	159.9	166.1	150.0
F10.7A	72.6	74.7	88.4	171.5	162.6	154.5	165.6	150.0

Table 3.3: *Solar flux index F10.7 and the associated 81 day averaged values F10.7A in W m^{-2} s as well as the distance between Jupiter and the sun d_{JS} for the times of each Galileo flyby at Callisto. The last column gives default values used to calculate the EUVAC-model solar photon flux for several test cases.*

[II] `http://www.ngdc.noaa.gov/stp/solar/flux.html`

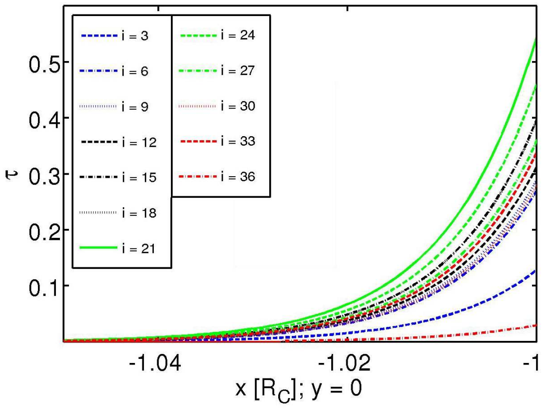

Figure 3.3: *Optical thickness τ for different wavelength intervals λ_i of the EUVAC model along the CphiO x-axis at $y = 0$ and $z = 0$. A symmetric combined CO_2 and O_2 neutral atmosphere is assumed here. τ reaches its maximum values for $i = 21$ (solid green line). The Sun is located toward $x = -\infty$.*

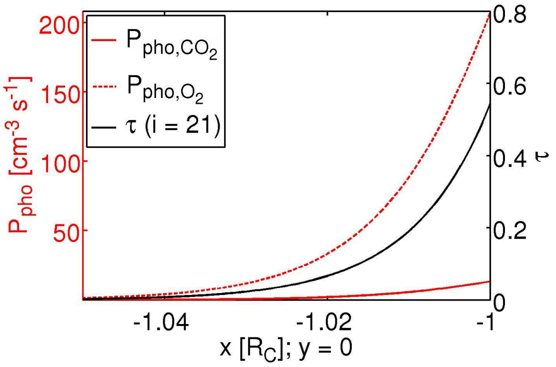

Figure 3.4: *Optical thickness τ for $i = 21$ as well as CO_2 and O_2 photo ionization rates (P_{pho,CO_2} and P_{pho,O_2}) along the CphiO x-axis at $y = 0$, $z = 0$. The Sun is located at $x = -\infty$.*

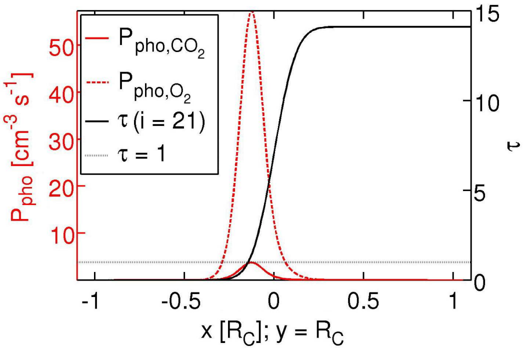

Figure 3.5: *Same as Figure 3.4 along the x-axis at $y = R_C$, z =0.*

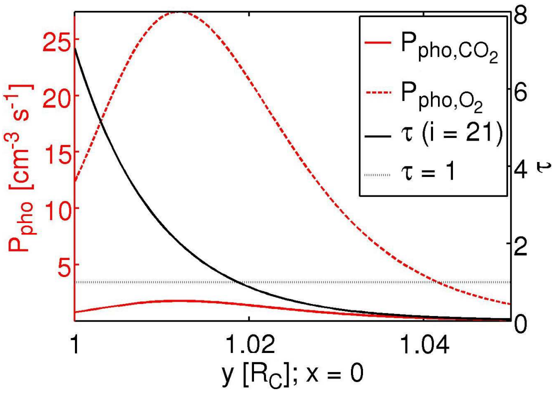

Figure 3.6: *Same as Figure 3.4 along the y-axis at $x = 0$, $z = 0$.*

3.2.2.2 Ionospheric particles

The ions and electrons generated in the photo ionization process generally represent additional ionospheric plasma populations. The temperature of these populations, which initially lies close to the neutral gas temperature of 150 K, is significantly lower than the temperature of the magnetospheric plasma. The change of the total internal plasma energy due to the ionization is already reflected by the production term in the energy equation (3.20). A further discrimination between the ionospheric and magnetospheric ion populations is unnecessary as the non-resonant collision frequencies for these particles do not depend on their temperature. However, both the electron collision frequencies and the electron impact ionization rates depend on the electron temperature T_e. Assuming an electron temperature close to the average plasma temperature for both electron species therefore leads to a potential under- and overestimation of these processes.

We solve this issue by discriminating between the newly generated ionospheric electrons (index is) with a relatively low temperature of $T_{e,is} = 300$ K and the magnetospheric electrons (index ms) with $T_{e,ms} = T_i$. The estimated value for $T_{e,is}$ was adapted from the discussion of the impact ionization processes given by *Kliore et al.* (2002). The abundances A for both species is calculated using:

$$\frac{\partial A_{is}}{\partial t} = \frac{P + L_{ms} - L_{is}}{n} \tag{3.28}$$

and

$$A_{ms} = 1 - A_{is}, \tag{3.29}$$

where we further distinguish between the loss processes L (see Section 3.2.2.4) for both species and account for all ionization processes in P. The spatial and temporal evolution for the magnetospheric electron species is taken into account by solving an additional continuity equation:

$$\frac{\partial(nA_{ms})}{\partial t} + \nabla \cdot (nA_{ms}\mathbf{v}) = 0. \tag{3.30}$$

The evolution of the ionospheric electrons, however, is still given by Equation (3.18).

3.2.2.3 Electron impact ionization

The magnetospheric electrons and ions impinging Callisto's atmosphere are a second major source for the generation of ionospheric particles. The respective rate coefficients for the ion impact ionization are, however, significantly lower than the rates for the electron impact ionization. At Io and Europa electron impact ionization is even the most important mass loading process (*Saur et al.* 1998, 1999). The production rate for the electron impact ionization of the neutral species ns can be calculated from:

$$P_{\text{imp},ns} = f_{\text{imp},ns}(T_e) n_e n_{ns}, \tag{3.31}$$

where the ionization rate $f_{\text{imp},ns}$ for a specific electron temperature of T_e can be written as:

$$f_{\text{imp},ns}(T_e) = \int_{E_{\text{ion}}}^{\infty} F_e(E)\sigma_{\text{imp},ns}(E)v_e(E)\mathrm{d}E. \tag{3.32}$$

Here

$$v_e(E) = \sqrt{\frac{2E}{m_e}} \tag{3.33}$$

denotes the electron velocity given at an energy E. The normalized distribution function for the electrons in energy space

$$F_e(E) = \frac{2\sqrt{E}}{\pi}(k_B T_e)^{-\frac{3}{2}} e^{-\frac{E}{k_B T_e}} \tag{3.34}$$

is assumed to be Maxwellian for our purposes. $\sigma_{\text{imp},ns}$ are the electron impact ionization cross sections at different energies. In this work we apply the so called BEB cross section model put forward by *Hwang and Kim* (1996) to perform a numerical integration of Equation (3.32). The impact ionization rates for both neutral species used in our model are shown in Figure 3.7. For the magnetospheric electrons with a temperature of $k_B T_{e,ms,0} = 635$ eV and an average density of $n_{e,ms,0} \approx 0.1$ cm^{-3} the respective production rates at Callisto's surface are $P_{\mathrm{imp},ms,\mathrm{CO_2}} = 6$ cm^{-3} s^{-1} and $P_{\mathrm{imp},ms,\mathrm{O_2}} = 73$ cm^{-3} s^{-1}. Due to the decreased surface neutral densities in our model these values are diminished by the factor $1/H_{\mathrm{rel}} = 1/10$ for our simulations. For the ionospheric electrons with $T_{e,is} = 300$ K the rate drops almost to zero (several decades of magnitudes lower) even though their densities are significantly higher. If we compare these production rates with the rates given in Section 3.2.2.1 it turns out that the photo ionization process at Callisto dominates by a factor of about three. However, the impact ionization process generates additional ionized particles in the geometrical shadow region of Callisto. Therefore, electron impact ionization still provides an important contribution to the overall ionospheric distribution.

Above calculations crucially depend on the temperature of the electrons T_e. Due to the nearly infinite heat conduction along the field lines the magnetospheric electrons which are cooled down during the interaction can be effectively reheated by the energy reservoir of the electrons in the other parts of the plasma torus. To account for this effect we introduce an effective ionization rate $f_{\mathrm{imp,max},ns}$ by equating:

$$E_{\mathrm{loss,imp}} = f_{\mathrm{imp,max},ns} n_{e,0} E_{\mathrm{ion,eff}} n_{ns,0} 4\pi \overbrace{\int_{r=\mathrm{R}_C}^{\infty} r^2 e^{-(r-\mathrm{R}_C)/H_{ns}} \mathrm{d}r}^{H_{ns}\mathrm{R}_C^2} \tag{3.35}$$

$$\overset{!}{=}$$

$$E_{\mathrm{torus}} = \frac{3}{2} k_B T_{e,0} v_0 2 \mathrm{R}_C \alpha_{\mathrm{wing}} n_{e,0} \underbrace{\int_{-H_{cs}}^{H_{cs}} e^{-|h|/H_{cs}} \, \mathrm{d}h}_{=5.45\mathrm{R}_J}, \tag{3.36}$$

$$\Rightarrow f_{\mathrm{imp,max},ns} = \frac{T_{e,0} v_0 2 \alpha_{\mathrm{wing}} 5.45 \mathrm{R}_J}{T_{\mathrm{ion,eff}} n_{ns,0} H_{ns} 4\pi \mathrm{R}_C}. \tag{3.37}$$

$E_{\mathrm{loss,imp}}$ denotes the total energy lost due to the impact ionization throughout the entire atmosphere. The total neutral density is given by the integral in Equation (3.35). $n_{ns,0}$ is the surface density of the neutral species. An effective ionization energy $E_{\mathrm{ion,eff}} = \frac{3}{2} k_B T_{\mathrm{ion,eff}}$ is used instead of the neutral species' ionization threshold potentials ($E_{\mathrm{ion,CO_2}} = 13.77$ eV and $E_{\mathrm{ion,O_2}} = 12.06$ eV) here. We do this to account for other potential energy loss processes occurring during electron impacts. Values of $E_{\mathrm{ion,eff,CO_2}} = 35$ eV and $E_{\mathrm{ion,eff,O_2}} = 32$ eV are given by *Bauer* (1973) and *Banks and Kockarts* (1973).

In the second Equation (3.36) E_{torus} denotes the energy reservoir within the torus which is available to heat the electrons involved in the plasma interaction. The electron energy influx is given in terms of the magnetospheric electron temperature $T_{e,0} = 635$ eV which is assumed to be constant along the field lines. v_0 is the velocity of the impinging plasma particles. The integral over the torus electron density along the field lines connected to Callisto is given for a torus scale height of $H_{cs} = 3.65$ R$_J$ (see Section 3.1.2). The width

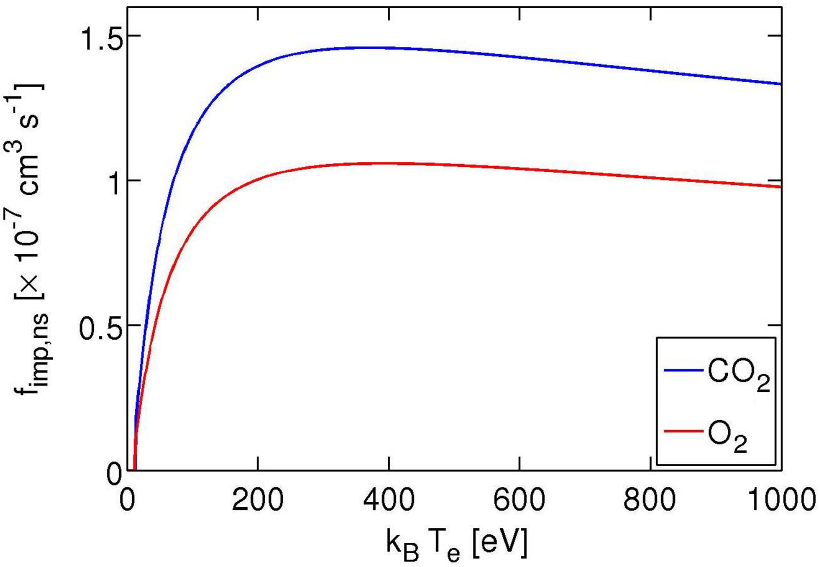

Figure 3.7: *Electron impact ionization rates $f_{imp,ns}$ in 10^{-7} cm^3 s^{-1} vs. electron temperature in eV for O$_2$ and CO$_2$.*

of the respective flux tubes (2 R$_C$) is diminished by the factor α_{wing}. As the electron flow follows the isolines of the electric potential, the fraction of the magnetospheric electrons impinging Callisto's interaction region is defined by the last isoline connected to this region (see Figure 3.8). For a strong interaction or for high Pedersen conductances the width of the flux tubes decreases. This is reflected by the factor α_{wing} which we already introduced as α in Section 2.3.1.2. Apart from the definition of given in Equation (2.31) we can "measure" the relative interaction strength by noting that $\alpha_{\mathrm{wing}} = v_{\mathrm{wing}}/v_0$, where v_{wing} denotes the diminished plasma velocity inside the Alfvén wings. For our simulations we determine v_{wing} at a distance of 3 R$_C$ from Callisto's center following both Alfvén characteristics (Section 1.2.2, Equation 1.3).

For our interaction model we use an approach which incorporates both methods presented above to determine the electron impact ionization rate. Using α_{wing} we can determine the maximum possible ionization rate $f_{\mathrm{imp,max},ns}$ assuming infinite heat conduction along the field lines. However, an upper limit for the applicable ionization frequency is defined by the ionization frequency of the background plasma $f_{\mathrm{imp},0,ns} = f_{\mathrm{imp},ns}(T_{e,ms,0})$ i.e.,

$$f_{\mathrm{imp},ns} = \begin{cases} f_{\mathrm{imp,max},ns} & \text{for } f_{\mathrm{imp,max},ns} < f_{\mathrm{imp},0,ns} \\ f_{\mathrm{imp},0,ns} & \text{for } f_{\mathrm{imp,max},ns} > f_{\mathrm{imp},0,ns} \end{cases} . \tag{3.38}$$

For the carbon dioxide atmosphere the energy within the torus allows for a maximum impact ionization rate of $f_{\mathrm{imp},max,\mathrm{CO_2}} = 4.87 \times 10^{-6}$ cm^3 s$^{-1}\alpha_{\mathrm{wing}}$, but the upper limit for the ionization assuming a homogeneous electron plasma with $k_B T_{e,ms,0} = 635$ eV and $n_{e,ms,0} = 0.1$ cm^{-3} is $f_{\mathrm{imp,0,CO_2}} = 1.4 \times 10^{-7}$ cm^3 s^{-1}. The respective values for molecular oxygen are $f_{\mathrm{imp},max,\mathrm{O_2}} = 3.08 \times 10^{-7}$ cm^3 s$^{-1}\alpha_{\mathrm{wing}}$ and $f_{\mathrm{imp,0,O_2}} = 1.04 \times 10^{-7}$ cm^3 s^{-1}. At the start of our simulations $v_{\mathrm{wing}} = v_0$ implies that $\alpha_{\mathrm{wing}} = 1$ and $f_{\mathrm{imp},0,ns}$ is used to initialize the impact ionization term. It should be already noted at this stage that typical values for α_{wing} encountered within our simulations lie between 0.01 and 0.1 (see Section 3.3). Therefore, the impact ionization rate is set to $f_{\mathrm{imp,max},ns}\alpha_{\mathrm{wing}}$ after a certain simulation time.

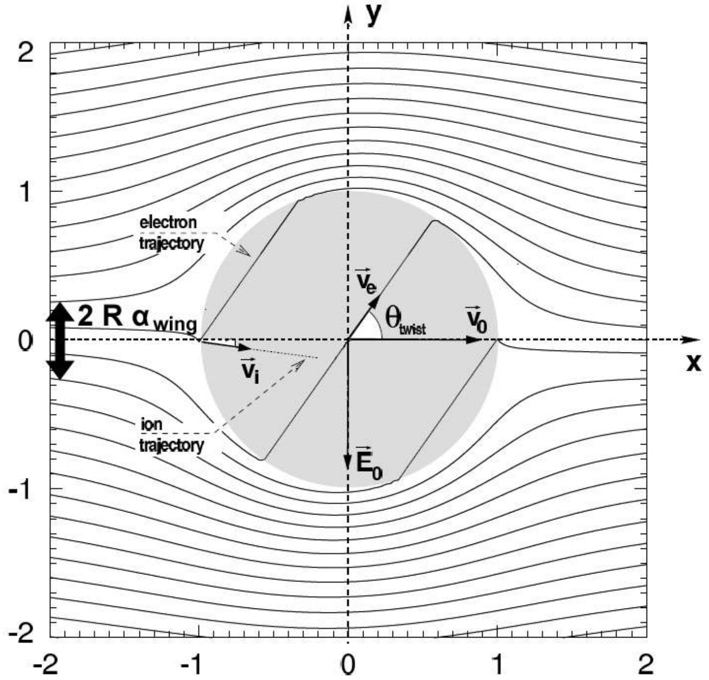

Figure 3.8: *Contours of the electric potential outside an interaction region (gray circle) with constant ionospheric conductances after Saur (2004). The ambient plasma flows in the positive x-direction and the magnetic field points in the negative z-direction. The diameter of the flux tubes reaching the interaction region is diminished up to a value of* $2R\alpha_{wing}$*, with the radius of the satellite R. For the significance of the additionally denoted parameters the reader is referred to the original publication.*

3.2.2.4 Dissociative recombination

The main sinks for plasma particles in Callisto's atmosphere are dissociative recombination processes. *Schunk and Nagy* (2000) give the following expressions for the dissociative recombination of carbon dioxide and molecular oxygen:

$$L_{\mathrm{CO}_2} = n_e^2\, 4.2 \times 10^{-7} \left(\frac{300\,\mathrm{K}}{T_e}\right)^{0.75} \mathrm{cm^3 s^{-1}} \tag{3.39}$$

and

$$L_{\mathrm{O}_2} = n_e^2\, 2.4 \times 10^{-7} \left(\frac{300\,\mathrm{K}}{T_e}\right)^{0.7} \mathrm{cm^3 s^{-1}}. \tag{3.40}$$

Due to the high temperature and low density of the background plasma, loss processes involving the magnetospheric electrons are basically negligible. To give a complete formulation we still compute the recombination rate for both species i.e., both for $n_e = n_{e,ms}A_{ms}$ and $n_e = n_{e,is}A_{is}$. The assumed temperatures for both electron species are $T_{e,is} = 300$ K and $T_{e,ms} = T_i$. The loss terms in Equation (3.18) eventually level the total production rate when a certain ionospheric electron density is reached. This chemical equilibrium is a necessary condition for the quasi-stationary state we require for the interpretation of our simulations results.

3.2.2.5 Collisions

Our plasma interaction model takes into account both electron and O^+-ion collisions with the molecular oxygen and carbon dioxide neutral particles. For the respective non-resonant ion collisions *Schunk and Nagy* (2000) give expressions for the collision frequencies by:

$$\nu_{O^+,CO_2} = 8.95 \times 10^{-10}\mathrm{cm}^3\mathrm{s}^{-1} n_{CO_2} \tag{3.41}$$

and

$$\nu_{O^+,O_2} = 6.64 \times 10^{-10}\mathrm{cm}^3\mathrm{s}^{-1} n_{O_2}. \tag{3.42}$$

The maximum ion collision frequencies at Callisto's surface are $\nu_{i,CO_2} = 0.36$ Hz and $\nu_{i,O_2} = 4.65$ Hz. Note that in our simulations these maximum values are diminished by the factor $1/H_{\mathrm{rel}} = 1/10$. *Schunk and Nagy* (2000) give similar expressions for the electron collision frequencies $\nu_{e,ns}$ depending on the temperature of the electrons T_e. However, for temperatures above 10 eV these functions yield unrealistically high values. Therefore, we use a more general formulation given by the same authors i.e.,

$$\nu_{e,ns} = \frac{8}{3\sqrt{\pi}} n_{ns} \frac{m_{ns}}{m_e + m_{ns}} \sqrt{2k_B \left(\frac{T_{ns}}{m_{ns}} + \frac{T_e}{m_e}\right)} \sigma_{\mathrm{mom},ns}(T_e). \tag{3.43}$$

The temperature for both neutral species can be assumed to be the surface temperature at Callisto i.e., $T_{ns} = 150$ K. $\sigma_{\mathrm{mom},ns}$ denotes the momentum transfer cross sections of the neutrals. *Itikawa* (2002) and *Jeon* (2003) give values for these cross sections for energies up to 100 eV (Tables 2 and 5 in the respective references). The corresponding plots for both neutral species shown in Figure 3.9 indicate that, in contrast to expressions given by *Schunk and Nagy* (2000), the momentum transfer cross sections and the associated collision frequencies approach zero for temperatures above 10 eV. We therefore use a double logarithmic interpolation between the values given by *Itikawa* (2002) and *Jeon* (2003) and extrapolate for values above 100 eV to obtain the momentum transfer cross sections for arbitrary electron temperatures.

For the background electron temperature of 635 eV used in the interaction model (assuming $T_0 = T_e = T_i$, see Section 3.1.2) the collision frequencies at the surface are: $\nu_{e,ms,CO_2} = 32$ Hz and $\nu_{e,ms,O_2} = 321$ Hz. Again, these values are lower by the factor $1/H_{\mathrm{rel}} = 1/10$ for our model setup. For the ionospheric electrons the respective values are about six orders of magnitude smaller due to their low temperatures. The contribution of the electron collisions to the momentum loss is negligible in Equation (3.19) due to the small electron mass. However, the diffusion of the magnetic field included in Equation (3.21) is dominated by the electron collisions. Note that the actual electron temperature at the surface lies well beneath the default value given here. In the course of our simulations the terms in the energy equation (3.20) lower the temperature in this region. However, electron heating by heat conduction along the magnetic field lines (see Section 3.2.2.3) is not considered in our formulation for the electron collisions.

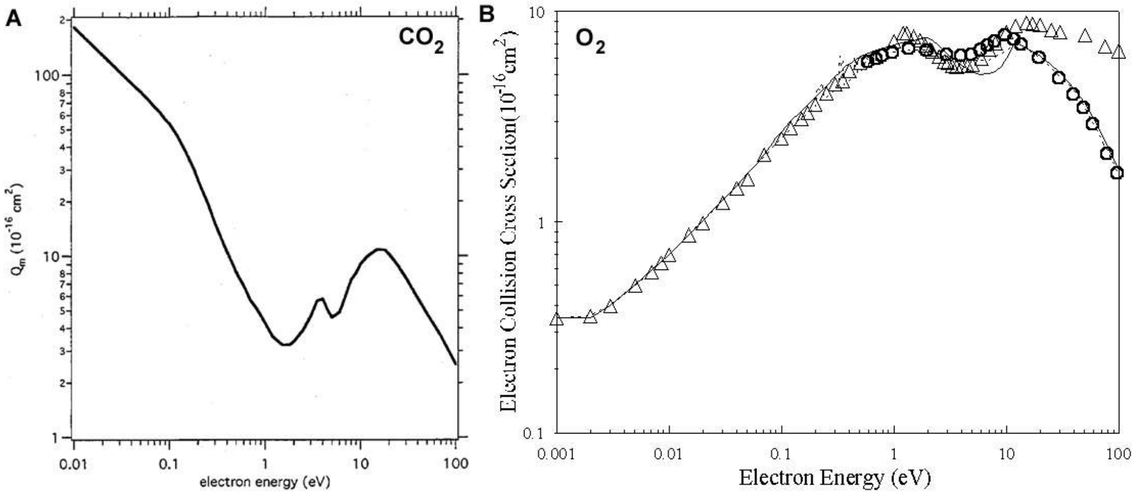

Figure 3.9: Electron transfer cross sections for (A) CO_2 given by Itikawa (2002) and (B) O_2 given by Jeon (2003). The Symbols given in (B) denote measurements for comparison.

3.2.3 Numerical implementation

The basic numerical solver used for our simulations is the ZEUS-MP code (*Hayes et al.* 2006). This MHD code uses finite differences on a staggered mesh in Cartesian, cylindrical or spherical coordinates. To implement the model equations outlined above we extended the ZEUS-MP source code to account for the additional terms given in Equations (3.18) to (3.21) with respect to the original ideal MHD equations (3.14) to (3.17). All newly implemented terms are considered for the time step calculation in the code in order to satisfy the Courant-Friedrichs-Lewy condition. The default Courant number for ZEUS-MP of 0.5 is used to compute the time step in our simulation. For the implementation and time step computation of the diffusion term we followed the approach given in the appendix by *Vigelius and Melatos* (2009). The diffusion term is included analogous to the solution for $\mathbf{v} \times \mathbf{B}$ which is solved by the Method of Characteristics - Constrained Transport or MOC-CT scheme. This scheme ensures an accurate evolution for all MHD wave modes and guarantees that the simulated magnetic field at all times satisfies the divergence-free constraint. To discriminate between the temporal evolution for the magnetospheric and ionospheric electrons we make use of the possibility to solve multiple continuity equations in ZEUS-MP. The ZEUS code further provides the possibility to use an artificial viscosity term to better resolve narrow shock structures arising in the simulations. For our model we use a nonlinear artificial viscosity term whose strength is scaled by the constant $q_{\mathrm{con}} = 2$ (alternatively denoted C_2 in the description given by *Stone and Norman* 1992a). Physically, the artificial viscosity for this value forces shocks to spread over at least two grid cells. In regions without shock structures the contribution of the artificial viscosity is negligibly small. The additional linear viscosity term in ZEUS-MP was not used for our simulations ($q_{lin} = 0$). For all our simulations we use a Cartesian grid with a step wise decreasing resolution away from the coordinate origin. Therefore, our model does not include an actual boundary at the satellite surface. Instead, we follow the approach of *Schilling* (2006) to simulate the influence of Callisto's interior. The treatment of the interior is discussed along with the applied boundary conditions in the next section.

3.2.3.1 Boundary conditions and treatment of the interior

A fluid code like ZEUS-MP does not include a physical description for the interaction of the plasma with a solid body like Callisto. Physically, we need a formulation which accounts for the loss of plasma particles at the surface and at the same time gives an adequate description for the evolution of the magnetic field in the interior. In our MHD model we treat the surface as a pseudo boundary. The production and loss terms in Equations (3.18) to (3.21) are not considered below the surface. Further, instead of the our full energy equation (3.20), we apply the original ZEUS energy equation (3.16). The plasma in our simulations is allowed to flow into the interior. However, an additional loss term

$$L_{\text{int}} = -\frac{9}{10}\frac{\partial \rho}{\partial t} \tag{3.44}$$

acting only within $r < \mathrm{R}_C$ instantly decreases the density of the inflowing plasma up to a predefined minimum value $\rho_{\text{int,min}}$. Consequently, throughout the interior the density is kept close to this constant value. Further, the plasma is decelerated by a collision term for a spatially constant interior collision frequency ν_{int}. This frequency is set equal to the surface values of $\nu_{i,ns}$ multiplied by a scalable factor δ_ν. For a suitably strong collision term the plasma comes almost to a halt and only a negligible amount of plasma escapes Callisto's body. As we can not ensure a complete confinement of the interior plasma, we apply a loss term similar to L_{int} (replacing ρ by e) to the energy equation. This term prevents the potential escape of a high energy plasma from the interior. The lower threshold for the internal energy density is set to a minimum value $e_{\text{int,min}}$. This value is chosen such that the temperature in the interior $T_{\text{int}} = e_{\text{int,min}} m_i/(3k_B\rho_{\text{int,min}})$ is at least two orders of magnitudes lower than the background plasma temperature T_0.

The values $\rho_{\text{int,min}}$ and δ_ν can be scaled to obtain a value $\eta = \sum_{ns} m_e \nu_{e,ns}/(nq_e^2)$ for the diffusivity which guarantees a suitably small magnetic Reynolds number R_m in the interior. The magnetic field within Callisto's body is than almost exclusively transported by diffusion. However, decreasing the value for $\rho_{\text{int,min}}$ below a certain level eventually leads to numerical difficulties due to steep gradients for ρ at the surface. Therefore, we define a value of $\rho_{\text{int,min}} = 0.05\,\rho_0$ and considerably increase the collision frequencies by $\delta_\nu = 50$. The resulting magnetic Reynolds number is of the order of $R_m = 10^{-10}$. This value for R_m does not account for the internal conductivity of the satellite. As we do not consider potential induced magnetic fields in our formulation of the plasma interaction model, we choose to stick with this low value for R_m as it prevents numerical difficulties for the evolution of the magnetic field in the interior. It should be noted that the collision frequencies in the interior contribute to the overall strength of the plasma interaction. However, the interaction caused by the collisions and the mass loading in Callisto's atmosphere is already rather strong. Therefore, the high collisions frequencies in the interior do not significantly alter the overall results presented in this thesis.

The main issue at the actual simulation boundaries are wave reflections which can artificially perturb the plasma interaction regions. A common approach to avoid these reflections is to set the boundaries at large distances to the region of interest ($x, y, z \approx \pm 10\ \mathrm{R}_C$) in the simulation. The time until the reflexions affect the region of interest should be long enough to obtain a quasi-steady state. Additionally, inflow boundary conditions have proven to be more transparent to outflowing waves. Therefore we use outflow conditions only for the downstream boundary in the positive x-direction and inflow conditions at the other simulation boundaries. The grid dimensions and initial conditions for the plasma parameters used in our simulations are presented in the next section.

3.2.4 Simulation setup

We now outline the initial setup for our simulation runs i.e., the assumed conditions at $t = 0$ as well as the dimensions and resolution of the Cartesian grid. The plasma parameters ρ, e and $\mathbf{B}$ are initialized to constant values ρ_0, e_0 and $\mathbf{B}_0$ throughout the entire simulation domain. To ensure a smooth transition between satellites interior and the outer plasma regime for the first simulation time steps $\mathbf{v}$ is linearly reduced within a spherical shell between 2.5 R$_C$ and 1.5 R$_C$ from the background value $\mathbf{v}_0$ up to zero below 1.5 R$_C$. For setups where $\mathbf{v}_0$ has contributions in the y- or z-direction we rotated the two vectorial parameters $\mathbf{B}$ and $\mathbf{v}$ so that the initial velocity vector always points in the x-direction. Both vectors were additionally rotated around the x-axis to obtain magnetic field vectors which lie in the xy-plane. The simulation results presented in this chapter are all given with respect to the CphiO coordinate system (see Page 49) i.e., the variables were rotated back accordingly. The initial values for the simulations presented in this thesis are summarized in Section 3.2.5.

The resolution of our model domain needs to be suitably high to resolve the gradient of the neutral atmospheric densities. As a common rule of thumb at least three grid points should be used to cover one neutral scale height H_{ns} i.e., 23 km in the case of Callisto. For a Cartesian grid this implies that at least 630^3 grid points would be necessary to resolve just the interior of Callisto with a diameter of 4,820 km. Nested grids which would allow to decrease the resolution within $r <$ R$_C$ and retain a suitable resolution for the atmosphere are not available for the ZEUS-MP code. The time step in our simulations is of the order of 10^{-3} s. Therefore, the chemical equilibrium state for the ionosphere ($P = L$) needed to obtain quasi-stationary conditions is reached not before 700 s or 700,000 time

x [R$_C$]	−30	⟷	−10	⟷	−6	⟷	−3	⟷	1.5	⟷	15.5	⟷	50	⟷	155
Cells		9		12		19		57		88		22		9	
Resol.		2.22		0.33		0.16		0.08		0.16		1.56		11.6	
y [R$_C$]	±155	⟷	±50	⟷	±20	⟷	±10	⟷	±1.5	⟷	0				
Cells		8		14		29		50		19					
Resol.		13.13		2.14		0.34		0.17		0.08					
z [R$_C$]	±100	⟷	±50	⟷	±10	⟷	±6	⟷	0						
Cells		4		10		11		75							
Resol.		12.50		4.00		0.36		0.08							

Table 3.4: *Grid layout in Cartesian coordinates. Given are the number of cells and the corresponding resolution in R$_C$ for each block of the grid. The y and z-axis are defined symmetrically with respect to the xz- and xy-plane, respectively.*

steps. Even though the CHEOPS cluster[III] used for our calculations provides vast computational resources, simulations with the desired resolution would take several month to reach quasi-steady state conditions.

Due to these complications it was necessary to perform our simulations with an artificially increased scale height. To retain an acceptable grid size we choose to scale H_{ns} with a factor $H_{\mathrm{rel}} = 10$ i.e., we use $H_{ns} = 230$ km. Even with this increased scale height our grid outlined in Table 3.4 still not fulfills the three grid points rule mentioned above. However, we found that for the given resolution and $H_{\mathrm{rel}} = 10$ the stability of the simulation runs is still guaranteed. One reason for this is the artificial viscosity term which smoothes steep gradients in the simulations. Note that the total particle content for a realistic neutral atmosphere is still matched for the given scale height when Equation (3.22) is applied. The Cartesian grid listed in Table 3.4 contains several blocks. Towards the simulation boundaries the resolution is decreased for each successive block in order to obtain a suitably large total box size. This ensures that wave reflections at the boundaries do not affect the region of interest. In the wake region of Callisto (positive x-direction) the resolution is kept at a high level to retain a realistic behavior of the downstream plasma flow. One reason for this is that most of the flybys considered in this thesis took place downstream of the satellite. A second reason is that complex plasma flow structures occur in this region.

The increased atmospheric scale height of our model leads to an overestimation of the size of the local interaction region and the cross section of the Alfvén wings. Further, the peak ionospheric densities in our model are generally lower than for a realistic value of H_{ns}. However, in reality the neutral scale height is presumably not constant but increases with height. For example *Liang et al.* (2005) discuss an increased scale height for hydrogen in Callisto's upper atmosphere. Therefore, the atmospheric setup used in our simulations still yields adequate results for Callisto's plasma interaction.

3.2.5 Model scenarios

To analyze Callisto's magnetic field environment, plasma environment and atmosphere-ionosphere system we performed various simulations for different initial setups. The model scenarios discussed in Section 3.3 can be divided into two main categories. First, we consider scenarios consistent with each flyby of Galileo to obtain results directly comparable with the magnetic field and radio occultation measurements. Secondly, we performed simulations for simplified standard scenarios to assess the general behavior of the plasma environment at Callisto. For each of this two sets of models we performed additional parameter studies using different setups for the ambient plasma conditions. Further, we investigated the impact of different configurations for Callisto's neutral atmosphere such as a symmetric pure CO_2 atmosphere or symmetric and asymmetric setups for a combined O_2 and CO_2 atmosphere (see Section 3.2.2). All scenarios considered in different sections of this thesis, the associated initial values of the plasma parameters and the atmospheric setups taken into account are summarized in Table 3.5.

[III] `http://rrzk.uni-koeln.de/cheops.html`, University of Cologne

Scenario	Default setup n_0 [cm^{-3}]	 $B_{x,0}$ [nT]	 $B_{y,0}$ [nT]	 $B_{z,0}$ [nT]	Param.	Atm.	Sections
			Flyby scenarios				
C3	0.07	-4	-27	-10	v_0, p.d.	-	(3.3.3.1)
C9	0.06	2	37	-11	p.d.	CO_2, as.	3.3.2.2 (3.3.3.1) [3.3.2.2, 3.3.3.1]
C10	0.10	-4	23	-8	e_0	-	3.3.3.2 (3.3.3.2)
C21	0.12	2	37	-7.5	p.d.	-	A.2 (A.2)
C22	0.04	7	23	-12	-	CO_2, as.	3.3.2.2, 3.3.3.2 [3.3.2.2, 3.3.3.2]
C23	0.14	-4	-19	-12	-	CO_2, as.	3.3.2.2, A.2 [3.3.2.2]
C30	0.06	4	5	-20	p.d.	-	A.2 (A.2)
			Standard scenarios				
$\alpha_\odot = 270°$	0.11	0	30	0	e_0	CO_2, as.	3.3.1, 3.3.2.1, 3.3.2.3, 3.3.2.4 (3.3.1.3) [3.3.2.1]
$\alpha_\odot = 180°$	0.11	0	30	0	-	-	3.3.2.1
$\alpha_\odot = 90°$	0.11	0	30	0	-	CO_2, as.	3.3.2.1, 3.3.2.3 [3.3.2.1, 3.3.2.3]
$\alpha_\odot = 0°$	0.11	0	30	0	-	-	3.3.2.1

Table 3.5: *Summary of the model scenarios discussed within Section 3.3 and Appendix A.2. The values in the central four columns give the number density n_0 of the background plasma and the ambient magnetospheric field components in CphiO coordinates assumed for the default flyby scenarios and the standard scenarios. For the internal energy density of the ambient plasma we use a default value of $e_0 = 1.72$ nPa for all of the above cases. For the absolute value of the plasma velocity pointing in the x-direction we assume $v_0 = 192$ km s^{-1}. Column six indicates that additional model setups assuming variations of the denoted plasma parameters or flyby scenarios using the measured plasma data (p.d.) are discussed in the sections given in parentheses in the last column. Column seven indicates that additional atmospheric setups such as a symmetric pure CO_2 atmosphere or an asymmetric setup for a combined CO_2 and O_2 atmosphere (as.) are analyzed in the sections given in square brackets in the last column.*

For the flyby scenarios we primarily use initial values for ρ_0 given by the *Bagenal and Delamere* (2011) model (Section 3.1.2) at the respective height of Callisto above the current sheet z_{cs} (see Table 3.1). The initial plasma velocity $\mathbf{v}_0$ is set to the corotational velocity at Callisto of 192 km s^{-1}. For the internal energy density of the plasma we assume a value of $e_0 = 1.72$ nPa. This value ensures a suitable plasma beta of ~1.3 to 13 depending on the background magnetic field for each flyby. The magnetic field conditions are inferred from an interpolation of the magnetometer data. For all components of the magnetic field in CphiO coordinates we use two time frames of 10 min starting 40 min before and 30 min after the closest approach. We use a second order polynomial fit to the combined time frames to derive values for $\mathbf{B}_0$ at times 35 min before and after as well as at the closest approach of Galileo. As the Jovian background field eventually changes during each flyby we need to define a value for $\mathbf{B}_0$ which suitably describes the plasma interaction during the whole encounter. We performed several test simulations to determine which of the three values above yields the best fit to the measured magnetic field data. The actual values used for each flyby scenario are summarized in Table 3.5. The photo ionization rates for each flyby were computed using the values for $\alpha_\odot$ given in Table 3.1 and for the solar flux given in Table 3.3. The above setups in combination with a symmetric configuration of a combined CO_2 and O_2 atmosphere are dubbed default flyby scenarios in the following discussions. Apart from these scenarios, we performed simulation runs using variations for the atmospheric setup and alternative models using the actual measured plasma parameters for ρ_0, e_0 and $\mathbf{v}_0$ given in Table 3.2.

The initial values chosen for the second set of models dubbed standard scenarios in the following sections represent average plasma conditions at Callisto. The main purpose of these test simulations is to infer the influence of different solar phase angle ($\alpha_\odot$) configurations on the ionospheric densities predicted by our MHD model. $\alpha_\odot$ is defined as the angle between the Callisto-Jupiter line and the Callisto-Sun line. The position of the Sun with respect to the CphiO coordinate system for different values of $\alpha_\odot$ is depicted in Figure 3.10.

The $\alpha_\odot = 270°$ scenario represents conditions when the upstream hemisphere of Callisto is sunlit. As this scenario resembles several of the actual flybys the respective results are discussed in greater detail as an example for the general plasma interaction of Callisto in Section 3.3.1.1. The second setup for $\alpha_\odot = 90°$ corresponds to a sunlit downstream

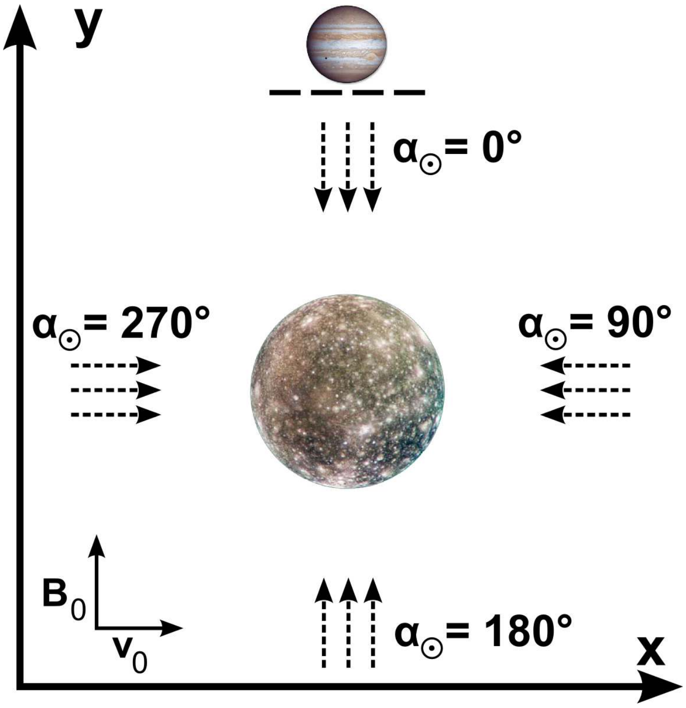

Figure 3.10: Definition of the solar phase angle $\alpha_\odot$ and the overall geometry for our standard simulation scenarios. Dashed arrows indicate the incident solar radiation for different values of $\alpha_\odot$. Solid arrows depict the background plasma velocity and magnetic field directions. Jupiter is located towards the positive y-direction. Note that the x- and y-axis are defined in analogy to the CphiO coordinate system for a coordinate origin shifted to the center of Callisto.

hemisphere. For $\alpha_\odot = 0°$ the Jupiter facing side ($-y$-direction) of Callisto is illuminated by the Sun while for $\alpha_\odot = 180°$ the anti-Jovian hemisphere is sunlit. The solar flux for all of these cases was computed for the default conditions given in Table 3.3. For all four standard scenarios we defined a standardized setup with a magnetic field of $\mathbf{B}_0 = 30$ nT pointing towards Jupiter (in the $-y$-direction), a plasma bulk velocity of $\mathbf{v}_0 = 192$ km s^{-1} in the x-direction, a plasma density of $\rho_0 = 0.11$ cm^{-3} and an internal energy density of $e_0 = 1.72$ nPa. As for the flyby scenarios discussed above we performed parameter studies assuming different atmospheric setups and ambient conditions for our standard scenarios. The respective setups are summarized in Table 3.1.

3.3 Results

We now discuss the numerical results obtained from the plasma interaction model outlined in the previous sections. The analysis of the simulations summarized in Table 3.5 is divided into three stages. First, we discuss the general nature of Callisto's plasma interaction and present features occurring for all our simulations in Section 3.3.1. This overall analysis is mainly based on the standard scenario for a solar phase angle of $\alpha_\odot = 270°$. Differences for the results of additional simulation setups are discussed along with the interpretation for this model. Secondly, we analyze Callisto's ionospheric configuration as predicted for the standard simulation scenarios for four different solar phase angles and the default flyby scenarios for C9, C22 and C23 in Section 3.3.2. We compare our model ionosphere with the results presented by *Kliore et al.* (2002) and discuss the plausibility of various hypothesis regarding the observed temporal variabilities. Further, we give predictions for the auroral intensities at Callisto and discuss the ionospheric currents and conductivities. In Section 3.3.3 we compare the magnetic field signatures predicted by our models for several flyby scenarios to the magnetometer data measured by Galileo. We also discuss the secondary magnetic fields generated in the interior of Callisto, as predicted by the induction model presented in Chapter 2.

3.3.1 The nature of Callisto's plasma interaction

In this section we discuss the general nature of Callisto's plasma interaction based on our standard scenario for $\alpha_\odot = 270°$. For our standard simulation setup we assume a simple interaction geometry with **v** pointing in the x- and **B** pointing in the y-direction. Our analysis for this setup includes the simulation results for all relevant plasma parameters. These general results in large parts also hold for the flyby scenarios and the other standard scenarios for different solar phase angles. All values in the following sections are given for a time step of 720 s when the ionosphere has reached a chemical equilibrium state and quasi-stationary conditions can be assumed.

3.3.1.1 Velocity and magnetic field

The simulation results for the velocity and the magnetic field in the xy- and xz-plane are depicted in Figures 3.11 to 3.14. The color codes of these figures illustrate the absolute values for the two fields. Gray cones indicate the field direction projected in the respective planes. The two field components in the respective plane are normalized to the absolute value of the field without the component perpendicular to the plane to obtain the cone direction. The flow patterns show the expected interaction geometry with two wing structures pointing along the two Alfvén characteristics indicated by thin white lines in Figures 3.11 and 3.13. The diameter of the wings is larger than 1 R_C due to the extended atmosphere which is part of the total obstacle to the plasma flow. In the inner regions of the Alfvén wings the velocity is decreased up to a value of 2 km s^{-1}. Our setup with v_0 = 192 km s^{-1} therefore represents an interaction scenario with a relative strength of $\alpha_{\text{wing}} = 0.01$. The magnetic field lines are bend towards the flow direction with an Alfvén

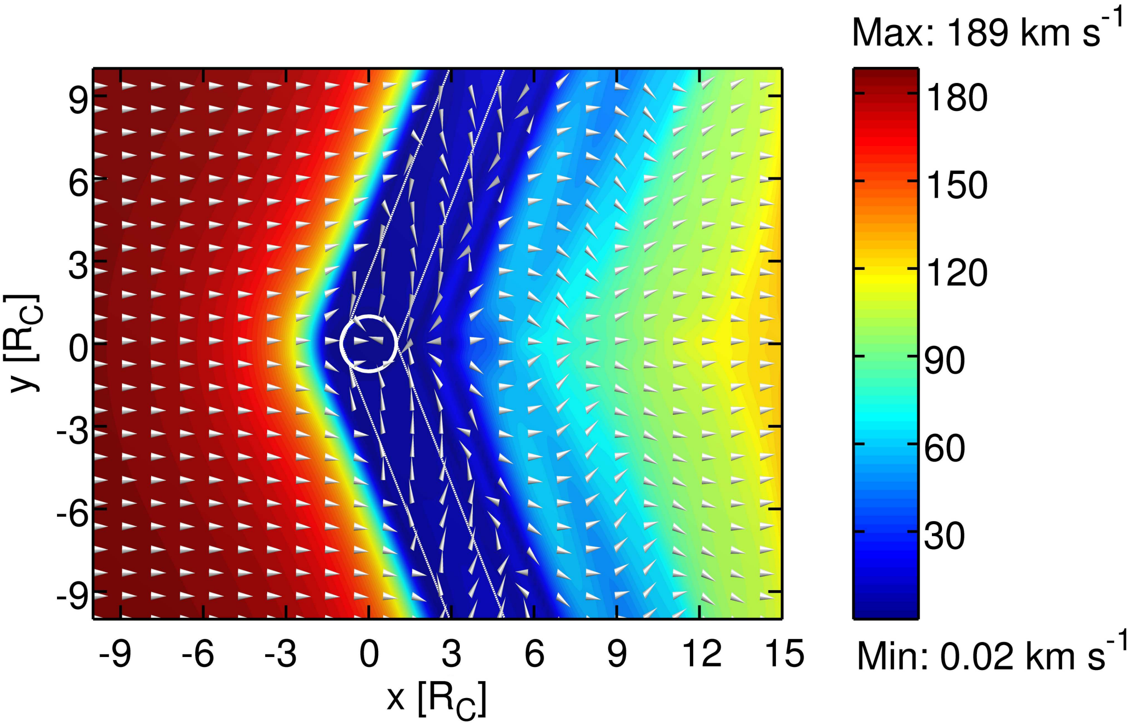

Figure 3.11: *Plasma bulk velocity* $\mathbf{v}$ *in the xy-plane at* $z = 0$ *for the* $\alpha_\odot = 270°$ *scenario. The absolute values of* $\mathbf{v}$ *in km* s^{-1} *are color encoded. Cones represent projections of the normalized velocity vectors indicating the flow direction. White lines indicate the direction of the Alfvén characteristics. The white circle represents the surface of Callisto.*

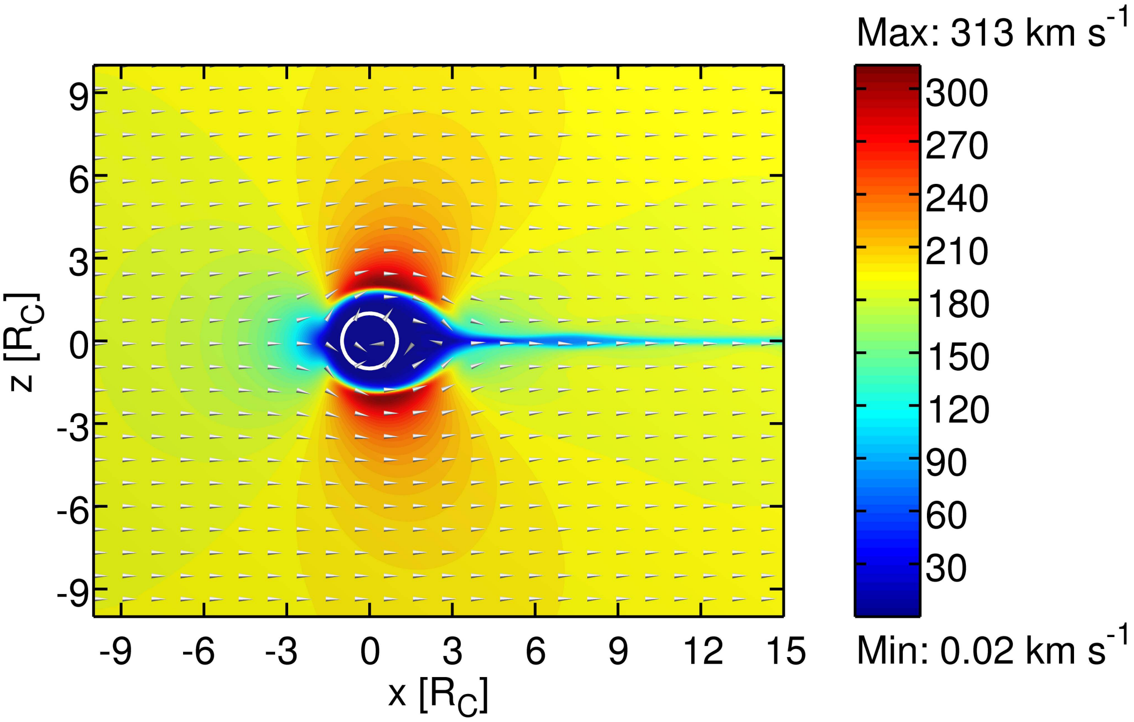

Figure 3.12: *Plasma bulk velocity* $\mathbf{v}$ *in the xz-plane at* $y = 0$ *for the* $\alpha_\odot = 270°$ *scenario. See Figure 3.11 for further explanations. Note the differences in the color scale with respect to Figure 3.11.*

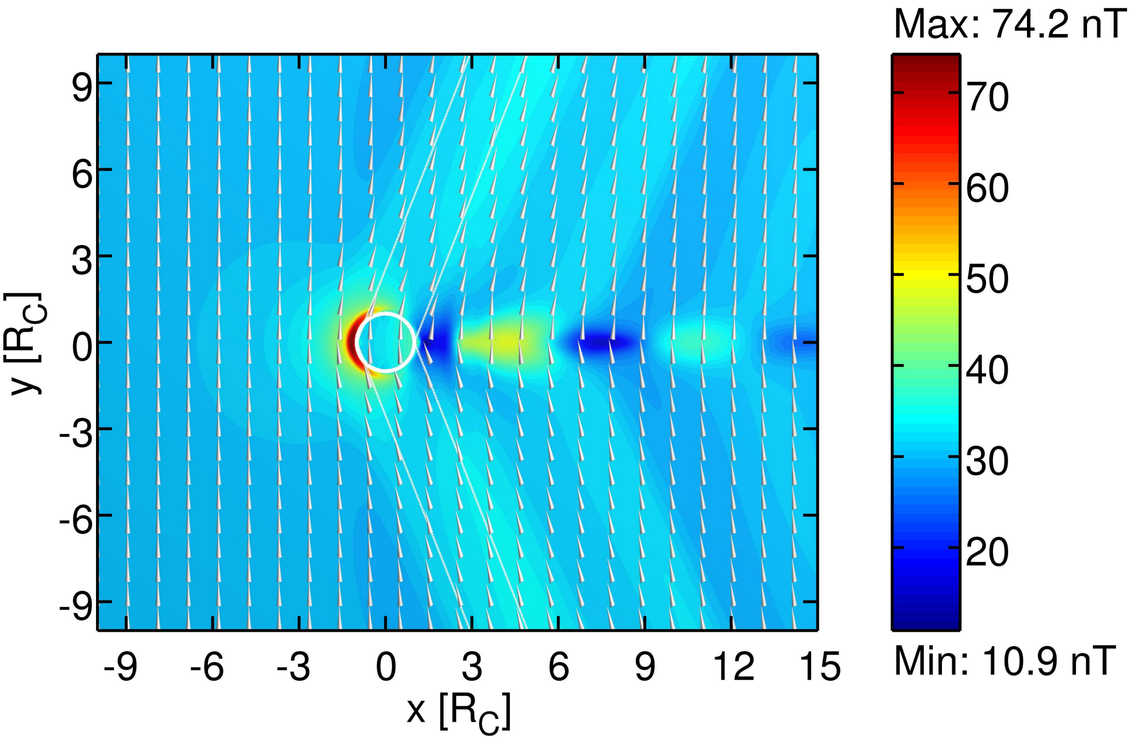

Figure 3.13: Magnetic field $\mathbf{B}$ *in the xy-plane at* $z = 0$ *for the* $\alpha_\odot = 270°$ *scenario. The absolute values of* $\mathbf{B}$ *in nT are color encoded. Cones represent projections of the normalized magnetic field vectors. White lines indicate the direction of the Alfvén characteristics. The white circle represents the surface of Callisto.*

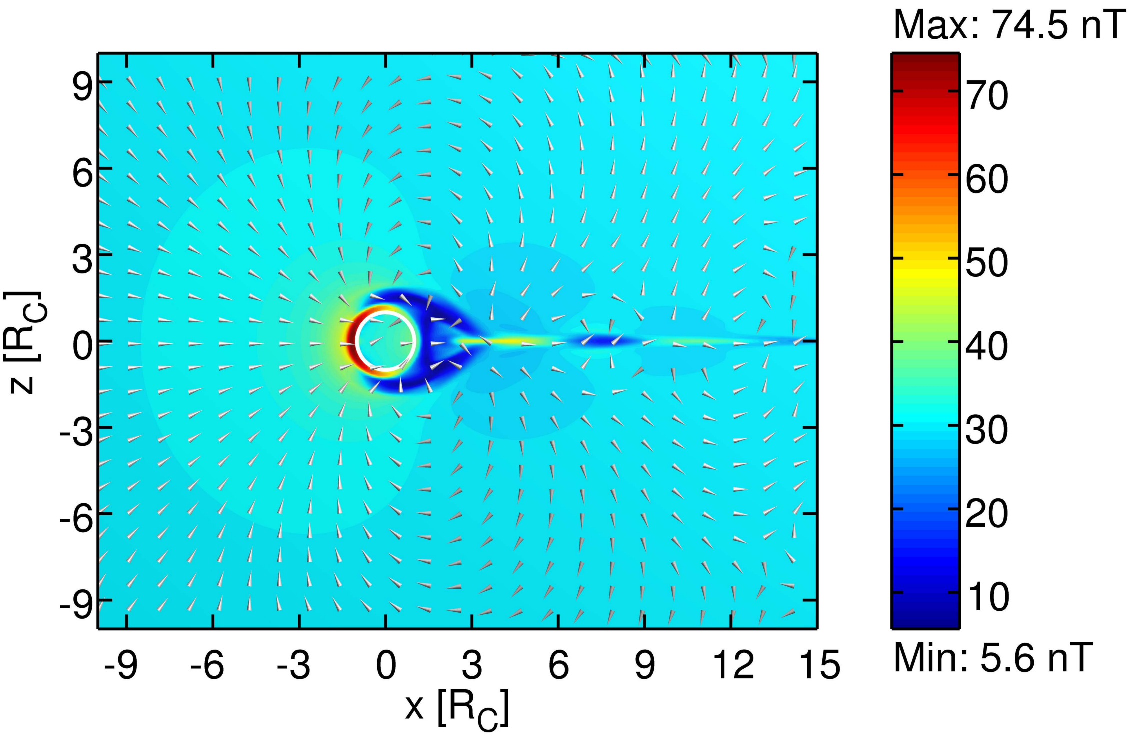

Figure 3.14: Magnetic field $\mathbf{B}$ *in the xz-plane at* $y = 0$ *for the* $\alpha_\odot = 270°$ *scenario. See Figure 3.13 for further explanations.*

angle of 21.5°. The absolute values of the field remain close to the background level of 30 nT. The disturbances generated in the B_x component are on the order of ±14 nT along both Alfvén characteristics (also see Figure 3.15, discussed below).

In the upstream region of the atmosphere the magnetic field lines pile up and the field strength reaches values of up to 74.5 nT. In the wake region of the atmosphere the field magnitude decreases to ~5 nT. In Figure 3.12 it can be seen that the flow is diverted around the obstacle in the z-direction. The velocity at the poles reaches maximum values of 313 km s^{-1} or $1.6 \times v_0$ in regions where the collision and mass loading effects are already sufficiently weak. The normalized values of B_x and B_y indicate a nearly dipolar behavior around the poles (Figure 3.14). However, the magnetic field is still primarily directed towards Jupiter and B_y yields by far the strongest contribution to the absolute field strength.

The patterns for **v** and **B** near the satellite continue along the Alfvén wings which also act as an obstacle to the flow. Figure 3.15 depicts the B_x and B_z components of the magnetic field for a cross section of the anti-Jovian Alfvén wing at $y = -3$ R_C. The magnetic field lines pile up in front of the wing and the magnitude of B_x increases. From this point, the flow is diverted in the z-direction and B_z increases up to ±7.2 nT while B_x decreases to zero. Above and below the inner wing ($z \approx \pm 2$ R_C) v_x exceeds v_0 and the field lines are twisted in the $-x$-direction. In this region B_x is disturbed by ~5 nT. In the downstream region of the wing ($x > 2$ R_C) B_z shows an opposite behavior to the upstream conditions while the flow returns to its original configuration. In the inner parts of the wing B_x shows some additional structuring owed to the nonlinear nature of the interaction in our simulations. The diameter of the wing is approximately 4 R_C. Because of the increased scale height in our model ($H_{\mathrm{rel}} = 10$) this diameter should be generally much smaller in reality. Additionally, secondary fields generated due to the induction effect, not taken into account here, would decrease the wing diameter (see Section 1.2.2).

While the general geometry of the interaction is very similar for the other standard scenarios with $\alpha_\odot = 0°, 90°$ and 180°, complex geometries arise for the flyby scenarios ex-

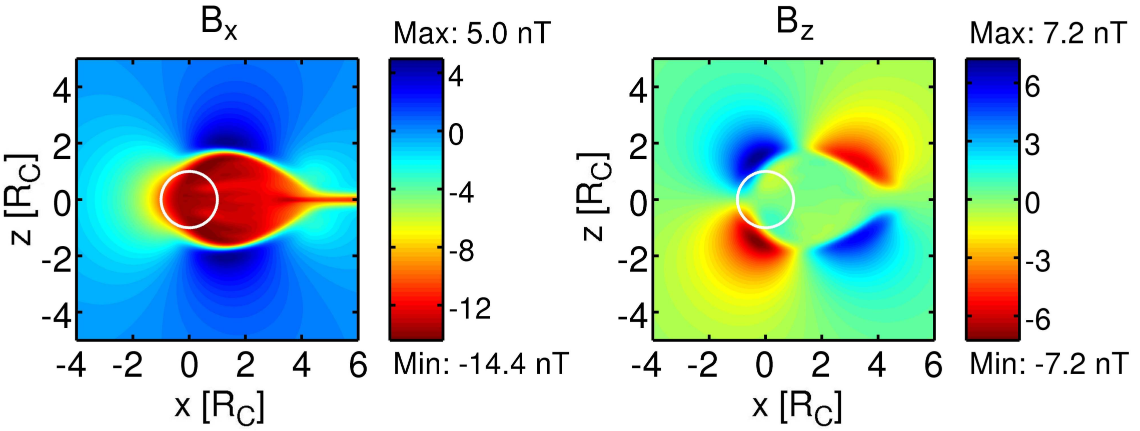

Figure 3.15: *B_x and B_y components of the magnetic field in nT in the xz-plane at $y = -3$ R_C for the $\alpha_\odot = 270°$ scenario. White circles represent the relative position of Callisto. Note the differences in the color scales of both figures.*

amined in this thesis. We present the respective geometries in Section 3.3.3 along with the associated magnetic field signatures. Apart from this standard picture of the plasma interaction, several unexpected wing like structures can be seen in the downstream region of Callisto and its Alfvén wings in Figures 3.11 and 3.13. We examine the plausibility of these features in Section 3.3.1.3 after the discussion of the plasma density and total pressure patterns in the next section.

3.3.1.2 Pressure, temperature and density

The plasma pressure (p or $2/3\,e$) pattern in the xz-plane for the $\alpha_\odot = 270°$ standard scenario is depicted in Figure 3.16. The pressure decreases rapidly over at least four orders of magnitudes towards the surface of the satellite. This decrease in the total plasma pressure is caused by the temperature coupling with the neutral gas and the loss term in Equation (3.20). The two terms opposing the decrease of the p are the production term which is negligible due to the low temperature of the neutral atmospheric particles (150 K) and the Joule heating term which is small due to the low velocities in the vicinity of the satellite ($<$ 10 km s^{-1}). The pressure pattern is nearly radially symmetric with a slightly steeper gradient in the downstream hemisphere. In the xy- and yz-plane (not given here) p shows a similar symmetric behavior. The pressure in the interior is suitably low ($< 10^{-3}$ nPa) to confine the internal plasma. Over the northern and southern poles the plasma pressure of $p \approx 1.3$ nPa is slightly increased with respect to the background level of $p_0 = 1.15$ nPa ($e_0 = 1.72$ nPa). This is a consequence of the compression of the flow while it is diverted around the satellite. In Callisto's wake there is a region of enhanced pressure ($p \approx 1.8$ nPa) where the southern and northern plasma flows converge. Both upstream and downstream of this convergence point the pressure of $p \approx 0.3$ nPa is decreased below the background level.

The plasma temperature T, which can be calculated at each location in our simulation box by using Equation (3.2), shows a behavior similar to the pressure in the vicinity of the satellite (Figure 3.17). In the interior the temperature is numerically kept at a level of $k_B T \approx 100$ eV, slightly higher than for the surrounding ionospheric plasma but two orders of magnitude lower than the background temperature T_0. The confinement of this medium temperature plasma to the interior again indicates that there is no significant leakage of the interior plasma contributing to the exterior plasma flow in our model. In the upper atmosphere (above $r \approx 1.2$ R$_C$) and the wake region of Callisto the temperature is mainly defined by the distribution of the plasma density discussed below. Apart from this qualitative behavior, the values for the temperature, especially for the inflowing plasma, are unrealistically high compared to the value of 635 eV suggested by *Bagenal and Delamere* (2011). Therefore, while the values for the total pressure are still realistic when we take into account the contributions of energetic plasma particles (~0.5 nPa compared to 0.4 nPa given by *Kivelson et al.* 2004), the obtained temperatures outside Callisto's inner atmosphere are greatly exaggerated in our model. However, we decided to stick with a realistic description of the pressure in order to account for a suitable plasma beta of ~3 and accept these unrealistic temperatures. The two parts of our model where the high temperatures affect the simulation are the electron collision terms and the temperature coupling with

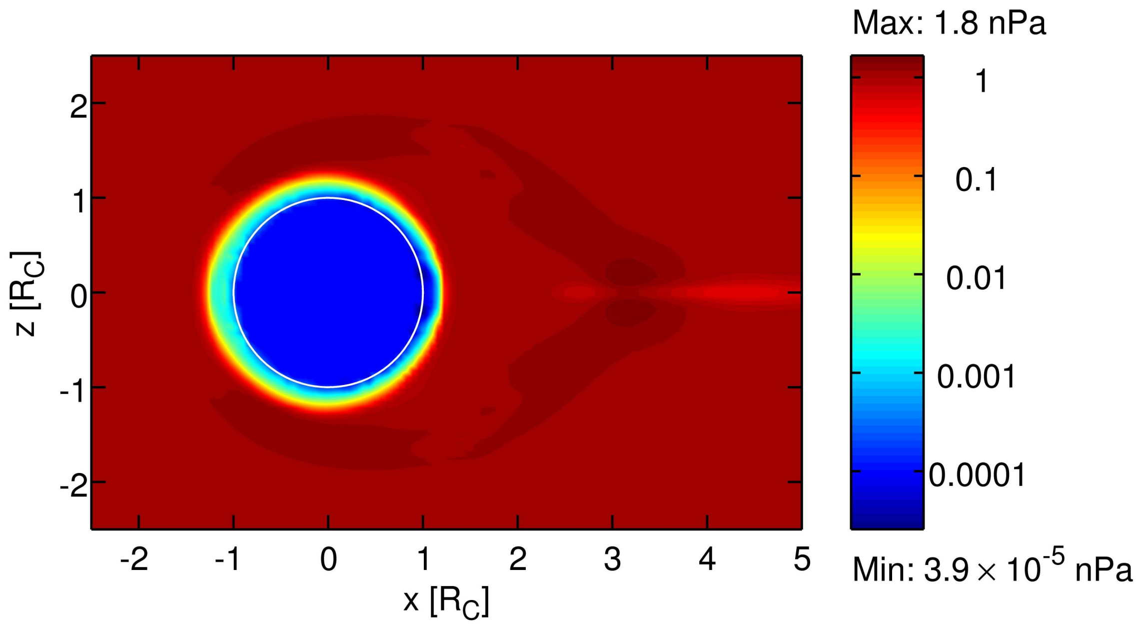

Figure 3.16: *Total plasma pressure p in nPa in the xz-plane at $y = 0$ for the $\alpha_\odot = 270°$ scenario. p is color encoded on a logarithmic scale. The white circle indicates the surface of Callisto.*

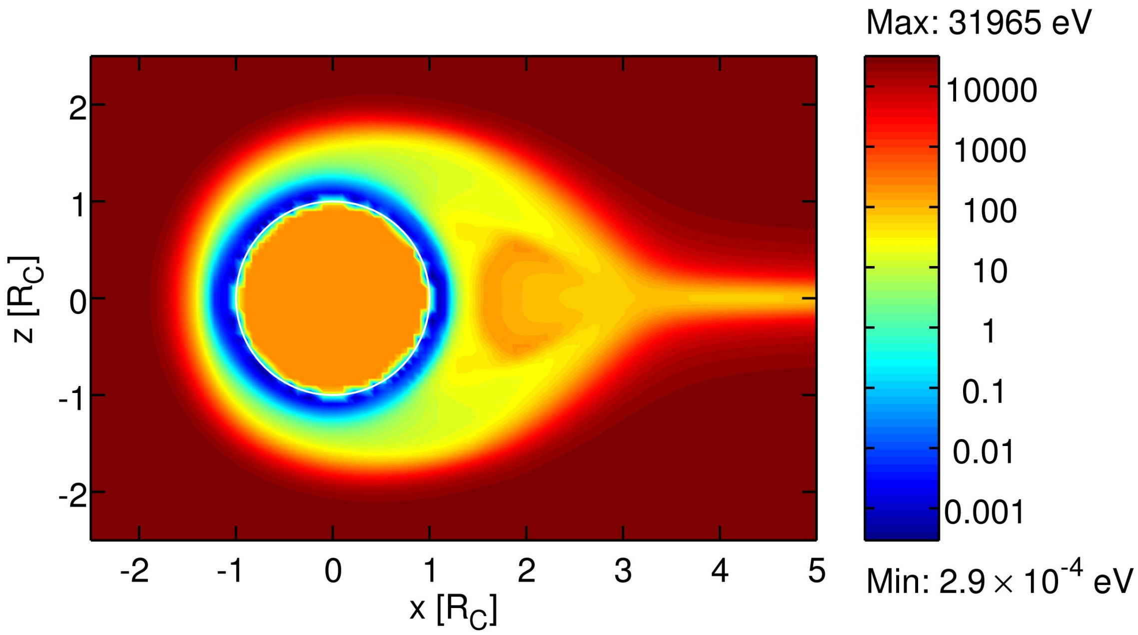

Figure 3.17: *Plasma temperature k_BT in eV in the xz-plane at $y = 0$ for the $\alpha_\odot = 270°$ scenario. The temperature is color encoded on a logarithmic scale. The white circle indicates the surface of Callisto.*

the neutral gas. In regions where the temperatures reach unrealistic values the neutral densities are, however, already sufficiently low to neglect the electron collision effects. The temperature coupling, on the other hand, causes a decrease of the plasma temperature to a more realistic level. Note that the loss term in the energy equation is also not affected by the high temperatures as we discriminate between the magnetospheric particles and the ionospheric particles with low temperatures for the evaluation of this term.

Further, the high temperature magnetospheric electrons which are treated by the separate continuity equation (3.30) are diverted around Callisto before they can reach atmospheric regions below an altitude of ~500 km (see Figure 3.18). Magnetospheric electrons which are initially located below 1.2 R_C are eventually lost at Callisto's surface. Slightly above this radius the number density n_{ms} increases from its upstream value of $n_0 = 0.11$ cm^{-3} to ~1 to 3 cm^{-3}. Within the shell defined by these peak values impact ionization occurs most efficiently. The maximum density of 3 cm^{-3} is even located in the shadow region for our $\alpha_\odot = 270°$ scenario, where mass loading can only occur due to impact ionization. In the inner wake region the number density of the magnetospheric electrons is decreased by a factor of ~0.5. The downstream flow of magnetospheric electrons is mainly confined to regions beyond 0.6 R_C above and below the inner wake, where it is slightly spread out in the xy-plane.

The total plasma number densities n which are dominated by the ionospheric electrons close to Callisto are depicted in Figures 3.19 and 3.20. The peak values of ~4,000 to 5,000 cm^{-3} are located in regions which are not reached by the magnetospheric particles. The overall maximum occurs in the upstream hemisphere where photo ionization is the dominant mass loading process. However, the total plasma densities are decreased very

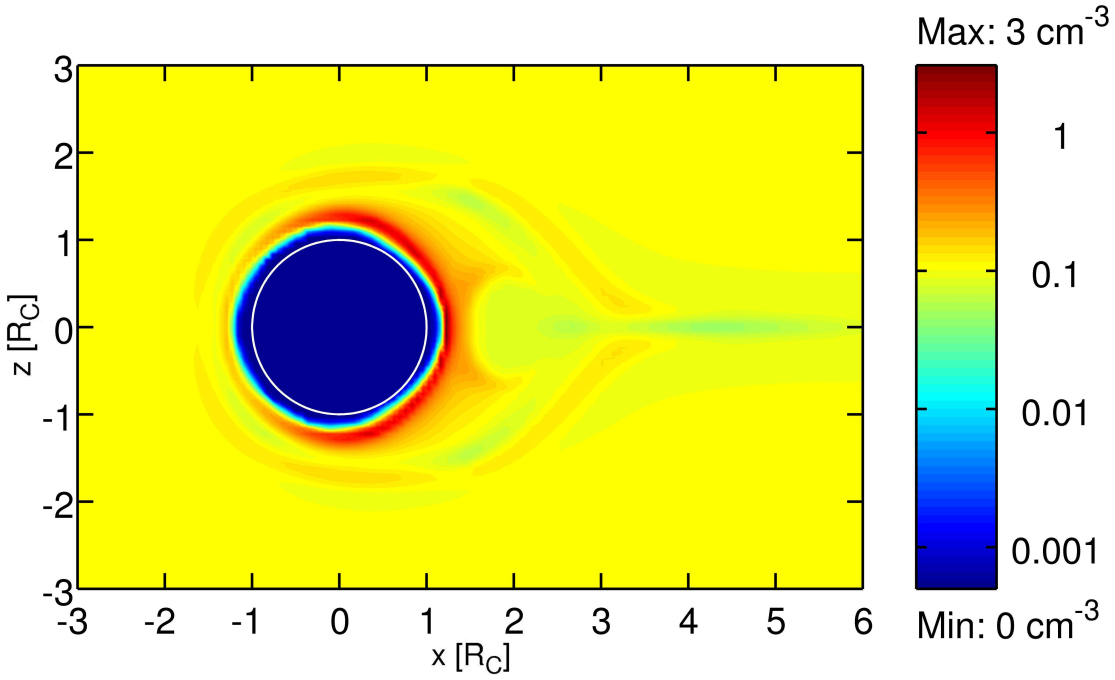

Figure 3.18: Number densities of the magnetospheric electrons n_{ms} in cm^{-3} (logarithmic scale) in the xz-plane at $y = 0$ for the $\alpha_\odot = 270°$ scenario. The white circle indicates Callisto's surface.

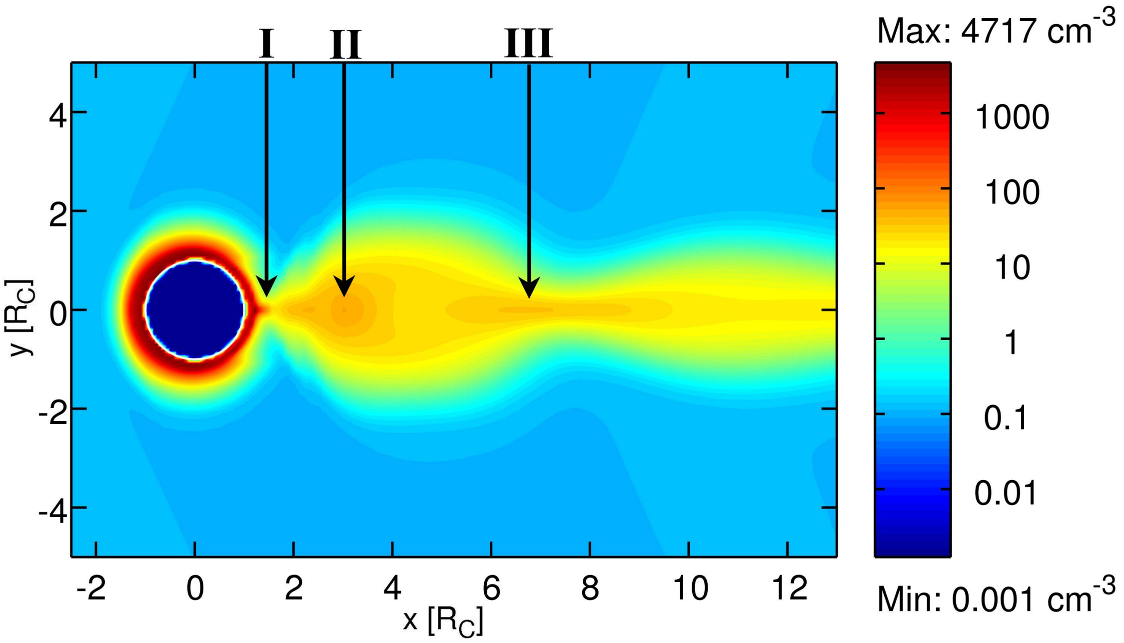

Figure 3.19: *Plasma number densities n in cm*$^{-3}$ *(logarithmic scale) in the xy-plane at* $z = 0$ *for the* $\alpha_\odot = 270°$ *scenario. Three plasma accumulation points labeled I, II and III can be identified in the tail region (see Section 3.3.1.3). The white circle indicates the surface of Callisto.*

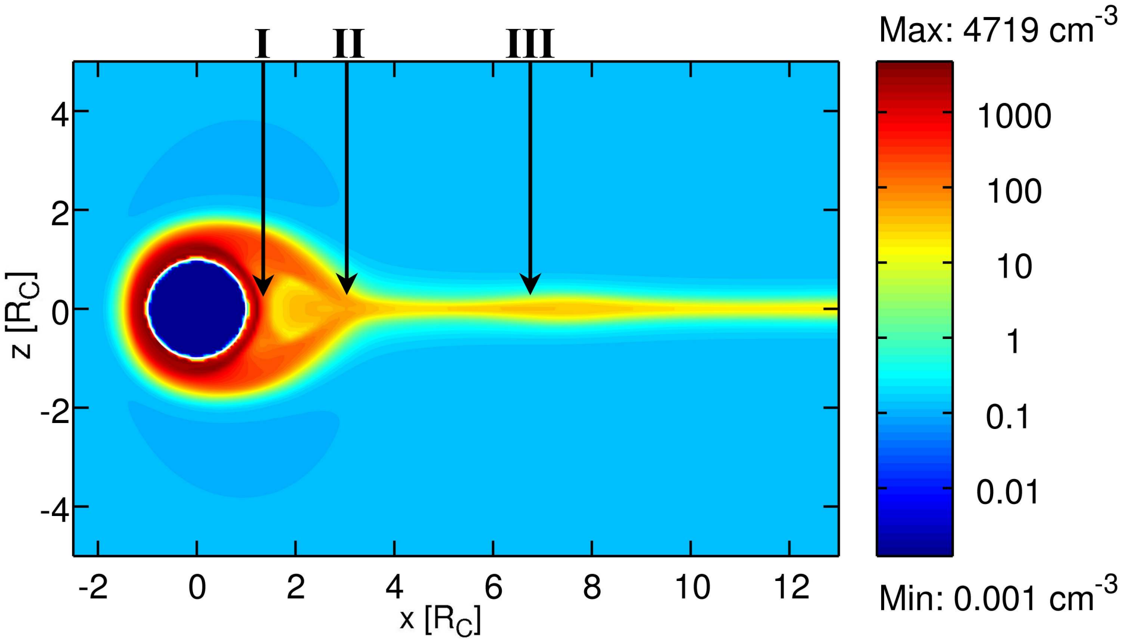

Figure 3.20: *Plasma number densities n in cm*$^{-3}$ *(logarithmic scale) in the xz-plane at* $y = 0$ *for the* $\alpha_\odot = 270°$ *scenario. Three plasma accumulation points labeled I, II and III can be identified in the tail region (see Section 3.3.1.3). The white circle indicates the surface of Callisto.*

close to the surface where particles are absorbed by Callisto's body (regions near the white circles in Figures 3.19 and 3.20). In regions where the bulk velocity of the plasma is low, such as the sub-Jovian and anti-Jovian regions in the xy-plane ($y = \pm \mathrm{R}_C$, $x = 0$ in Figure 3.11), the plasma densities are mainly defined by the chemical equilibrium between mass loading and loss processes. Almost no plasma is transported downstream in the xy-plane close to the satellite. Instead Callisto's plasma tail is mainly fed by ionospheric particles generated at northern and southern latitudes (see Figures 3.20 and 3.12). The downstream near-surface region is mainly populated by particles generated by impact ionization. However, there is an additional contribution by tail particles with are slowly transported in the upstream direction and accumulate near a region at $x = 1.5\ \mathrm{R}_C$, $y = 0$ extending slightly along the z-direction. Evidence for this unexpected upstream transport process can be seen in the velocity vector field depicted in Figures 3.11 and 3.12 (near $x = 3\ \mathrm{R}_C$, $z = 0$ and within $y = \pm 3\ \mathrm{R}_C$). While we, so far, omitted a detailed discussion of the downstream and tail structures evident in Figures 3.11 to 3.20, we now take a closer look at the plausibility of those features in a separate section.

3.3.1.3 Tail structures

So far, we were not able to find a conclusive explanation for the behavior of the plasma in the tail region of Callisto predicted by our model. In this section we describe the associated patterns for the plasma parameters and suggest a potential generation process. The density in Callisto's tail for the $\alpha_\odot = 270°$ standard scenario shows a wave like behavior in the xy-plane and, less pronounced, in the xz-plane (Figures 3.19 and 3.20). Three regions labeled I, II and III can be identified where the plasma accumulates. Region II is the located where the plasma flows from the northern and southern hemispheres unite. Consequently, the thermal pressure of the initially cold ionospheric plasma increases in this region. The ionospheric plasma flow now primarily pushes in the z- and to a lesser extent in the y-direction, opposing the pressure of the ambient thin but hot magnetospheric plasma. This effect is visible in the red curve in Figure 3.21 which presents the forces acting in the x-direction along the center of the tail. However, a force balance is reached due to the magnetic pressure force which compensates the thermal pressure. Note that due to the quasi-stationary state of the simulation Figure 3.21 can only give hints for the processes generating the simulated flow pattern but gives no conclusive explanations. The pressure of the deflected flow decreases in the y- and z-directions as the tail plasma thins out and eventually balances the pressure of the magnetospheric plasma ($x = 4\ \mathrm{R}_C$ and $y = \pm 3\ \mathrm{R}_C$ in Figure 3.19). Further downstream the ionospheric plasma is again pushed towards the inner tail and a second accumulation region (III) forms. This interaction between the ionospheric plasma and the surrounding high temperature magnetospheric plasma continues further downstream but eventually vanishes when the pressures of both plasmas adjust. Additional simulations performed for a lower ambient plasma temperature of $k_B T_0 = 635\ eV$ ($e_0 = 0.02$ nPa) show no indications for these wave like density structures. Instead the tail plasma is spread out over the entire downstream region in the xy-plane (see Figure 3.22). The plasma is, however, still confined to regions near $z = 0$. Apart from these density patterns the results for this additional simulation are very similar to the $\alpha_\odot = 270°$ standard scenario.

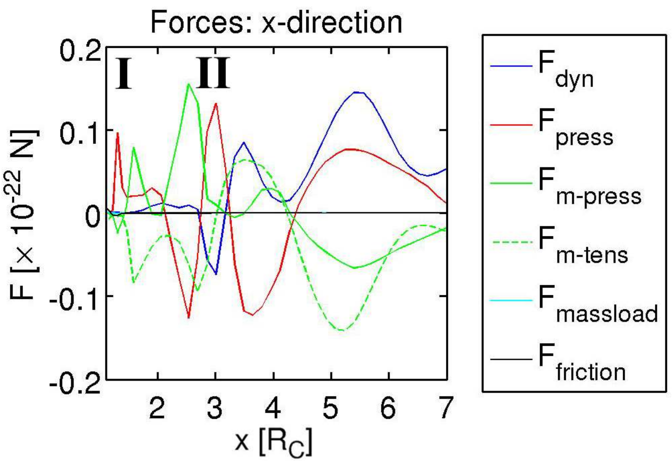

Figure 3.21: *Dynamic (F_{dyn}), thermal pressure (F_{press}), magnetic pressure ($F_{m\text{-}press}$) and magnetic tension forces ($F_{m\text{-}tens}$) in 10^{-22} N acting in the x-direction along the plasma tail center at x, $y = 0$. Mass loading ($F_{massload}$) and frictional forces ($F_{friction}$) are too weak to give apparent curves. Note that an exact force balance is not given due to uncertainties in the interpolation of the simulation results and the artificial viscosity term in ZEUS-MP. However, the displayed quantities do not change significantly for simulations without an artificial viscosity term. See text for the significance of the regions labeled by roman numbers.*

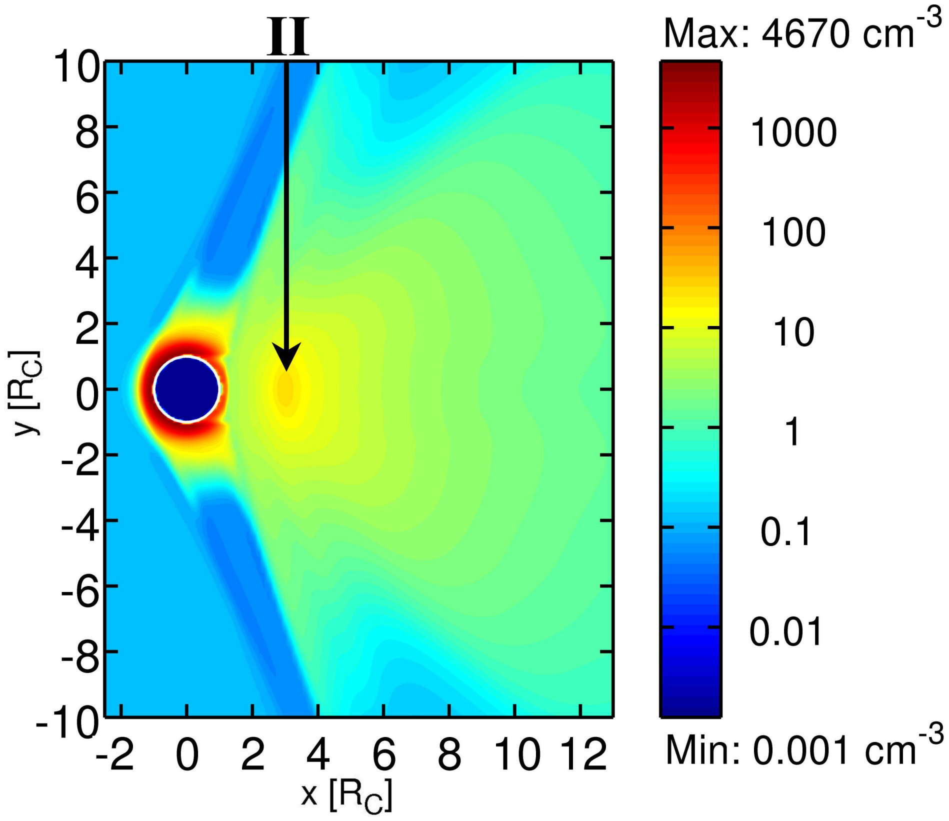

Figure 3.22: *Number densities n of the plasma flow in cm^{-3} (logarithmic scale) in the xy-plane at $z = 0$ for a variation of the $\alpha_{\odot} = 270°$ scenario with $k_B T_0 = 635$ eV. The white circle indicates the surface of Callisto. See text for the significance of the region labeled with II.*

Figure 3.23 depicts a close up view of the velocity streamlines of the tail plasma flow in the xz-plane. At the accumulation point II the plasma is not only redirected in the y- and z-direction but also in the negative x-direction. Figure 3.21 indicates two regions where the thermal pressure term acts in this direction (at $x \approx 2.5$ R$_C$ and $x \approx 3.5$ R$_C$). Downstream of region II ($x \approx 3.5$ R$_C$) the thermal forces are compensated by dynamic forces and the magnetic tension. Nevertheless, it is intriguing that the flow is still directed away from the satellite in this region. Upstream ($x \approx 2.5$ R$_C$) the dynamic pressure of the plasma does not oppose the thermal forces and the magnetic tension. Here the magnetic pressure completes the force balance. The plasma flow is directed towards Callisto in this region. An explanation for this behavior might be that the dynamic pressure of the ionospheric plasma between region I and region II is too low to oppose the deflected tail plasma flow as it gains only little momentum from the magnetospheric plasma. In region I close to Callisto the ionospheric plasma densities and therefore the thermal pressure are high enough to stop the tail flow from reaching the surface. Due to the low plasma velocities at region I a third accumulation point for the plasma arises. Between the upstream tail flow and the northern and southern ionospheric flow regions two eddy structures form (region IV in Figure 3.23). At the surface of these eddies plasma particles are again transported towards the northern and southern ionospheric plasma flow and are eventually fed into the tail.

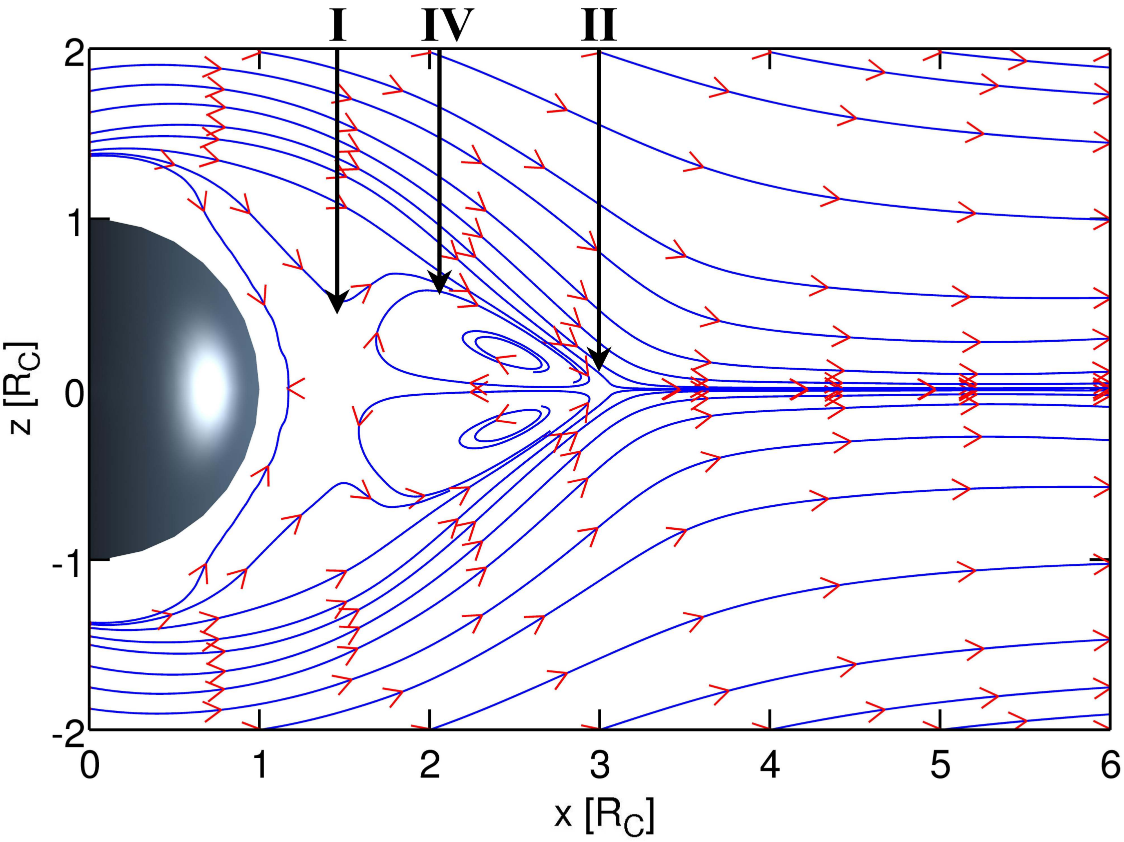

Figure 3.23: *Velocity streamlines (blue) and flow directions (red arrow heads) in Callisto's tail in the xz-plane at* $y = 0$ *for the* $\alpha_\odot = 270°$ *scenario. Callisto's surface is indicated by the dark sphere. See text for the significance of the regions labeled by roman numbers.*

The upstream flow between regions I and II is not only confined to the location where the ionospheric plasma merges, but also extends along the Alfvén characteristics downstream of the actual Alfvén wings. Figure 3.24 depicts a 3D representation of all regions where v_x is negative for both the $\alpha_\odot = 270°$ standard scenario and the comparative simulation with $k_B T_0 = 635$ eV. The most prominent features for the standard scenario (upper panel) are regions with $v_x < 0$ in the inner parts of the two Alfvén wings. These features do not occur for the comparative simulation depicted in the lower panel of Figure 3.24. However, similar regions may still be present but not associated with negative velocities. In both cases we see regions of negative velocities in the tail which are mainly confined to the xy-plane. The Alfvén wings are obviously affected by these disturbed tail regions. A similar pattern to the one visible in the cross section of the anti-Jovian wing can also be seen in the magnetic field depicted in Figure 3.15. One hint why the Alfvén wings are not as strongly affected for the $k_B T_0 = 635$ eV case might be that the negative velocities in the tail with a maximum of -3.3 km s^{-1} are nearly five times lower than the value of -15 km s^{-1} obtained for the standard simulation. These velocities are reached nearly throughout the entire interior of the disturbed tail region. For the standard scenario the negative velocities are nearly doubled with respect to values in the inner parts of the Alfvén wings. One hint for the interaction between the Alfvén wings and the tail velocity patterns is that both regions are actually connected. Figure 3.13 also shows an apparent overlap of the two regions.

The disturbances for the density in the $k_B T_0 = 635\ eV$ case depicted in Figure 3.22 spread out in the initial phase of the simulation with a velocity which is close to the speed of sound. The magnetic perturbations in the tail for both simulations spread with a velocity close to the Alfvén speed. The fact that the disturbances travel along the direction of the Alfvén characteristics additionally suggests that both slow mode and shear Alfvén waves are triggered in the tail region. The generation of magnetic disturbances is also apparent for the magnetic field lines in the xy-plane of the tail given in Figure 3.25. Along the x-direction the magnetic field lines are initially relatively smooth when they exit Callisto's body. This is caused by the strong diffusion term in the interior. Near region I, however, the upstream plasma flow leads to over-stretched field lines close to Callisto. Further downstream the field lines relax. Downstream of region II, where the inner tail plasma is finally accelerated in the x-direction, the centers of the field lines overshoot in the y-direction. This leads to an oppositely directed magnetic tension which again stretches the field lines in the $-x$-direction. This tail process is apparently an effective generator for Alfvén waves which show as secondary wing structures in Figure 3.13.

The detection of regions where the tail plasma velocity is directed in the opposite direction to the magnetospheric plasma flow has, so far, not been reported in the peer review literature for the plasma interaction of any satellite. Therefore, the plausibility of these unexpected features occurring in all our simulations can not be conclusively verified. We performed several diagnostic simulations to rule out a numeric cause for the tail disturbances. Among these were tests with different resolutions, without resolution or processor boundaries in the tail region, without an additional artificial viscosity term and with different initial setups for the plasma parameters. However most of these simulations yield similar tail features. The only exception were simulations without mass loading by the neutral atmosphere (but with collisions). This suggests that the convergence point of the

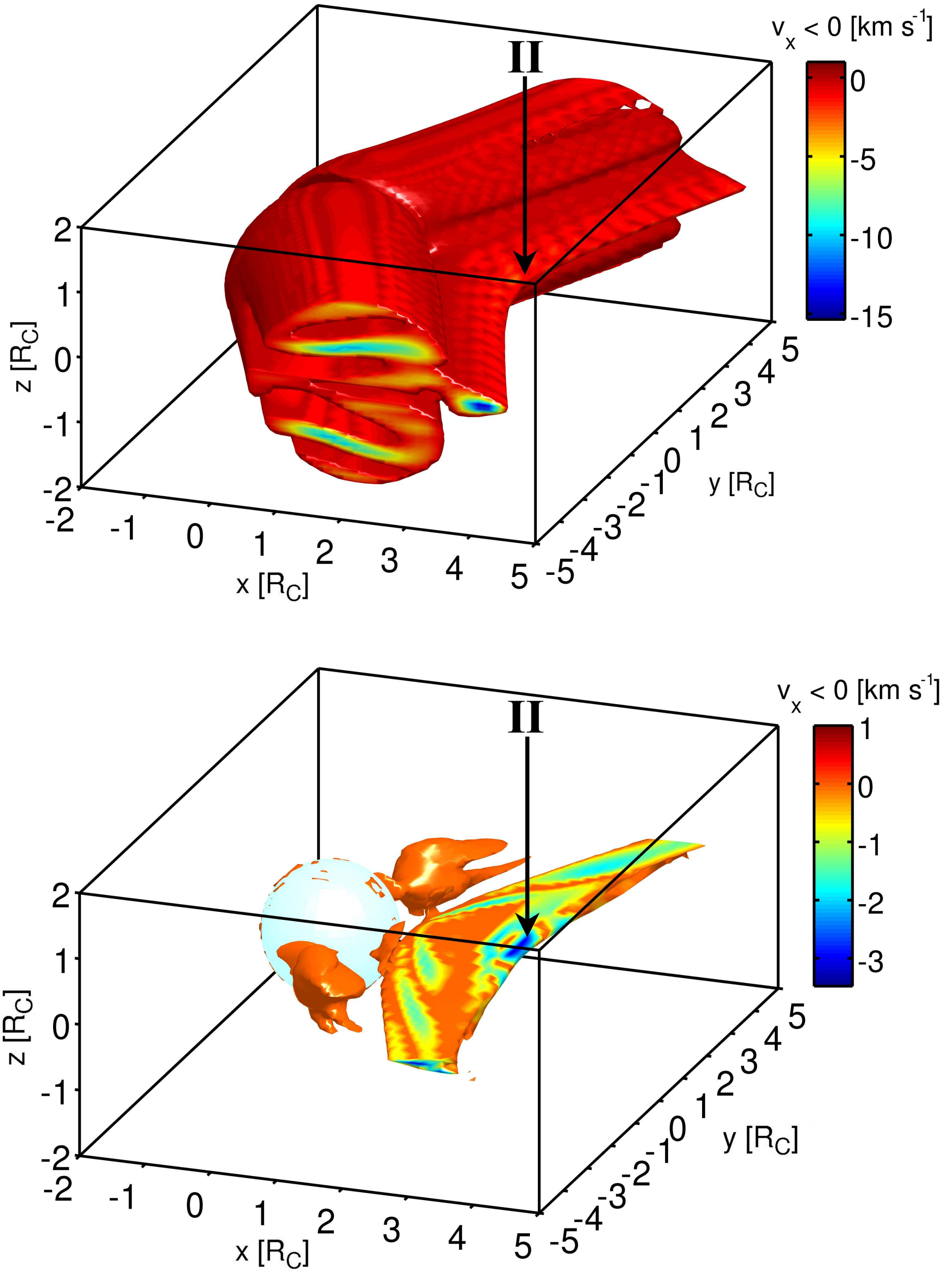

Figure 3.24: *3D iso-surface representing regions where $v_x < 0$ for the $\alpha_\odot = 270°$ standard scenario (upper panel) and a comparative simulation with $k_B T_0 = 635$ eV (lower panel). Color encoded: negative plasma velocities in km s^{-1}. Note that the apparent textures on top of the 3D surfaces are due to the finite resolution of the simulation. Arrows indicate the location of the accumulation point II (see text). The blue sphere represents the surface of Callisto.*

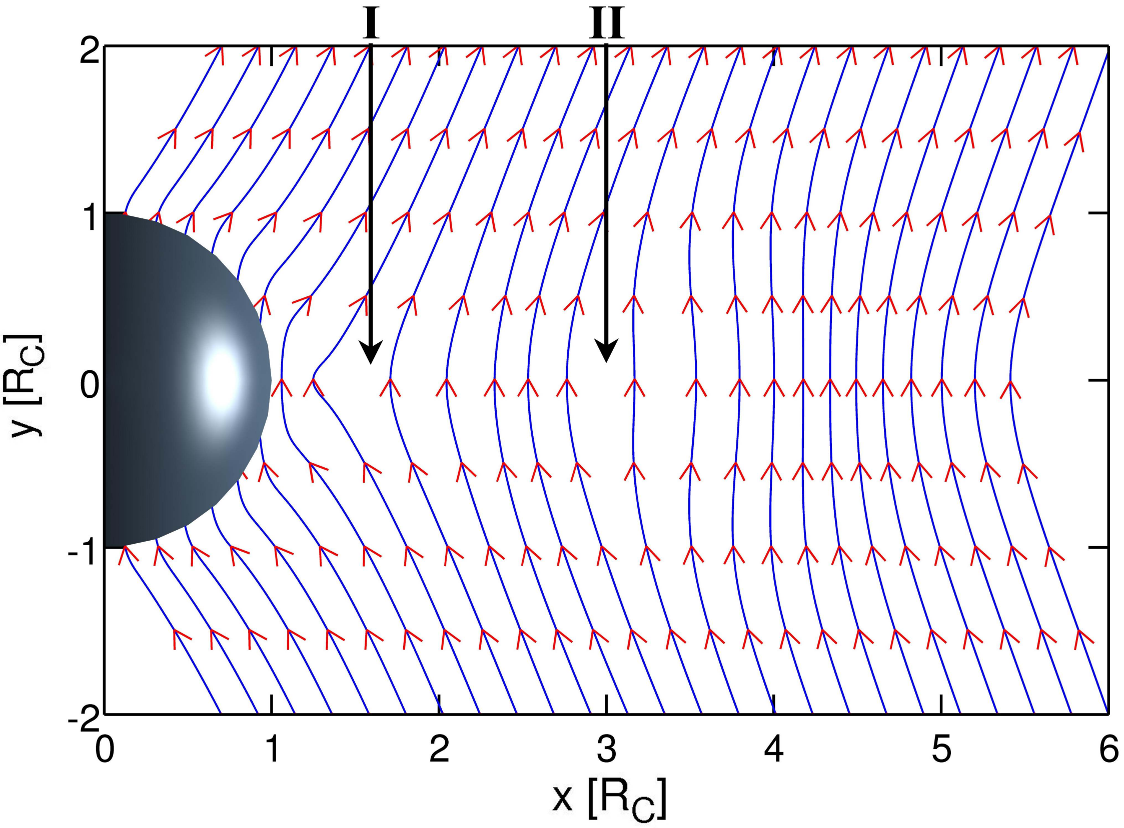

Figure 3.25: *Magnetic field lines in Callisto's tail in the xy-plane at $z = 0$ for the $\alpha_\odot = 270°$ scenario. Red arrow heads indicate the direction of the field. Callisto's surface is indicated by the dark sphere. See text for the significance of the regions labeled by roman numbers.*

southern and northern ionospheric plasma flows is indeed the generation region for the tail disturbances. It should be noted that simulations for Europa carried out using the ZEUS-MP by *Schilling* (2006) gave similar tail features. They further occurred for ZEUS-MP simulations of cometary plasma interactions. To ultimately rule out a numerical nature of the tail disturbances comparative studies using other simulation codes are inevitable. A more detailed analysis of the forces generating these features may give additional hints for the plausibility of the results presented in this section.

3.3.2 Neutral atmosphere and ionosphere

After this general discussion of Callisto's plasma interaction we now analyze the predicted ionospheric densities arising for standardized models assuming different solar phase angles $\alpha_\odot$ and different setups for Callisto's neutral atmosphere. Further, the simulation results for the C9, C22 and C23 default flyby scenarios are compared to the electron density profiles presented by *Kliore et al.* (2002). The main goal of this analysis is to explain the temporal variabilities of the ionospheric densities observed for different values of $\alpha_\odot$ at the flanks of Callisto, i.e along altitude profiles at $x, z \approx 0$. The wave path of the radio signal which gives the electron column densities underlying the derived density profiles for the respective entry and exit cases (see Figure 3.1) is essentially the same for all measurements. The two key aspects which may lead to differences in the observed densities are the overall amount of ionospheric particles generated by ionization and the redistribution of the ionospheric plasma by transport processes.

Three hypothesis may be raised to explain the absence of a substantial ionospheric layer for the C9 flyby with respect to these key aspects. First, the electron densities at the flanks may be increased due to the transport of ionospheric particles primarily generated at the upstream hemisphere for the $\alpha_\odot \approx 270°$ case, corresponding to the C22 and C23 flyby scenarios. For a sunlit downstream hemisphere the plasma might be redistributed along Callisto's tail instead. In this case the ionosphere would still be present for both solar illumination geometries but the measurements at the flanks would give lower densities for C9 or $\alpha_\odot \approx 90°$. Secondly, for a sputtering generated asymmetric atmosphere and an ionosphere which is primarily generated by photo ionization the overall ionospheric density is significantly lower if only the downstream hemisphere is sunlit. The transport of the upstream high density plasma in the $\alpha_\odot \approx 270°$ case could then lead to large differences in the amount of electrons observable at the flanks. Thirdly, a decreased solar flux and different magnetospheric conditions for the C9 flyby may yield a lower overall ionospheric density and decrease the particle flux towards the flanks. Apart from these hypothesis we investigate if the redistribution of the ionospheric plasma in the case of a pure CO_2 atmosphere may explain the observed densities without the additional assumption of an O_2 atmospheric constituent. Further, we analyze the total amount of plasma generated in Callisto's vicinity through ionization and lost due to transport and recombination processes. We start with an analysis for the standardized simulation setups which give directly comparable results for different solar phase angles and different atmospheric configurations. The actual flyby cases are discussed in Section 3.3.2.2.

3.3.2.1 Solar phase angle and atmospheric configurations

To analyze the ionospheric configuration arising for varying solar illumination geometries and due to different assumptions for the shape and composition of the neutral atmosphere, several diagnostic parameters can be used. First, we can directly analyze the plasma densities for our standard simulation scenarios with $\alpha_\odot = 270°$ and $\alpha_\odot = 90°$, variations of these setups assuming a pure CO_2 atmosphere and for asymmetric atmospheric setups (defined in Section 3.2.2) displayed in Figure 3.26. For comparison, Figure 3.27 further depicts the results for the $\alpha_\odot$ = 0° and $\alpha_\odot$ = 180° standard scenarios. To assess the three hypothesis raised in the previous paragraph one can compare the maximum densities and the overall density distribution obtained in the simulations. Note, however, that the absolute maximum electron densities within the entire simulation regime are not directly comparable to the *Kliore et al.* (2002) data. Therefore, we additionally present column density profiles above the sub-Jovian point in Figure 3.28. The respective profiles are obtained by an integration along the x-direction on the Jupiter facing flank of Callisto i.e., for height profiles at x, $z = 0$ starting at $y = \mathrm{R}_C$. A further diagnostic tool for the generation of the ionospheric layers are the values for the volume integrated particle production and loss frequencies given in Table 3.6. We integrate over a cube V' spanning ±3 R_C from Callisto's center to obtain the total amount of particles per second which are produced by photo and impact ionization for the two neutral species, the particles lost due to recombination and the total flux of particles from V' using the divergence theorem. Note that the discrepancies which arise from summing all production and loss processes listed in Table 3.6 occur as the additional loss term in Callisto's interior is not considered here.

For a symmetric combined CO_2 and O_2 atmosphere the maximum densities within the total simulation regime are decreased by only ~4% for $\alpha_\odot$ = 90° with respect to the $\alpha_\odot$ = 270° standard scenario (upper two panels in Figure 3.26). Obviously, a significant ionospheric layer forms even if the upstream hemisphere of Callisto is not sunlit. As expected, the regions with the highest ionospheric densities are shifted from the upstream hemisphere for $\alpha_\odot$ = 270° to the downstream hemisphere for $\alpha_\odot$ = 90°. However, for both simulations a comparable total amount of ionospheric particles are created by photo and impact ionization (Table 3.6). Surprisingly, the plasma densities in the downstream hemisphere for $\alpha_\odot$ = 270° are rather high ($> 1,000$ cm^{-3}). One might suspect that almost no particles are produced by impact ionization in this region. However, Figure 3.18 illustrates that the relevant magnetospheric electrons actually accumulate in the downstream hemisphere. Note that the impact ionization frequencies depend on the temperature of the electrons rather than on the low bulk velocity in this region. Figure 3.29 shows that due to this accumulation the impact ionization frequencies in the downstream hemisphere are enhanced with respect to the upstream conditions. The maxima for both ionization

	Atmosphere	Symmetric				CO_2		Asymmetric	
	$\alpha_\odot$	270°	90°	0°	180°	270°	90°	270°	90°
$\int P_{\mathrm{pho},CO_2} \mathrm{d}V'$	[$\times 10^{26}$ s^{-1}]	0.70	0.70	0.70	0.70	0.70	0.70	0.56	0.40
$\int P_{\mathrm{pho},O_2} \mathrm{d}V'$	[$\times 10^{26}$ s^{-1}]	5.71	5.71	5.71	5.71	-	-	4.90	3.44
$\int P_{\mathrm{imp},CO_2} \mathrm{d}V'$	[$\times 10^{26}$ s^{-1}]	0.16	0.15	0.16	0.16	0.26	0.23	0.12	0.13
$\int P_{\mathrm{imp},O_2} \mathrm{d}V'$	[$\times 10^{26}$ s^{-1}]	1.50	1.41	1.46	1.47	-	-	1.57	1.12
$\int L \mathrm{d}V'$	[$\times 10^{26}$ s^{-1}]	-7.42	-7.17	-7.39	-7.40	-0.14	-0.12	-6.47	-4.50
$\int \nabla \cdot (n\mathbf{v}) \mathrm{d}V'$	[$\times 10^{26}$ s^{-1}]	-0.06	-0.05	-0.05	-0.05	-0.06	-0.31	-0.05	-0.04
n_{max}	[cm^{-3}]	5,645	5,391	5,416	5,459	4,506	4,469	5,650	4,213

Table 3.6: *Particle balance for several atmospheric setups and solar phase angles for a volume V' defined by a cube spanning ±3 R_C. Given is the amount of plasma particles produced by photo and impact ionization, lost by recombination and the net flux out of V' per second. The last row lists the maximum plasma densities in cm^{-3} within V' for comparison. Note that the above rates do not exactly sum up to zero as particles are additionally lost at Callisto's surface.*

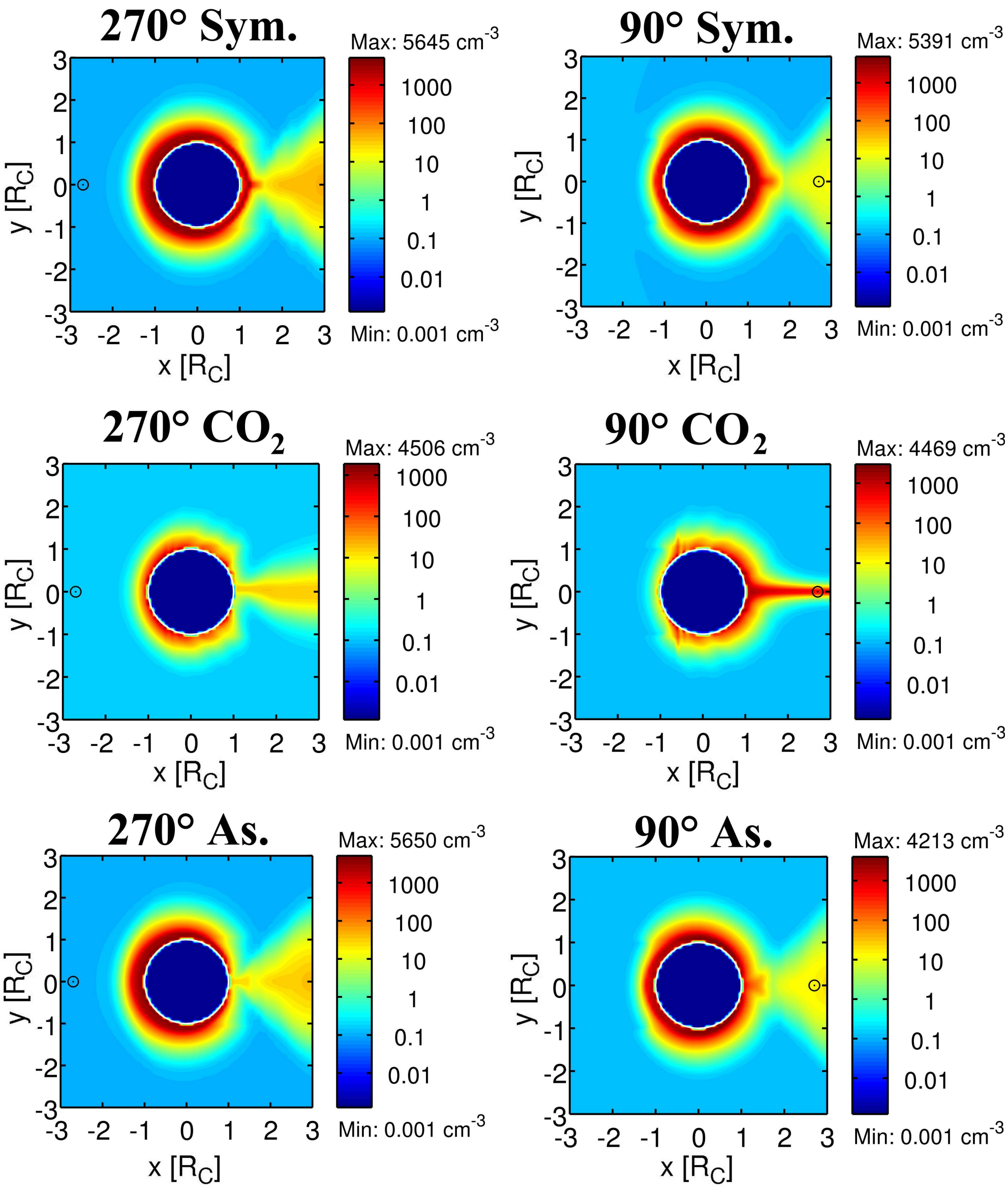

Figure 3.26: Plasma densities n in cm^{-3} (logarithmic scale) in the xy-plane at $z = 0$ for the $\alpha_\odot = 270^\circ$ and $\alpha_\odot = 90^\circ$ scenarios for a symmetric $CO_2 + O_2$ atmosphere (upper panels), a symmetric pure CO_2 atmosphere (center) and an asymmetric $CO_2 + O_2$ atmosphere (lower panels). The location of the Sun with respect to Callisto's center is denoted by the symbol ⊙. The white circles indicate the surface of Callisto.

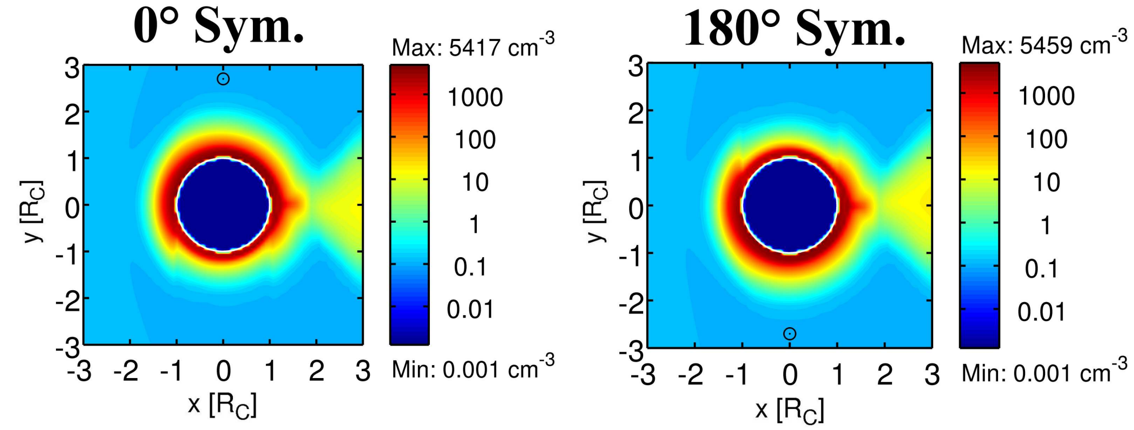

Figure 3.27: *Plasma densities n in cm^{-3} (logarithmic scale) in the xy-plane at $z = 0$ for the $\alpha_\odot = 0°$ and $\alpha_\odot = 180°$ standard models for a symmetric $CO_2 + O_2$ atmosphere. See Figure 3.26 for further explanations.*

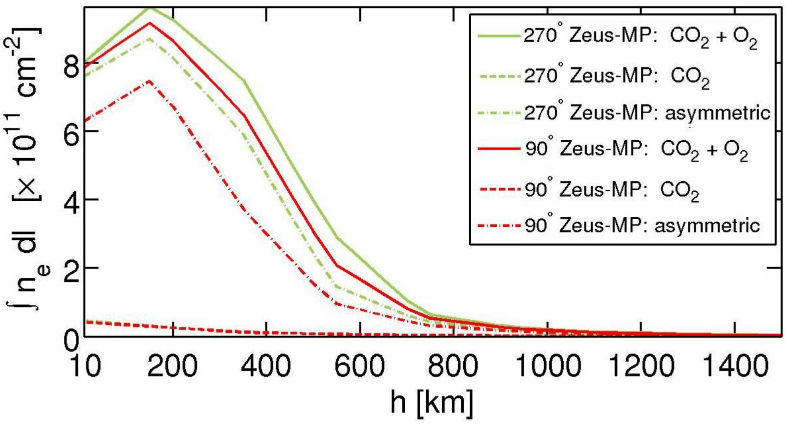

Figure 3.28: *Electron column densities in 10^{11} cm^{-2} at the Jupiter-facing flank of Callisto (x, $z = 0$) for various atmospheric setups (different line styles) for $\alpha_\odot = 270°$ (green) and $\alpha_\odot = 90°$ (red). The line of sight for the integration was assumed to be parallel to the x-axis.*

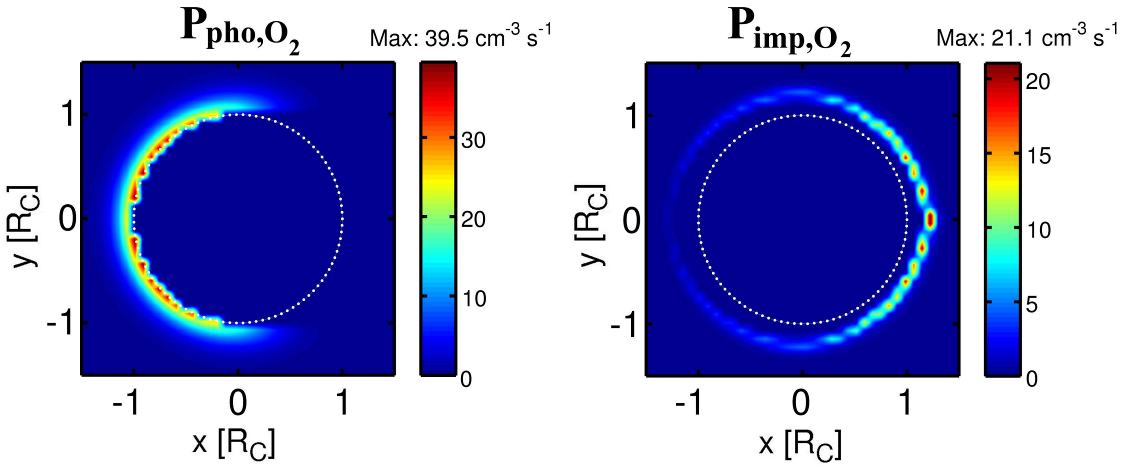

Figure 3.29: *Photo and impact ionization rates for O_2 (P_{pho,O_2} and P_{imp,O_2}) in cm^{-3}s^{-1} for the $\alpha_\odot = 270°$ standard scenario in the xy-plane at $z = 0$. The dotted circle indicates the surface of Callisto.*

frequencies suggest that photo ionization dominates by a factor of 1.8 instead of the analytically deduced value of 3 (Section 3.2.2.3). Still, the total amount of particles generated by photo ionization is four times larger (Table 3.6), emphasizing the crucial role of photo ionization at Callisto. The amount of ionospheric particles flowing out of the test volume V' is about two orders of magnitude lower than the loss due to recombination. In other words, the loss of ionospheric plasma due to the acceleration of the particles caused by momentum exchange with the background plasma is insignificant with respect to the other production and loss processes. No considerable differences in the plasma outflow arise for different solar phase angles. Further, the column density profiles for a symmetric atmosphere show only a slight increase of ~2% for $\alpha_\odot = 270°$ (solid lines in Figure 3.28). This suggests that only a small amount of particles primarily ionized at the upstream hemisphere for $\alpha_\odot = 270°$ is actually transported towards the flanks and that very few particles are swept out of Callisto's ionosphere. These results suggest that substantial and comparable ionospheric layers should be present and detectable regardless of the solar phase angle. In other words, the hypothesis that the redistribution of the ionospheric plasma by transport processes alone causes the observed temporal ionospheric variabilities does not hold. Still, the transport of ionospheric particles may to a small extent contribute to the discrepancies in the measured electron densities for different solar phase angles.

The additional results for the $\alpha_\odot = 0°$ and $\alpha_\odot = 180°$ standard scenarios show that the inferred values of the maximum densities and for the particle balance change gradually between the two previously discussed cases (Table 3.6). The only notable difference between the two intermediate cases themselves is the geometry of the generated ionosphere (Figure 3.27).

At first glance, the result that transport only plays a minor role for the distribution of Callisto's ionosphere also seems to be reflected by the lack of deviations in the column density profiles for both solar phase angles obtained for a pure CO_2 atmosphere (dashed lines lying on top of each other in Figure 3.28). However, the maximum densities obtained for both values of $\alpha_\odot$ are only decreased by ~25% with respect to the values for a combined CO_2 and O_2 neutral atmosphere (central panels in Figure 3.26). The neutral densities for CO_2 ($n_{CO_2,0} = 4 \times 10^8$ cm^{-3}) are ~18 times lower than the assumed O_2 densities ($n_{O_2,0} = 7 \times 10^9$ cm^{-3}). These two facts suggests that the transport of ionospheric particles contributes substantially to the generation of the simulated ionospheric layers for a pure CO_2 atmosphere. Further, for the CO_2, $\alpha_\odot = 90°$ scenario the flow of particles out of the test volume V' increases by a factor of about five with respect to all other simulations (Table 3.6). For both CO_2 setups the relative discrepancy in the sum of produced and lost particles of 0.5 to 0.75×10^{26} s^{-1} is remarkably high. This indicates that a large amount of particles is lost at Callisto's surface. Note that the implementation of Callisto's interior in our model affects the density structure close to the satellite for the pure CO_2, $\alpha_\odot = 90°$ scenario (right central panel of Figure 3.26). Due to this presumably unphysical features, the obtained results should only be interpreted with great caution. Still, the above facts indicate that particle transport becomes increasingly relevant for lower atmospheric neutral densities. The reason for this behavior is that the magnetospheric plasma is not as efficiently decelerated by Callisto's atmosphere and affects the ionosphere more directly by momentum exchange and pressure forces. This is also reflected by the increased impact ionization rates for CO_2 of ~0.25×10^{26} s^{-1} with respect to the values of

~0.16×10^{26} s^{-1} reached for the standard scenarios. These values indicate that the magnetospheric electrons penetrate the pure CO_2 atmosphere more effectively. In the range of possible atmospheric setups, a pure CO_2 atmosphere represents the lower limit for the atmospheric densities and therefore the upper limit for the possible control of the ionospheric plasma by transport processes. Figure 3.26 shows that the ionosphere is much more confined close to the satellite for this atmospheric setup. Consequently, the column densities obtained by integration along the x-direction are much too low to explain the *Kliore et al.* (2002) profiles (Figure 3.28). This confirms that the observed CO_2 neutral densities are not sufficient to generate ionospheric electron densities in agreement with the radio occultation measurements, regardless of potential transport processes. However, intermediate cases with lower O_2 abundances but with a more effective plasma transport could generate sufficient peak densities at Callisto's flanks. Unfortunately, due to the increased neutral scale heights within our model we can not predict the actual amount O_2 particles necessary to generate the observed profiles.

The largest deviations in both the column density profiles and the total density maxima for different solar angles are given for an asymmetric combined CO_2 and O_2 neutral atmosphere. The decrease of ~26% in the total maximum for $\alpha_\odot = 90°$ is a consequence of the lack of ionized neutral particles in the downstream hemisphere (lower two panels in Figure 3.26). Note that the asymmetric setup chosen here not purely confines the atmosphere to the upstream hemisphere. Therefore, the deviations in the total amount of particles produced by ionization are only moderate (Table 3.6). While the maximum density of 4,213 cm^{-3} for $\alpha_\odot = 90°$ is even lower than for the pure CO_2, $\alpha_\odot = 90°$ scenario (4,469 cm^{-3}) the overall ionospheric structure is much less compressed. Therefore, the column densities at the flanks are much higher and more realistic for an asymmetric atmosphere (Figure 3.28). At the same time the deviations in the profiles for both values of $\alpha_\odot$ (~5% to 10%) are larger than for the comparative simulations with a symmetric atmosphere (~2%). However, the respective electron column densities are still high enough to allow a detection of the ionospheric layer for both solar illumination geometries. The hypothesis that the variability of the ionosphere could be caused by a neutral atmosphere generated by sputtering is therefore partially confirmed. A vanishing ionosphere for a sunlit downstream hemisphere, however, can not be explained by both of the hypothesis discussed so far. We now turn to the actual flyby scenarios and examine the hypothesis that the temporal variations could be caused by differences in the solar flux or the ambient plasma properties, keeping in mind the results obtained so far.

3.3.2.2 Data comparison for the ionospheric densities

A similar analysis as for the standard scenarios in Section 3.3.2.1 can be performed for the model results of the C9, C22 and C23 default flybys scenarios. For these encounters electron density profiles were deduced by *Kliore et al.* (2002) from Galileo radio occultation measurements (see Section 3.1.1). Note that we omit the radio occultation measurements for the C20 case here as no magnetometer and plasma parameter data necessary for our model setup were recorded during this flyby. The *Kliore et al.* (2002) electron density profiles were obtained by interpreting the electron column densities inferred from the modulated radio transmissions as integrated densities caused by a radially symmetric ionosphere. In order to directly compare our model ionospheres to the data, we choose to reconstruct the underlying column densities by integrating along the radio wave path through a radial symmetric ionosphere defined by the respective density profiles. Note, however, that we assumed the wave path to be a straight line towards the location of the Earth and neglected wave refractions. Only the cases which correspond to the entry phase of the occultation measurements are discussed here, as they contain the most substantial ionospheric signals. We briefly note differences for the C9 exit case below, but refrain from discussing the potential reasons for the decreased electron densities during the C22 and C23 exit phases. To account for the error bars given for each observation, a similar procedure was applied for profiles given by a polynomial fit to the minimum and maximum error bar values. The resulting electron column density profiles at Callisto's flank are displayed as red curves in Figure 3.30 for each of the three flybys. For C9 the maximum error bar profile is given by the dashed red curve while the fit minimum values are displayed for C22 and C23.

The profiles can be compared to the integrated electron density of our simulation results given by the green curves, where the line styles depict different setups for the atmosphere. However, as the scale height in our models was increased by the factor $H_{\mathrm{rel}} = 10$, the simulation results are almost constant within the given altitude range. To allow for a better comparison we choose to rescale the x-axis for the simulation results (upper green axes in Figure 3.30) with H_{rel}^{-1}. One should bear in mind, that these results are, strictly speaking, not directly comparable to the data and should not be taken as realistic column density profiles for the Callisto case. Instead, they should be interpreted as indicators for the behavior of a Callisto-like ionosphere under different ambient conditions and for different atmospheric configurations. A more direct comparison is possible for the two blue profiles which illustrate analytic calculations of the ionospheric densities for a chemical equilibrium state between ionization and recombination processes. For these calculations we applied our aeronomic models for the relevant processes presented in Section 3.2.2 to an atmosphere with a realistic scale height and surface density. The photo ionization rates were calculated in a similar way as the values used for our MHD model. For the impact ionization we assumed homogeneous magnetospheric electron densities using the initial values $n_{e,ms,0}$ for each flyby (n_0 in Table 3.5) and applied Equations (3.31) to (3.34). Solving the expression $P = L$ for the density allows to compute the equilibrium values for a static ionosphere (neglecting transport processes) at arbitrary locations. Integration along the defined wave path gives the desired column densities for a pure CO_2 atmosphere (blues dashed line in Figure 3.30) or for both atmospheric species (blue solid line).

In analogy to the analysis presented in Section 3.3.2.1, Figure 3.31 and Table 3.7 give the ionospheric densities for the default atmospheric setup in the xy-plane and the values for the particle balance for all flyby scenarios and atmospheric setups within ±3 R_C. Qualitatively, the distribution of the ionospheric densities is very similar to the results given in the previous section. Therefore the density patterns for the pure CO_2 and asymmetric atmospheres are not given here. It should, however, be noted that Callisto's plasma tail exhibits a much more asymmetric structure for the flyby scenarios, primarily due to the different orientations of the background magnetic field.

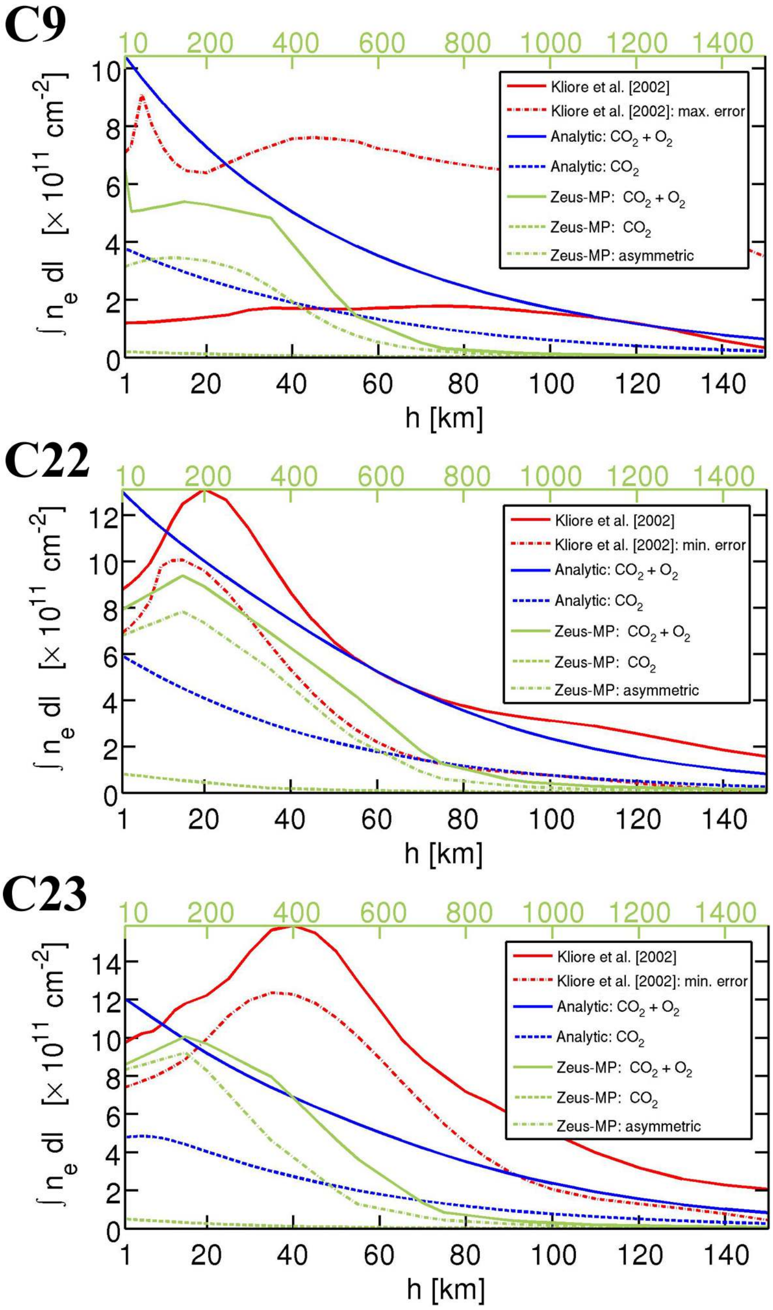

Figure 3.30: *Electron column densities in* 10^{11} cm^{-2} *for three Galileo flybys at Callisto. The red solid curve represents the column densities for a radial symmetric ionosphere defined by a fit to the Kliore et al. (2002) electron density profiles. The red dashed curves were calculated for density profiles fit to the Kliore et al. (2002) maximum (C9) or minimum (C22, C23) error bar values. The blue profiles for a combined* O_2 *and* CO_2 *(solid lines) and a pure* CO_2 *atmosphere (dashed lines) result from analytic calculations using the aeronomic models presented in Section 3.2.2, assuming an ionosphere in chemical equilibrium (*$P = L$*). The green curves represent profiles deduced from our flyby scenarios for three different atmospheric setups. The upper x-axis gives the height above the surface in km for the simulations while the lower x-axis corresponds to the other profiles.*

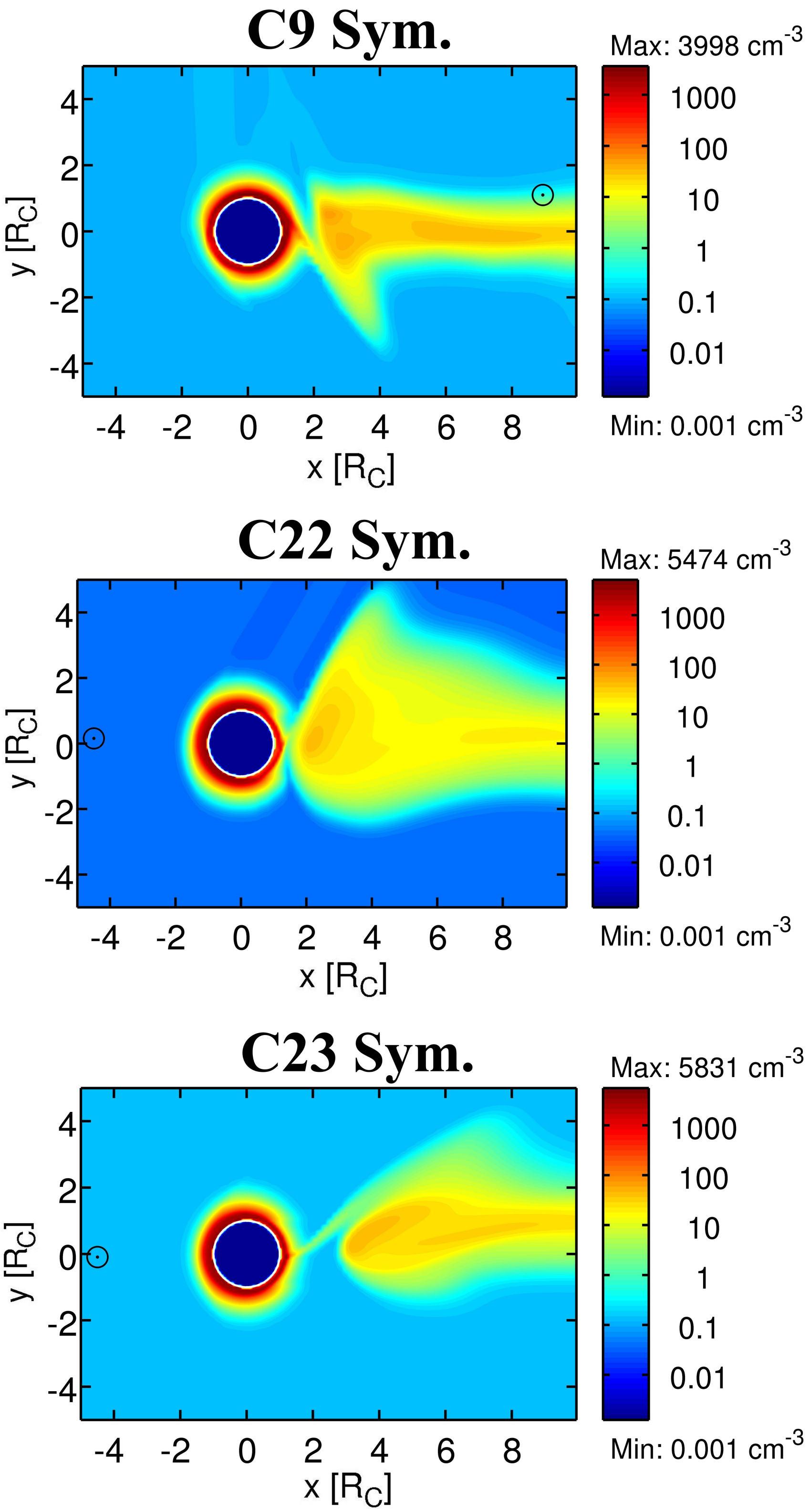

Figure 3.31: *Plasma densities n in cm^{-3} (logarithmic scale) in the xy-plane at $z = 0$ for the C9, C22 and C23 default flyby scenarios. The symbol ⊙ indicates the location of the Sun with respect to the center of Callisto. The setup for the neutral atmosphere is symmetric and includes both O_2 and CO_2 particles for all depicted scenarios. Callisto's surface is indicated by white circles.*

	Flyby	C9 ($\alpha_\odot$ = 83°)			C22 ($\alpha_\odot$ = 272°)			C23 ($\alpha_\odot$ = 269°)		
	Atmosphere	Sym.	CO_2	Asym.	Sym.	CO_2	Asym.	Sym.	CO_2	Asym.
$n_{\max,Kliore}$	[cm^{-3}]		$< 5,000$			$15,300$			$17,400$	
$n_{\max}$	[cm^{-3}]	$3,998$	$3,411$	$2,632$	$5,474$	$4,694$	$5,459$	$5,831$	$5,050$	$5,601$
$\int P_{\text{pho},CO_2}\mathrm{d}V'$	[$\times 10^{26}$ s^{-1}]	0.38	0.38	0.22	0.70	0.70	0.56	0.74	0.74	0.60
$\int P_{\text{pho},O_2}\mathrm{d}V'$	[$\times 10^{26}$ s^{-1}]	3.18	-	1.92	5.71	-	4.91	6.04	-	5.19
$\int P_{\text{imp},CO_2}\mathrm{d}V'$	[$\times 10^{26}$ s^{-1}]	0.13	0.10	0.14	0.03	0.09	0.03	0.19	0.30	0.19
$\int P_{\text{imp},O_2}\mathrm{d}V'$	[$\times 10^{26}$ s^{-1}]	1.25	-	1.21	0.27	-	0.26	1.77	-	1.79
$\int L\mathrm{d}V'$	[$\times 10^{26}$ s^{-1}]	-4.65	-0.04	-2.56	-6.37	-0.11	-5.15	-8.33	-0.11	-7.28
$\int \nabla \cdot (n\mathbf{v})\mathrm{d}V'$	[$\times 10^{26}$ s^{-1}]	-0.06	-0.21	-0.05	-0.05	-0.04	-0.04	-0.05	-0.05	-0.04

Table 3.7: *Particle balance for the C9, C22 and C23 flyby scenarios, assuming different atmospheric setups. The first row gives the peak electron densities presented by Kliore et al. (2002). Differences with respect to the obtained maximum ionospheric densities in our simulations are mainly due to the increased scale height in the model. See Table 3.6 for comparison and additional information.*

The maximum densities in the simulation regime for the different flybys given in Figure 3.31 indicate that Callisto's ionosphere is much less established for the C9 scenario. The deviations with respect to the other flyby scenarios of up to 30% are considerably larger than for the comparative standard scenarios, where variations of ~5% can be attributed to the differences in $\alpha_\odot$. The differences in the amount of particles created by photo ionization given in Table 3.7 indicate that the main reason for these large variations is the solar photon flux which was ~50% lower during the C9 encounter (see Table 3.3). However, the respective values are still high enough to create a distinct ionospheric layer in the C9 simulations. Additionally, impact ionization generates a substantial amount of particles for the C9 default flyby scenario. The corresponding rates given in Table 3.7 mainly depend on the magnetospheric electron density which is comparatively low for C22 (0.04 cm^{-3}), high for C23 (0.14 cm^{-3}) but at an intermediate level for C9 (0.06 cm^{-3}, see Table 3.5). These values are manifestations of the different locations of Callisto with respect to the center of the current sheet. For C22 the distance to this center of $z_{cs} = -4.31$ R$_J$ was the largest for all flybys of Galileo while the C23 case occurred very close to magnetic equator at $z_{cs} = 1.08$ R$_J$ (see Table 3.1). The actual measured plasma densities for C23, which themselves are rather uncertain, instead suggest a relatively low value for the background density of 0.05 cm^{-3}. This illustrates that the conditions for the background plasma can vary over a broad range and present additional uncertainties to the results obtained from our simulations.

Despite of the decreased photo ionization rates, the column densities for a symmetric CO_2 and O_2 atmosphere given for C9 in Figure 3.30 (green solid line) lie well above the profile inferred from the *Kliore et al.* (2002) results. A small amount of the deviations of the C9 profile with respect to the C22 and C23 profiles also occurs due to the ray path which to some extent lies within Callisto's shadow for the C9 entry case (see Figure 3.1). The corresponding values for the C9 exit phase (not shown here), which took place at the flank of Callisto which was more affected by the solar radiation, show even stronger deviations from the measurements. The upper limit given by the maximum error profile is still matched for the default atmospheric setup in the C9 entry case. However, the decreased neutral densities at the surface for our simulations create artificially low column densities. For that reason, the results for C9 using a default atmospheric setup should not be interpreted as a vanishing ionosphere. On the other hand, the resulting column densities for C22 and C23 and a symmetric two species atmosphere lie close to or slightly below the profile obtained for the minimum error values. The remaining differences can be primarily attributed to the decreased scale height in our model.

The analytically derived profiles for a symmetric combined CO_2 and O_2 atmosphere were derived for a realistic atmospheric scale height. A comparison with the measured profiles also gives no hint for a vanishing ionosphere in the C9 case. Even though the column densities are again decreased due to the low solar photon flux, the profile exceeds the maximum error in this case. The respective profile for C22 instead gives a rather good fit to measured data. This suggests that the assumed photo and impact ionization rates and neutral densities, indeed, present a good approximation for the generation of Callisto's ionosphere, though the deviations to the C23 measurements are rather large. A pure CO_2 atmosphere which corresponds to a lower surface neutral density yields no adequate representation of the measured profiles both for the analytically derived values and for the corresponding simulation scenarios. Apart from the decreased scale height, the deviations between the analytic calculations and the simulation results may be caused by plasma transport processes (mainly for a pure CO_2 atmosphere, see Section 3.3.2.1) and by the differences for the impact ionization due to the assumed homogeneous magnetospheric electrons densities. The differences in the peak values obtained for the two approaches are of the order of 20% for C23, 35% for C22 and 70% for C9. However, a large part of the differences for C9 is presumably attributed to the neglected plasma transport for the analytical calculations. The above values can, however, be used as a very rough measure for the impact of the decreased scale height in the simulations.

Regarding the hypothesis that the observed ionospheric variabilities might be caused by different ambient condition, we can conclude that, while both the solar flux and the background plasma parameters indeed play a significant role, their variations can not explain the observed deviations alone. This holds also true if we additionally consider our first hypothesis that plasma particles transported to Callisto's flanks may increase the measured densities. This factor is already included in the simulation results for C9, C22 and C23. However, if we again account for the possibility that Callisto's atmosphere may be asymmetric the deviations between the simulation results for C9 and the other flyby cases additionally increase (dash dotted green lines in Figure 3.30). The reason for these deviations are, again, the decreased overall electron densities for $\alpha_\odot \approx 90°$ and the increased transport of ionospheric particles from or towards the flanks due to the decreased collision and mass loading terms in these regions. The effect of an asymmetric neutral density distribution decreases the electron column densities for the C9 simulations to ~40% of the values obtained for the default atmospheric configuration. At the same time the corresponding differences for the C22 and C23 cases are less than 20%.

Taking into account the approximate deviations due to the decreased scale height in our model given above, we can conclude that all column densities inferred from the measurements should still be relatively well matched for realistic scenarios which consider deviations for the different flybys due to plasma transport, the ambient conditions and, additionally, an asymmetric distribution of Callisto's neutral atmosphere. The approximate contributions to the decreased column densities for C9 due to transport, ambient conditions and an asymmetric atmosphere are 5%, 25% and 40%, respectively. Note that these values present only very crude approximations for the relative role of the three suggested effects which can generally not be treated independently.

Though our simulation results favor an asymmetric configuration as an explanation for the temporal variability of Callisto's ionosphere, we can give no conclusive explanation for the observations. This is also due to the fact that the interpretation of a vanishing ionosphere for a sunlit downstream hemisphere by *Kliore et al.* (2002) is based only on one flyby and due to the comparatively large uncertainties for these specific measurements. A verification of the hypothesis raised above therefore requires additional data potentially provided by the upcoming JUICE mission or earthbound observations of Callisto's aurora.

3.3.2.3 UV aurora

In contrast to all other Galilean moons (See e.g., *Hall et al.* 1998, *Roesler et al.* 1999, for Europa and Ganymede or Io, respectively.) the search for UV emissions produced by electrons which excite the CO_2 and O_2 neutral particles in Callisto's atmosphere was not successful so far. *Strobel et al.* (2002) inferred only an upper limit for the disk integrated intensity of the radiation of 5×10^{-5} photons cm^{-2} s^{-1} or 15 R[IV] from measurements by the Hubble Space Telescope (HST). One reason for the absence of substantial UV emissions at Callisto is the low magnetospheric electron density at the orbit of the satellite. Additionally, *Strobel et al.* (2002) predict that the plasma interaction leads to a very effective deflection of the magnetospheric electrons around the satellite while only 0.07% of the particles actually reach the atmosphere and, potentially, generate UV emissions.

This conclusion is also supported by our simulation results for the magnetospheric electron densities $n_{e,ms}$ (Figure 3.18). We find that the near surface region of the atmosphere is virtually depleted of magnetospheric electrons. In contrast, $n_{e,ms}$ is increased at higher altitudes above the north and south poles and in the downstream region. In regions where a considerable amount of magnetospheric electrons encounters sufficiently large atmospheric densities sporadic UV emissions should, however, still be generated. These emissions could give hints for the distributions and densities of the neutral atmosphere and the electrons in Callisto's vicinity. Note that the ionospheric electrons generally have much lower temperatures than their magnetospheric counterparts. Therefore, in spite of their high number densities, they do not significantly contribute to the UV emissions generated at Callisto and are neglected in the following discussion.

We can use the results from our MHD model to predict both the intensity and the spatial distribution of Callisto's aurora. The emission rate per volume element is given by:

$$\epsilon = n_{e,ms} n_{ns} f_{\mathrm{rad}}(T_{e,ms}). \tag{3.45}$$

The emission frequency f_{rad} for a certain magnetospheric electron temperature $T_{e,ms}$ can be computed in analogy to the impact ionization frequencies by using Equations (3.32) to (3.34). Here we again assume a Maxwellian distribution for the electron energies. The

---

[IV] In this section R denotes the unit Rayleigh.

ionization cross sections $\sigma_{\mathrm{imp},ns}$ need to be replaced by the electron impact dissociative excitation cross sections $\sigma_{\mathrm{exc},ns}(\lambda)$ for a certain wavelength. In this work we use cross sections for the O_2, $\lambda = 1356$ Å emission line given by *Kanik et al.* (2003). For the CO_2 atmospheric component we use CO_2, $\lambda = 1304$ Å[V] cross sections provided by Darrell F. Strobel (personal communication). We choose the above wavelengths among the available emission lines for CO_2 and O_2 as they presumably yield the highest intensities for Callisto's aurora. As the above emissions are both associated with oxygen both neutral species cause radiation at the two given wavelengths. The results presented below, however, only refer to the emission caused by a single molecular species.

One of the main parameters affecting the auroral intensities is the distribution of the temperature for the magnetospheric electrons $T_{e,ms}$. In contrast to the electron number densities, we do not explicitly consider spatial and temporal variations of $T_{e,ms}$ within the framework of our model. Especially the results for the spatial distribution of the auroral intensities should therefore only be interpreted with great care. Despite of this caveat, our model allows a rough estimate for $T_{e,ms}$, taking into account the loss of internal energy due to the impact ionization process and the heating of the electrons by heat conduction within the magnetic flux tubes connected to Callisto. We compare the impact ionization frequencies $f_{\mathrm{imp,max},ns}$ obtained in our simulations (Equation 3.37) to theoretical values $f_{\mathrm{imp},ns}(T_e)$ calculated using Equation (3.32) to infer the temperature associated with $f_{\mathrm{imp,max},ns}$. The parameter $f_{\mathrm{imp,max},ns}$ is constant within our simulation regime. Therefore, we can determine a single average value of $k_B T_{e,ms} \approx 45$ eV for our standard simulation setups with both $\alpha_\odot = 90^\circ$ and $\alpha_\odot = 270^\circ$. The associated volume emission rates $\epsilon(T_{e,ms})$ predicted by our simulations can be integrated along arbitrary lines of sight to obtain the intensities I of the UV emissions for certain viewing geometries. An additional integration over the visible plane perpendicular to the line of sight and a normalization by dividing by the disk area of Callisto further yields the total intensities I_{tot} for each viewing direction.

Figure 3.32 illustrates the predicted auroral intensities I for the O_2, $\lambda = 1356$ Å line for a symmetric atmosphere. Depicted are views along the y-direction (xz-plane) and both downstream and upstream views of Callisto for the $\alpha_\odot = 90^\circ$ and $\alpha_\odot = 270^\circ$ standard scenarios. Figures highlighted by the symbol * depict the viewing geometry consistent with observations from the Earth's direction. The total intensities for all viewing directions considered in Figure 3.32 are summarized in Table 3.8 along with the total intensities for the CO_2, $\lambda = 1304$ Å emission line.

All of the total intensities given in Table 3.8 are in agreement with the upper limit of 15 R given by *Strobel et al.* (2002). Due to the comparatively low neutral densities for CO_2 the intensities for the associated $\lambda = 1304$ Å emission line are generally very weak (~0.03 R). As the dissociation of the O_2 molecule also causes emissions at $\lambda = 1304$ Å, measured intensities which clearly exceed the given value for CO_2 may be interpreted as additional evidence for the existence of an O_2 atmosphere. The O_2, $\lambda = 1356$ Å emissions yield intensities of ~6 to 10 R. These values are two orders of magnitude higher than for the CO_2, $\lambda = 1304$ Å emissions. Therefore, in analogy to Europa and Ganymede, the main emissions at Callisto presumably occur at $\lambda = 1356$ Å, if an O_2 atmosphere is present.

[V] Another common notation for the two emissions lines is: OI1356 and OI1304. We choose the notation given in the text to clearly distinguish between excitation of the CO_2 and the O_2 molecules.

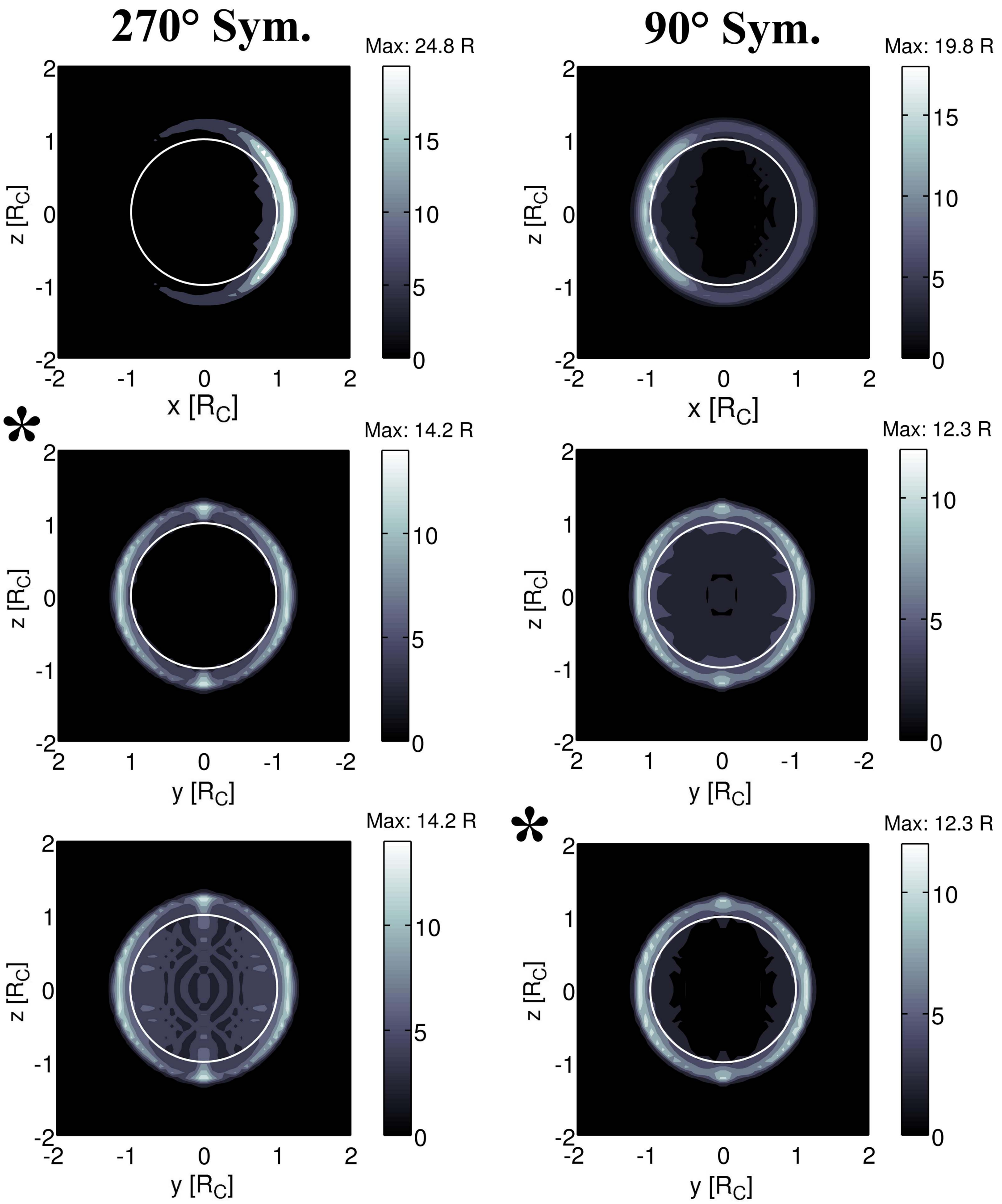

__Figure 3.32:__ Auroral intensities I for the O_2, $\lambda = 1356$ *Å emission line in R for the* $\alpha_\odot = 270°$ *and* $\alpha_\odot = 90°$ *standard scenarios. The upper two figures illustrate views along the positive y-direction. The central figures assume a line of sight in the downstream direction along the positive x-axis. The lower figures depict an upstream view along the −x-direction. The symbol * indicates figures depicting a viewing direction from the Earth's location.*

$\alpha_\odot$	270°			90°		
Line of sight	$+y$	$-x$ (up)	$+x$ (do)*	$+y$	$-x$ (up)*	$+x$ (do)
$I_{\mathrm{tot}}(O_2)$ [R]	8.1	9.6	5.8	7.4	6.5	8.0
$I_{\mathrm{tot}}(CO_2)$ [R]	0.03	0.04	0.02	0.03	0.03	0.03

Table 3.8: *Total disk integrated intensities I_{tot} for the O_2, λ = 1356 Å and the CO_2, λ = 1304 Å emission lines in R. Different lines of sight were assumed along the given axes (±x and +y) of the CphiO coordinate system. In the context of the viewing geometry (up) denotes a view along the upstream direction and (do) along the downstream direction. The symbol * indicates the viewing geometry for observations from the direction of Earth.*

Our model for $\alpha_\odot$ = 270° predicts that the strongest local auroral intensities for O_2 are located downstream of Callisto (see upper left panel in Figure 3.32). This emission is associated with magnetospheric electrons accumulating in the wake region (Figure 3.18). Consequently, the emission is hidden behind the satellite for a downstream view of Callisto's atmosphere (central left panel in Figure 3.32). An upstream view of Callisto gives maximum local emissions of 14.2 R which are comparable to the values for the downstream viewing direction. The total intensities, however, are almost twice larger for the upstream viewing direction (Table 3.8). This is caused by the additional emissions located on the disk of Callisto. For both upstream and downstream viewing directions, the maximum local emissions are slightly shifted away from Callisto's disk. These emissions are caused by the magnetospheric electrons deflected around the satellite. The bright spots near Callisto's north and south pole physically correspond to the equatorial spots detected in Io's UV emission (e.g., *Roesler et al.* 1999, *Roth et al.* 2011). Their location is shifted towards Callisto's poles in our simulation as the magnetic field points towards Jupiter and not in the z-direction as for Io.

For the simulation with $\alpha_\odot$ = 90° the main emission in the xz-plane is shifted to the upstream hemisphere. This is a consequence of the decreased ionospheric densities upstream of Callisto due to the lack of photo ionized particles. The lower upstream plasma pressure allows for more magnetospheric electrons to penetrate the atmosphere in this case. Consequently, the total intensities for $\alpha_\odot$ = 90° are lowest for a upstream view. In this case the emission is again blocked by Callisto's disk. The Sun and the Earth are both located in same direction seen from the position of Callisto for each value of $\alpha_\odot$. Therefore, the magnetospheric electron inflow is always higher on the hemisphere of Callisto not visible from the Earth. Consequently, only the lowest intensities for all possible viewing directions are available for observations performed along the line of sight starting at Earth (columns indicated by the symbol * in Table 3.8). Among all viewing geometries available for these kind of observations the upstream view for $\alpha_\odot$ = 90° gives the highest total intensity of 6.5 R. However, the total intensities only show variations of $\sim$15%. Furthermore, the results obtained for $\alpha_\odot$ = 90° depend on the plausibility of plasma transport processes predicted for Callisto's tail region (Section 3.3.1.3). Regarding the hypothesis of an asymmetric atmosphere raised in Section 3.3.2, it should be briefly noted that the total intensity for $\alpha_\odot$ = 90° of 4.8 R is also slightly increased with respect to the value of 4.6 R obtained for a sunlit upstream hemisphere. The distribution of the intensities for both cases are comparable with the results for a symmetric atmospheric setup given in Figure 3.32.

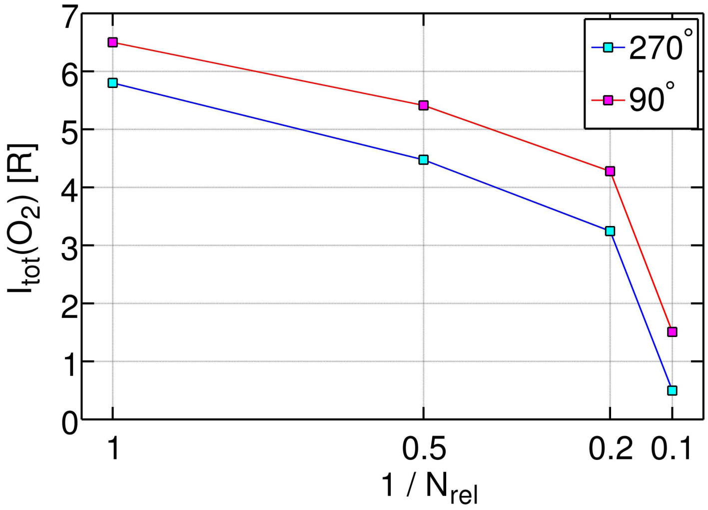

Figure 3.33: *Total auroral intensities I_{tot} for the O_2, λ = 1356 Å emissions in R. Values for a line of sight from the direction of Earth for $\alpha_\odot$ = 270° (blue line) and $\alpha_\odot$ = 90° (red line) are given as a function of the scaling factor $1/N_{rel}$. The actual O_2 surface density for the MHD model is given by $n_{O_2,surf} = n_{O_2,0}/(N_{rel}H_{rel})$ with $n_{O_2,0} = 7 \times 10^9$ cm^{-3} and $H_{rel} = 10$. Note that the total amount of O_2 particles only scales with $1/N_{rel}$ and not H_{rel}, as the neutral scale height is increased by H_{rel}.*

Observations of Callisto's aurora can be used to infer the density of the O_2 atmosphere. Figure 3.33 depicts the total auroral intensities for a line of sight from the direction of Earth calculated for models with an O_2 surface density decreased by a factor $1/N_{\mathrm{rel}}$. The values given for $\alpha_\odot = 270°$ and $\alpha_\odot = 90°$ indicate that $I_{\mathrm{tot}}(\mathrm{O_2})$ declines slowly to ~45% of the initial intensity for surface densities decreased up to a factor of 0.2. However, for $1/N_{\mathrm{rel}} = 0.1$ the auroral intensities drop significantly to ~90% of the initial value or 0.5 to 1.5 R. This indicates that Callisto's O_2 aurora is presumably only detectable if the surface number density lies above ~10% to 20% of the value suggested by *Kliore et al.* (2002).

In summary our model predicts that observations of Callisto's aurora from the Earth's direction always encounter unfavorable viewing geometries regarding the observable total intensity. Among the available geometries our model favors the conditions for a sunlit downstream hemisphere. If the O_2 density at the surface is close to 7×10^9 cm^{-3}, Callisto's atmosphere should be observable, even though the total intensities predicted by our model of 6 R are rather low. If the surface density is at least 90% lower a detection of Callisto's aurora is, presumably, not possible.

3.3.2.4 Currents and conductivities

Callisto's ionosphere is the source region of a current system which is connected to the Jovian ionosphere by currents flowing in the outer regions of the Alfvén wings i.e., along both Alfvén characteristics (see Section 1.2.2). Figure 3.34 illustrates this current system for the $\alpha_\odot = 270°$ standard scenario in the xz- and the yz-plane. The depicted current densities were calculated using Ampères law $\mathbf{j} = \frac{1}{\mu_0}\nabla \times \mathbf{B}$. The Alfvénic currents flow towards Jupiter in the outer wing regions in the southern hemisphere and towards Callisto for the northern parts of the wings (yz-plane in Figure 3.34). Not visible here are currents perpendicular to the Alfvén characteristics which deflect the plasma flow around the wing structures. The current is closed in the ionosphere by currents directed southwards close to the surface in the yz-plane and in the densest ionospheric regions slightly shifted away from Callisto in the xz-plane. The currents in the equatorial downstream region are also shifted away from the surface in contrast to their upstream counterparts. Further, the downstream current density is slightly increased with respect to the upstream conditions. Even though our model, unfortunately, allows a small amount of the currents to flow slightly below the surface of Callisto, our boundary conditions still prohibit a current closure through the satellites deep interior. A secondary current system is formed along Callisto's tail. This system is connected to the ionospheric currents along the northern and southern plasma flow regions, visible near $x = 2$ R$_C$, $y = \pm 1.5$ R$_C$ in the xz-plane. In the inner tail the current is repeatedly closed near regions which are correlated with the accumulation points of the plasma flow described in Section 3.3.1.3 (indicated by roman numbers in Figure 3.34).

By integrating over a half cross section of the northern and southern Alfvén wings at $y = 5$ R$_C$ we obtain a value for the total Alfvén current of $I_{\text{Alfvén}} = 2 \times 10^5$ A. This total current is comparable to the analytically deduced value for Callisto of 1.5×10^5 A given by *Strobel et al.* (2002).

While the conductivities parallel to the magnetic field are high both inside and outside Callisto's ionosphere, the parallel currents that close the interaction current system are a consequence of the increased Pedersen conductivity close to the satellite. The Pedersen conductivity (parallel to **E**, perpendicular to **B**) and the Hall conductivity (perpendicular to **B** and **E**) are defined by:

$$\sigma_P = \frac{qn_i}{B}\left(\frac{\omega_{ci}\tilde{\nu}_{i,ns}}{\omega_{ci}^2 + \tilde{\nu}_{i,ns}^2} + \frac{\omega_{ce}\tilde{\nu}_{e,ns}}{\omega_{ce}^2 + \tilde{\nu}_{e,ns}^2}\right) \tag{3.46}$$

and

$$\sigma_H = \frac{qn_i}{B}\left(\frac{\tilde{\nu}_{e,ns}^2}{\omega_{ce}^2 + \tilde{\nu}_{e,ns}^2} - \frac{\tilde{\nu}_{i,ns}^2}{\omega_{ci}^2 + \tilde{\nu}_{i,ns}^2}\right). \tag{3.47}$$

Therefore in our model σ_P and σ_H depend on the magnitude of the magnetic field B, the density distribution of the ions n_i and the effective collision frequencies $\tilde{\nu}_{e/i,ns} = \nu_{e/i,ns} + P/n$. The values for σ_P and σ_H predicted by our $\alpha_\odot = 270°$ model are given for the xz-plane in Figure 3.35.

Both conductivities approach comparable maximum values in our simulation regime. By integrating from the equatorial plane along the magnetic field lines we can determine the

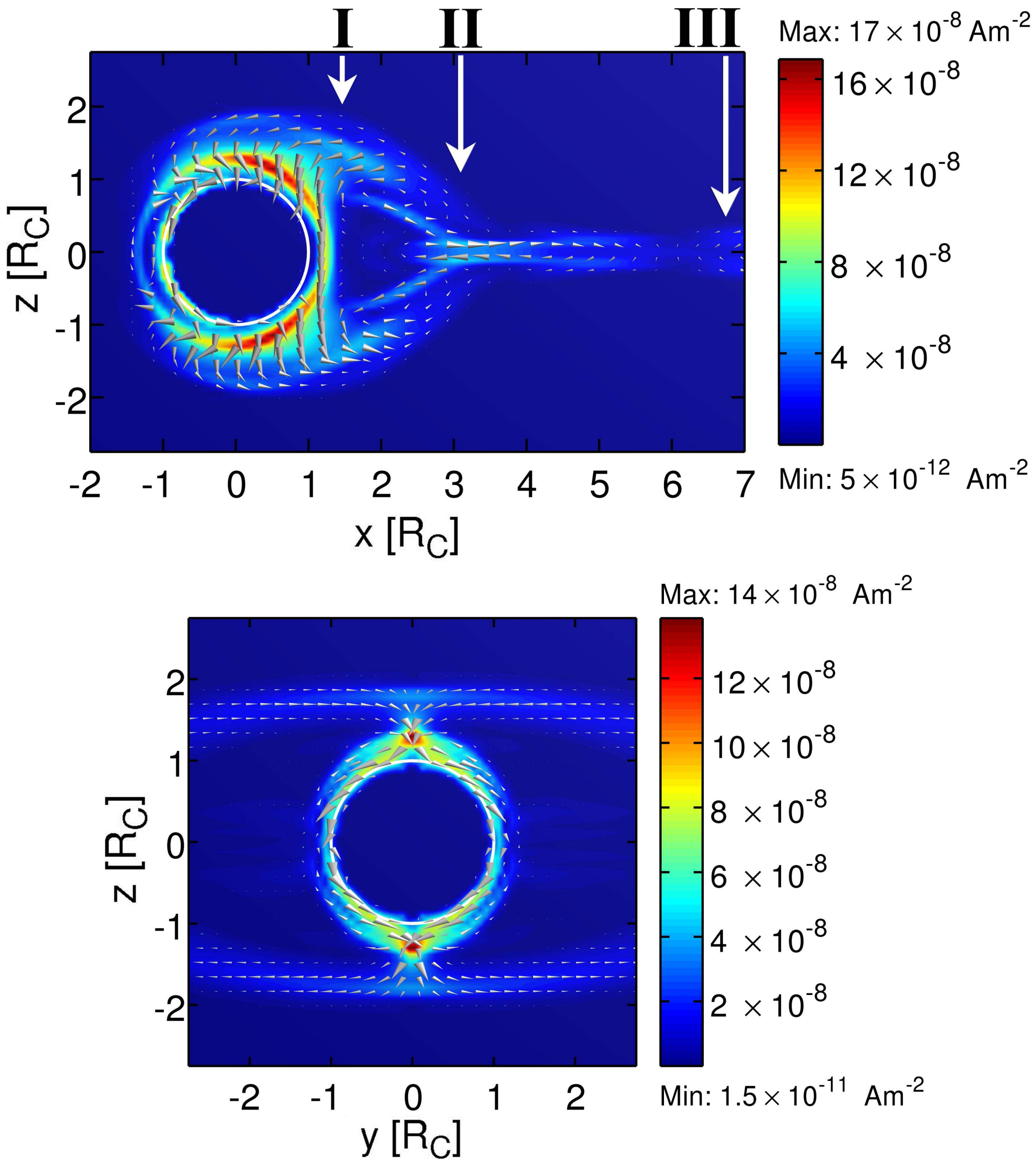

Figure 3.34: *Current densities* $\mathbf{j}$ *in A* m^{-2} *for the* $\alpha_{\odot} = 270°$ *standard model in the xz-plane at* $y = 0$ *(upper figure) and yz-plane at* $x = 0$ *(lower figure). The color contours depict the total current densities while cones give the direction of the current density vectors projected to the respective plane. Note that the maximum length of the cones is limited to* 8×10^{-8} *A* m^{-2} *to give a better representation of the currents in the tail and along the Alfvén characteristics. Above this threshold all cones are of the same length. Arrows associated with roman numbers indicate the plasma accumulation points described in Section 3.3.1.3.*

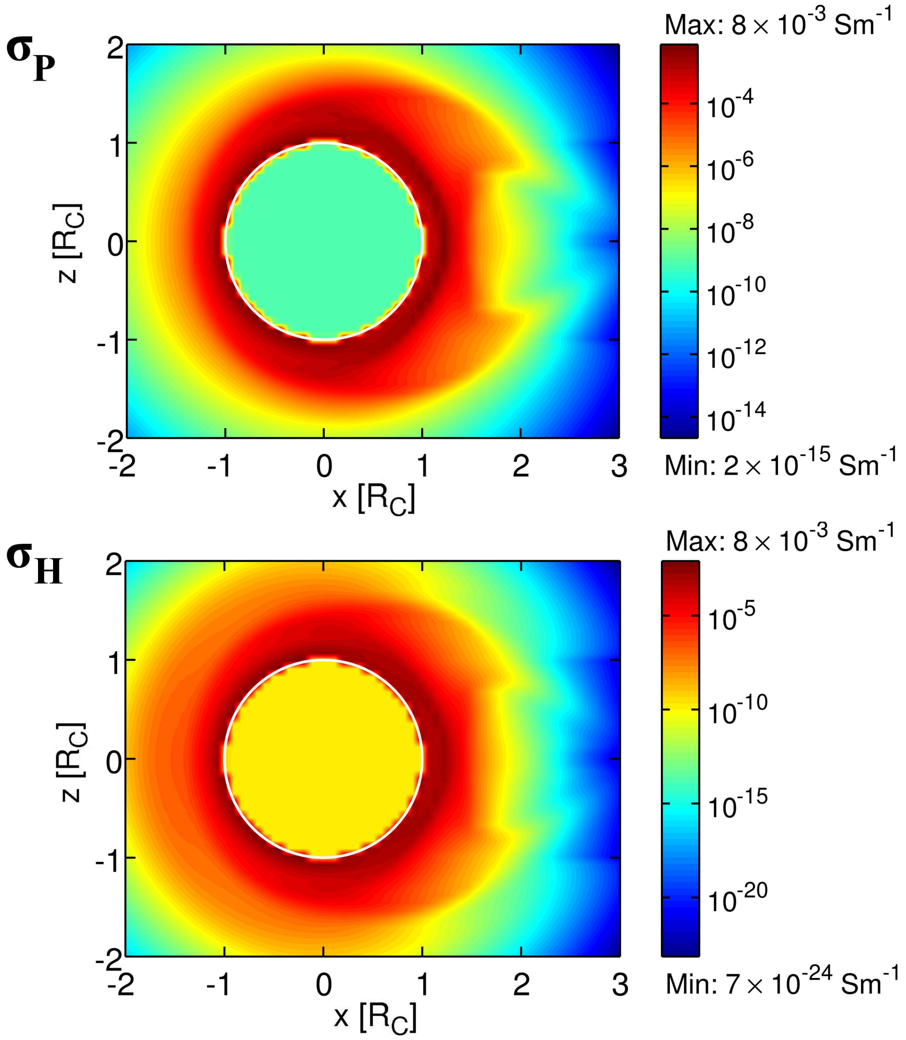

Figure 3.35: *Pedersen (upper panel) and Hall conductivities (lower panel) in S m^{-1} obtained for the standard $\alpha_\odot = 270°$ model setup in the xz-plane at $y = 0$. Note that the color contours are given in a logarithmic scale.*

Pedersen and Hall conductances Σ_P and Σ_H. We infer peak values of $\Sigma_P = 8,400$ S and $\Sigma_H = 6,900$ S. These values are again comparable to the conductances of $\Sigma_P = 15,000$ S and $\Sigma_H = 7,000$ S analytically predicted by *Strobel et al.* (2002) but slightly deviate from the conductances given in Table 21.1 by *Kivelson et al.* (2004). The two conductances can be used to assess the significance of the Hall term which we not considered within the formulation of our model. The Hall effect leads to a rotation of the electric field about an angle $\theta_{\text{twist}} = \Sigma_H(\Sigma_P + 2\Sigma_A)^{-1}$, where $\Sigma_A = (\mu_0 v_A)^{-1}$ is the Alfvén conductance. With a value of $\Sigma_A = 1.63$ S for our standard scenarios we can conclude that the electric field should be substantially twisted by an angle of $\theta_{\text{twist}} = 82°$. Therefore, the Hall effect potentially has a considerable influence on the magnetic plasma interaction signatures measured at Callisto.

3.3.3 Comparison with magnetic field data

The magnetic field data recorded by the Galileo spacecraft yield valuable information about both Callisto's interior and plasma environment. A combined model for the secondary magnetic fields $\mathbf{B}_{\text{sec}}$ generated due to the induction effect and the plasma interaction fields $\mathbf{B}_p$ arising outside the satellite potentially allows to distinguish the respective contributions to the measured field perturbations. Conversely, a comparison with magnetic field data can be used to assess the validity of a plasma interaction model. The major goal of the analysis presented in this section is to determine whether the magnetic perturbations measured by Galileo are in fact correlated with induced magnetic fields or if they can be equally explained by plasma interaction signatures. To answer this question, we use a superposition of the magnetic fields predicted by the induction model (Chapter 2) and our MHD model to evaluate the generation processes underlying the observed perturbations. Further, different simulation setups for the interaction model are used to perform parameter studies considering various aspects of Callisto's plasma interaction. In the present work we use data comparisons to assess the plausibility of different setups for Callisto's neutral atmosphere, of the tail structures predicted by our model and of the measured plasma data with respect to idealized plasma conditions. Additionally, the model results for the plasma velocity are used to determine the interaction geometry i.e., the location of the Alfvén wing and wake structures with respect to the trajectories of Galileo.

Regarding the interpretation of our results there are several notable caveats. (1) A simple superposition of $\mathbf{B}_p$ and $\mathbf{B}_{\text{sec}}$ neglects the feedback between the plasma interaction and the induction effect (see Section 1.2.2), although the formulation of our MHD model itself is self-consistent. This leads to an overestimation of the Alfvén wing cross sections and to uncertainties regarding the magnitude of $\mathbf{B}_p$ and $\mathbf{B}_{\text{sec}}$. (2) The increased scale height in our model also leads to an overestimation of the size of the perturbation region, which is reflected, for example, by deviations in the predicted timing of the Alfvén wing crossings with respect to the data. (3) As stated in Section 3.3.2.4 the neglected Hall term introduces additional uncertainties regarding the predicted perturbation field strength and potentially causes a rotation of $\mathbf{B}_p$ of up to $\theta_{\text{twist}} = 82°$. (4) A general problem for the interpretation of magnetic field data recorded during flybys at a planetary body is that temporal and spatial variations can not be separated. The temporal dependence of the background field $\mathbf{B}_0(t)$ generates variabilities in $\mathbf{B}_p(t)$ which are not reflected by the quasi-steady conditions of our model. In the following discussions we indicate where the above caveats need to be taken into account. Despite of these constrains our combined induction and MHD model suitably allows us to examine the subjects raised above.

As a base for our induction model we chose the interior model of *Kuskov and Kronrod* (2005a) given in Table 2.1. Within the plausible range of ocean conductivities and thicknesses for this model we pick values of $\sigma = 5\ \text{S m}^{-1}$ and $h = 10$ km. The respective value for σ resembles the conductivity of sea water in the Earth's oceans (*Beblo et al.* 1985). The chosen thickness still falls in the lower range of plausible ocean extensions. However, the associated value for the amplitude of the secondary field relative to the primary field of $A = 81\%$ given in Figure 2.14 shows that Callisto's ocean nearly acts as a perfect conductor for this configuration. The perfect conductor case ($A = 100\%$, see Section 2.2.1) was also suggested as an explanation for the measured field perturbations at C3 and C9 by *Zimmer et al.* (2000), as discussed in Section 1.2.1. The phase shift of the induced signals given in Figure 2.15 of $\phi = 5°$ is almost negligible for the given ocean parameters. Due to the uncertainties introduced by the caveats above we omit a more detailed analysis considering different values of A i.e., different ocean configurations.

For the MHD model we primarily use default setups including a symmetric combined CO_2 and O_2 atmosphere and standard values for the plasma velocity (192 km s^{-1}) and internal energy density (1.72 nPa). To estimate the background plasma densities for each flyby we applied the model of *Bagenal and Delamere* (2011). The respective values are given in Section 3.2.5. In addition to this default flyby scenarios, variations of the basic model setup are used to analyze implications arising for different assumptions. The associated setups are briefly described along with our discussion in the following sections. Note that for models where two parameters are changed with respect to the original setup additional simulations for each separate variation were performed to ensure that the physical conclusions are correctly attributed. The components of the magnetospheric background field for all interaction models were derived from the measured data within a time frame spanning 10 min, starting 40 and 30 min before and after the closest approach. Note that these time frames lie outside the range for the data presented in this section. The exact values and associated assumptions are also given in Section 3.2.5. All of the model results and data presented in this section are given with respect to the CphiO coordinate system.

For the data comparison we subtract the constant initial background field from our simulation results and add the field components predicted by our magnetospheric field model (Section 2.2.4) for the respective locations within the magnetosphere instead. The background field $\mathbf{B}_0(t)$ is therefore treated separately from the steady state perturbations $\mathbf{B}_p$ given by our model. This procedure is necessary due to the temporal variations of $\mathbf{B}_0(t)$ during the flyby phases as stated in caveat (4). We choose to use our magnetosphere model instead of a simple polynomial fit to the actual data as the model generally gives equally good or even slightly more suitable fits to the overall field structures. We limit our discussion to the results for the C3, C9, C10 and C22 flyby scenarios as no important additional results were obtained for the remaining flybys. The results for C21, C23 and C30 can be found in Appendix A.2. We also indicate some notable similarities in the following sections.

3.3.3.1 C3 and C9

We start our discussion with the magnetic field data for the C3 and C9 flybys. *Khurana et al.* (1998) were the first who interpreted the magnetic perturbations detected during these two flybys as evidence for the existence of induced magnetic fields and a subsurface ocean layer at Callisto. These authors neglected the contributions by the plasma interaction and considered them to be weak for situations when Callisto is located outside the current sheet. Though the results below indicate that this assumption to some extent holds for C3 and C9, we show in the discussion of C10 and C22 that it is generally not justified (Section 3.3.3.2). The subsequent, more detailed analysis by *Zimmer et al.* (2000)

confirmed the results obtained by *Khurana et al.* (1998), again neglecting the influence of the plasma interaction at Callisto. However, as stated by *Neubauer* (1998b), a detailed study taking into account the plasma magnetic fields is necessary to conclusively confirm the existence of induced magnetic fields and, consequently, of an interior ocean layer at Callisto.

In agreement with the results of *Khurana et al.* (1998) and *Zimmer et al.* (2000) we find that the induced fields $\mathbf{B}_{\text{sec}}$ predicted by our induction model, depicted as a superposition with $\mathbf{B}_0(t)$ by the red lines in the Figures 3.36 and 3.37, indeed give a suitable data fit (compare to the black solid lines) without considering the plasma interaction. The associated perturbations yield components of $\delta B_x = 6$ nT, $\delta B_y = -4.5$ nT for C3 and $\delta B_x = \pm 9$ nT, $\delta B_y = 10$ nT for C9. These values reflect the secondary field strength at Callisto's surface of 16 nT given in Section 2.3.3, taking into account the altitudes of the flybys (Table 3.1) and a decrease of the dipolar field by $(r/\mathrm{R}_C)^3$. In the absence of any plasma interaction signals we could therefore conclude that the existence of an ocean layer with the conductivity of sea water and a thickness of 10 km located at a depth of 150 km yields a good explanation for the magnetic field observations. One exception to this good overall data fit is the B_x component for the flyby phase after the closest approach. In this phase the magnetic field shows oscillations of ~5 nT around $\mathbf{B}_0(t)$ which are presumably related to the plasma environment.

The plasma interaction signals for the default C3 model setup, given in term of a superposition of $\mathbf{B}_0(t)$, $\mathbf{B}_{\text{sec}}$ and $\mathbf{B}_p$ by the green dashed lines in Figure 3.36, not only fail to explain the oscillations in B_x but also worsen the overall data fit. The modeled perturbation fields $\mathbf{B}_p$ can be understood in context of the predicted relative position of Galileo with respect to the local interaction region and Alfvén wings[VI]. Figure 3.38 depicts the C3 Galileo trajectory and a 3D-surface of the perturbation region which for the present discussion shall be defined as the region where the plasma velocity falls below a certain threshold ($v < 19.2$ km s^{-1} for C3), associated with substantial magnetic perturbations. Our model predicts a close encounter towards the anti-Jovian wing for the early flyby phase and a crossing of the sub-Jovian wing after the closest approach. Both predictions are not reflected by the data in Figure 3.36. In addition to caveat (1) and (2), two assumptions can be made to explain the deviations of our model results. First, the location of the Alfvén wings for C3 in reality might have been such that Galileo never actually encountered them. Secondly, we may have overestimated the strength of the plasma interaction for C3, as suggested by the deviations of ~50% with respect to the B_x oscillations after the closest approach (~10 nT relative to the measured 5 nT).

Simulations for a setup using the actually measured plasma velocities for C3 (Table 3.2), indeed give a slightly better data fit, suggesting that the simple interaction geometry assumed for our default model causes some of the deviations. For this simulation (not explicitly shown here) the deviations with respect to $\mathbf{B}_0(t)$ for the predicted B_x peaks before and after the closest approach (see green dashed line in Figure 3.36) drop by ~2 nT to 3 nT. For a simulation in which we additionally scale down the absolute value for the

---

[VI] The term "Alfvén wing" refers, strictly speaking, to the far-field interaction outside the regions discussed in this section. In the given context the term is also used to refer to the structures generated along the Alfvén characteristics near the local interaction region.

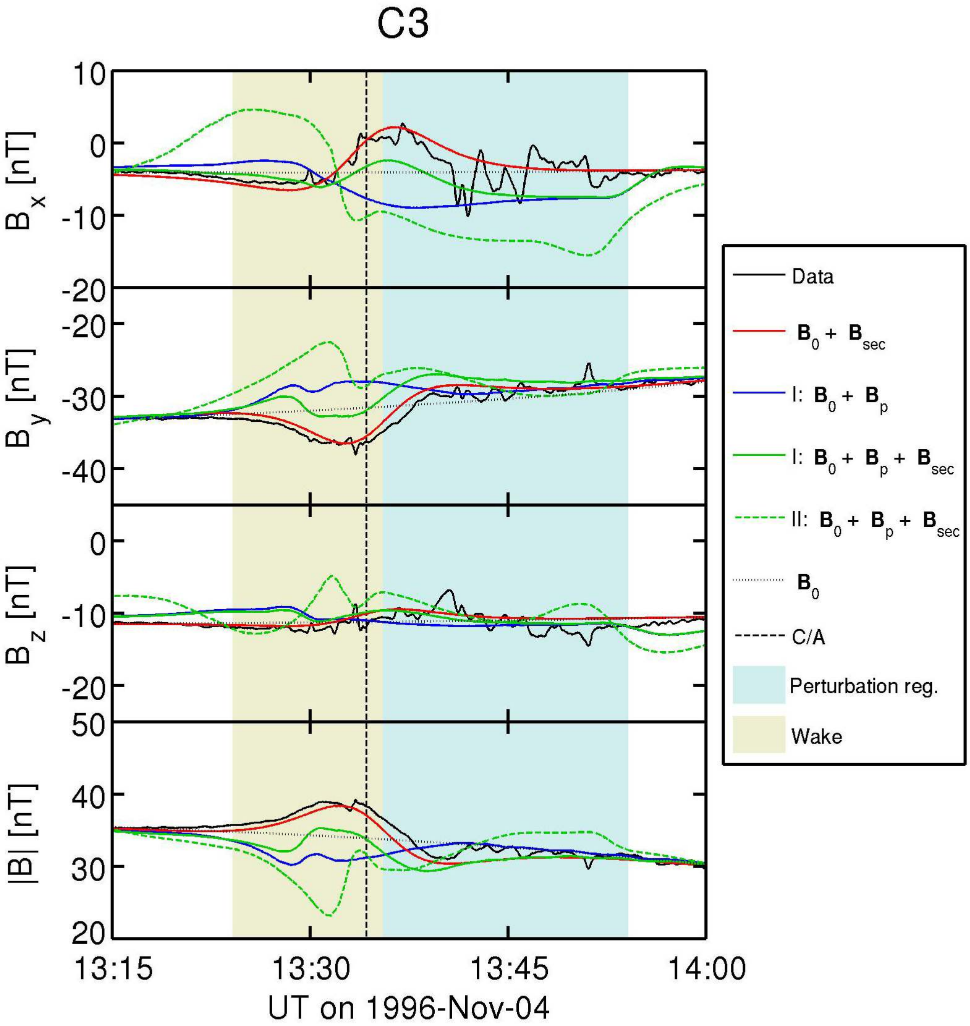

Figure 3.36: *C3 magnetic field data (black solid lines) and model results in nT and CphiO coordinates. The superposition of the background magnetic field (black dotted lines) and the induced fields is given in red. The blue solid lines depict a superposition of the background field and the modeled plasma interaction fields for a model (case I) using the measured plasma data with a velocity decreased by a factor of five. The green solid lines represent a superposition of the plasma interaction and the induced fields for case I. The green dashed lines give a similar superposition for the default C3 flyby model (case II). Blue and ocher areas indicate the locations where the perturbation region and the geometrical wake for case I are crossed by the spacecraft trajectory (see Figure 3.39). The vertical dashed line indicates the time of the closest approach.*

measured velocities by an empiric factor of five to artificially decrease the strength of the interaction the magnetic field data is considerably better matched (green solid line in Figure 3.36). The deviations with respect to the two prominent peaks in the data near the closest approach drop to ~3 nT for B_x and ~3.5 nT for the B_y component. The initially predicted peak in B_x before the closest approach almost drops to the background field level. In addition to the weaker overall interaction, this drop is caused by the rotation of the perturbation region away from the Galileo trajectory in the anti-Jovian hemisphere as indicated in Figure 3.39. However, a data comparison using $\mathbf{B}_p$ and $\mathbf{B}_0(t)$, not taking into account $\mathbf{B}_{\text{sec}}$ (solid blue line) shows that the modeled values for $\mathbf{B}_p$ are generally directed

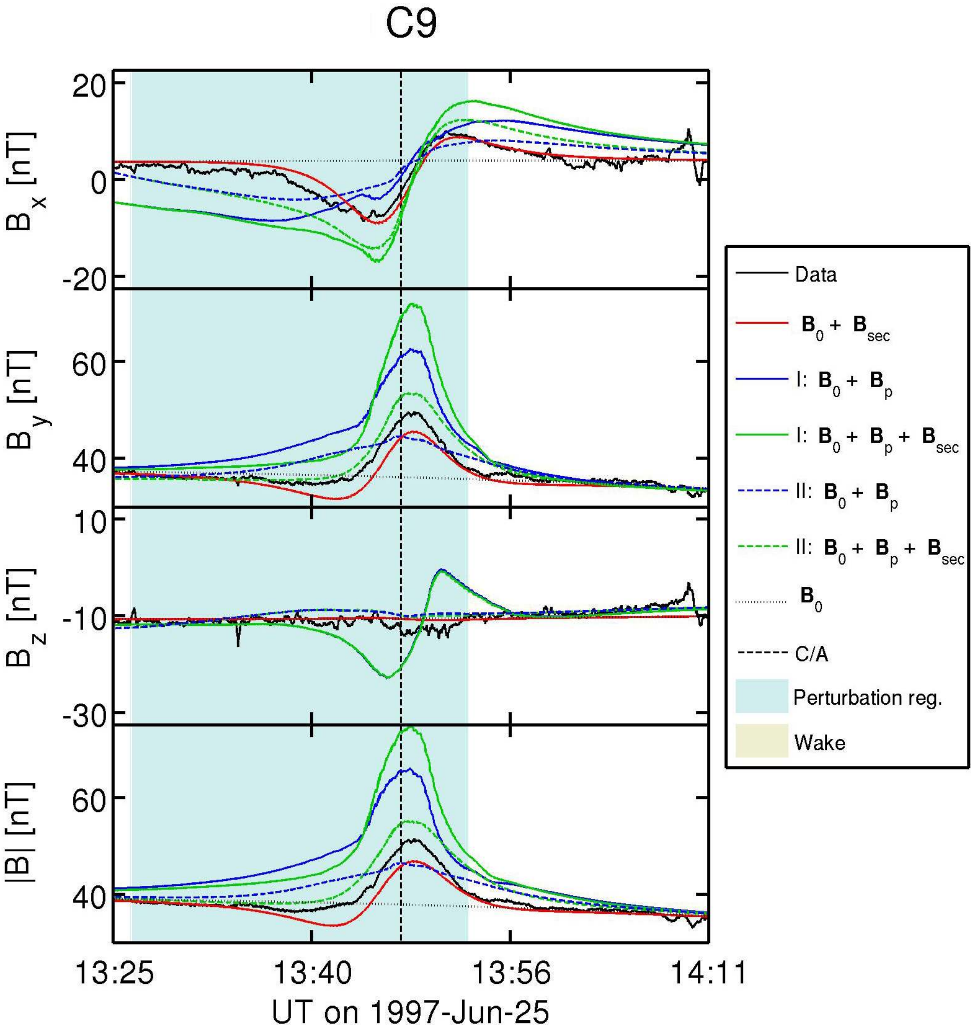

Figure 3.37: *C9 magnetic field data and model results. Case I (solid lines) refers to a model setup using the C9 plasma data and a combined CO_2 and O_2 atmosphere, while case II (dashed lines) refers to the default C9 model setup for a pure CO_2 atmosphere. The associated interaction and flyby geometries for the plasma data model are given in Figure 3.40. See Figure 3.36 for further explanations.*

oppositely to observed magnetic field perturbations everywhere. Only the B_x oscillations after the closest approach may be interpreted as sporadic signs of signals generated by the plasma flow. The opposite behavior of $\mathbf{B}_p$ with respect to $\mathbf{B}_{\text{sec}}$ is given for all C3 simulations mentioned above.

Therefore, despite caveat (3), we consider it highly unlikely that the observed perturbations can be explained by the plasma interaction alone. This result considerably strengthens the hypothesis of a subsurface ocean at Callisto. Regarding the amplitude of the induced fields the opposite behavior of $\mathbf{B}_p$ may actually lead to an underestimation of $\mathbf{B}_{\text{sec}}$. In the context of induced fields one could therefore speculate if Callisto's ocean lies at a shallower depth than the 150 km assumed for the *Kuskov and Kronrod* (2005a) model.

A completely different picture regarding the predicted plasma interaction signals arises for

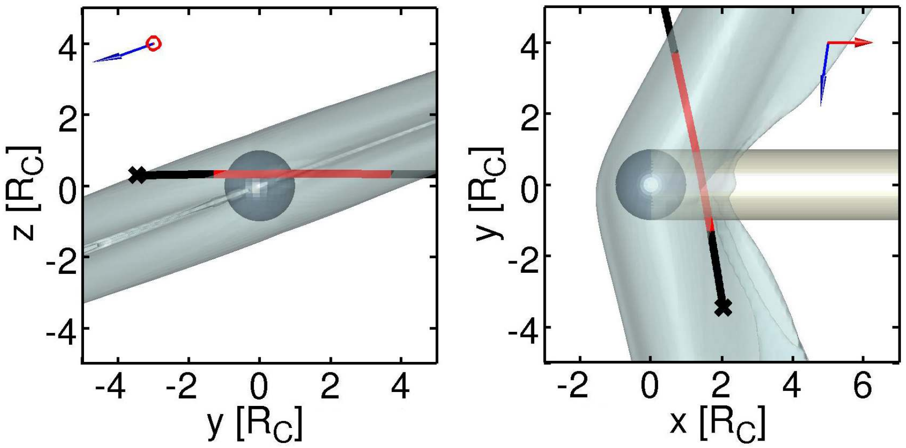

Figure 3.38: *3D-isosurfaces of the perturbation region defined by the condition* $v < 19.2$ *km s*$^{-1}$ *(*$v_0/10$*) for the C3 default flyby scenario. The left figure depicts an upstream view of the perturbation region and additionally indicates the trajectory of the Galileo C3 flyby by the solid line starting at the position marked with* x*. The line color is changed to red where the trajectory lies within the perturbation region. A top view of the flyby and interaction geometries is shown in the figure to the right. The ocher cylinder indicates the geometrical wake of Callisto. The red and blue arrows indicate the direction of* $\mathbf{B}_0$ *and* $\mathbf{v}_0$*, respectively. Note, that the predicted locations where the Galileo trajectory intersects the modeled perturbation or wake regions are highlighted by blue and ocher areas for the data comparison in Figure 3.36, respectively.*

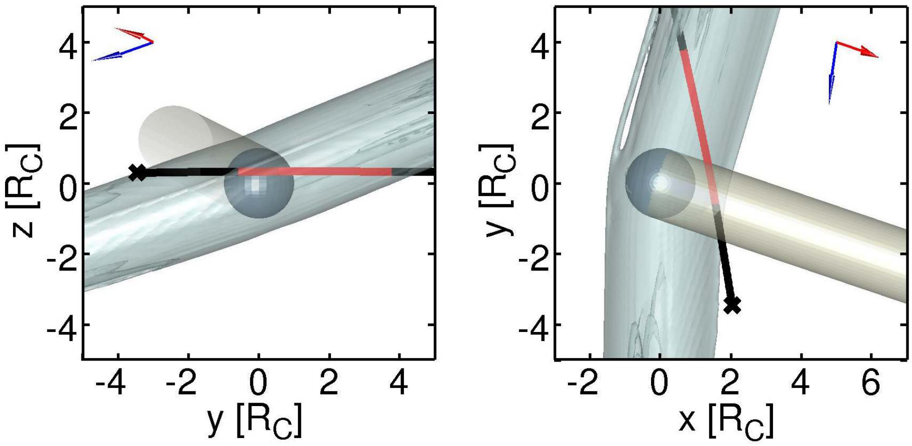

Figure 3.39: *3D-isosurfaces of the perturbation region defined by* $v < 5.4$ *km s*$^{-1}$ *for a model using the C3 plasma data and a reduced initial velocity (see text). See Figure 3.38 for further explanations.*

the C9 flyby. Though the perturbations for a model using the C9 plasma data overestimate the signatures measured in B_y by ∼14 nT (blue lines in Figure 3.37), we obtain a much better qualitative data fit in both B_x and B_y than for C3. The B_x perturbation strength for C9 of about ±9 nT nearly agrees with the predicted interaction signatures. Only the variations in B_z of ∼11 nT are not reflected in the measured signatures. A comparison of the plasma interaction fields with the field signatures due to the induction effect (red lines), indicates that both processes generate similar magnetic field structures. Therefore, the interpretation of the measured signatures as pure induced field signals may not hold for C9.

Figure 3.40 shows that Galileo's trajectory coincides with the predicted location of the anti-Jovian Alfvén wing in the early flyby phase with a transition to the pileup region upstream of the satellite near the closest approach. Both caveat (1) and (2) should be noted for the deviations with respect to the data during the passage of the wing and for the overall perturbation strength. In analogy to C3, we can artificially scale down the interaction strength using a variation of the above model. In addition to the upstream plasma conditions, the interaction strength is affected by the abundance of neutral particles in Callisto's atmosphere. Our results for the ionospheric densities during C9 show that the assumption of a pure CO_2 atmosphere is consistent with the measured electron density profiles (Section 3.3.2), even though it is contradicted by the C22 and C23 measurements. Regarding the hypothesis of an asymmetric atmosphere our results for the C9 magnetic field data, unfortunately, allow no conclusions. This is due to the fact that the neutral densities close to the pileup region are nearly equal for both asymmetric and the symmetric atmospheric setups. The dashed green and blue lines in Figure 3.37 therefore additionally depict the simulation results for a setup not considering the measured the plasma data and assuming a pure CO_2 atmosphere.

For this case we obtain a better data fit (~50% less deviations) for the early flyby phase. This is caused by the angular deviation of $\mathbf{v}_0$ in the xy-plane of 20° between the plasma data model and the CO_2 model setup (see Figure 3.41). The decreased interaction strength also yields a significantly better quantitative data fit near the closest approach. If we do not take into account possible induced fields, the perturbations in B_x and B_y predicted by the CO_2 atmosphere model underestimate the observed signatures by ~5 nT to 7 nT. The B_z component is almost unperturbed in contrast to our results for the plasma data model. A superposition of $\mathbf{B}_0(t)$, $\mathbf{B}_{\text{sec}}$ and $\mathbf{B}_p$ (green dashed line) reasonably explains all magnetic components observed for C9.

We can conclude that our C9 simulation results for both the magnetic field data and the ionospheric densities discussed in Section 3.3.2.2 are consistent with the assumption of a pure CO_2 atmosphere. However, taking into account caveats (1) and (2), the existence of an O_2 atmospheric component and the hypothesis of an asymmetric atmosphere, which both are consistent with the C9, C22 and C23 radio occultation measurements, may equally explain the C9 magnetometer measurements. As $\mathbf{B}_{\text{sec}}$ and $\mathbf{B}_p$ show a similar behavior for C9 the interpretation of the measured field perturbations as induction signals is not straight forward. Only the results obtained for C3, where $\mathbf{B}_{\text{sec}}$ and $\mathbf{B}_p$ can be separated due to their opposite signs allow us to carefully conclude that a substantial ocean layer at Callisto is the most reasonable explanation for the magnetic field observations. The largest uncertainty regarding the configuration of the potential ocean is given by the strength of the plasma perturbation fields. This strength can not be conclusively determined using our MHD model. As both the model results for C3 and C9 generally overestimate the observed magnetic perturbations we now consider two additional flybys and assess the validity of the results given above.

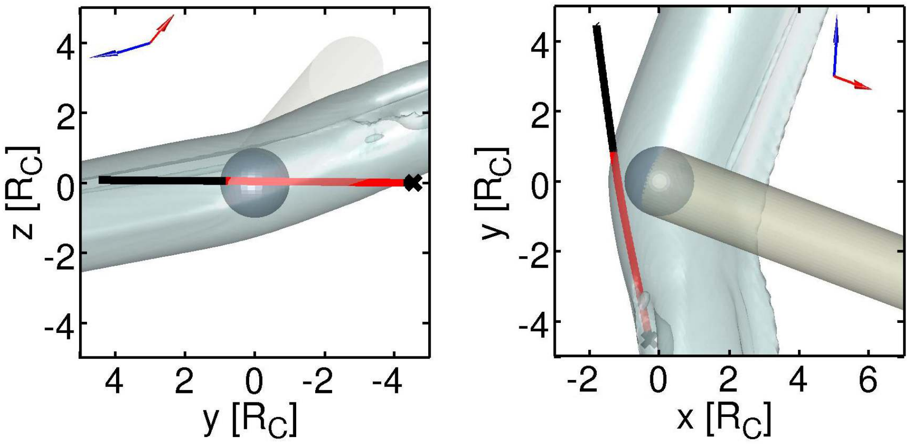

Figure 3.40: *3D-isosurfaces of the perturbation region defined by* $v < 19.2$ *km* s^{-1} *for a model using the C9 plasma data. See Figure 3.38 for further explanations. Note that other than for C3 a downstream view is given in the left figure.*

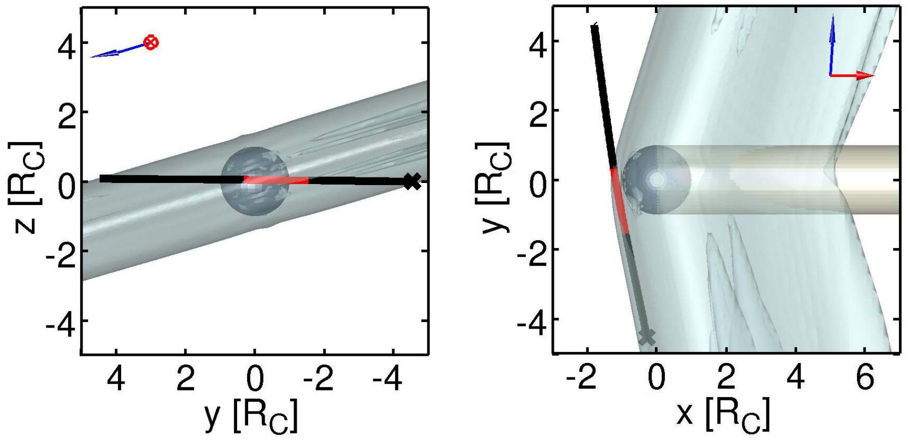

Figure 3.41: *3D-isosurfaces of the perturbation region defined by* $v < 30$ *km* s^{-1} *for the default C9 model assuming a pure* CO_2 *atmosphere. See Figure 3.38 for further explanations. The left figure shows a downstream view of the interaction region.*

3.3.3.2 C10 and C22

While the data for C3 and C9 can alternatively be explained by the existence of induced fields alone the remaining measurements indicate a more complex picture of Callisto's magnetic field environment. A comparison of the magnetic field data obtained during C10 and the induced fields predicted for this flyby (black and red lines in Figure 3.42) shows that except for the signatures near the closest approach the data can qualitatively not be explained by a superposition of $\mathbf{B}_0(t)$ and $\mathbf{B}_{\rm sec}$. The magnetic signatures predicted by our default C10 flyby model (blue solid lines) suggest that the perturbations of $\delta B_x = -10$ nT before and $\delta B_x = 10$ nT after the closest approach are associated with Callisto's plasma interaction. Figure 3.43 indicates that Galileo first crossed the anti-Jovian Alfvén wing whose inner region is associated with a negative δB_x component. Shortly before the closest approach the spacecraft entered Callisto's geometrical wake. Finally Galileo crossed the second Alfvén wing which features a positive δB_x perturbation in the central

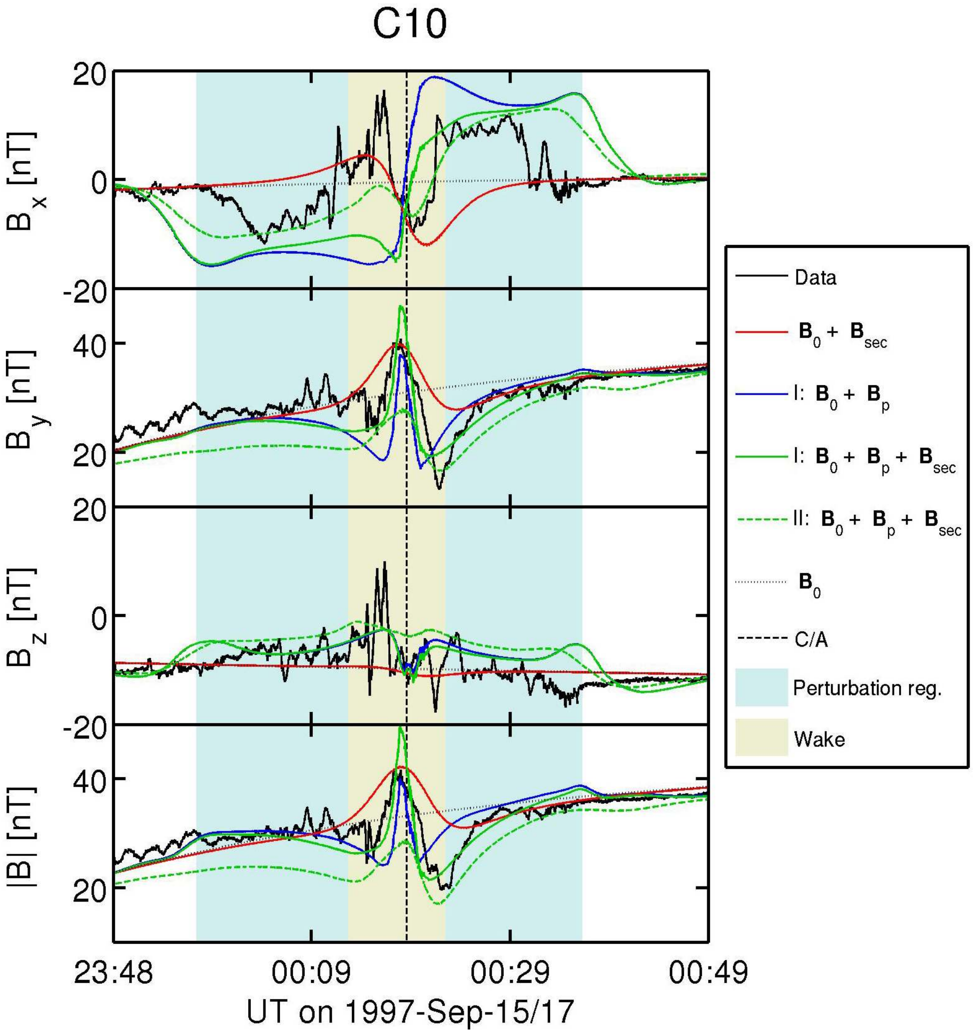

Figure 3.42: C10 magnetic field data and model results. Case I (solid lines) refers to a model setup using the C10 default flyby setup. Case II (dashed lines) refers to a variation of the default C10 model assuming a decreased plasma internal energy of 0.02 nPa. The associated interaction and flyby geometries for the default model are given in Figure 3.43. See Figure 3.36 for further explanations.

region. Caveat (1) and (2) should be noted for the extended size of the B_x signatures predicted by our model.

In contrast to the C3 and C9 scenarios, the modeled amplitude for the B_x perturbations of ~13 nT to 16 nT only marginally exceeds the measured signals of ~12 nT to 13 nT. This suggests that the plasma parameters and the atmospheric setup (CO_2 and O_2 abundances) used in our model present valid assumptions for the C10 flyby. Note that the interaction geometry for C10 does not significantly change when we assume conditions according to the measured plasma data instead of the idealized conditions for our default model. The Alfvén angle defining the direction of the wings only changes from ~24° to 26° for the measured data as the higher plasma velocity is compensated by increased plasma density (see Table 3.2). During both of the predicted wing crossings (blue areas in Figure 3.42) the B_y and B_z component of the measured field are, in agreement with our model results,

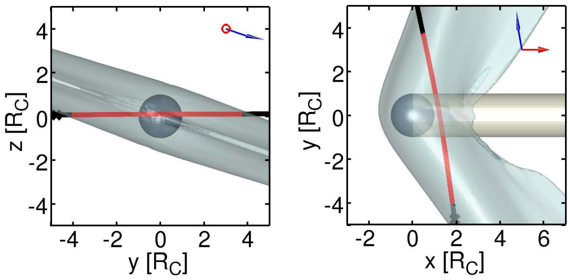

Figure 3.43: 3D-isosurfaces of the perturbation region defined by $v < 19.2$ km s^{-1} for the default C10 flyby model. The general geometry for a model assuming a decreased plasma internal energy of 0.02 nPa and for models using the measured plasma parameters are nearly equal to the depicted case. See Figure 3.38 for further explanations.

almost unperturbed. The δB_y perturbations of 9 nT and −18 nT in the wake region (ocher areas) are also well represented by our model results of $\delta B_y = 7$ nT and −14 nT. Taking into account the induction effect yields a slightly worse data fit with $\delta B_y = 15$ nT for the initial positive peak. Considering caveat (4) it should be noted that the B_y component of the magnetospheric background field increases by ∼14 nT during the C10 flyby phase of Galileo. Consequently, $\mathbf{B}_{\text{sec}}$ is also subject to temporal variations not taken into account in our models.

The most prominent deviations of our model results arise for the gradual rotation of the measured B_x component shortly before and during the wake crossing. The general shape of B_x in this region is better represented by the perturbations due to the induced field of ±5 nT (red lines in Figure 3.42). The corresponding signatures may therefore again be manifestations of the induction effect. The strong peak in B_x shortly before the closest approach of ∼17 nT can neither be explained by the induction signals nor by the interaction signatures. This peak coincides with a similar signal in B_z which to ∼40% is also represented by our interaction model. Note that a similar remarkably strong signature (∼50 nT in B_x and ∼30 nT in B_z) also occurred for the C21 flyby (see Appenix A.2). So far, we can give no explanation for the respective signatures. A superposition of the modeled plasma interaction and induced fields for our default C10 flyby setup, given by the green solid lines in Figure 3.42, slightly improves the fit to the B_x component in the wake. The green dashed lines depict the results for an additional simulation which, in contrast to the default model, assumes a background plasma pressure decreased by a factor of 100 of $e_0 = 0.02$ nPa. Compared to the high energy case (1.72 nPa), the data fit for B_x is considerably improved. In the wake region, however, the data is only well fit if we assume the presence of induced magnetic fields. In contrast to B_x, the B_y component is better represented by the high pressure model.

In analogy to the results given for the standard $\alpha_\odot = 270°$ model in Figures 3.19 and 3.22 (Sections 3.3.1.2 and 3.3.1.3), the main differences between both C22 simulations occur in the tail region of Callisto. For the high pressure case the tail plasma is confined to the inner wake region whereas for lower ambient pressures the plasma spreads out in the xy-plane. Due to the ambigueties regarding the data fit of B_x and B_y for the two models and the lack of suitable plasma measurements in the tail region, a conclusive evaluation of the conditions in Callisto's tail for C10 is not possible. However, the data comparison suggests that physical processes in the tail play a crucial role for the generation of the magnetic field signatures measured in the wake region.

Our data comparison for C10 proves that plasma interaction effects need to be taken into account for the interpretation of magnetometer data at Callisto. The amplitudes of the plasma interaction signals for C10 are well matched by our model. This indicates that the overestimated strength of the perturbations for the C3 and C9 scenarios, in addition to the noted caveats, may be attributed to the uncertainties regarding the variability of the background plasma conditions. Induced signals from a subsurface water ocean generally improve the data fit for C10.

To assess the validity of our results for Callisto's ionosphere (Section 3.3.2), we now conclude our discussion of the magnetic field data with the C22 magnetometer measurements. Other than for C9, a comparison of the results obtained for a symmetric and an asymmetric atmosphere promises more decisive results due to the downstream trajectory of the C22 flyby. Figure 3.44 therefore depicts the magnetic field data along with our simulation results for the default C22 setup assuming a symmetric (solid lines) and an asymmetric (dashed line) combined CO_2 and O_2 atmosphere. While at first glance both B_y and B_z exhibit rather weak and unstructured field perturbations, the B_x component clearly shows three successive positive peaks with a similar amplitude of ~5 nT. A rough comparison with both the predicted plasma interaction (blue lines) and induced field signals (red lines) suggests that the central peak is associated with induced magnetic fields while the remaining peaks may be manifestations of the plasma interaction signatures.

Galileo's trajectory with respect to the predicted perturbation region is depicted in Figure 3.45. The simulation results indicate that the first positive peak in B_x occurs due to a crossing of inner region of the sub-Jovian Alfvén wing. Shortly before the closest approach Galileo crossed Callisto's geometrical wake (ocher areas in Figure 3.44). In this region our results for $\mathbf{B}_p$ still adequately match the observations for B_x. Right after the closest approach our model predicts a crossing of the inner region of the anti-Jovian wing. This region is associated with a negative B_x perturbation field. The oppositely directed, measured B_x perturbation suggests that Galileo either was still located in a quiet wake region or encountered an outer region of the wing. In the first case the positive central B_x peak can be approximately explained by the induction signals of ~2.5 nT (red line in Figure 3.44). However, in the outer regions of the Alfvén wing the sign of δB_x is also reversed with respect to the conditions in the wing center (see e.g., Figure 3.15). Therefore, both $\mathbf{B}_{\text{sec}}$ and $\mathbf{B}_p$ could contribute to the central B_x peak. Our model predicts that the third peak is also associated with the lower outer region of the anti-Jovian wing (Figure 3.45). The measured B_x perturbation of ~5 nT is nearly matched by our model results due to the rotation of δB_x from -10 nT to +3.5 nT. The above discussion shows that the last two B_x peaks may actually be similarly associated with measurements in the southern region of the anti-Jovian Alfvén wing. The interruption of the B_x signature between the two peaks can be interpreted as a short approach towards the wing center.

During the wake encounter near the closest approach our model predicts perturbations of 5.5 nT and -7.5 nT arising in the B_y component. These perturbations are not given in the actual measurements. Instead a small positive perturbation of 2.5 nT occurs which is closely matched by the predicted induced field. The initially increased B_y component

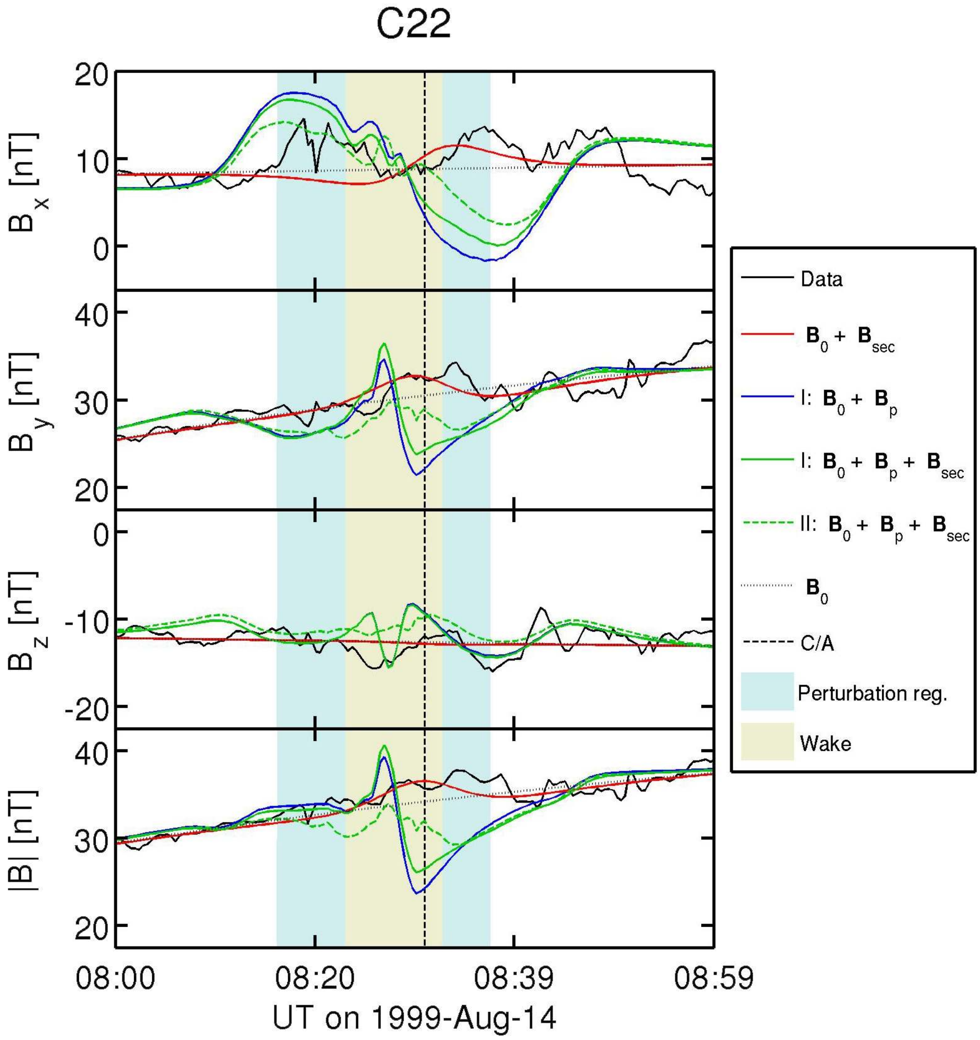

Figure 3.44: *C22 magnetic field data and model results. Colored solid lines refer to a model using the C22 default setup while dashed lines depict the results for an asymmetric atmospheric setup. The associated interaction and flyby geometries for the default setup are given in Figure 3.45. See Figure 3.36 for further explanations.*

for $\mathbf{B}_p$ of ~7 nT coincides with a location in Callisto's tail where the magnetic field piles up due to the flow patterns discussed in Section 3.3.1.3. Similar magnetic field patterns occur in the central tail for the standard $\alpha_{\odot} = 270°$ model as shown in Figure 3.13 (in the xy-plane near $x = 4$ R_C, $y = 0$). The successive drop of the plasma perturbation field to $\delta B_y = -7.5$ nT occurs in regions south of the central tail as depicted in Figure 3.14 (in the xz-plane near $x = 3$ R_C, $z = -\mathrm{R}_C$). These southern regions coincide with the Galileo trajectory for C22 as the interaction geometry is rotated towards the north in the anti-Jovian hemisphere (left panel in Figure 3.45).

However, for an asymmetric atmospheric setup (dashed line in Figure 3.44) the shape of the B_y perturbations significantly changes. For this simulation B_y exhibits a rather smooth profile instead of the previously noted oscillations. The deviations with respect to the measurement decrease to ~3 nT to 5 nT. The data fit for B_x and B_z also improves if we consider the case of an asymmetric atmosphere. This may be interpreted as a hint

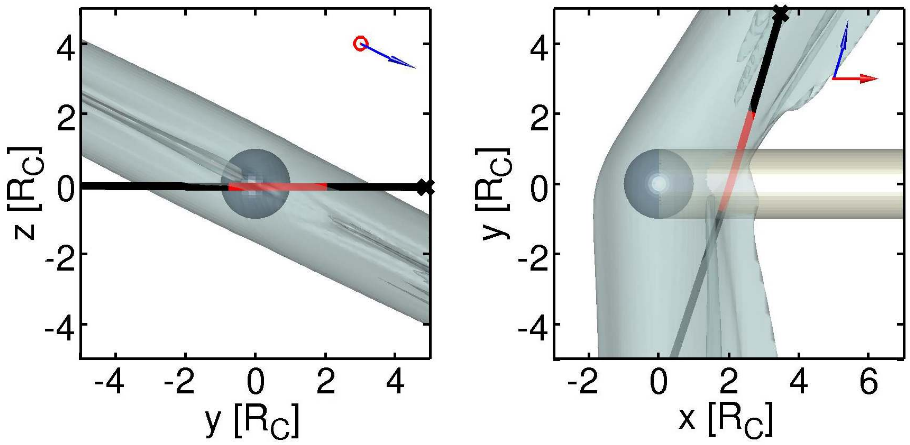

Figure 3.45: *3D-isosurfaces of the perturbation region defined by* $v < 19.2$ *km* s^{-1} *for the default C22 flyby model. The simulation results for an asymmetric atmosphere yield no significant differences with respect to the depicted geometries. See Figure 3.38 for further explanations.*

for unrealistically high neutral densities in the downstream atmosphere for a symmetric setup, although caveat (2) should be noted here.

We can conclude that both our results for the ionospheric electron densities and for the magnetic field data at C9 and C22 are consistent with an asymmetric sputtering induced atmosphere at Callisto. In agreement with the results obtained for the C10 flyby scenarios, the strength of the plasma perturbation fields in our C22 simulations realistically fits the measured signatures. Although, the central B_x peak occurring for C22 may be equally explained by plasma interaction and induction signatures, the presence of induced fields is probably reflected by the B_y perturbation of ~2.5 nT around the closest approach.

3.3.4 Conclusions

The results from our MHD model are used to infer information about the general plasma interaction, the configuration of the atmosphere-ionosphere system and possible induced magnetic fields at Callisto. Our model predicts a complex behavior of the flow in Callisto's plasma tail. The associated velocities in the negative x-direction and eddy structures in the wake region are presumably generated near the convergence point of the primary ionospheric plasma flows from the pole regions of the satellite. The Galileo magnetometer data recorded downstream of the satellite do not contradict the associated magnetic perturbations in the tail. However, to verify the existence of the predicted flow structures additional measurements and an extended analysis using different simulation codes is inevitable.

The observed temporal variabilities in the ionospheric electron densities can only be explained by models which assume an asymmetric neutral density distribution primarily confined to the upstream hemisphere. Again, the recorded magnetometer data do not contradict the predicted perturbation fields for these models, but allow no conclusive verification for the distribution of the atmosphere at Callisto. The conclusion by *Kliore et al.* (2002) that a substantial O_2 atmospheric constituent must be present at Callisto is confirmed by our simulations which, in contrast to previous studies, include plasma transport processes. Despite the fact that our model for the C9 flyby which assumes a pure CO_2 atmosphere yields a more suitable magnetometer data fit, most of the other flyby data is in agreement with simulations taking into account Callisto's O_2 atmosphere.

We can identify two classes of flybys with respect to the quality of the magnetic field data fit for our models. For C3, C9 and C23 (Section 3.3.3.1 and Appendix A.2) the strength of the perturbations predicted by our simulations exceeds the observed signatures. For C10, C21, C22 and C30 (Section 3.3.3.2 and Appendix A.2) the amplitudes of the measured perturbation fields are well matched by our model results. The overestimation of the strength of Callisto's plasma interaction for the first class of observations (C3, C9 and C23) can be in large parts attributed to the uncertainties regarding the ambient plasma conditions. However, we can not rule out other reasons for the variations of the overall interaction strength such as a temporal variability for Callisto's neutral atmosphere. Although fluctuations in the atmospheric neutral density potentially explain the results of the radio occultation measurements, we see no other theoretical or observational indications for such a temporal dependence. Despite these uncertainties regarding the obtained magnetometer data fit, our data comparison clearly confirms the existence of a subsurface water ocean layer associated with induced magnetic fields, taking into account the signatures generated by the plasma interaction at Callisto.

4 Summary

In this thesis we analyze the plasma interaction and the atmosphere-ionosphere system of the Jovian satellite Callisto as well as the induced magnetic fields at all Galilean moons. Our studies are based on two numerical models. To investigate the plasma interaction and the atmospheric system we develop the first 3D MHD model for Callisto's plasma environment. Further, we use a model for the inducing primary and the induced secondary fields to predict the strength of the induction signals at the Galilean moons. A superposition of the magnetic field perturbations predicted by both of these models is used to examine the contribution of the induced magnetic field to the magnetic perturbations measured by the Galileo spacecraft at Callisto. Several studies (*Khurana et al.* 1998, *Zimmer et al.* 2000) interpreted these perturbations as an evidence for the existence of a liquid water ocean layer in the interior of the satellite. This possibly conductive ocean layer is the source region of induced magnetic fields caused by the temporally variable Jovian background field. All previous studies omitted the analysis of the additional magnetic perturbations generated due to the interaction of Callisto with the ambient magnetospheric plasma. These magnetic signatures potentially raise ambiguities regarding the interpretation of the measurements as they can mimic induced field signals. One key goal of this thesis is to verify the existence of the subsurface water ocean layer taking into account the plasma interaction signatures. Our MHD model includes a detailed aeronomic formulation for collision, ionization and recombination processes occurring in Callisto's CO_2 and O_2 neutral atmosphere. The ionospheric electron densities generated in our simulations can be used to study the atmosphere-ionosphere system of the satellite. Based on Galileo radio occultation measurements, *Kliore et al.* (2002) inferred electron density profiles for the ionosphere. The measurements indicate that Callisto possesses a substantial ionospheric layer which is subject to large temporal variations. The second key goal of the thesis at hand is to analyze possible reasons for this temporal variability and to infer information about the state of Callisto's atmosphere.

For our MHD model, we extend the ideal MHD equations solved by the ZEUS-MP code (*Hayes et al.* 2006) to account for the neutral atmosphere and the solid body of Callisto. To simulate the influence of the neutral particles on the background plasma we use aeronomic models of the photo ionization, impact ionization, dissociative recombination as well as electron- and ion-neutral collision processes. The variability of the solar photon flux for different flybys of Galileo at Callisto is fully included in our formulation for the photo ionization process. For the impact ionization we develop a procedure which takes into account the heating of the magnetospheric electrons near Callisto by heat conduction along the magnetic field lines connected to the satellite. Callisto's interior, which for numerical reasons needs to contain a suitable amount of plasma, is implemented by separate loss terms for the density and internal energy and by an enhanced collision term. These terms remove the plasma penetrating the surface and confine the virtual interior plasma. Our model is used to perform a series of simulations using idealized ambient plasma conditions as well as simulations for conditions during the Galileo flybys.

The general results of our MHD simulations, which consider ambient conditions occurring in the outer parts of the Jovian current sheet, indicate a strong interaction of Callisto's atmosphere and surface with the magnetospheric plasma. We predict a deceleration of the plasma flow in Callisto's vicinity and along the two Alfvén wing structures to $\sim 1\%$ of the ambient plasma velocities. Our simulation results indicate that complex flow patterns occur in the plasma tail of the satellite. These patterns are associated with velocities pointing towards Callisto and with eddy structures located in the vicinity of the satellite. The generation region for these tail structures is presumably located where the primary ionospheric plasma flows from northern and southern latitudes unite. Due to the lack of plasma parameter measurements and due to numerical uncertainties, the plausibility of the predicted tail features can, unfortunately, not be conclusively confirmed.

Photo ionization plays the dominant role for the generation of Callisto's ionosphere. Our model predicts that the contributions of ionospheric particles by the electron impact ionization are about three to four times lower. However, the magnetospheric electrons involved in the impact ionization accumulate in Callisto's shadow region with densities of up to 3 cm^{-3}. Therefore, electron impact ionization additionally generates a substantial amount of ionospheric particles ($n > 1{,}000\ \mathrm{cm}^{-3}$) in regions not affected by the sun. Regarding the reasons for the temporal variability of the ionospheric electron profiles observed for different directions of the solar irradiation (different solar phase angles) we discuss three hypotheses. First, the transport of ionospheric particles from their generation region to the location where the measurements were performed varies for different solar phase angles. Secondly, an asymmetric, sputtering generated atmosphere only allows the formation of a substantial ionospheric layer when the upstream hemisphere is sunlit. Thirdly, different ambient conditions for the solar photon flux or the ambient plasma conditions may explain the differences in the measurements for the relevant Galileo flybys C9, C22 and C23. For a combined O_2 and CO_2 atmosphere transport processes only play a minor role for the differences in the observed electron densities. Though transport becomes increasingly important for low neutral atmospheric densities, a pure CO_2 atmosphere still generates an amount of ionospheric electrons insufficient to explain the measured densities. This confirms the conclusion by *Kliore et al.* (2002) that an additional, presumably O_2 atmospheric constituent must be present at Callisto. Our simulation results prove that the decreased solar flux for C9 with respect to C22 and C23 causes some of the observed deviations for the electron densities. However, both the impacts of the plasma transport and of different ambient conditions are not sufficient to explain the absence of an ionosphere for C9. For an asymmetric neutral density distribution we infer the largest deviations in the ionospheric densities for the three relevant flybys. Therefore, we suggest that a sputtering induced atmosphere presents the best explanation for the observed temporal variabilities in the electron density profiles at Callisto.

As additional results from our interaction model, we calculate auroral intensities for the O_2, $\lambda = 1356$ Å emissions of ~6 R and of ~0.03 R for the CO_2, $\lambda = 1304$ Å emissions. These values indicate that Callisto's O_2 atmosphere should detectable using observations of the associated auroral radiation. If we decrease the O_2 surface densities by a factor of 0.1 the emissions for $\lambda = 1356$ Å drop by ~90% of the initial value. Therefore, a detection of Callisto's airglow is presumably not possible in this case. We further show that the major auroral intensities on Callisto's disk always occur in the shadow region of the satellite which is not directly observable from Earth. For all possible earthbound viewing geometries the case when Callisto's downstream hemisphere is sunlit yields the highest total intensities. For the current system near Callisto our model predicts a total Alfvén current of $I_{\text{Alfvén}} = 2 \times 10^5$ A through each Alfvén wing. Further, we infer values for the ionospheric Hall and Pedersen conductances of $\Sigma_P = 8,400$ S and $\Sigma_H = 6,900$ S. These values indicate that the Hall effect, not considered within the formulation of our MHD model, has an important impact at Callisto.

To analyze the induced magnetic fields at the Galilean moons we use an induction model which includes several sub-models. The temporally variable background magnetic field is inferred from a combined model for the intrinsic Jovian magnetic field, the field of the magnetospheric current sheet and for the field generated by Chapman-Ferraro currents at the magnetopause boundary. The inductive response of the interior is calculated using an analytical model for a spherical multi-layered conductivity distribution. The conductivity inside the satellite is inferred from two interior models for each satellite which include a subsurface ocean layer. For all four satellites we infer the amplitudes and frequencies of the available primary fields given by the magnetospheric field model. The primary field results are used to predict the induced magnetic fields caused by the possibly conductive ocean and core layers at the Galilean moons.

Our magnetospheric field model predicts field fluctuations for three major periodicities. The major signals occur for the synodic Jovian rotation period of ~10 h. These signals with a strength of up to 750 nT for Io, ~210 nT at Europa, ~80 nT at Ganymede and ~40 nT at Callisto are caused by the rapid rotation of the intrinsic Jovian field and the current sheet. Further, the inclination and eccentricity of the satellites' orbits as well as the shape of the magnetopause cause field fluctuations at the orbital periods of 42.45 h for Io, 85.22 h for Europa, 171.70 h for Ganymede and 400.55 h for Callisto. The respective primary field strengths are 26 nT for Io, 17 nT for Europa, 2.5 nT for Ganymede and 3 nT for Callisto. Thirdly, the solar rotation at a period of 641.9 h induces fluctuations of the magnetopause field which yield primary signals of 1.1 to 1.2 nT for all satellites.

The secondary magnetic fields induced in the potential ocean layers inside the satellites reach amplitudes which allow for measurements analyzing several of the frequencies mentioned above. The major signal strengths at the surface of 16 nT for Callisto, 32 nT for Ganymede, 80 nT for Europa and 210 nT for Io occur for the synodic Jovian rotation periods. The signal contributions of the core layers could be used to infer information about the conductivity and, hence, the state of the core. The respective amplitudes with a maximum of 0.4 nT for Callisto, 2 nT for Ganymede and 5 nT for Europa and Io are, however, possibly too weak to allow for suitable measurements.

The magnetic perturbations measured for the C3 and C9 Galileo flybys at Callisto which were interpreted as induced field signals were the base of previous studies reporting the discovery of Callisto's ocean layer (*Khurana et al.* 1998, *Zimmer et al.* 2000). The results of our MHD and induction models prove that for C9 the perturbations caused by both the plasma interaction and the induction effect generate similar signatures. Therefore, based on the C9 measurements alone, the verification of Callisto's ocean is not possible. However, the MHD model results for C3 predict magnetic signatures which are directed oppositely to the measured perturbations. The induced fields predicted by our induction model and therefore the existence of a conductive layer inside the satellite provide the only reasonable explanation for the C3 measurements. Induced fields generated in a subsurface water ocean are therefore consistent with both the C3 and the C9 measurements when the plasma interaction of Callisto is taken into account. This conclusion holds also true for the C10, C22, C23 and C30 Galileo magnetic field measurements. Only for C21 the induced fields are directed oppositely to the observed perturbations. However, for this flyby the induced signals are presumably obscured by strong plasma interaction signals and could therefore still be present. Though we can not infer precise information about the state of Callisto's ocean, the configuration assumed for our induction model with a conductivity of terrestrial sea water of $\sigma = 5$ S m^{-1}, an extension of $h = 10$ km and a depth of 150 km below the surface yields a suitable data fit for all of the discussed flybys. It should finally be noted that the magnetic field perturbations predicted for simulations assuming an asymmetric atmosphere at Callisto do not contradict the measurements.

Summarizing the conclusions regarding the key goals of this thesis, we can state that induced fields generated in a conductive ocean layer inside Callisto are consistent with the magnetic field measurements, even when the plasma interaction signatures are taken into account. A sputtering generated neutral atmosphere which is primarily confined to the upstream hemisphere presents the best explanation for the temporal variability of Callisto's ionosphere. An O_2 atmospheric constituent, whose existence is still not directly verified, is, indeed, needed to explain the high ionospheric electron densities, even when plasma transport processes are taken into account. To verify the conclusions presented above additional measurements of Callisto's magnetic field and atmospheric environment are inevitable. The next opportunity to perform these measurements is the upcoming JUICE mission which will, presumably, arrive at Jupiter in 2030.

A Appendix

A.1 Maxwell's equations

In SI units Maxwell's equations can be written in the following macroscopic form (e.g., *Kivelson and Russell* 1995, *Baumjohann and Treumann* 1996, *Jackson* 1998):

Poisson's equation:

$$\nabla \cdot \mathbf{D} = \rho_q \tag{A.1}$$

Faraday's law:

$$\frac{\partial \mathbf{B}}{\partial t} = -\nabla \times \mathbf{E} \tag{A.2}$$

Ampere's law:

$$\nabla \times \mathbf{H} = \mathbf{j} + \frac{\partial \mathbf{D}}{\partial t} \tag{A.3}$$

Gauss's law for magnetism:

$$\nabla \cdot \mathbf{B} = 0 \tag{A.4}$$

Lorenz-force law:

$$\mathbf{F} = q\,(\mathbf{E} + \mathbf{v} \times \mathbf{B}) \tag{A.5}$$

For the above equations **D** and **E** denote the displacement field and electric field connected trough $\mathbf{D} = \epsilon\mathbf{E} = \epsilon_0\,(1 + \chi_e)\,\mathbf{E}$, with the permittivity of free space ϵ_0 and the electric susceptibility χ_e. **H** and **B** are the magnetic intensity and field related by $\mathbf{H} = \mathbf{B}/\mu = \mu_0\,(1 + \chi_m)\,\mathbf{B}$, with the permeability of free space μ_0 and the magnetic susceptibility χ_m. Further, ρ_q is the charge density, t denotes the time, **j** the current density, q the particle charge and **v** the velocity.

A.2 Data comparison for C21, C23 and C30

Apart from the measurements for C3, C9, C10 and C22 presented in Section 3.3.3, Galileo recorded magnetic field data during three additional encounters of Callisto. In analogy to the procedure for the other flybys, we modeled the magnetic field environment for the C21, C23 and C30 encounters using the default flyby setups introduced in Section 3.2.5. Figures A.1, A.3 and A.5 depict the resulting magnetic field signatures for these three flybys, based on a superposition of the background field $\mathbf{B}_0(t)$ and the modeled plasma perturbation fields $\mathbf{B}_p$ (blue lines), of $\mathbf{B}_0(t)$ and the induced field $\mathbf{B}_{\text{sec}}$ predicted by our induction model (red lines) and of all three contributions to the measured field (solid green lines). For C21 and C30 a superposition of $\mathbf{B}_0(t)$, $\mathbf{B}_{\text{sec}}$ and the plasma interaction fields for a model using the measured background plasma parameters is given by the green dashed lines. Note that for C23 a model setup for the plasma parameters given in Table 3.2 is not considered due to the unrealistic strong negative v_x velocity component (v_ϕ in System III coordinates). The perturbation regions and flyby geometries for each case are given in Figures A.2, A.4 and A.6. We now shortly mark some notable aspects of the observed and modeled signatures.

For the C21 flyby the magnitude of the predicted induction signatures of ~5 nT in B_x and B_y is considerably lower than the measured perturbations of 50 nT in B_x and ~25 nT in B_y. The sign of $\mathbf{B}_{\text{sec}}$ is generally reversed with respect to the measured signatures. Peaks similar to the ones measured B_x and B_z for C21 are also given for the C10 flyby (Section 3.3.3.2). The good data fit of the B_y and, in parts, the B_x component indicate that all of the measured perturbations for C21 are primarily caused by Callisto's plasma interaction.

For C23 the measured perturbations show a unstructured oscillating behavior. For this encounter Callisto was located closer to the current sheet center than for any other Galileo flyby. Therefore, the primary field and the associated induced signals were close to their zero crossings. This is in agreement with the low perturbation signatures measured in B_x and B_y around the closest approach. The data comparison shows large deviations between the measurements and the predicted plasma magnetic fields of up to 20 nT both in B_x and B_y. These deviations are probably related to the plasma conditions in the vicinity of the current sheet which are generally not well matched by the conditions assumed for our default flyby setups.

During the C30 flyby Galileo reached the lowest altitude for all Callisto encounters of only 132 km. The timing of the first distinct positive perturbation signatures in B_x and B_z is slightly displaced with respect to the predicted plasma induction signatures in our model. This indicates the the general geometry of the plasma interaction is not well matched both our model scenarios. During the closest approach the positive B_y peak can be identified as induced field signals of about 14 nT. The signatures in all magnetic component shortly after the closest approach are well represented by our interaction model. They can be attributed to a short encounter of the anti-Jovian Alfvén wing, which is shifted towards the north in this case. Note that in contrast to all other flybys of Galileo the background magnetic field for C30 primarily points in the north-south direction.

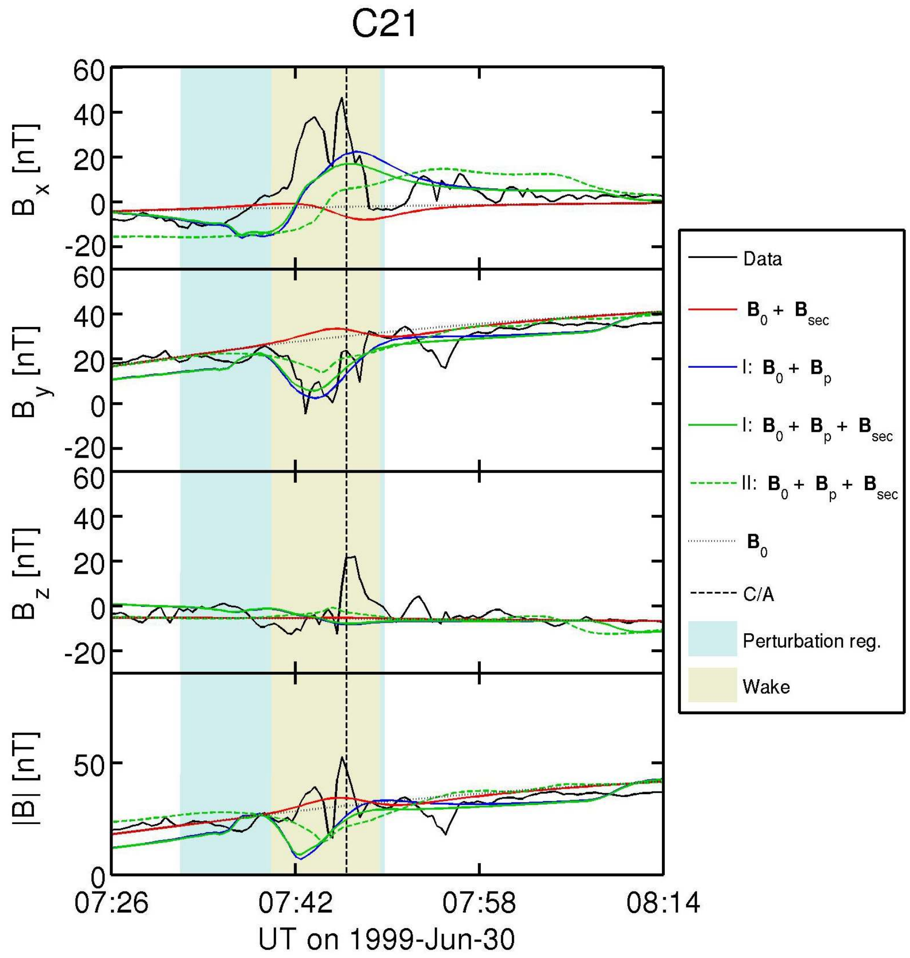

Figure A.1: *C21 magnetic field data and model results. Case I (solid lines) refers to a scenario using the C21 plasma data, while case II (dashed lines) refers to the C21 default flyby scenario. See Figure 3.36 for further explanations.*

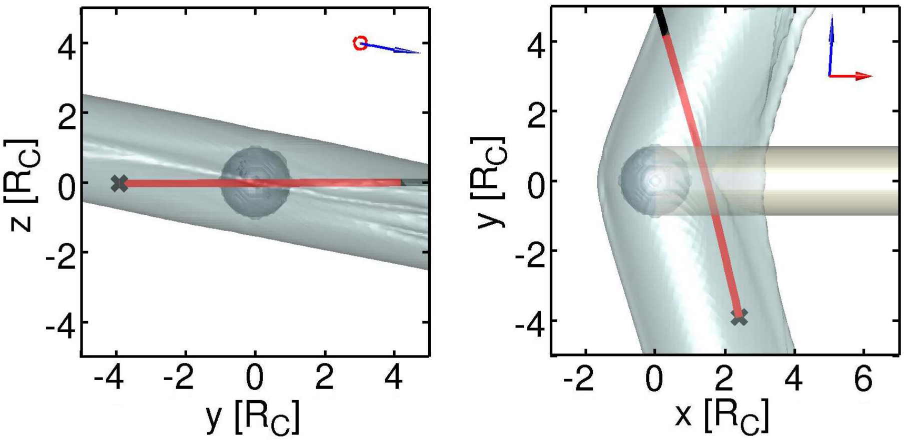

Figure A.2: *3D-isosurfaces of the perturbation region defined by* $v < 19.2$ *km* s^{-1} *for the C21 default flyby scenario. See Figure 3.38 for further explanations.*

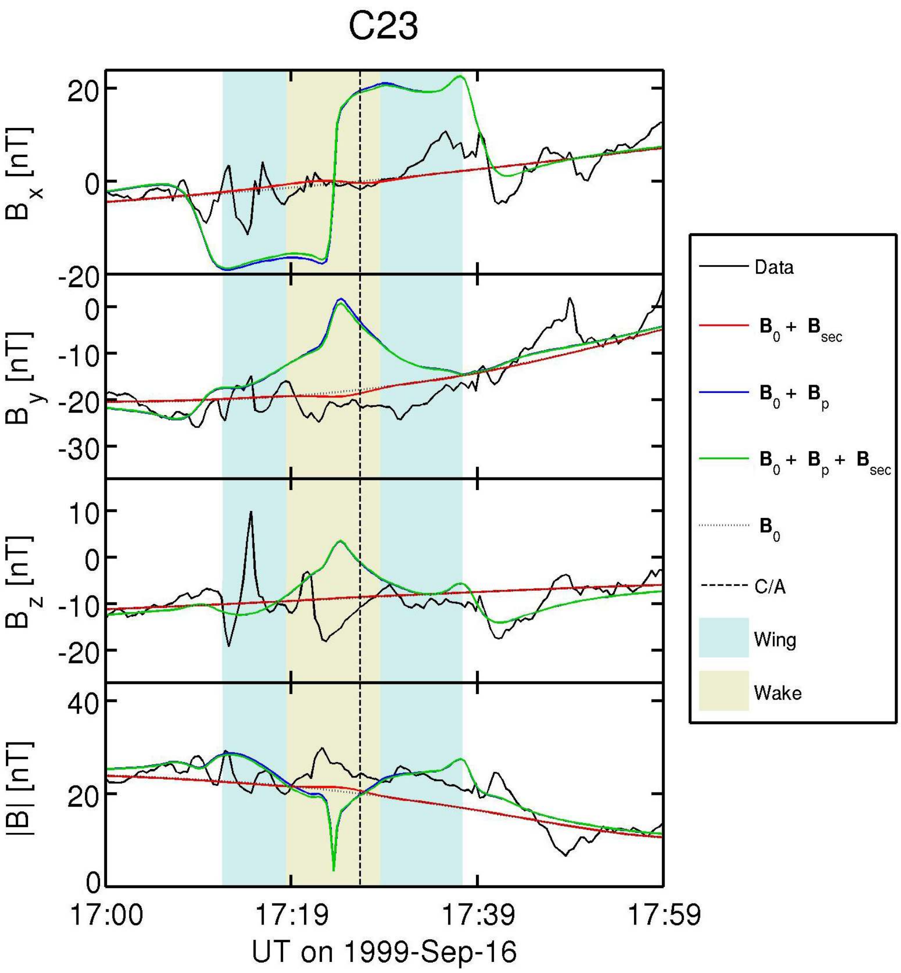

Figure A.3: *Magnetic field data and model results for the C23 default flyby scenario. See Figure 3.36 for further explanations.*

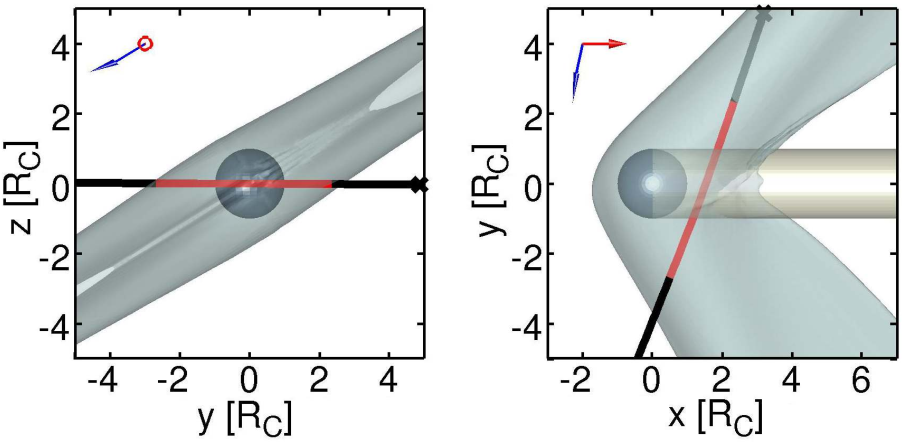

Figure A.4: *3D-isosurfaces of the perturbation region defined by* $v < 19.2$ *km* s^{-1} *for the C23 default flyby scenario. See Figure 3.38 for further explanations.*

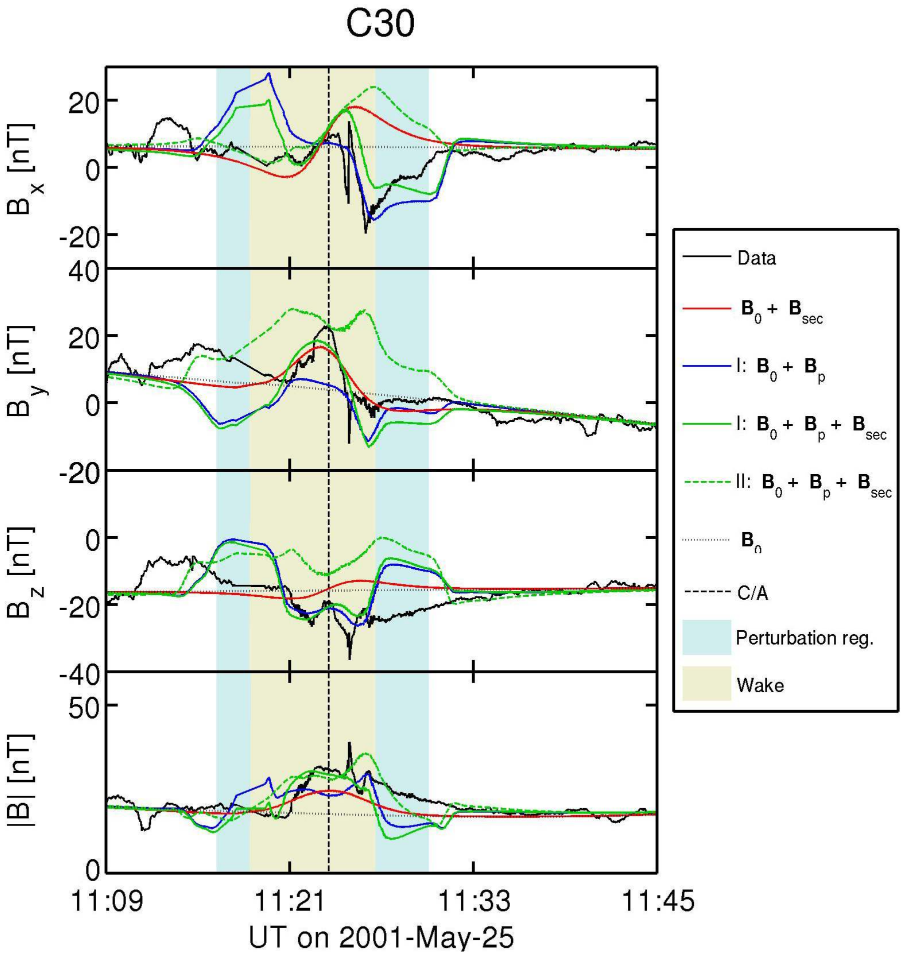

Figure A.5: *C30 magnetic field data and model results. Case I (solid lines) refers to the C30 default flyby scenario while case II (dashed lines) refers to a scenario using the C30 plasma data. See Figure 3.36 for further explanations.*

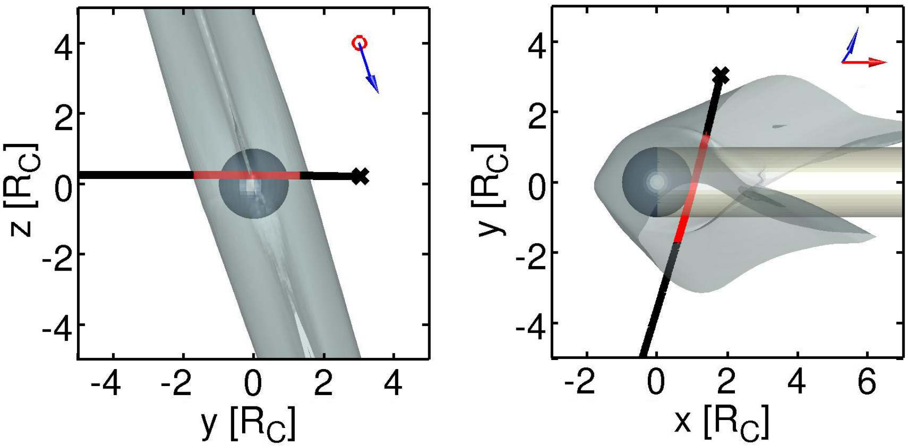

Figure A.6: *3D-isosurfaces of the perturbation region defined by* $v < 19.2$ *km* s^{-1} *for the C30 default flyby scenario. See Figure 3.38 for further explanations.*

Bibliography

Abramowitz, M., and I. Stegun (1964), *Handbook of Mathematical Functions*, fifth ed.

Acuna, M. H., and N. F. Ness (1976), The main magnetic field of Jupiter, *J. Geophys. Res.*, *81*, 2917–2922.

Alexeev, I. I., and E. S. Belenkaya (2005), Modeling of the Jovian Magnetosphere, *Ann. Geophysicae*, *23*, 809–826.

Anderson, J. D., E. L. Lau, W. L. Sjogren, G. Schubert, and W. B. Moore (1996), Gravitational constraints on the internal structure of Ganymede, *Nature*, *384*, 541–543.

Anderson, J. D., G. Schubert, R. A. Jacobson, E. L. Lau, W. B. Moore, and W. L. Sjogren (1998), Europa's differentiated internal structure: Inferences from four Galileo encounters, *Science*, *281*, 2019–2022.

Anderson, J. D., R. A. Jacobson, E. L. Lau, W. B. Moore, and G. Schubert (2001a), Io's gravity field and interior structure, *J. Geophys. Res.*, *106*, 32,963–32,970.

Anderson, J. D., R. A. Jacobson, T. P. McElrath, W. B. Moore, G. Schubert, and P. C. Thomas (2001b), Shape, Mean Radius, Gravity Field, and Interior Structure of Callisto, *Icarus*, *153*, 157–161.

Backes, H. (2004), Titan's Interaction with the Saturnian Magnetospheric Plasma, Dissertation, Institut für Geophysik und Meteorologie der Universität zu Köln.

Bagenal, F., and P. A. Delamere (2011), Flow of mass and energy in the magnetospheres of Jupiter and Saturn, *J. Geophys. Res.*, *116*, 5209.

Bagenal, F., and J. D. Sullivan (1981), Direct plasma measurements in the Io torus and inner magnetosphere of Jupiter, *J. Geophys. Res.*, *86*, 8447–8466.

Banks, P. M., and G. Kockarts (1973), *Aeronomy.*, New York: Academic Press.

Barr, A. C., and R. M. Canup (2010), Origin of the Ganymede-Callisto dichotomy by impacts during the late heavy bombardment, *Nature Geoscience*, *3*, 164–167.

Bauer, S. J. (1973), *Physics of planetary ionospheres*, Berlin: Springer.

Baumjohann, W., and R. A. Treumann (1996), *Basic space plasma physics*, London: Imperial College Press.

Beblo, M., A. Berktold, U. Bleil, H. Gebrande, B. Grauert, U. Haack, V. Haak, H. Kern, H. Miller, N. Petersen, J. Pohl, F. Rummel, and J. R. Schopper (1985), Physical Properties of Rocks, in *Landolt-Börnstein New-Series*, vol. V/1 Subvolume B, 6 ed., pp. 1–604, Springer-Verlag.

Behannon, K. W., L. F. Burlaga, and N. F. Ness (1981), The Jovian magnetotail and its current sheet, *J. Geophys. Res.*, *86*, 8385–8401.

Bellan, P. M. (2006), *Fundamentals of Plasma Physics*, Cambridge, UK: Cambridge University Press.

Bland, M. T., A. P. Showman, and G. Tobie (2009), The orbital thermal evolution and global expansion of Ganymede, *Icarus*, *200*, 207–221.

Bode, T. D. (1994), Modeling the Diurnally Precessing Jovian Magnetospheric Field, U.S.N.A. - Trident Scholar Project Report.

Buratti, B. J. (1991), Ganymede and Callisto - Surface textural dichotomies and photometric analysis, *Icarus*, *92*, 312–323.

Carlson, R. W. (1999), A Tenuous Carbon Dioxide Atmosphere on Jupiter's Moon Callisto, *Science*, *283*, 820–821.

Cassen, P., R. T. Reynolds, and S. J. Peale (1979), Is there liquid water on Europa, *Geophys. Res. Lett.*, *6*, 731–734.

Chapman, S., and J. Bartels (1940), *Geomagnetism*, vol. 2, Oxford Univ. Press.

Chapman, S., and V. C. A. Ferraro (1930), A New Theory of Magnetic Storms., *Nature*, *126*, 129–130.

Clarke, J. T., S. Wannawichian, N. Hernandez, B. Bonfond, J.-C. Gerard, and D. Grodent (2011), Detection of Auroral Emissions from Callisto's Magnetic Footprint at Jupiter, in *EPSC-DPS Joint Meeting 2011*, p. 1468.

Connerney, J. E. P., M. H. Acuña, and N. F. Ness (1981), Modeling the Jovian current sheet and inner magnetosphere, *J. Geophys. Res.*, *86*, 8370–8384.

Connerney, J. E. P., M. H. Acuña, N. F. Ness, and T. Satoh (1998), New models of Jupiter's magnetic field constrained by the Io flux tube footprint, *J. Geophys. Res.*, *103*(A6), 11,929–11,940.

Constable, S., and C. Constable (2004), Observing geomagnetic induction in magnetic satellite measurements and associated implications for mantle conductivity, *Geochem. Geophys. Geosyst.*, *5*(1), Q01,006.

Dessler, A. J. (2002), *Physics of the Jovian Magnetosphere*, Cambridge, UK: Cambridge University Press.

Dobson, D. P., and J. P. Brodholt (2000), The Electrical Conductivity and Thermal Profile of the Earth's mid-mantle, *Geophys. Res. Lett.*, *15*(27), 2325–2328.

Engle, I. M. (1992), Diurnal Variation in Jovian Subsolar Magnetopause Position, *J. Geophys. Res.*, *97*(A11), 17,169–17,172.

Engle, I. M., and D. B. Beard (1980), Idealized Jovian Magnetosphere Shape and Field, *J. Geophys. Res.*, *A2*(85), 579–592.

Frank, L. A., and W. R. Paterson (2002), Galileo observations of electron beams and thermal ions in Jupiter's magnetosphere and their relationship to the auroras, *J. Geophys. Res.*, *107*, 1478.

Goertz, C. K., and P. A. Deift (1973), Io's interaction with the magnetosphere, *Planet. Space Sci.*, *21*, 1399–1415.

Goldreich, P., and D. Lynden-Bell (1969), Io, a jovian unipolar inductor, *Astrophys. J.*, *156*, 59–78.

Greeley, R., J. E. Klemaszewski, and R. Wagner (2000), Galileo views of the geology of Callisto, *Planet. Space Sci.*, *48*, 829–853.

Greeley, R., C. F. Chyba, J. W. Head, III, T. B. McCord, W. B. McKinnon, R. T. Pappalardo, and P. H. Figueredo (2004), Geology of Europa, in *Jupiter. The Planet, Satellites and Magnetosphere*, edited by Bagenal, F., Dowling, T. E., & McKinnon, W. B., pp. 329–362, Cambridge Univ. Press.

Grimm, R. E., D. E. Stillman, S. F. Dec, M. A. Bullock, and J. C. Priscu (2007), Charge Mobility in Ice Brines and Ice-Silicate Mixtures, *Annual report*, NASA Exobiology Program.

Grün, E., H. Krüger, A. L. Graps, D. P. Hamilton, A. Heck, G. Linkert, H. A. Zook, S. Dermott, H. Fechtig, B. A. Gustafson, M. S. Hanner, M. Horányi, J. Kissel, B. A. Lindblad, D. Linkert, I. Mann, J. A. M. McDonnell, G. E. Morfill, C. Polanskey, G. Schwehm, and R. Srama (1998), Galileo observes electromagnetically coupled dust in the Jovian magnetosphere, *J. Geophys. Res.*, *103*, 20,011–20,022.

Gurnett, D. A., W. S. Kurth, A. Roux, and S. J. Bolton (1997), Absence of a magnetic-field signature in plasma-wave observations at Callisto, *Nature*, *387*, 261–262.

Gurnett, D. A., A. M. Persoon, W. S. Kurth, A. Roux, and S. J. Bolton (2000), Plasma densities in the vicinity of Callisto from Galileo plasma wave observations, *Geophys. Res. Lett.*, *27*, 1867–1870.

Hall, D. T., P. D. Feldman, M. A. McGrath, and D. F. Strobel (1998), The Far-Ultraviolet Oxygen Airglow of Europa and Ganymede, *Astrophys. J.*, *499*, 475.

Hanel, R., B. Conrath, M. Flasar, L. Herath, V. Kunde, P. Lowman, W. Maguire, J. Pearl, J. Pirraglia, and L. Horn (1979), Infrared observations of the Jovian system from Voyager 2, *Science*, *206*, 952–956.

Hayes, J. C., M. L. Norman, R. A. Fiedler, J. O. Bordner, P. S. Li, S. E. Clark, A. ud-Doula, and M.-M. Mac Low (2006), Simulating Radiating and Magnetized Flows in Multiple Dimensions with ZEUS-MP, *Astrophys. J. Suppl. Ser.*, *165*, 188–228.

Hill, T. W. (1979), Inertial limit on corotation, *J. Geophys. Res.*, *84*, 6554–6558.

Hill, T. W. (2001), The Jovian auroral oval, *J. Geophys. Res.*, *106*, 8101–8108.

Huddleston, D. E., C. T. Russell, M. G. Kivelson, K. K. Khurana, and L. Bennett (1998), Location and shape of the Jovian magnetopause and bow shock, *J. Geophys. Res.*, *103*(E9), 20,075–20,082.

Hwang, W., and Y.-K. Kim (1996), New model for electron-impact ionization cross sections of molecules, *J. Chem. Phys.*, *104*, 2956–2966.

Ip, W.-H. (1996), Europa's Oxygen Exosphere and Its Magnetospheric Interaction, *Icarus*, *120*, 317–325.

Itikawa, Y. (2002), Cross Sections for Electron Collisions With Carbon Dioxide, *J. Phys. Chem. Ref. Data*, *31*, 749–767.

Jackson, J. D. (1998), *Classical electrodynamics*, New York: John Wiley and Sons, INC., 3nd ed.

Jacobsen, S. (2011), Three-Dimensional Magnetohydrodynamic Simulations of Io's Nonlinear Interaction with the Jovian Magnetosphere, Dissertation, Institut für Geophysik und Meteorologie der Universität zu Köln.

Jeon, B.-H. (2003), Determination of Electron Collision Cross-Sections for the Oxygen Molecule by Using an Electron Swarm Study, *J. Kor. Phys. Soc.*, *43*, 513–525.

Jia, X., R. J. Walker, M. G. Kivelson, K. K. Khurana, and J. A. Linker (2008), Three-dimensional MHD simulations of Ganymede's magnetosphere, *J. Geophys. Res.*, *113*, 6212.

Jia, X., M. G. Kivelson, K. K. Khurana, and R. J. Walker (2009), Magnetic Fields of the Satellites of Jupiter and Saturn, *Space Sci. Rev.*

Joy, S. P., M. G. Kivelson, R. J. Walker, K. K. Khurana, C. T. Russell, and T. Ogino (2002), Probabilistic models of the Jovian magnetopause and bow shock locations, *J. Geophys. Res.*, *107*, 1309.

Kanik, I., C. Noren, O. P. Makarov, P. Vattipalle, J. M. Ajello, and D. E. Shemansky (2003), Electron impact dissociative excitation of O_2: 2. Absolute emission cross sections of the OI(130.4 nm) and OI(135.6 nm) lines, *J. Geophys. Res.*, *108*, 5126.

Keszthelyi, L., A. S. McEwen, and G. J. Taylor (1999), Revisiting the Hypothesis of a Mushy Global Magma Ocean in Io, *Icarus*, *141*, 415–419.

Keszthelyi, L., W. L. Jaeger, E. P. Turtle, M. Milazzo, and J. Radebaugh (2004), A post-Galileo view of Io's interior, *Icarus*, *169*, 271–286.

Khurana, K. K. (1997), Euler potential models of Jupiter's magnetospheric field, *J. Geophys. Res.*, *102*, 11,295.

Khurana, K. K., and M. G. Kivelson (1993), Inference of the angular velocity of plasma in the Jovian magnetosphere from the sweepback of magnetic field, *J. Geophys. Res.*, *98*, 67–79.

Khurana, K. K., M. G. Kivelson, C. T. Russell, R. J. Walker, and D. J. Southwood (1997), Absence of an internal magnetic field at Callisto, *Nature*, *387*, 262–264.

Khurana, K. K., M. G. Kivelson, D. J. Stevenson, G. Schubert, C. T. Russell, R. J. Walker, and C. Polanskey (1998), Induced magnetic fields as evidence for subsurface oceans in Europa and Callisto, *Nature*, *395*, 777–780.

Khurana, K. K., M. G. Kivelson, V. M. Vasyliunas, N. Krupp, J. Woch, A. Lagg, B. H. Mauk, and W. S. Kurth (2004), The configuration of Jupiter's magnetosphere, in *Jupiter. The Planet, Satellites and Magnetosphere*, edited by Bagenal, F., Dowling, T. E., & McKinnon, W. B., pp. 593–616, Cambridge Univ. Press.

Khurana, K. K., X. Jia, M. G. Kivelson, F. Nimmo, G. Schubert, and C. T. Russell (2011), Evidence of a Global Magma Ocean in Io's Interior, *Science*, *332*, 1186–1189.

Kimura, J., T. Nakagawa, and K. Kurita (2009), Size and compositional constraints of Ganymede's metallic core for driving an active dynamo, *Icarus*, *202*, 216–224.

Kivelson, M. G. (2004), Moon-magnetosphere interactions: a tutorial, *Advances in Space Research*, *33*, 2061–2077.

Kivelson, M. G., and C. T. Russell (1995), *Introduction to Space Physics*.

Kivelson, M. G., K. K. Khurana, J. D. Means, C. T. Russell, and R. C. Snare (1992), The Galileo magnetic field investigation, *Space Sci. Rev.*, *60*, 357–383.

Kivelson, M. G., K. K. Khurana, C. T. Russell, R. J. Walker, J. Warnecke, F. V. Coroniti, C. Polanskey, D. J. Southwood, and G. Schubert (1996), Discovery of Ganymede's magnetic field by the Galileo spacecraft, *Nature*, *384*, 537–541.

Kivelson, M. G., K. K. Khurana, R. J. Walker, J. Warnecke, C. T. Russell, J. A. Linker, D. J. Southwood, and C. Polanskey (1996), Io's Interaction with the Plasma Torus: Galileo Magnetometer Report, *Science*, *274*, 396–398.

Kivelson, M. G., K. K. Khurana, D. J. Stevenson, L. Bennett, S. Joy, C. T. Russell, R. J. Walker, C. Zimmer, and C. Polanskey (1999), Europa and Callisto: Induced or intrinsic fields in a periodically varying plasma environment, *J. Geophys. Res.*, *104*, 4609–4626.

Kivelson, M. G., K. K. Khurana, C. T. Russell, M. Volwerk, R. J. Walker, and C. Zimmer (2000), Galileo magnetometer measurements: A Stronger case for a subsurface ocean at Europa, *Science*, *289*, 1340–1343.

Kivelson, M. G., K. K. Khurana, C. T. Russell, S. P. Joy, M. Volwerk, R. J. Walker, C. Zimmer, and J. A. Linker (2001), Magnetized or unmagnetized: Ambiguity persists following Galileo's encounters with Io in 1999 and 2000, *J. Geophys. Res.*, *106*, 26,121–26,136.

Kivelson, M. G., K. K. Khurana, and M. Volwerk (2002), The Permanent and Inductive Magnetic Moments of Ganymede, *Icarus*, (157), 507–522.

Kivelson, M. G., F. Bagenal, W. S. Kurth, F. M. Neubauer, C. Paranicas, and J. Saur (2004), Magnetospheric interactions with satellites, in *Jupiter. The planet, satellites and magnetosphere.*, edited by F. Bagenal, T. E. Dowling, and W. B. McKinnon, pp. 513–536, Cambridge Univ. Press.

Kliore, A. J., D. P. Hinson, F. M. Flasar, A. F. Nagy, and T. E. Cravens (1997), The ionosphere of Europa from Galileo radio occultations, *Science*, *277*, 355–358.

Kliore, A. J., A. Anabtawi, R. G. Herrera, S. W. Asmar, A. F. Nagy, D. P. Hinson, and F. M. Flasar (2002), Ionosphere of Callisto from Galileo radio occultation observations, *Journal of Geophysical Research (Space Physics)*, *107*, 1407.

Kriegel, H., S. Simon, J. Müller, U. Motschmann, J. Saur, K.-H. Glassmeier, and M. K. Dougherty (2009), The plasma interaction of Enceladus: 3D hybrid simulations and comparison with Cassini MAG data, *Planet. Space Sci.*, *57*, 2113–2122.

Krupp, N., V. M. Vasyliunas, J. Woch, A. Lagg, K. K. Khurana, M. G. Kivelson, B. H. Mauk, E. C. Roelof, D. J. Williams, S. M. Krimigis, W. S. Kurth, L. A. Frank, and W. R. Paterson (2004), Dynamics of the Jovian magnetosphere, in *Jupiter. The Planet, Satellites and Magnetosphere*, edited by Bagenal, F., Dowling, T. E., & McKinnon, W. B., pp. 617–638, Cambridge Univ. Press.

Kuramoto, K., Y. Saiganji, and T. Yamamoto (1998), Oscillating Magnetic Dipole Moment of Europa Induced by Jovian Magnetic Field: A Possible Probe for Detecting Europa's Ocean, *29*, 1254.

Kuskov, O. L., and V. A. Kronrod (2005a), Internal structure of Europa and Callisto, *Icarus*, *177*, 550–569.

Kuskov, O. L., and V. A. Kronrod (2005b), Models of the Internal Structure of Callisto, *Solar System Research*, *39*, 283–301.

Lahiri, B. N., and A. T. Price (1939), Electromagnetic Induction in Non-Uniform Conductors, and the Determination of the Conductivity of the Earth from Terrestrial Magnetic Variations, *Phil. Trans. Roy.*, *237*, 509–540.

Lellouch, E., M. A. McGrath, and K. L. Jessup (2007), Io's atmosphere, in *Io After Galileo: A New View of Jupiter's Volcanic Moon*, edited by R. M. C. Lopes and J. R. Spencer, p. 231, Springer Praxis Books.

Liang, M.-C., B. F. Lane, R. T. Pappalardo, M. Allen, and Y. L. Yung (2005), Atmosphere of Callisto, *J. Geophys. Res.*, *110*, 2003.

Liu, Y., A. F. Nagy, K. Kabin, M. R. Combi, D. L. Dezeeuw, T. I. Gombosi, and K. G. Powell (2000), Two-species, 3D, MHD Simulation of Europa's Interaction with Jupiter's Magnetosphere, *Geophys. Res. Lett.*, *27*, 1791.

Mauk, B. H., and J. Saur (2007), Equatorial electron beams and auroral structuring at Jupiter, *J. Geophys. Res.*, *112*, 10,221.

Maumus, J., N. Bagdassarov, and H. Schmeling (2005), Electrical conductivity and partial melting of mafic rocks under pressure, *Geochimica et Cosmochimica Acta*, *69*(19), 4703–4718.

McGrath, M. A., E. Lellouch, D. F. Strobel, P. D. Feldman, and R. E. Johnson (2004), Satellite atmospheres, in *Jupiter. The Planet, Satellites and Magnetosphere*, edited by Bagenal, F., Dowling, T. E., & McKinnon, W. B., pp. 457–483, Cambridge Univ. Press.

McKinnon, W. B. (2007), Formation and early evolution of Io, in *Io After Galileo: A New View of Jupiter's Volcanic Moon*, edited by R. M. C. Lopes and J. R. Spencer, pp. 61–88, Springer Praxis Books / Geophysical Sciences.

Moore, J. M., E. Asphaug, D. Morrison, J. R. Spencer, C. R. Chapman, B. Bierhaus, R. J. Sullivan, F. C. Chuang, J. E. Klemaszewski, R. Greeley, K. C. Bender, P. E. Geissler, P. Helfenstein, and C. B. Pilcher (1999), Mass Movement and Landform Degradation on the Icy Galilean Satellites: Results of the Galileo Nominal Mission, *Icarus*, *140*, 294–312.

Moore, J. M., C. R. Chapman, E. B. Bierhaus, R. Greeley, F. C. Chuang, J. Klemaszewski, R. N. Clark, J. B. Dalton, C. A. Hibbitts, P. M. Schenk, J. R. Spencer, and R. Wagner (2004), Callisto, in *Jupiter. The Planet, Satellites and Magnetosphere*, edited by Bagenal, F., Dowling, T. E., & McKinnon, W. B., pp. 397–426, Cambridge Univ. Press.

Moore, W. B., and G. Schubert (2003), The tidal response of Ganymede and Callisto with and without liquid water oceans, *Icarus*, *166*, 223–226.

Mueller, S., and W. B. McKinnon (1988), Three-layered models of Ganymede and Callisto - Compositions, structures, and aspects of evolution, *Icarus*, *76*, 437–464.

Neubauer, F. M. (1980), Nonlinear standing Alfven wave current system at Io - Theory, *J. Geophys. Res.*, *85*, 1171–1178.

Neubauer, F. M. (1998a), Oceans inside Jupiter's moons, *Nature*, *395*, 749–750.

Neubauer, F. M. (1998b), The sub-Alfvénic interaction of the Galilean satellites with the Jovian magnetosphere, *J. Geophys. Res.*, *103*(E9), 19,843–19,866.

Neubauer, F. M. (1999), Alfvén wings and electromagnetic induction in the interiors: Europa and Callisto, *J. Geophys. Res.*, *104*(A12), 28,671–28,684.

Olsen, N. (1999), Induction studies with satellite data, *Surveys in Geophysics*, *20*, 309–340.

Pappalardo, R. T., M. J. S. Belton, H. H. Breneman, M. H. Carr, C. R. Chapman, G. C. Collins, T. Denk, S. Fagents, P. E. Geissler, B. Giese, R. Greeley, R. Greenberg, J. W. Head, P. Helfenstein, G. Hoppa, S. D. Kadel, K. P. Klaasen, J. E. Klemaszewski, K. Magee, A. S. McEwen, J. M. Moore, W. B. Moore, G. Neukum, C. B. Phillips,

L. M. Prockter, G. Schubert, D. A. Senske, R. J. Sullivan, B. R. Tufts, E. P. Turtle, R. Wagner, and K. K. Williams (1999), Does Europa have a subsurface ocean? Evaluation of the geological evidence, *J. Geophys. Res.*, *104*, 24,015–24,056.

Pappalardo, R. T., G. C. Collins, J. W. Head, III, P. Helfenstein, T. B. McCord, J. M. Moore, L. M. Prockter, P. M. Schenk, and J. R. Spencer (2004), Geology of Ganymede, in *Jupiter. The Planet, Satellites and Magnetosphere*, edited by Bagenal, F., Dowling, T. E., & McKinnon, W. B., pp. 363–396, Cambridge Univ. Press.

Parkinson, W. D. (1983), *Introduction to Geomagnetism*, Scottish Academic Press Ltd.

Parthasarathy, G., and S. R. Sharma (2004), High-temperature electrical and thermal properties of Burdett, Dalhart, Faucet and Wellman ordinary chondrites, *Current Science*, *86*(10), 1366–1368.

Peale, S. J., P. Cassen, and R. T. Reynolds (1979), Melting of Io by tidal dissipation, *Science*, *203*, 892–894.

Piddington, J. H., and J. F. Drake (1968), Electrodynamic Effects of Jupiter's Satellite Io, *Nature*, *217*, 935–937.

Pospieszalska, M. K., and R. E. Johnson (1989), Magnetospheric ion bombardment profiles of satellites - Europa and Dione, *Icarus*, *78*, 1–13.

Richards, P. G., J. A. Fennelly, and D. G. Torr (1994), EUVAC: A solar EUV flux model for aeronomic calculations, *J. Geophys. Res.*, *99*, 8981–8992.

Riley, K., M. Hobson, and S. S.J. Bence (2006), *Mathematical Methods for Physics and Engineering*, 3 ed., Cambridge Univ. Press.

Roesler, F. L., H. W. Moos, R. J. Oliversen, R. C. Woodward, Jr., K. D. Retherford, F. Scherb, M. A. McGrath, W. H. Smyth, P. D. Feldman, and D. F. Strobel (1999), Far-Ultraviolet Imaging Spectroscopy of Io's Atmosphere with HST/STIS, *Science*, *283*, 353.

Roth, L., J. Saur, K. D. Retherford, D. F. Strobel, and J. R. Spencer (2011), Simulation of Io's auroral emission: Constraints on the atmosphere in eclipse, *Icarus*, *214*, 495–509.

Saur, J. (2004), A model of Io's local electric field for a combined Alfvénic and unipolar inductor far-field coupling, *J. Geophys. Res.*, *109*(A18), 1210.

Saur, J., and D. F. Strobel (2004), Relative contributions of sublimation and volcanoes to Io's atmosphere inferred from its plasma interaction during solar eclipse, *Icarus*, *171*, 411–420.

Saur, J., D. F. Strobel, and F. M. Neubauer (1998), Interaction of the Jovian magnetosphere with Europa: Constraints on the neutral atmosphere, *J. Geophys. Res.*, *103*, 19,947–19,962.

Saur, J., F. M. Neubauer, D. F. Strobel, and M. E. Summers (1999), Three-dimensional plasma simulation of Io's interaction with the Io plasma torus: Asymmetric plasma flow, *J. Geophys. Res.*, *104*, 25,105–25,126.

Saur, J., F. M. Neubauer, D. F. Strobel, and M. E. Summers (2002), Interpretation of Galileo's Io plasma and field observations: I0, I24, and I27 flybys and close polar passes, *J. Geophys. Res.*, *107*, 1422.

Saur, J., F. M. Neubauer, J. E. P. Connerney, P. Zarka, and M. G. Kivelson (2004), Plasma interaction of Io with its plasma torus, in *Jupiter. The Planet, Satellites and Magnetosphere*, edited by Bagenal, F., Dowling, T. E., & McKinnon, W. B., pp. 537–560, Cambridge Univ. Press.

Saur, J., F. M. Neubauer, and K. Glassmeier (2010), Induced Magnetic Fields in Solar System Bodies, *Space Sci. Rev.*, *152*, 391–421.

Schilling, N. (2006), Time Varying Interaction of Europa's Atmosphere-Ionosphere and its Conducting Ocean with the Jovian Magnetosphere, Dissertation, Institut für Geophysik und Meteorologie der Universität zu Köln.

Schilling, N., F. M. Neubauer, and J. Saur (2007), Time-varying interaction of Europa with the jovian magnetosphere: Constraints on the conductivity of Europa's subsurface ocean, *Icarus*, *192*, 41–55.

Schilling, N., F. M. Neubauer, and J. Saur (2008), Influence of the internally induced magnetic field on the plasma interaction of Europa, *J. Geophys. Res.*, *113*(A12), 3203.

Schmucker, U. (1985), Magnetic and electric fields due to electromagnetic induction by external sources, in *Landolt-Börnstein New-Series*, vol. V/2 Subvolume B, pp. 100–125, Springer-Verlag.

Schubert, G., J. D. Anderson, T. Spohn, and W. B. McKinnon (2004), Interior composition, structure and dynamics of the Galilean satellites, in *Jupiter. The Planet, Satellites and Magnetosphere*, edited by Bagenal, F., Dowling, T. E., & McKinnon, W. B., pp. 281–306, Cambridge Univ. Press.

Schubert, G., F. Sohl, and H. Hussmann (2009), Interior of Europa, in *Europa*, edited by Pappalardo, R. T., McKinnon, W. B., & Khurana, K. K., p. 353, Univ. of Arizona Press.

Schunk, R. W., and A. F. Nagy (2000), *Ionospheres - Physics, Plasma Physics, and Chemistry*, Cambridge, UK: Cambridge University Press.

Seidelmann, P. K., and N. Divine (1977), Evaluation of Jupiter longitudes in System III (1965), *Geophys. Res. Lett.*, *4*, 65–68.

Seufert, M., J. Saur, and F. M. Neubauer (2011), Multi-frequency electromagnetic sounding of the Galilean moons, *Icarus*, *214*, 477–494.

Showman, A. P., and R. Malhotra (1997), Tidal Evolution into the Laplace Resonance and the Resurfacing of Ganymede, *Icarus*, *127*, 93–111.

Simon, S., A. Bößwetter, T. Bagdonat, U. Motschmann, and K.-H. Glassmeier (2006), Plasma environment of Titan: a 3-D hybrid simulation study, *Annales Geophysicae*, *24*, 1113–1135.

Sohl, F., T. Spohn, D. Breuer, and K. Nagel (2002), Implications from Galileo Observations on the Interior Structure and Chemistry of the Galilean Satellites, *Icarus*, *157*, 104–119.

Spohn, T., and G. Schubert (2003), Oceans in the icy Galilean satellites of Jupiter?, *Icarus*, *161*, 456–467.

Stacey, F. (1992), *Physics of the Earth*, Brookfield Press, Brisbane.

Stone, J. M., and M. L. Norman (1992a), ZEUS-2D: A radiation magnetohydrodynamics code for astrophysical flows in two space dimensions. I - The hydrodynamic algorithms and tests., *Astrophys. J. Suppl. Ser.*, *80*, 753–790.

Stone, J. M., and M. L. Norman (1992b), ZEUS-2D: A Radiation Magnetohydrodynamics Code for Astrophysical Flows in Two Space Dimensions. II. The Magnetohydrodynamic Algorithms and Tests, *Astrophys. J. Suppl. Ser.*, *80*, 791.

Stone, J. M., D. Mihalas, and M. L. Norman (1992), ZEUS-2D: A radiation magnetohydrodynamics code for astrophysical flows in two space dimensions. III - The radiation hydrodynamic algorithms and tests, *Astrophys. J. Suppl. Ser.*, *80*, 819–845.

Strobel, D. F., J. Saur, P. D. Feldman, and M. A. McGrath (2002), Hubble Space Telescope Space Telescope Imaging Spectrograph Search for an Atmosphere on Callisto: A Jovian Unipolar Inductor, *Astrophys. J. Lett.*, *581*, L51–L54.

Vigelius, M., and A. Melatos (2009), Resistive relaxation of a magnetically confined mountain on an accreting neutron star, *Mon. Not. R. Astron. Soc.*, *395*, 1985–1998.

Waff, H. S., and D. F. Weill (1975), Electrical Conductivity of Magmatic Liquids: Effects of Temperature, Oxygen Fugacity and Composition, *Earth and Planetary Science Letters*, *28*, 254–260.

Ward, W. R., and R. M. Canup (2006), The Obliquity of Jupiter, *Astrophys. J. Lett.*, *640*, L91–L94.

Weiss, J. W. (2004), Appendix 2: Planetary parameters, in *Jupiter. The Planet, Satellites and Magnetosphere*, edited by Bagenal, F., Dowling, T. E., & McKinnon, W. B., pp. 699–706, Cambridge Univ. Press.

Zhang, H. (2003), Internal Structure models and Dynamical Parameters of the Galilean Satellites, *Cel. Mech. and Dynam. Astron.*, *87*, 189–195.

Zimmer, C., K. K. Khurana, and M. G. Kivelson (2000), Subsurface oceans on Europa and Callisto: Constraints from Galileo magnetometer observations, *Icarus*, *147*, 329–347.

Danksagung

Zunächst möchte ich mich bei Prof. Dr. Joachim Saur bedanken. Seine Begeisterung für die extraterrestrische Geophysik, sein profundes wissenschaftliches Know-how und seine zuvorkommende Art waren häufig eine wichtige Motivationsquelle für meine Arbeit. Zudem möchte ich mich für das große Vertrauen bedanken, das er zu jeder Zeit meinen wissenschaftlichen Fertigkeiten entgegenbrachte.

Des Weiteren danke ich Prof. Dr. Fritz M. Neubauer für seine stets hilfreichen und zielführenden wissenschaftlichen Ratschläge. Ich fühle mich sehr geehrt, dass ich an seinem enormen wissenschaftlichen Erfahrungsschatz teilhaben durfte. Zudem möchte ich mich bei ihm für die Übernahme des Koreferats trotz seiner Emeritierung bedanken.

Ein besonderer Dank gebührt Fabrizio Musacchio, Michael von Papen, Emmanuel Chané und Stefan Duling für das Lektorat verschiedener Teile dieser Arbeit sowie für viele interessante und freundschaftliche Diskussionen.

Für die ausführlichen wissenschaftlichen und persönlichen Diskussionen möchte ich meinem Zimmerkollegen Lorenz Roth danken, der mit mir zusammen die langen Tage, Wochenenden und Nächte der Endphase unserer Promotion durchgestanden hat. Ein nicht minderer Dank für den regen wissenschaftlichen Austausch und lehrreiche Diskussionen gebührt auch Sven Simon.

Weiterhin danke ich Alexandre Wennmacher für eine stets lehrreiche und freundschaftliche Zusammenarbeit in der Systemgruppe unseres Instituts sowie in den Lehrveranstaltungen zur Datenverarbeitung und Programmierung. Von seiner großen Erfahrung in den unterschiedlichsten Bereichen der Informatik habe ich viele Male während meiner wissenschaftlichen Arbeit profitiert.

Bedanken möchte ich mich auch bei meinen ehemaligen Zimmerkollegen und Kommilitonen Sven Jacobsen, Nico Schilling und Anna Müller sowie allen weiteren Mitarbeitern des Instituts für Geophysik und Meteorologie in Köln, die meine Studienzeit stets mit Freude sowie mit Begeisterung für die wissenschaftliche Arbeit erfüllten.

Schließlich möchte ich mich bei meinen Eltern, meinem Bruder und meinen Großeltern für die moralische Hilfe während der letzten Jahre bedanken. Ein besonders großer Dank gebührt zuletzt meiner Frau Gabi. Ohne ihre liebevolle und geduldige Unterstützung wäre sicher ein Großteil meiner Arbeit nicht möglich gewesen. Insbesondere während ihrer Schwangerschaft in der Endphase meiner Promotion stand sie mir stets hilfreich und fürsorglich zur Seite.

Ich versichere, dass ich die von mir vorgelegte Dissertation selbständig angefertigt, die benutzten Quellen und Hilfsmittel vollständig angegeben und die Stellen der Arbeit - einschließlich Tabellen, Karten und Abbildungen -, die anderen Werken im Wortlaut oder dem Sinn nach entnommen sind, in jedem Einzelfall als Entlehnung kenntlich gemacht habe; dass diese Dissertation noch keiner anderen Fakultät oder Universität zur Prüfung vorgelegen hat; dass sie - abgesehen von unten angegebenen Teilpublikationen - noch nicht veröffentlicht worden ist sowie, dass ich eine solche Veröffentlichung vor Abschluss des Promotionsverfahrens nicht vornehmen werde. Die Bestimmungen dieser Promotionsordnung sind mir bekannt. Die von mir vorgelegte Dissertation ist von Prof. Dr. Joachim Saur betreut worden.

Köln, August 2012 Mario Seufert

Teilpublikationen

Seufert, M., Saur, J., Neubauer, F. M., Multi-frequency electromagnetic sounding of the Galilean moons., Icarus, 214, 477-494, 2011.